

University of Alberta

**High Resolution Mid-Infrared Spectroscopy of Molecular
Complexes Containing Water and Ammonia**

by

Xunchen Liu

A thesis submitted to the Faculty of Graduate Studies and Research
in partial fulfillment of the requirements for the degree of

Doctor of Philosophy

Department of Chemistry

©Xunchen Liu
Spring 2013
Edmonton, Alberta

Permission is hereby granted to the University of Alberta Libraries to reproduce single copies of this thesis and to lend or sell such copies for private, scholarly or scientific research purposes only. Where the thesis is converted to, or otherwise made available in digital form, the University of Alberta will advise potential users of the thesis of these terms.

The author reserves all other publication and other rights in association with the copyright in the thesis and, except as herein before provided, neither the thesis nor any substantial portion thereof may be printed or otherwise reproduced in any material form whatsoever without the author's prior written permission.

To My Mother

Abstract

In this thesis, the results of high resolution molecular spectroscopic studies of several prototype molecular complexes containing either water or ammonia molecule and the instrumentation development of an infrared spectrometer which is used to carry out the main part of the experimental work are reported.

Quantum Cascade Lasers are utilized as the infrared light source for the infrared spectrometer. To increase the sensitivity and resolution of the spectrometer, several spectroscopic techniques such as cavity enhanced absorption and frequency modulation techniques are evaluated. The rapid scan techniques with an astigmatic multipass cell is found to be the most suitable combination to measure the bending modes of the water or ammonia in the $6\ \mu\text{m}$ region.

Several prototype molecular complexes held together by intermolecular hydrogen bond or van der Waals forces are investigated. The microwave spectra of four conformers of the 2-fluoroethanol complex are measured to investigate the self-recognition effects of the transient chiral molecules. The binary Ar-H₂O complex is extensively investigated to identify a number of previously unidentified internal rotor states, which are modeled by the pseudo-diatomic Hamiltonian with Fermi resonance and Coriolis coupling terms. Spectra of the related van der Waals complexes including the Ne-H₂O, Ar-NH₃, and Ne-NH₃ complexes are also studied. The high resolution infrared spectra and the microwave spectra of the HCCH-NH₃ and OCS-NH₃ complexes reveal that the structure of both complexes are C_{3v} symmetric semi-rigid rotors, which provides a unique opportunity to compare the weak C-H \cdots N hydrogen bond interaction and S \cdots N bond. The high

resolution infrared spectra of the propylene oxide-(water)_{*N*} complexes are measured in order to elucidate the sequential solvation of a chiral molecule and to aid in the interpretation of chirality transfer events observed in aqueous solutions of chiral molecules.

Acknowledgements

Foremost, I owe an immense debt of gratitude to my supervisor Dr. Yunjie Xu for the continuous support of my Ph.D study and research. I would like to express my most sincere appreciation for her patience, enthusiam, motivation, and immense knowledge. Her guidance helped me in all the time of research and writing of this thesis. I am very grateful for the considerable latitude and independence she has allowed me in research.

Besides my advisor, I would like to thank the rest of my thesis committee: Prof. Frank Hegmann, Prof. Michael Serpe, Prof. Rod Wasylshen, Prof. Alex Brown, Prof. Gabriel Hanna, and Prof. Nasser Moazzen-Ahmadi for their encouragement, invaluable advice, insightful comments and detailed changes to the errors and typos in this thesis.

My sincere thanks also goes to Dr. Wolfgang Jäger and the colleagues in the high resolution spectroscopy group: Javix Thomas, PeiYan Zhu, Zahra Dezhahang, Mohammad Reza Poopari, Steve Dempster, Chrisay Knapp, Elijah Schnitzl, Dr. Christian Merten, Dr. M. Qamrul Huda, T. M. Fahim Amin, Dr. Jagadeeshwari Manne, Dr. Fumie Sunahori, Jensen Yiu, Johannes Rebling, Andre Charbonneau, Igor Leonov, Liu Yang, Dr. Guochun Yang, Dr. Zheng Su, Dr. Qing Wen, Dr. Nicole Borho, Dr. Rudolf Lehnig, Dr. Julie M. Michaud, Jennifer Landry, Dr. Martin Losada, Dr. Matthew Parsons, Dr. Paul Raston, Dr. Oleksandr Sukhorukov, Ihor Sydoryk, Bie Zhi, XiaoDan Deng, Qi Yi Tracy Lei, Nan Nan Sun, and all the other members of the Center for Molecular Structure and Dynamics: Dr. Mariusz Klobukowski, Dr. John Klassen, Dr. Gabriel Hanna, Sun Shuai,

Ryan Zaari, Stephanie Wong. Discussions with Dr. Pierre-Nicholas Roy, Dr. Zeng Tao, Dr. Wang Xiao Gang, Dr. Li Hui greatly helped my research.

I want to thank the funding agencies for the scholarships: Alberta Ingenuity, NSERC, and BMO financial group. My Ph.D study in the Department of Chemistry, University of Alberta is helped by Dr. D. Jed Harrison, Dr. Charles A. Lucy, Dr. Josef Takats, Dr. Todd L. Lowary and members of the machine shop: Dirk Kelm, Randy Benson, Paul Crothers, and Allan Chilton, Kim Do of electronics shop.

I am grateful to Dr. Yu Xiang Bu from Shandong University for enlightening me the first glance of research. I want to thank all my friends in Edmonton and other places, Dr. Xuefeng Zhang, Dr. Dong Li, Fu Jie and Liu Yang for their friendship.

This thesis is dedicated in loving memory to my mother Liu Ling Shu who passed during my Ph.D study and sacrificed so much for me. She must be very pleased to know that I received my Ph.D degree. I would also like to thank my father Liu Cheng Zhong who has always been my best-friend and spiritual support.

Contents

List of Tables

List of Figures

1	Introduction	1
2	Molecular Spectroscopy	8
2.1	Introduction	8
2.2	Molecular Hamiltonian	11
2.2.1	Molecular Rovibrational Hamiltonian	14
2.2.2	Perturbations	17
2.3	Harmonic and Anharmonic Oscillators	20

CONTENTS

2.3.1	Harmonic Oscillator	20
2.3.1.1	Non-degenerate Harmonic Oscillator	20
2.3.1.2	Doubly-degenerate Isotropic Harmonic Oscillator	21
2.3.2	Anharmonic Oscillator	22
2.4	Rigid Rotor and Semi-rigid Rotor	26
2.4.1	Rotational Energy Levels of Rigid Rotors	26
2.4.1.1	Spherical Top, Diatomic and Linear Molecules	27
2.4.1.2	Symmetric Top Molecules	29
2.4.1.3	Asymmetric Top Molecules	29
2.4.2	Centrifugal Distortion Constants	34
2.4.2.1	Diatomic Molecules and Linear Molecules	34
2.4.2.2	Symmetric Top Molecules	35
2.4.2.3	Asymmetric Top Molecules	36
2.4.3	Coriolis Coupling	37
2.4.3.1	Perpendicular Band of Linear or Symmetric Top Molecules	38
2.4.3.2	Second Order Coriolis Coupling	39
2.4.4	Atom-Asymmetric Top van der Waals Complex	40
2.5	Rovibrational Transitions	43
2.5.1	Vibrational Transitions	45
2.5.2	Rovibrational Transitions	47
2.5.2.1	Linear and Symmetric Top Molecules	47
2.5.2.2	Asymmetric Top Molecules	50
2.5.3	Population Distribution of Rovibrational States	51
2.5.3.1	Boltzmann Distortion	51
2.5.3.2	Spin Statistical Weights	53
2.5.4	Fitting of Spectroscopic Constants	54

3 Molecular Self-Recognition: Rotational Spectra of the Dimeric

2-Fluoroethanol Conformers	56
3.1 Introduction	57
3.2 Methods	58
3.2.1 Experimental Details	58
3.2.2 Computational Methods	59
3.3 Results	59
3.3.1 Preliminary Model Calculations	59
3.3.2 Assignment of the FE Dimer Rotational Spectra	61
3.4 Discussions	68
3.4.1 Stability Order of the Dimeric FE Conformers	68
3.4.2 Comparison with the Previous Studies of the FE and Ethanol Dimers	71
3.5 Conclusions	73
4 Experimental Instrumentation	74
4.1 Introduction	75
4.2 The Light Source	81
4.2.1 The Distributed-Feedback QCL	81
4.2.2 The External-Cavity QCL	84
4.3 Vacuum Chamber and Slit Jet	87
4.4 Ring-Down Cavity	93
4.5 Astigmatic Multipass Absorption Cavity	95
4.6 Data Acquisition and Control	98
4.6.1 Rapid Scan Method	98
4.6.2 Wavelength Modulation (WLM) Method	101
4.6.3 Frequency Calibration	104
4.7 Experimental Results with MPA Spectrometer	110
4.7.1 Room-Temperature Nitrous Oxide Spectra (N ₂ O)	111
4.7.1.1 Rapid Scan Spectra of N ₂ O	111
4.7.1.2 Wavelength-Modulation Spectra of N ₂ O	114
4.7.2 Jet-cooled Ar-para-water Spectra	116

4.7.2.1	Rapid Scan Spectra of Jet-Cooled Ar- <i>para</i> -water	116
4.7.2.2	Wavelength-Modulation Spectra of Ar- <i>para</i> -water	119
4.8	Experimental Results with CEA Spectrometer	123
4.8.1	Room-Temperature Molecules	123
4.8.1.1	NH ₃ Measured with Distributed-Feedback QCL .	123
4.8.1.2	N ₂ O Measured with External-Cavity QCL	125
4.8.2	Jet-Cooled Complex	128
4.8.2.1	Methyl Lactate Measured with Distributed-Feedback QCL	128
4.8.2.2	Ar-water Measured with External-Cavity QCL .	129
4.9	Conclusion	131

5 High Resolution Infrared Spectra of Binary Molecular

Complexes of A Rare gas atom and Water or Ammonia		133
5.1	High Resolution Infrared Spectra of Ar-H ₂ O Complex	134
5.1.1	Introduction	134
5.1.1.1	Potential Energy Surface of the binary complex of a rare gas atom and water	135
5.1.1.2	Nearly free internal rotor model of Ar-H ₂ O complex	138
5.1.1.3	Previous Measurement	142
5.1.2	Results and Discussion	145
5.1.2.1	$n = 1, (1_{01})$ states	146
5.1.2.2	(2_{12}) states	150
5.1.2.3	Ambiguous bands	156
5.1.3	Discussion	165
5.1.4	Conclusion	169
5.2	High Resolution Infrared Spectra of Ne-H ₂ O	171
5.2.1	Introduction	171
5.2.2	Results	172

5.2.3	The He-H ₂ O complex	177
5.3	High Resolution Infrared Spectra of “Ar+NH ₃ ” and Ne-NH ₃	181
5.3.1	“Ar+NH ₃ ” Complex	181
5.3.2	Ne-NH ₃ Complex	184

6 Infrared and microwave spectra of the acetylene-ammonia and

carbonyl sulfide-ammonia complexes		193
6.1	Introduction	194
6.2	Microwave and Infrared Experiments	196
6.3	Results	196
6.3.1	<i>Ab initio</i> Calculations	196
6.3.2	The HCCH-NH ₃ Complex	198
6.3.3	The OCS-NH ₃ Complex	202
6.4	Discussion	213
6.4.1	Structure and Dynamics	213
6.4.2	Dissociation energies	216
6.4.3	Calculations of electrostatic interactions	217
6.5	Conclusions	220
6.6	Propylene Oxide (PO)-(water) _N complex	220

7 Conclusions 230

A Measurement of Infrared Frequency	233
A.1 Frequency standard	233
A.2 HITRAN database	234

A.3 Spectra line shape	236
A.4 Detection Limit	239
B The Classical Treatment of Molecular Vibration and Rotation	241
B.1 Rigid Rotor	242
B.1.1 Definition of the rigid rotor coordinate	242
B.1.2 Moment of inertia	243
B.1.3 Dynamics of rigid rotor	247
B.2 Separation of Rotations and Vibrations	248
B.3 Normal mode Vibration	250
B.4 Classical rotation-vibration Hamiltonian	251
C Angular momentum	253
C.1 Operators	253
C.1.1 compatible operators	254
C.1.2 Incompatible operators	254
C.2 Eigenstates	255
C.3 Eigenfunctions	256
D Order of Magnitude	258
E Supersonic Free Jet Expansion	260

CONTENTS

F Confocal Off-axis cell	265
G Interference fringes	269
H Nuclear Quadrupole Interaction	270
I Supplementary Materials for Chapter 3	272
References	280

List of Tables

2.1	Identification Convention Table	27
2.2	Group characters of the $D_2(V)$ group	31
2.3	Rotational energy levels of asymmetric top rigid rotor	32
2.4	C_{2v} Character Table	46
2.5	Hönl-London Factors	49
3.1	Binding energies and spectroscopic constants from <i>ab initio</i> calculation of FE dimer	62
3.2	Experimental parameters of FE dimer	65
3.3	Distortion and Interaction energies of FE dimer	70
4.1	Frequency calibration: Etalon fringe	108
4.2	Frequency calibration with reference lines	109
5.1	<i>ortho</i> ArH ₂ O transitions	149
5.2	<i>ortho</i> ArH ₂ O transitions	153
5.3	Spectroscopic constants of internal rotor states of <i>ortho</i> ArH ₂ O	157
5.4	<i>ortho</i> ArH ₂ O transitions	159
5.5	<i>ortho</i> ArH ₂ O transitions	160
5.6	Fitted spectroscopic constants of the bands that cannot be unambiguously assigned.	165

LIST OF TABLES

5.7	$\Sigma - \Pi$ splitting of the internal rotor state of Ar-H ₂ O	170
5.8	Averaged internal rotor state of Ar-H ₂ O	170
5.9	Ne-H ₂ O transitions	174
5.10	Spectroscopic Constants of Ne-H ₂ O	174
5.11	“Ar-NH ₃ ” transitions	187
5.12	Spectroscopic Constants of “Ar-NH ₃ ”	188
6.1	<i>Ab initio</i> calculation of HCCH-NH ₃ and OCS-NH ₃	205
6.2	Microwave transitions of HCCH-NH ₃ and OCS-NH ₃	207
6.3	Infrared transitions of HCCH-NH ₃ and OCS-NH ₃	208
6.4	Fitted spectroscopic constants for HCCH-NH ₃	209
6.5	Fitted spectroscopic constants for OCS-NH ₃	210
6.6	Structural constants for HCCH-NH ₃ and OCS-NH ₃	216
6.7	Electrostatic interaction energies of HCCH-NH ₃ and OCS-NH ₃ (in kJ/mol)	218
6.8	Spectroscopic constants of PO-H ₂ O	226
6.9	Spectroscopic constants of PO-(H ₂ O) ₂	227

List of Figures

2.1	Electromagnetic radiation range and orders of magnitude	10
2.2	The harmonic and the Morse potentials	23
2.3	The wave functions of the harmonic and anharmonic oscillators . .	24
2.4	Rovibrational energy levels and spectrum of a linear molecule . .	28
2.5	Correlation between the asymmetric rotor energy levels and the symmetric top rotor energy levels	31
2.6	Rovibrational energy levels of H_2^{16}O in ground and $\nu_2=1$ bending states	33
2.7	Schematic diagram of the P, Q, R branches of a linear molecule . .	48
2.8	A typical spectrum of P, Q, R branches of a linear molecule	48
2.9	Rovibrational transitions of the $\nu_2=1$ bending band of H_2^{16}O . . .	52
3.1	Optimized geometries of the six dimeric FE conformers	63
3.2	Microwave spectrum of the FE dimer	67
3.3	Scheme of binding energies	72
4.1	Energy diagram and TEM picture of QCL	76
4.2	Tunable external-cavity diode lasers	77
4.3	Design of the external cavity QCL (EC-QCL) system	78

LIST OF FIGURES

4.4	Schematic diagram of the slit-jet QCL cavity enhanced absorption (CEA) spectrometer	79
4.5	Schematic diagram of the slit-jet QCL multipass absorption (MPA) spectrometer	79
4.6	Picture of the spectrometer (Side View)	80
4.7	Picture of the spectrometer (Top View)	81
4.8	The DFB QCL	82
4.9	Laser head of the External Cavity QCL	84
4.10	PZT scan of the External-Cavity QCL	86
4.11	Drawing of homemade nozzle body (4 cm)	89
4.12	Drawing of homemade nozzle caps (4 cm)	90
4.13	Drawing of homemade nozzle body (8 cm)	91
4.14	Drawing of homemade nozzle caps (8 cm)	92
4.15	On-axis and Off-axis alignment of ring-down cavity	94
4.16	Geometry of the astigmatic cell	95
4.17	“Space Map” of the AMAC-100 astigmatic cell	97
4.18	Astigmatic multipass absorption cavity	97
4.19	Rapid Scan	99
4.20	Rapid Scope	99
4.21	<i>step-scan</i> WLM scheme	103
4.22	Averaging of raw data	106
4.23	Procedure of frequency calibration	107
4.24	Rough scan of the QCL	111
4.25	Room temperature N ₂ O spectrum	112
4.26	WLM spectra of room temperature H ₂ ¹⁷ O	115
4.27	WLM spectra of N ₂ O	115
4.28	Rapid scan and WLM spectra of N ₂ O	116
4.29	Rapid scan spectrum of Ar- <i>para</i> -water	117
4.30	Rapid scan spectrum of Ar- <i>para</i> -water	118
4.31	step scan WLM spectrum of N ₂ O R(1) line	119
4.32	Rapid scan and WLM spectra of N ₂ O R(1) line	120
4.33	<i>Pseudo-cw-jet</i> WLM spectra of Ar- <i>para</i> -water	121
4.34	Effects of modulation depth	122

LIST OF FIGURES

4.35 Room temperature NH ₃ spectra measure with CEA spectrometer	124
4.36 Rapid Scan and WLM spectra of N ₂ O	126
4.37 WLM spectra of N ₂ O measured with CEA spectrometer	127
4.38 Room temperature and jet spectra of methyl lactate	129
4.39 Rapid scan and WLM spectra of Ar- <i>para</i> -water	130
5.1 Geometry of the Ar-H ₂ O complex	136
5.2 The AW2 Potential Energy Surface	137
5.3 The <i>ab initio</i> Potential Energy Surface of Ar-H ₂ O	137
5.4 The lowest rotational energy levels of H ₂ O.	139
5.5 Classical depiction of the internal rotor states of Ar-H ₂ O	141
5.6 Internal rotor states of <i>ortho</i> Ar-H ₂ O complex.	143
5.7 Internal rotor states of <i>para</i> Ar-H ₂ O complex.	144
5.8 The $n = 1, \Pi(1_{01}) \leftarrow \Sigma(1_{01})$ band of <i>ortho</i> Ar-H ₂ O	147
5.9 The complicated spectral feature of Ar-H ₂ O at 1630 cm ⁻¹	148
5.10 The $\Pi(2_{12}) \leftarrow \Pi(1_{01})$ band	151
5.11 The $\Pi(2_{12}) \leftarrow \Sigma(1_{01})$ band	154
5.12 The $\Sigma(2_{12}) \leftarrow \Sigma(1_{01})$ band	155
5.13 The “ $n = 1, \Pi(2_{12}) \leftarrow \Pi(1_{01})$ ” band at 1664 cm ⁻¹	161
5.14 The “ $n = 1, \Sigma(2_{12}) \leftarrow \Pi(1_{01})$ ” band at 1655 cm ⁻¹	162
5.15 The “ $n = 1, \Sigma(1_{11}) \leftarrow \Sigma(0_{00})$ ” band of <i>para</i> Ar-H ₂ O	163
5.16 Internal rotor states of Ar-H ₂ O complex	164
5.17 The rovibrational energy levels of H ₂ O and H ₂ O subunit in Ar-H ₂ O	168
5.18 Equilibrium geometries of Rg-H ₂ O complexes	172
5.19 The $\Pi(1_{10}) \leftarrow \Sigma(1_{01})$ band of Ne-H ₂ O	173
5.20 The $\Sigma(1_{10}) \leftarrow \Pi(1_{01})$ band of Ne-H ₂ O	175
5.21 The internal rotor states of <i>ortho</i> Ne-H ₂ O	176
5.22 The $\Pi(1_{11}) \leftarrow \Sigma(0_{00})$ band of Ne-H ₂ O	178
5.23 The “ $n = 1, \Sigma(0_{00}) \leftarrow \Sigma(0_{00})$ ” band of Ne-H ₂ O	179
5.24 The internal rotor states of <i>para</i> Ne-H ₂ O	180
5.25 Internal rotor states of the <i>ortho spin</i> modification of the Ar-NH ₃ complex	182

LIST OF FIGURES

5.26	Internal rotor states of the <i>para</i> spin modification of the Ar-NH ₃ complex	183
5.27	$\Sigma(1_1) \leftarrow \Sigma(0_0)$ band of <i>ortho</i> "Ar+NH ₃ "	185
5.28	$\Pi(1_1) \leftarrow \Sigma(0_0)$ band of <i>ortho</i> "Ar-NH ₃ "	186
5.29	The $\Pi(1_1) \leftarrow \Sigma(0_0)$ band of Ne-NH ₃	189
5.30	Ne-NH ₃ spectrum	190
5.31	Spectrum of larger clusters of Ne and NH ₃	191
6.1	High resolution infrared spectrum of HCCH-NH ₃	200
6.2	High resolution infrared spectrum of HCCH-NH ₃	206
6.3	Proposed Fermi resonance causing the shift of $K=1$ level of HCCH-NH ₃	210
6.4	Microwave spectra of HCCH-NH ₃ and OCS-NH ₃	211
6.5	High resolution infrared spectrum of OCS-NH ₃	212
6.6	Structure of HCCH-NH ₃ and OCS-NH ₃	213
6.7	Electrostatic potential of HCCH-NH ₃	219
6.8	Electrostatic potential of HCCH-NH ₃	219
6.9	Geometry of PO-H ₂ O	222
6.10	Geometry of PO-(H ₂ O) ₂	222
6.11	Spectrum of PO water complexes from 1650 cm ⁻¹ to 1655 cm ⁻¹	223
6.12	Spectrum of PO water complexes from 1655 cm ⁻¹ to 1660 cm ⁻¹	223
6.13	Spectrum of PO water complexes from 1660 cm ⁻¹ to 1665 cm ⁻¹	224
6.14	Spectrum of PO water complexes from 1665 cm ⁻¹ to 1670 cm ⁻¹	224
6.15	Spectrum of PO water complexes from 1670 cm ⁻¹ to 1675 cm ⁻¹	225
6.16	Spectrum of PO water complexes from 1675 cm ⁻¹ to 1680 cm ⁻¹	225
6.17	Simulation of PO-H ₂ O spectrum	229
A.1	HITRAN line-by-line parameters	235
B.1	Euler angles	242
B.2	Space-fixed and body-fixed coordinate	244
B.3	Plot of a prolate and an oblate spheroid	247
B.4	Poinsot's construction	248
E.1	Velocity distribution in a Supersonic free jet expansion	261

LIST OF FIGURES

E.2	Spectra of NO ₂ in supersonic beam	262
E.3	Supersonic free jet expansion	263
E.4	Simulation of temperature, pressure and density in supersonic free jet expansion	264
F.1	Beam geometry in a Herriott cell	266

1

Introduction

The research described in this thesis falls into the general category of high resolution molecular spectroscopy of intermolecular interactions. The emphasis is on the studies of water- and ammonia-containing complexes using high resolution infrared laser spectroscopy, although complementary work in the microwave region has also been carried out. To study intermolecular interactions, binary and larger molecular complexes have been generated in a pulsed supersonic free jet expansion since such complexes are typically unstable at room temperature. Two major instruments have been used in this work: a cavity-based pulsed Fourier transform microwave spectrometer and a quantum cascade laser based infrared absorption spectrometer with an astigmatic multipath cell built as part of this work. A number of prototype molecular complexes held together by intermolecular hydrogen bond and van der Waals forces have been investigated. Also, recent progress in high resolution spectroscopy of intermolecular interactions relevant to my thesis work is first highlighted. The motivations for the projects described in this thesis are then presented, followed by a discussion of the advantages of high resolution spectroscopy. Finally, the results presented in the subsequent chapters are briefly introduced.

High resolution spectroscopy determines the rotationally resolved energy levels of isolated molecules. In combination with a supersonic jet expansion, it has been widely used in the last two decades to characterize the interactions in complexes consisting of atoms and simple molecules.^(11, 298, 295, 117) High resolution infrared spectra are measured for single molecular complex in the gas phase at extremely low temperatures with high frequency resolution. Under such conditions, each peak in the low resolution infrared spectrum becomes a series of

sharp lines that can be associated with changes of the rotational-vibrational energy states of a molecular complex. For transitions between rotational states on the *ground* vibrational level, the transition frequency is in the microwave range. Microwave spectroscopy and high resolution infrared spectroscopy can accurately capture various information about the molecular complex, such as bond length, bond angle, and the strength of the bond connecting the vibrating atoms. They provide the most accurate information about the potential energy surface (PES) for both small molecules with strong covalent bonds and weakly-bound molecular complexes. The models used to interpret the rotational-vibrational energy levels provide us with unique and irreplaceable insight into the molecular complexes.

There has been significant progress in the past ten years in high resolution spectroscopic investigations of molecular complexes both in terms of the size and complexity of the molecular system studied and of frequency coverage. For small molecular complexes containing a small number of atoms, the PES of the molecular complex can be obtained from *ab initio* calculations and the rotation-vibration wave function can be calculated. Measurements of the high resolution infrared and microwave spectra of these systems provide stringent tests of the quantum mechanical calculations. These spectroscopic studies of such clusters have greatly enriched our understanding of intermolecular interactions and provided the essential steps to build a link between the properties of bulk matter and the properties of the constituent atoms and molecules. For example, the pure rotational studies of helium clusters doped with a polar linear molecule have provided a unique opportunity to probe superfluidity, a formally bulk property, at the molecular level with atom-by-atom resolution.(252, 292, 293, 166, 291, 247, 210, 209, 117)

More recently, N. Moazzen-Ahmadi, A. R. W. McKellar and co-workers have, for the first time, been able to clearly identify the high resolution infrared spectra of carbon dioxide clusters from dimer up to 13 CO₂ subunits.(214, 191) This and their later publications(213) provide new insights into the transition between gas phase and condensed phase carbon dioxide and other small linear molecules. For larger molecular complexes that are too large to be completely solved from first principles, intermolecular functions can be used to obtain the equilibrium geometries. The work is also of importance because of the significant role carbon dioxide plays in atmospheric chemistry and because of the substantial use of supercritical carbon dioxide as an industrial solvent. Intermolecular forces play a key role in this transition region from small molecular systems to the packing of a large number molecules to obtain molecular clusters. These studies represent

the missing link between single molecules or molecular pairs and the bulk liquid or solid phases.

A particularly interesting aspect of intermolecular interactions is the chirality recognition effect, which refers to the omnipresent, fascinating ability of nature to discriminate between right- and left-handed forms (called enantiomers) of chiral molecules. For example, our nose can distinguish the left-handed carvone, a naturally occurring compound found in caraway seeds, that smells like cumin, from the right-handed carvone, an extract from spearmint that smells like mint. High resolution spectroscopy offers great promises for the studies of chiral molecular systems. Xu and co-workers have investigated a number of chiral molecular contact pairs using Fourier transfer microwave spectroscopy where the molecular subunits involved carry either permanent stereogenic centers or possess only transient chirality, which often have an amazingly large number of possible conformers that have different equilibrium geometries.(32, 34, 36, 141, 255) As a junior graduate student, I investigated the of self-recognition phenomena in the binary 2-fluoroethanol complex using rotational spectroscopy. 2-fluoroethanol is a transient chiral molecule and its four binary conformers were unambiguously identified and their recognition process discussed. The molecular self-recognition in the four dimeric 2-fluoroethanol conformers studied by microwave spectroscopy is presented in Chapter 3.

To link the chirality recognition events of isolated chiral contact pairs in the gas phase to the biological chirality recognition events in aqueous solution, there are many other additional factors one needs to consider. One of them is the interactions of chiral molecules with water molecules since the associated chiral molecule-water interaction energies are of similar order of magnitude as those involved in chirality recognition. The Xu research group has reported a number of the earliest studies on the effects of “chirality transfer” from chiral solute molecules to water solvent molecules using vibrational circular dichroism (VCD) spectroscopy.(146, 145, 299, 300) Chirality transfer refers to the phenomena when water vibrational bands, such as the water bending band, show chiroptical responses in aqueous solution with a chiral solute because of the formation of chiral molecule-(H₂O)_N clusters, which reveals the solvation mechanism of the chiral molecule in liquid water. Although complexes of chiral molecules with water and other organic solvents have been studied in the microwave region,(242, 244, 245) no such chiral complexes have been studied using high resolution infrared spectroscopy so far. In order to probe such chiral molecule-(water)_N clusters in detail using high resolution infrared spectroscopy, I built a high-sensitivity infrared

spectrometer to detect such species to study other molecular complexes of interest. The measured high resolution infrared spectra and preliminary studies of the propylene oxide-(water)_N clusters are discussed in Sec. 6.6.

Both high-resolution infrared and microwave spectroscopy can reveal rovibrational spectroscopic constants that are directly linked to the structure of the molecular complex. One of the advantages of microwave spectroscopy is its kHz range resolution that reveals the fine structure and hyper fine structure of the molecular complex (Sec. 2.2.1) such as nuclear quadrupole interaction introduced in Appendix H. For the high-resolution infrared spectrum measured in this work, the resolution is in the MHz range, so no fine or hyper-fine structure of the molecular system can be revealed. One main advantage of high resolution infrared spectroscopy lies in the fact that the band origins of molecular complexes often differ significantly for different sizes of clusters, which is especially the case for those which are connected by intermolecular hydrogen bonding interactions. Furthermore, due to their vibrational band shifts, various conformers of the same molecular complex can usually be distinguished in their high resolution infrared spectra, unlike in microwave spectra where the ground state rotational transitions are all in a similar frequency region. Another interesting property to study in high resolution infrared spectroscopy is the vibrational life time and vibrational energy redistribution upon excitation of the vibrational mode. The observed predissociation broadening of the transitions indicates the limit of the upper state life time.

To analyze high resolution spectra, the semi-rigid rotor Hamiltonian provides a good starting point, which works well for rigid molecular systems that have well defined geometries, but fails to interpret spectra of weakly bound molecular complexes with large amplitude motions that prevent the successful separation of rotational and vibrational degrees of freedom of the molecular complex. The models to interpret the rovibrational spectra of molecular complexes with large amplitude motions provide us with unique insight into these highly floppy systems. Although the basic theory of rotation-vibration spectroscopy is known and is not discussed in the current study, the relevant parts are briefly introduced in Chapter 2. There are three main properties of a transition in the absorption spectrum: position, intensity, and line shape. The position of an absorption line depends on the rovibrational energies of the *upper* and *lower* states of the molecular complex, which are based on its vibrational energy (introduced in Sec. 2.3), rotational energy (introduced in Sec. 2.4), and the coupling between the rotation and vibration (introduced in Sec. 2.2.2). The intensity of the absorption depends

on the population of the molecular system on the rotation-vibration energy levels, and the transition dipole moment (introduced in Sec. 2.5). The spectral line shape is introduced in Appendix A.3. In principle, the rovibrational spectrum of a molecule is directly related to its PES.

Tunable diode laser absorption spectroscopy in combination with a supersonic free jet expansion is a commonly used technique to measure high resolution infrared spectra. Since there is no commercial instrument to carry out such high resolution infrared measurements of molecular complexes, a homemade spectrometer was constructed. Quantum Cascade Laser (QCL) is a new type of semiconductor laser with high output power and wide continuous frequency tuning range, which make it a particularly suitable light source for high resolution infrared spectroscopy. The direct absorption and cavity enhanced absorption techniques are applied with a distributed feedback QCL and an external cavity QCL to measure spectra of molecules under ambient conditions and in supersonic free jet expansion. The design, construction, and testing of the spectrometer are presented in Chapter 4.

In the main parts of the thesis, rotation-vibration spectroscopic studies of molecular complexes containing water or ammonia are reported as a foundation for studying the chiral recognition effects in larger molecular complexes. The molecular complexes that have been studied include the floppy van der Waals complexes and the relatively rigid hydrogen-bonded complexes. In Chapter 3, the study of molecular self recognition in the hydrogen-bonded 2-fluoroethanol complex using microwave spectroscopy is presented. For the infrared studies, the QCL available covers the frequency region of the ν_2 mode of water and ν_4 mode of ammonia, which allows investigations of the molecular complexes containing water or ammonia subunits. The simplest molecular complex containing water or ammonia is the binary complex with a rare gas atom. Study of the high resolution infrared spectrum of Ar-H₂O complex is reported in Chapter 5. The van der Waals Ar-H₂O complex is very floppy and exhibits large amplitude internal rotations and van der Waals stretching motions. Its spectra can be interpreted using a pseudo-diatomic Hamiltonian with internal rotor states mixed by Coriolis couplings. Similar systems such as Ne-H₂O, Ar-NH₃, and Ne-NH₃ are also measured and analyzed. Molecular complexes with greater intermolecular binding energies can be usually modeled by semi-rigid rotors. The spectra of the HCCH-NH₃ complex and the OCS-NH₃ complex are reported in Chapter 6. Both molecular complexes have C_{3v} symmetric structure with N of ammonia as the binding

site. The highly dense and complex infrared spectra propylene oxide-(H₂O)_N complexes are included in this chapter.

The author has published the following five articles in peer-reviewed academic journals during his PhD graduate study which are included in this thesis:

1. Xunchen Liu, Yunjie Xu, “A new sub-band of the acetylene-ammonia complex in the vicinity of ν_4 mode of ammonia”, *J. Mol. Spec.*, **2012**, 275, 28-30.
2. Xunchen Liu, Yunjie Xu, “Infrared and microwave spectra of the acetylene-ammonia and carbonyl sulfide-ammonia complexes: a comparative study of weak hydrogen bond and electric multipole interaction”, *Phys. Chem. Chem. Phys.*, **2011**, 13, 14235-14242, Special issue on Weak Hydrogen Bond.
3. Xunchen Liu, Yunjie Xu, Zheng Su, Wai Shun Tam, Igor Leonov “Jet-cooled infrared spectra of molecules and complexes with a cw mode-hop-free external-cavity QCL and a distributed-feedback QCL”, *Appl. Phys. B.*, **2011**, 102(3), 629-639.
4. Xunchen Liu, Nicole Borho, Yunjie Xu, “Molecular Self-Recognition: Rotational Spectra of the Dimeric 2-Fluoroethanol Conformers” *Chem. Eur. J.*, **2009**, 15, 270-277.
5. Yunjie Xu, Xunchen Liu, Zheng Su, Raviraj M. Kulkarni, Wai Shun Tam, Cheolhwa Kang, Igor Leonov, Lisa D’Agostino, “Application of quantum cascade lasers for infrared spectroscopy of jet-cooled molecules and complexes”, *Proc.SPIE*, **2009**, 7222 *Quantum Sensing and Nanophotonic Devices VI*, 722208.

The author has also co-authored two publications and the following book chapter:

1. Fumie X. Sunahori, Nicole Borho, Xunchen Liu, Yunjie Xu, “High-resolution infrared spectrum of jet-cooled methyl acetate in the C=O stretching region: Internal rotations of two inequivalent methyl tops”, *J. Chem. Phys.*, **2011**, 135(23), 234310.
<http://link.aip.org/link/doi/10.1063/1.3668140>

-
2. Xunchen Liu and Yunjie Xu, “High resolution microwave spectroscopy of chiral molecular contact pairs”, in “Chiral Recognition in the Gas Phase” by Anne Zehnacker, CRC Press, **2010**, 27-38.
<http://www.crcnetbase.com/doi/abs/10.1201/9781420082289-c2>

2

Molecular Spectroscopy

2.1 Introduction

Spectroscopy studies the interaction between matter and electromagnetic radiation. The photon energy is related to the wavelength, λ (m), and wavenumber, $\tilde{\nu}$ (cm^{-1}), of the electromagnetic radiation:

$$E = h\nu = \frac{hc}{\lambda} = 100hc\tilde{\nu} \quad (2.1.0.1)$$

As introduced in Appendix A, the absorbed radiation energy, $E = h\nu$, equals the energy gap of the quantized energy levels in the substance.

$$|\Delta E_{fi}| = |E_f - E_i| = hv_{fi} \quad (2.1.0.2)$$

One of the simplest types of systems to study is small-size molecules in the gas phase at low pressures, which exhibit absorption spectra with narrow lines that provide experimental information about the energy level structures of molecules. A summary of the orders of magnitude of atomic and molecular interactions are provided by Takeshi OKa (Appendix D) and reproduced in Fig. 2.1. The radiation in the 390-750 nm region is visible to (can be detected by) the human eye. The spectrum measured in this region provides information of the electronic structure of a molecule. In the mid-infrared region from 3 μm -50 μm , the infrared and Raman spectra record transitions between quantum states related to vibrational and rotational motions of a molecule, which allow for the study of the molecular rovibrational Hamiltonian. From the measured high resolution infrared transitions, the vibrational energy W_{vib} , rotational energy W_{rot} , vibrational-rotational coupling W_{vr} , and the centrifugal distortion energy W_{cent} can be obtained.

The author would like to point out several aspects of the application of high resolution rovibrational spectroscopy:

1. Currently, high resolution mid-infrared spectroscopy is applied to study small rigid molecules in gas phase. Generally speaking, spectroscopy is the most important method to provide information about molecules. In the mid-infrared range, rovibrational spectra provide unique identification of different molecules. The “finger print” mid-IR spectroscopy is widely used to monitor molecules in the atmosphere and pollutants in the air.
2. For molecules in the condensed phase, the collective vibrational peaks from the single molecule vibrational energy level shift due to the interaction with the surrounding environment. However, the overall spectral finger print of the single molecule is preserved and the magnitude of the shift is small. Mid-infrared spectroscopy is therefore routinely used as an analytical tool by chemists to identify molecular structure and conformational changes. Although the system under study is in the condensed phase and only vibrational levels are concerned, further progress to investigate the system’s infrared spectroscopy, such as the shape of the vibrational band, would be impossible without a detailed knowledge from gas phase studies.
3. Spectroscopy is the only technique which provides information of systems that beyond human reach, such as other planets in the solar system, and interstellar clouds inside and outside of our galaxy.
4. The new type of Quantum Cascade Laser (QCL) light source, with very high output power and wide tunability, are much superior to traditional infrared light source such as the Pd-salt laser and infrared lamp. With the high performance and continuous progress in room temperature operation, the QCL has huge potential to be applied in chemical analysis and detection.

Theories of molecular spectroscopy have been well studied during the past half century. The following is a short list of representative books on the subject.

1. Molecular spectra and molecular structure. I. Spectra of diatomic molecules. II. Infrared and Raman Spectra of Polyatomic Molecules. III. Electronic Spectra and Electronic Structure of Polyatomic Molecules. IV. Constants of Diatomic Molecules, by Gerhard Herzberg(98, 97, 99)
2. Molecular structure and dynamics, by W. H. Flygare(73)

2.1 Introduction

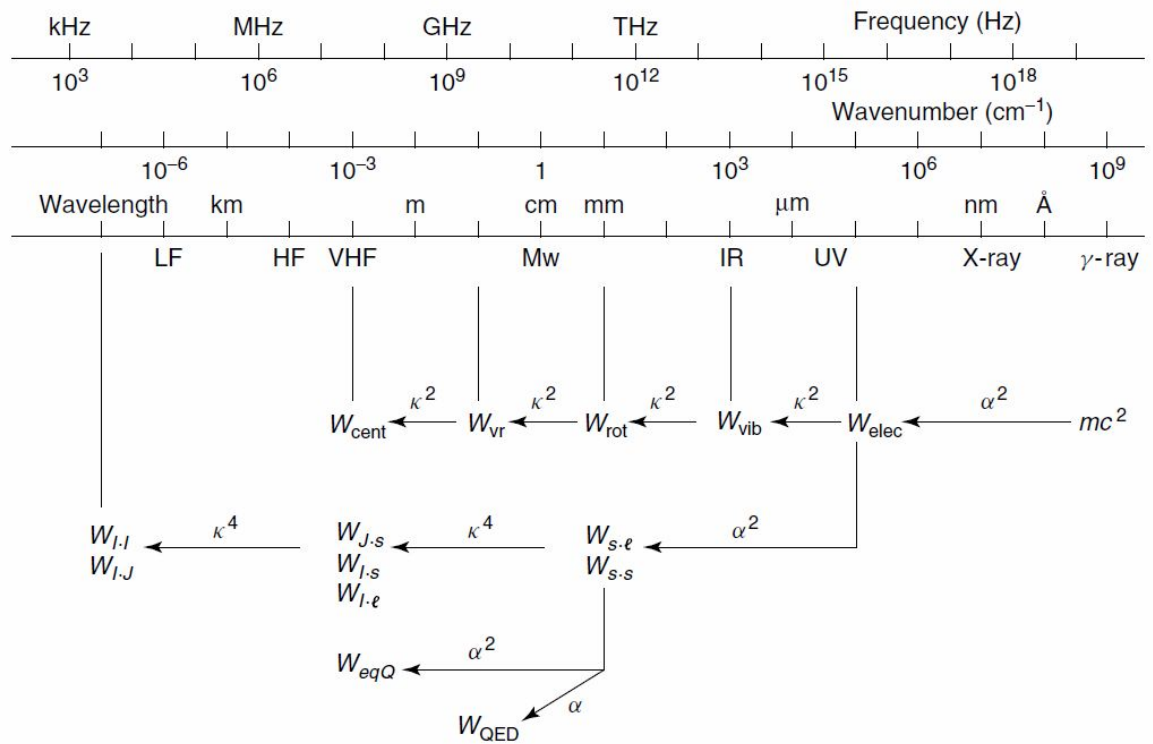


Figure 2.1: Electromagnetic radiation range and orders of magnitude - Summary of the orders of magnitude of atomic and molecular interactions. In this thesis, energy levels in the mid-IR range are studied. High resolution mid-IR spectroscopy allows study of the vibrational energy W_{vib} , rotational energy W_{rot} , and vibrational-rotational coupling W_{vr} and W_{cent} . Reproduced from Ref. (192)

3. Molecular Vibrations: The Theory of Infrared and Raman Vibrational Spectra, by B. Wilson, J. C. Decius, P. C. Cross(280)
4. Vibrational states, by S. Califano(47)
5. Rotation-vibration of polyatomic molecules: higher order energies and frequencies of spectral transitions, by G. Amat, H. H. Nielsen, G. Tarrago(7)
6. Molecular vibrational-rotational spectra: theory and applications of high resolution infrared, microwave, and Raman spectroscopy of polyatomic molecules, by D. Papoušek and M. R. Aliev(195)
7. Molecules and Radiation: An Introduction to Modern Molecular Spectroscopy, by Jeffrey I. Steinfeld(237)
8. Angular momentum: understanding spatial aspects in chemistry and physics, by Richard N. Zare(306)
9. Molecular Symmetry and Spectroscopy, by Philip R. Bunker and Per Jensen(45)
10. Fundamentals of Molecular Symmetry, by Philip R. Bunker and Per Jensen(46)
11. Computational molecular spectroscopy, Edited Per Jensen and Philip R. Bunker(115)
12. Spectra of Atoms and Molecules, by Peter F. Bernath(45)
13. Handbook of high-resolution spectroscopy edited by M. Quack and F. Merkt(207)

The information pertinent to the molecular complexes studied in this thesis are summarized in the following sections of this chapter.

2.2 Molecular Hamiltonian

The rotational and vibrational energy levels of a molecular system are determined by its rovibrational Hamiltonian in quantum mechanics. The quantum mechanical study starts with a separation method based on the order of magnitude of the timescale, which leads to the multi-step separation of the electronic, vibrational, rotational, and translational degrees of freedom using perturbation theory.

2.2 Molecular Hamiltonian

First, the translational degree of freedom can be completely separated from the internal degree of freedom. The total energy of the molecular system is the sum of its translational Hamiltonian \hat{H}_{trans} and its internal Hamiltonian, \hat{H}_{int} .

$$\hat{H}_{\text{total}} = \hat{H}_{\text{trans}} + \hat{H}_{\text{int}} \quad (2.2.0.3)$$

For our study of the molecular system moving in an unconstrained way in field free space, the translational energy has no quantization of the translational states and a plane waves solution of the translational wave function.

Second, the Hamiltonian for the internal energy of the system is separated to the sum of kinetic and potential energies of the nuclei and electrons, which is the molecular rovibronic Hamiltonian \hat{H}_{rve} containing rotational vibrational and electronic energies and the spin contributions \hat{H}_{es} and \hat{H}_{hfs} :

$$\hat{H}_{\text{int}} = \hat{H}_{\text{rve}} + \hat{H}_{\text{es}} + \hat{H}_{\text{hfs}} \quad (2.2.0.4)$$

\hat{H}_{es} denote the interactions arising from electronic spin, including electron spin-spin interaction and electron spin-orbit interaction. It mainly accounts for the fine structure observed in electronic multiplet states like radicals and ions with unpaired electrons, and electronic-excited states, or multiplet ground state like in O_2 . \hat{H}_{hfs} denotes the hyperfine structure, which results from the interaction of the spin of nucleus with the electric and magnetic fields inside the molecule. One of the largest interactions is the nuclear quadrupole interaction. The magnitude of such coupling is usually smaller than 10 MHz and cannot be resolved in high resolution infrared spectroscopy. However, the nuclear quadrupole coupling can be well studied in microwave spectroscopy. Observing certain patterns of nuclear quadrupole splitting can identify the presence of certain nuclei. In studies of molecular complexes, measuring nuclear quadrupole couplings can determine the orientation of subunits. For example, in the study of the HCCH-NH_3 and OCS-NH_3 complexes in Chapter 6, the relative orientation of the NH_3 and the HCCH/OCS subunits is determined by measuring the nuclear quadrupole coupling constant of the complex. Together with the nuclear spin-electron spin interaction, nuclear spin-electron orbital interaction, these interactions are denoted as \hat{H}_{hfs} , because it accounts for the hyperfine structures in high resolution spectroscopy. A detailed discussion of the nuclear quadrupole coupling is presented in Appendix H.

Third, the electronic and nuclear parts of the molecular rovibronic Hamiltonian \hat{H}_{rve} are separated. To study the rovibronic Hamiltonian of a molecule, the

2.2 Molecular Hamiltonian

orders of magnitude of the various terms in \hat{H}_{rve} have to be considered. A brief introduction to the order of magnitude considerations is given in Appendix D. Using the well known Born-Oppenheimer approximation, the electronic and the nuclear parts of the Hamiltonian can be separated based on the mass ratio of the nuclei and electrons. The total wave function is the product of the electronic and nuclear wave functions. The molecular rovibronic Hamiltonian can be written as:

$$\hat{H}_{\text{rve}} = \hat{T}_{\text{e}} + \hat{T}_{\text{N}} + V_{\text{ee}} + V_{\text{NN}} + V_{\text{eN}} \quad (2.2.0.5)$$

By fixing the nuclear motion, i.e., set $\hat{T}_{\text{N}}=0$, the electronic wave function can be calculated for the electronic Hamiltonian with a fixed nuclear configuration (R):

$$\hat{H}_{\text{e;R}} = \hat{T}_{\text{e}} + V_{\text{ee}} + V_{\text{NN;R}} + V_{\text{eN;R}} \quad (2.2.0.6)$$

The energy obtained for a certain electronic state from $\hat{H}_{\text{e;R}}$ is therefore the potential energy, V_{N} , associated with the nuclear kinetic operator \hat{T}_{N} . The **potential energy surface** for the nuclear motion can therefore be calculated.

As shown in this thesis, high resolution rovibrational spectroscopy allows us to determine the vibrational and rotational energy, i.e., the nuclear kinetic energy term \hat{T}_{N} in Eqn. 2.2.0.5. The electronic energy V_{N} at certain nuclear geometry in Eqn. 2.2.0.5 and therefore the PES of the molecular system can be routinely obtained by *ab initio* software packages such as Gaussian, GAMESS, ADF, MOLPRO, TURBOMOLE, etc. Depending on the size of the system, the accuracy of such *ab initio* calculation can approach *chemical accuracy*, which is the energy scale that determines the rates of chemical reactions and the equilibrium ratios of products. Based on the $\exp(-\Delta E/kT)$ distribution, the *chemical accuracy* scale is of the order of kT , which is about 1 kcal/mol at room temperature.

In the above *ab initio* software packages, the nuclear kinetic energy term \hat{T}_{N} is usually treated in a highly simplified procedure.(1, 2) Usually, the rotational part of the Hamiltonian is totally ignored. The harmonic vibrational frequencies are calculated from the Hessian matrix applying the GF method as described in “Molecular Vibrations” by Wilson, Decius, and Cross(280), and anharmonic effect are usually considered by numerical differentiation along normal modes. The rotational constants are calculated from the equilibrium or zero-point geometries and anharmonic vibrational-rotational couplings can be numerically calculated. Partition functions of the electronic, translational, rotational and vibrational contributions are calculated using statistical mechanics to obtain the thermo-corrected

energy of the molecular system. Wave function-based methods such as the vibrational self-consistent field (VSCF), correlation corrected VSCF (cc-VSCF), and its configuration interaction analog (VCI) are also available to calculate the anharmonic effects. With electronic structure calculations carried out at the MP2 level of theory with triple zeta basis sets, these VSCF methods are thought to give accuracy to 50 cm^{-1} for fundamentals bands in the molecular finger print region. For the low frequency modes in the weak interaction complexes, use of internal coordinates is known to give improved accuracies.

Part of the reason for the seemingly crude treatment is that the nuclear kinetic energy term is small compared to the electronic energy term, considering that the accuracy of the electronic structure calculation is close to room temperature “chemical accuracy” of 1 kcal/mol , which is 350 cm^{-1} . The accuracy of the harmonic and anharmonic frequency calculations is usually around a couple of wavenumber, depending on the size of the system and the frequency region. An example of the accuracy of such a calculation is done for the harmonic and anharmonic H_2O bending frequencies of $\text{PO-H}_2\text{O}$ complex shown in Sec. 6.6.

Another reason for the lack of mature rovibrational wave function calculation packages is the difficulty in choosing the coordinate and basis sets to calculate the energy levels and wave functions, as well as a lack of high quality PESs from *ab initio* calculations. Considerable amount of development on both the theoretical techniques and computer hardware are needed before a quantitative understanding of the molecular rovibrational Hamiltonian can be obtained. The high resolution rovibrational spectra measured in this thesis provide experimental data for the testing of high accuracy calculation of rovibrational states of molecular complexes by future generations of physical chemists.

2.2.1 Molecular Rovibrational Hamiltonian

The molecular rovibrational Hamiltonian is the nuclear kinetic operator \hat{T}_N in Eqn. 2.2.0.5 . In Appendix B, the analysis of the vibration and rotation of a semi-rigid molecule using classical mechanics is summarized and the coordinate is developed, in which although the rotation and vibration of a molecule cannot be completely separated, the molecule-fixed axis obeying Eckart conditions is chosen so that rotation-vibration separation is achieved to the maximum extent. The six degrees of freedom to describe the overall translation and rotation are the center of mass of the molecule XYZ and the Euler angle θ, ϕ, χ . Following

Wilson's GF method(283), we adapt the $3N-6$ normal coordinates Q to describe the vibrations of the molecule.

From the classical Hamiltonian given in Eqn. B.4.0.35:

$$\begin{aligned}
 H &= \sum_{\alpha,\beta} \frac{1}{2} (J_\alpha - \Pi_\alpha) \mu_{\alpha\beta} (J_\beta - \Pi_\beta) \\
 &\quad + \frac{1}{2} \sum_r P_r^2 \\
 &\quad + V
 \end{aligned}$$

the quantum mechanical Hamiltonian of a rotational-vibrational semi-rigid molecule can be derived. This problem was studied by Wilson and Howard(284, 281, 282), Darling and Dennison(62), and Louck(147, 148). James K. G. Watson considerably simplified the Hamiltonian using commutation relations and sum rules.(275) Due to his great contribution, the effective rovibrational Hamiltonian is often referred to as Watsonian.

The final result of Wilson-Howard-Watson Hamiltonian is:(271)

$$\hat{H}_{vr} = \frac{\hbar^2}{2} \sum_{\alpha,\beta} \mu_{\alpha\beta} (J_\alpha - \Pi_\alpha) (J_\beta - \Pi_\beta) \tag{2.2.1.1}$$

$$+ \frac{1}{2} \sum_k P_k^2 - \frac{\hbar^2}{8} \sum_\alpha \mu_{\alpha\alpha} + V \tag{2.2.1.2}$$

The first term (Eqn. 2.2.1.1) is the rotational part of the Hamiltonian \hat{H}_r , there, \hat{J}_α stands for the angular momentum operator; Π_α stands for the internal vibrational angular operator given in Eqn. B.4.0.32 along certain axis α ; μ is the 3×3 inverse tensor corresponding to the effective moment of inertia tensor I' , which contains the vibrational and electronic contribution to angular momentum given in Eqn. B.4.0.33. The last three terms (Eqn. 2.2.1.2) form the vibrational part of the Hamiltonian \hat{H}_v , there, P_k is the normal vibration kinetic energy operator; the $-\frac{\hbar^2}{8} \sum_\alpha \mu_{\alpha\alpha}$ term comes from Watson's rearrangement and can be considered as part the potential energy function, which is very small and usually absorbed into the vibration potential term V .

Although quite compact and elegant, in practice Eqn. 2.2.1.1 is further expanded in a perturbation approach. The inverse of the effective moment of inertia is rigidly held at the equilibrium geometry as μ^e , so that the rotational part of

the rovibrational Hamiltonian can be expanded as:

$$\hat{H}_r = \frac{\hbar^2}{2} \left\{ \sum_{\alpha, \beta} \mu_{\alpha\beta}^e J_\alpha J_\beta \right. \quad (2.2.1.3)$$

$$\left. + \mu_{\alpha, \beta}^e \Pi_\alpha \Pi_\beta - \mu_{\alpha, \beta}^e (J_\alpha \Pi_\beta + J_\beta \Pi_\alpha) \right. \quad (2.2.1.4)$$

$$\left. + \sum_{\alpha, \beta} (\mu_{\alpha, \beta} - \mu_{\alpha\beta}^e) (J_\alpha - \Pi_\alpha) (J_\beta - \Pi_\beta) \right\} \quad (2.2.1.5)$$

This means that the rotational Hamiltonian \hat{H}_r can be divided into 4 parts: The first term (Eqn. 2.2.1.3, $\hat{H}_r^{(0)}$) assumes that the nuclei are held rigidly at their equilibrium positions and omits the vibrational angular momentum, due to the rigid rotor approximation; the second and third terms (Eqn. 2.2.1.4) take into account the vibrational angular momentum contribution and constitute the operator for the Coriolis coupling. The fourth term (Eqn. 2.2.1.5) represents the non-rigidity of the molecule and forms the centrifugal distortion constants.

Similarly, the vibrational Hamiltonian \hat{H}_v in Eqn. 2.2.1.2 may be expanded around the equilibrium position:

$$\hat{H}_v = \frac{1}{2} \sum_i (P_i^2 + \lambda_i Q_i^2) \quad (2.2.1.6)$$

$$+ \frac{1}{6} \sum_{kst} \Phi_{kst} Q_k Q_s Q_t \quad (2.2.1.7)$$

$$+ \frac{1}{24} \sum_{kstu} \Phi_{kstu} Q_k Q_s Q_t Q_u + \dots$$

The first term, $\hat{H}_v^{(0)}$ (Eqn. 2.2.1.6) is the harmonic approximation and the remaining high order terms (Eqn. 2.2.1.7) are the anharmonic corrections to the vibrational Hamiltonian.

Following the order of magnitude consideration in Section D, we can expand μ and V in terms of the normal coordinates. So the rovibrational Hamiltonian \hat{H}_{vr} of a molecule can be expanded as a series of vibrational, rotational, rotational-vibrational coupling terms, known as the Coriolis terms.

$$\hat{H}_{vr} = \hat{H}_{20} + \hat{H}_{30} + \hat{H}_{40} + \dots \text{(vibrational terms)} \quad (2.2.1.8)$$

$$+ \hat{H}_{21} + \hat{H}_{31} + \hat{H}_{41} + \dots \text{(Coriolis terms)} \quad (2.2.1.9)$$

$$+ \hat{H}_{02} + \hat{H}_{12} + \hat{H}_{22} + \dots \text{(rotational terms)} \quad (2.2.1.10)$$

Here, we adapt the notation by Aliev and Watson that in \hat{H}_{mn} , m stands for the sum of the power of the vibrational operators and n stands for the sum of the power of the rotational operators.

In the lowest order approximation, the rotational-vibrational coupling terms can be completely neglected and only the pure rotational term $\hat{H}_r^{(0)} = \hat{H}_{02}$ is kept. Also, only the harmonic approximation is applied, so that only the $\hat{H}_v^{(0)} = \hat{H}_{20}$ term is kept, dropping the \hat{H}_{30} , \hat{H}_{40} terms, i.e., V is truncated to the quadratic form. This give us the zero order simplification of rotational-vibrational Hamiltonian as a sum of Eqn. 2.2.1.1 and Eqn. 2.2.1.2,

$$H_{rv}^0 = \frac{1}{2} \left(\frac{J_x^2}{I_{xx}^0} + \frac{J_y^2}{I_{yy}^0} + \frac{J_z^2}{I_{zz}^0} \right) + \frac{1}{2} \sum_{k=1}^{3N-6} P_k^2 + \frac{1}{2} \sum_{k=1}^{3N-6} \lambda_k Q_k^2 \quad (2.2.1.11)$$

The first term is the rigid rotor Hamiltonian H_r^0 with the choice of principal axis (Eqn. B.1.2.25) that will be introduced in section 2.4 and the rest are the harmonic oscillator Hamiltonian H_v^0 that will be introduced in Section 2.3.

In summary, the complete separation of the overall rovibronic wave function in the zeroth order approximation is written as:

$$\Phi_{rve}^0 = \Phi_e \Phi_v^0(Q_i) \Phi_r^0(\theta, \phi, \chi) \quad (2.2.1.12)$$

$$|rve\rangle = |e\rangle |Q_i\rangle |\theta, \phi, \chi\rangle \quad (2.2.1.13)$$

Although cruder than the Born-Oppenheimer approximation, the approximated rigid rotor and harmonic oscillator Hamiltonian are extremely important, because they form the basis set for the Rayleigh-Schrödinger perturbation treatment of the other high order terms that carry clear meanings of rovibrational couplings.

2.2.2 Perturbations

The harmonic oscillator and rigid rotor approximations made in Eqn. 2.2.1.11 are of course not sufficient to analyze experimental data on vibrational-rotational transitions.(195) The other terms in the molecular rotational-vibrational Hamiltonian, Eqn. 2.2.1.1 and Eqn. 2.2.1.2 should be considered. For example, \hat{H}_{12} and \hat{H}_{22} are the centrifugal distortion operators, \hat{H}_{21} is the Coriolis interaction term between rotation and vibration, and the \hat{H}_{30} and \hat{H}_{40} terms are the anharmonicity of molecular vibrations. They are often referred to as “*spectroscopic perturbation*” to the regular behavior of the zeroth order rovibrational Hamiltonian. As stated by J. Hougen, “...what is considered to be a perturbation

and what is not depends largely on what behavior for experimentally observable quantities is initially expected, or on what interaction terms in the theoretical formalism are initially included.”(107)

Basically, there are 3 types of rovibrational perturbations:

1. Anharmonic Effects

It arises from the deviation of the real molecular potential energy surfaces from the harmonic potential approximation. The operators for the anharmonicity terms are given in Eqn. 2.2.1.7.

2. Centrifugal Distortion

It arises from the non-rigidity of the molecule. The Hamiltonian for the centrifugal distortion is Eqn. 2.2.1.5

3. Coriolis Coupling

It arises from the vibrational contribution of angular momentum to the molecular rotational Hamiltonian Eqn. 2.2.1.1. The operators for the Coriolis Coupling are given in Eqn. 2.2.1.4.

In the following sections, the anharmonic effect is discussed after the harmonic approximation treatment of molecular vibrations in Sec. 2.3. The centrifugal distortion and Coriolis coupling are discussed after the rigid rotor treatment of molecular rotation in Sec. 2.4.

To use perturbation theory to study these effects, it is crucial to understand the order of magnitude of the individual terms in the Hamiltonian. The general formula is: (192)

$$\hat{H}_{mn} \simeq \kappa^{m+2n-2} r^m J^n \omega_{vib} \quad (2.2.2.1)$$

where r^m is the abbreviation for p, q operators and is usually ignored for low vibration quantum states. κ is the smallness parameter introduced in the Born-Oppenheimer approximation of the order of 1/10; J is the typical value for the rotational quantum number. In the microwave region, the \hat{H}_{02} term generally in the order of

$$B_{\alpha}^e \simeq \kappa^2 \omega_{vib} \quad (2.2.2.2)$$

and in the infrared region, we have

$$H_{mn} \simeq \kappa^{m+n-2} \omega_{vib} \quad (2.2.2.3)$$

In general, the perturbations are small in magnitude but large in number, and it is impractical to diagonalize the semi-infinite number of the interacting levels

most of which are often poorly known. The contact transformation method, also known as van Vleck transformation method, is used to obtain the effective Hamiltonian. (7, 208) The contact transformation essentially keeps the first-order interactions and eliminates interactions between the distant states, which brings the molecular Hamiltonian with higher order terms to block diagonal form and decouple the individual vibrational states. The contact transformation matrix \hat{S} transfers the “exact” Hamiltonian, \hat{H}^{ex} , to the “effective” Hamiltonian, \hat{H}^{eff} , for each isolated vibrational state or polyad of close vibrational states in resonance.

$$e^{i\hat{S}} \begin{bmatrix} \hat{H}_{v_1v_1}^{\text{ex}} & \hat{H}_{v_2v_1}^{\text{ex}} & \hat{H}_{v_3v_1}^{\text{ex}} & \cdots \\ \hat{H}_{v_1v_2}^{\text{ex}} & \hat{H}_{v_2v_2}^{\text{ex}} & \hat{H}_{v_3v_2}^{\text{ex}} & \cdots \\ \hat{H}_{v_1v_3}^{\text{ex}} & \hat{H}_{v_2v_3}^{\text{ex}} & \hat{H}_{v_3v_3}^{\text{ex}} & \cdots \\ \vdots & \vdots & \vdots & \ddots \end{bmatrix} e^{-i\hat{S}} = \begin{bmatrix} \hat{H}_{v_1v_1}^{\text{eff}} & 0 & 0 \cdots & \\ 0 & \hat{H}_{v_2v_2}^{\text{eff}} & 0 \cdots & \\ 0 & 0 & \hat{H}_{v_3v_3}^{\text{eff}} & \cdots \\ \vdots & \vdots & \vdots & \ddots \end{bmatrix} \quad (2.2.2.4)$$

The idea of effective Hamiltonian is widely applied in spectroscopic fit. For example, the centrifugal distortion constants are usually used together with the A, B, C rotational constants to describe an effective vibrational state.

The general procedures to calculate the transformation matrix \hat{S} is as follows. The rovibrational Hamiltonian with higher order terms that needs to be factorized, \hat{H}_{rv} , and the transformation matrix, \hat{S} , are each expanded according to the order of magnitude consideration with the bookkeeping parameter λ :

$$\hat{H}_{rv} = \hat{H}_0 + \lambda\hat{H}_1 + \lambda^2\hat{H}_2 + \lambda^3\hat{H}_3 + \cdots \quad (2.2.2.5)$$

$$e^{i\lambda\hat{S}_1} = 1 + i\lambda\hat{S}_1 - \frac{1}{2}\lambda^2\hat{S}_2^2 + \cdots \quad (2.2.2.6)$$

Therefore, the transformed Hamiltonian \tilde{H}^{eff} becomes:

$$\tilde{H} = \tilde{H}_0 + \lambda\tilde{H}_1 + \lambda^2\tilde{H}_2 \quad (2.2.2.7)$$

$$\tilde{H}_0 = \hat{H}_0 \quad (2.2.2.8)$$

$$\tilde{H}_1 = \hat{H}_1 + i[\hat{S}_1, \hat{H}_0] \quad (2.2.2.9)$$

The operator \hat{S}_1 is obtained satisfying for non-degenerate $E_n^0 - E_m^0$,

$$\langle n|\tilde{H}_1|m\rangle = \langle n|\hat{H}_1|m\rangle - i(E_n^0 - E_m^0)\langle n|\hat{S}_1|m\rangle = 0 \quad (2.2.2.10)$$

This means after the contact transformation, the off-diagonal terms are absent in \tilde{H}_1 . Similarly, the operator \hat{S}_2 is obtained by diagonalization of \tilde{H}_2 after the first contact transformation, $\tilde{H}_2^{(2)}$, and so on.

2.3 Harmonic and Anharmonic Oscillators

In principle, all the rotational, vibrational and rovibrational coupling parameters can be calculated in such a way based on the potential energy surface (PES)(279) of a molecule, from which the equilibrium rotational constants (A_e, B_e, C_e) and the force constants (Φ) in Eqn. 2.2.1.7 can be derived. Details of the calculation of centrifugal distortion constants and Coriolis coupling constants following such procedures can be found, for example, in Amat, Neilson, and Tarrago(7), and in compact form by Aliev and Watson(208). These complicated formulae clearly connects the spectroscopic constants to physical meaning of a molecular system. However, from a practical point of view, these complex formulae are needed only if the spectroscopic constants are used to determine the force field and to reconstruct the PES of interest. Currently these can be routinely obtained from first principle electronic structure calculation with considerable accuracy and reasonable cost compared to the spectroscopic method.

2.3 Harmonic and Anharmonic Oscillators

2.3.1 Harmonic Oscillator

Following the Wilson's GF method in Appendix. B.3, vibration of the semi-rigid molecule can be represented by $3N - 6$ normal modes. In the harmonic oscillator approximation, the infinitesimal amplitudes of the vibration explores potential that only includes the diagonal quadratic terms, so the cubic, quartic and higher order terms in the potential energy are neglected.

2.3.1.1 Non-degenerate Harmonic Oscillator

The potential of the non-degenerate harmonic oscillator is:

$$V(Q) \approx V_e + \frac{1}{2} \sum_k \lambda_k Q_k^2 \quad (2.3.1.1)$$

where $\lambda_k = m\omega^2$, m is the particles's mass and ω is the angular frequency of the oscillator. Since the potential at the equilibrium geometry is a constant, the Hamiltonian for the harmonic oscillator is:

$$\hat{H}_v^{(0)} = \frac{1}{2} \sum_k (\hat{P}_k^2 + \lambda_k Q_k^2) \quad (2.3.1.2)$$

Eigenvalues of this operator are given by:

$$E_k^{(0)} = \hbar\sqrt{\lambda_k}(v_k + 1/2) \quad (2.3.1.3)$$

2.3 Harmonic and Anharmonic Oscillators

where v_k is the vibrational quantum number. With $\gamma = \sqrt{\lambda}/\hbar$, eigenfunctions are given by:

$$|v\rangle = N_v H_v(\sqrt{\gamma}Q) e^{-\gamma Q^2/2} \quad (2.3.1.4)$$

with the normalization factor:

$$N_v = \frac{\gamma^{1/4}}{(\pi^{1/2} 2^v v!)^{1/2}} \quad (2.3.1.5)$$

and the Hermite polynomial H_v . The non-vanishing matrix elements of normal coordinates \hat{Q} and momentum \hat{P} are *only* between the adjacent vibrational levels: $\langle v+1 | \hat{P}, Q | v \rangle$. Therefore the selection rule for the optical transitions of the harmonic oscillator is $\Delta v = \pm 1$.

2.3.1.2 Doubly-degenerate Isotropic Harmonic Oscillator

For the doubly degenerate isotropic harmonic oscillators, instead of simply addition of two one-dimensional harmonic oscillators with Q_a and Q_b , the polar coordinates Q and α are used

$$Q_a = Q \cos \alpha \quad (2.3.1.6)$$

$$Q_b = Q \sin \alpha \quad (2.3.1.7)$$

Now the wave function can be separated into a function which is only of Q and a function only of α :

$$\Phi_{v,l} = F_{v,l}(Q) \times e^{il\alpha} \quad (2.3.1.8)$$

The total eigenvalue is:

$$E_v = (v+1)\hbar^2\gamma \quad (2.3.1.9)$$

The vibrational angular momentum operator $\hat{\Pi}$ and vibrational operator \hat{M} are given by:

$$\hat{\Pi} = -i\hbar \frac{\partial}{\partial \alpha} = (Q_a \hat{P}_b - Q_b \hat{P}_a) \quad (2.3.1.10)$$

$$\hat{M} \Phi_{v,l} = l\hbar \Phi_{v,l} \quad (2.3.1.11)$$

Where the vibrational quantum number l can take $v+1$ values $v, v-2, v-4, \dots, 4-v, 2-v, -v$.

2.3 Harmonic and Anharmonic Oscillators

Such coordinates are applied to molecules with linear equilibrium geometries. Linear molecules have only 2 rotational degree of freedom (DOF). For a linear molecule with N atoms, there are $3N-5$ vibrational DOF. There are $N-1$ stretching DOF and $N-2$ two-dimensional bending DOF. Each pair of 2-dimensional normal modes Q_{ra} and Q_{rb} is described by the pair of coordinates Q_r, α_r given in Eqn. 2.3.1.7 and has a vibrational angular momentum $\hbar j_r$ about the axis of the molecule according to Eqn. 2.3.1.11.

The perpendicular bending mode of a symmetric top molecule is degenerate. Therefore, they are also described by a pair of quantum numbers v, l , the vibrational momentum v and vibrational angular momentum l , which leads to the “first-order Coriolis coupling” as shown in Sec. 2.4.3 that significantly shifts the rovibrational sub-bands.

2.3.2 Anharmonic Oscillator

In reality, the vibrational potential of a molecule is not harmonic. A more suitable description of the vibration of the semi-rigid molecule is provided by the anharmonic oscillator model, in which the cubic, quartic, and higher order terms of the vibration potential function are considered in Eqn. 2.2.1.7. In spectroscopy, the vibrational frequency term value is expanded in terms of the anharmonicity constants χ :

$$G(\nu_1, \nu_2, \nu_3, \dots) = \sum_i \omega_i \left(\nu_i + \frac{d}{2} \right) \quad (2.3.2.1)$$

$$+ \sum_i \sum_{k \geq i} \chi_{ik} \left(\nu_i + \frac{d}{2} \right) \left(\nu_k + \frac{d}{2} \right) \quad (2.3.2.2)$$

$$+ \dots$$

where d is the degeneracy of the normal mode.

A useful approximation for the anharmonic oscillator on the one-dimensional vibrational potential energy for a diatomic molecule, and conceptually equal for the $3N - 6$ normal mode vibrations, is the Morse potential that is shown in Fig. 2.2:

$$V(r) = D_e (1 - e^{-a(r-r_e)})^2 \quad (2.3.2.3)$$

As can be seen in Fig. 2.2, when the internuclear distance approaches a large value, the Morse potential energy approaches zero, which is a realistic representation of the dissociation of the diatomic molecule rather than the unlimited high

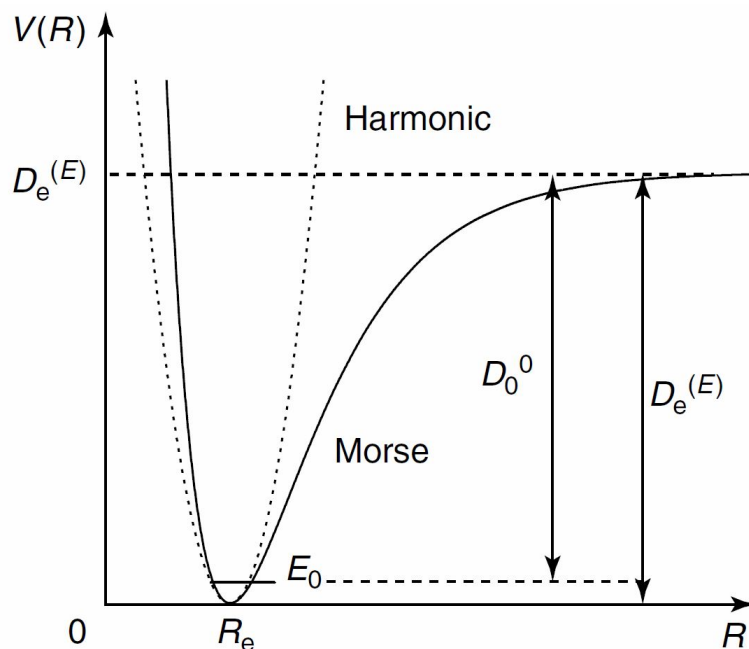


Figure 2.2: The harmonic and the Morse potentials - D_e is the dissociation energy and D_0 is the zero-point corrected dissociation energy.

binding energy in the harmonic oscillator model. The energy difference between the zero value and the minimum equilibrium point of the potential is the equilibrium dissociation energy D_e . Since most of the population of the molecules under investigation is on the ground vibrational level $v = 0$, (Sec. 2.5.3) the measured dissociation energy should take into account of the zero-point-energy (D_0). The wave function and probability densities of the harmonic and anharmonic Morse oscillator are shown in Fig. 2.3. It is clearly shown in Fig. 2.3 that as the vibrational quantum number increases, the anharmonic eigenvalues increasingly deviate from the harmonic eigenvalues, and finally we approach the dissociation continuum.

To evaluate the anharmonic effect, the higher order anharmonic terms (take the form of Eqn. 2.2.1.7) are considered as the perturbation to the harmonic oscillator Hamiltonian $H_v^{(0)}$ and the harmonic oscillator wave function in Eqn. 2.3.1.4 as the basis set. Besides the diagonal eigenstates of the harmonic oscillator, we have the off-diagonal terms (take the form $\langle v'|Q^n|v\rangle$) that need to be evaluated by the rule of matrix multiplication:

$$\langle v'|Q^n|v\rangle = \sum_{v'',v''',\dots} \langle v'|Q|v''\rangle \langle v''|Q|v'''\rangle \cdots \langle v''''|Q|v\rangle \quad (2.3.2.4)$$

2.3 Harmonic and Anharmonic Oscillators

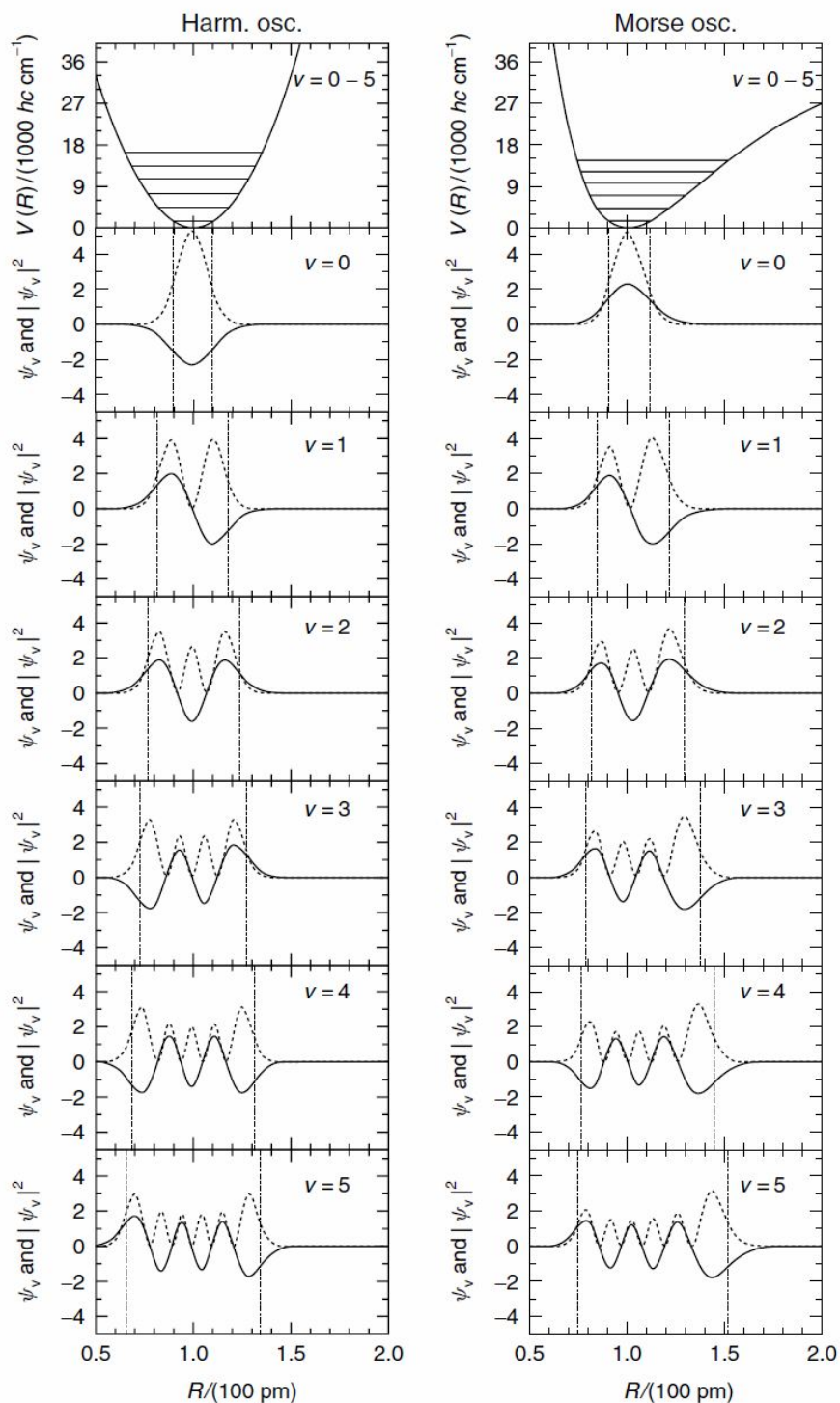


Figure 2.3: The wave functions of the harmonic and anharmonic oscillators - Wave function (solid line) and probability densities (dotted line) of the harmonic and anharmonic Morse oscillators. Figure adapted from Ref. (5).

2.3 Harmonic and Anharmonic Oscillators

Therefore, the non-vanishing off-diagonal terms are not only the $\Delta v = 1$ terms in the harmonic oscillator model but also the $\Delta v > 1$ terms. For example, the lowest order anharmonic correction is the cubic term:

$$V^3 = \frac{1}{6} \sum_{kst} \Phi_{kst} Q_k Q_s Q_t \quad (2.3.2.5)$$

The non-vanishing off-diagonal terms are:

$$\langle v|Q^3|v+3\rangle = (1/\sqrt{8\gamma^3})\sqrt{(v+1)(v+2)(v+3)} \quad (2.3.2.6)$$

$$\langle v|Q^3|v+1\rangle = (3/\sqrt{8\gamma^3})(v+1)\sqrt{(v+1)} \quad (2.3.2.7)$$

$$\langle v|Q^3|v-1\rangle = (3/\sqrt{8\gamma^3})v\sqrt{v} \quad (2.3.2.8)$$

$$\langle v|Q^3|v-3\rangle = (1/\sqrt{8\gamma^3})\sqrt{(v-1)(v-2)(v-3)} \quad (2.3.2.9)$$

The off-diagonal terms mix the harmonic eigenstates so that the anharmonic eigenstates are linear combinations of the harmonic eigenstates. The off-diagonal terms also shift the eigenstates from the harmonic value in such a way that the levels become closer and closer together as the vibration quantum number increases, as represented in the Morse potential in Fig. 2.2. These off-diagonal elements that connect the $\Delta v > 1$ levels lead to the overtone transition selection rules that we discuss in Sec. 2.5.1.

The classical picture of such mixing is that introducing anharmonicity into one-dimensional oscillator means that the vibration is still periodic although no longer harmonic (different time dependence). But for multi-dimensional oscillator, the change is fundamental. If the potential energy contains higher than quadratic terms, the decomposition of vibrational motion into a number of normal vibrations, in which all atoms move in the same frequency, *fails*.

For polyatomic molecules, the anharmonicity terms in the potential can also mix vibrational states that belong to different normal modes but close in energy. Effects on the spectrum from such mixing include:

1. Shift of the vibrational band.
2. A weak or forbidden band will gain significant intensity. Due to the mixing character of the vibrational band, the transition dipole moment is no longer from a pure state.

When such an off-diagonal term is the cubic term, such mixing is called “Fermi resonance”, after first been discussed by Fermi in the case of the v_1 and $2v_2$

2.4 Rigid Rotor and Semi-rigid Rotor

states of CO_2 . As the ν_1 symmetric stretch is at 1388 cm^{-1} , $2\nu_2$ is not present at $2 \times 667 = 1334\text{ cm}^{-1}$, but shifted to 1286 cm^{-1} . When the anharmonic mixing is caused by a quartic term, it is called “Darling-Dennison” resonance. For example in the case of H_2O , the $(2,0,0)$ and $(0,0,2)$ terms are mixed by the $(\frac{1}{4}\Psi_{1133}Q_1^2Q_3^2)$ term. The term “Fermi resonance” is generally applied when the coupling of the vibrational states are caused by anharmonicity and is allowed by symmetry considerations. For example, in our study of the HCCH-NH_3 complex, the absence of the $K = 1 \leftarrow 0$ subband is attributed to an “unknown” Fermi resonance that shifts the $K = 1$ level in the upper state. In the $\text{Ar-H}_2\text{O}$ spectrum presented in this study, such mixing causes the van der Waals stretching mode which has near zero intrinsic oscillator strength to “borrow” significant intensity from transitions between other states. In the spectroscopic fitting procedures, Fermi resonances are treated as a constant that mixes the two perturbed states.

2.4 Rigid Rotor and Semi-rigid Rotor

A rigid rotor in molecular spectroscopy may be defined as a molecule such that the distance between the nuclei do not vary.(132) It should be noted that in the language of high resolution spectroscopy, the term “rigid molecules” sometimes refer to molecules with no tunneling motion but allows distortion and vibration.(45)

The classical treatment of rigid body dynamic is provided in Appendix B. In this section, we discuss the rotational energy of a rigid molecule using quantum mechanics, essentially the eigenstates of H_r^0 or \hat{H}_{02} in Eqn. 2.2.1.10. With the moment of inertia as defined by $I = \mu R^2$, we can re-write \hat{H}_{02} as:

$$\hat{H}_{02} = \sum_{\alpha=x,y,z} B_{\alpha}^e \hat{J}_{\alpha}^2 \quad (2.4.0.10)$$

The eigenvalue of the rotational Hamiltonian is closely related to the angular momentum operator J , discussed in Appendix C.

2.4.1 Rotational Energy Levels of Rigid Rotors

the basic strategy to derive the rotational energy levels of a rigid rotor is to write the Hamiltonian of the rigid body in terms of angular momentum operators. The classical treatment of the Hamiltonian of a rigid body is provided in Sec. B.1. Then, the basis set of spherical harmonics Y_{Jm} is used to determine the matrix

2.4 Rigid Rotor and Semi-rigid Rotor

	I^r	II^r	III^r	I^l	II^l	III^l
x	b	c	a	c	a	b
y	c	a	b	b	c	a
z	a	b	c	a	b	c

Table 2.1: Identification of a, b, c axes with the x, y, z axes. Depending on whether z axis is identified with the a, b , or c axis, we name the convention adopted as type I, II , or III . We add a superscript r or l depending on whether a right-hand or left-hand xyz axis system is used.

elements of the angular momentum operator. The general form of \hat{H}_{rot} can be written as:

$$\begin{aligned}\hat{H}_{\text{rot}} &= \frac{\hat{J}_x^2}{2I_x} + \frac{\hat{J}_y^2}{2I_y} + \frac{\hat{J}_z^2}{2I_z} \\ &\equiv A_e \hat{J}_a^2 + B_e \hat{J}_b^2 + C_e \hat{J}_c^2\end{aligned}\tag{2.4.1.1}$$

where A_e, B_e , and C_e are rotational constants, which in units of Joules (J) are

$$A_e, B_e, C_e = \frac{\hbar^2}{2I_{aa,bb,cc}^e}\tag{2.4.1.2}$$

In the following discussion, we omit the equilibrium symbol and simply use A, B , and C as equilibrium rotational constants. The convention to identify molecular-fixed a, b, c axes with the space-fixed x, y, z axes are given in Table 2.1.

2.4.1.1 Spherical Top, Diatomic and Linear Molecules

Spherical top molecules such as $\text{CH}_4, \text{CCl}_4$, have $I_{aa}^e = I_{bb}^e = I_{cc}^e = I^e$ as constant:

$$\hat{H}_{\text{rot}} = \frac{1}{2I^e}(\hat{J}_x^2 + \hat{J}_y^2 + \hat{J}_z^2)\tag{2.4.1.3}$$

$$= \frac{\hat{J}^2}{2I^e}\tag{2.4.1.4}$$

Since H commutes with J^2 , the rotational energies are easily obtained:

$$E_J = \langle J, m | H_{\text{rot}} | J, m \rangle\tag{2.4.1.5}$$

$$= \frac{\hbar^2}{2I^e} J(J+1)\tag{2.4.1.6}$$

$$= BJ(J+1)\tag{2.4.1.7}$$

2.4 Rigid Rotor and Semi-rigid Rotor

The energy expression is the same for diatomic molecules or molecules with linear equilibrium geometries, where $I_{bb}^e = I_{cc}^e = I^e$ and $I_{aa} = 0$. However for a linear molecule, as discussed in Sec. 2.3.1.2, each pair of 2-dimensional normal modes Q_{ra} and Q_{rb} is described by the pair of coordinates Q_r, α_r given in Eqn. 2.3.1.7 and has a vibrational angular momentum $\hbar l_r$ about the linear axis according to Eqn. 2.3.1.11. Therefore, K for the linear molecule should be $K = L + \Delta$, where L and Δ are the sum of vibrational and electronic angular momenta. An example of the rovibrational energy levels with $BJ(J + 1)$ spacing and rovibrational transitions is shown in Fig. 2.4.

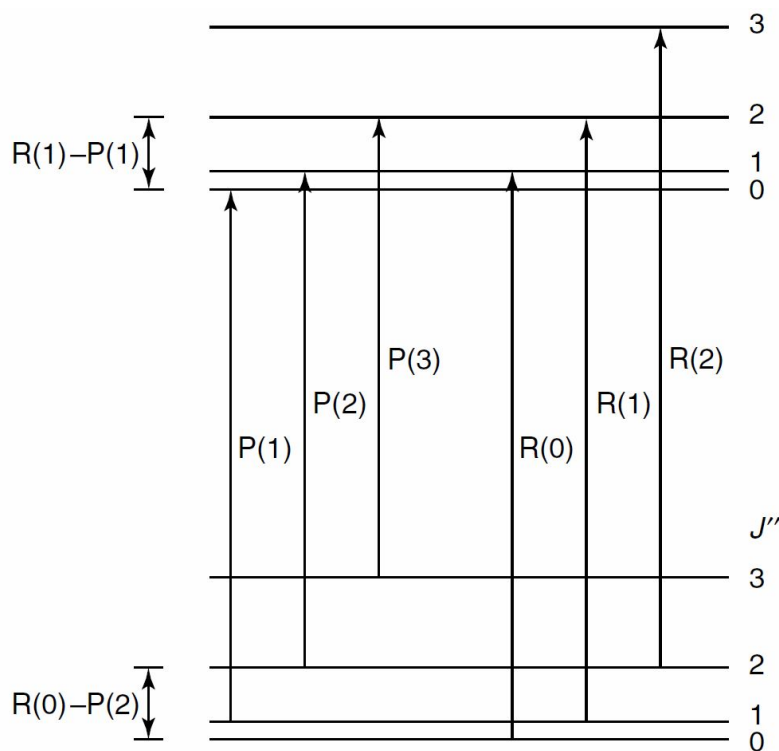


Figure 2.4: Rovibrational energy levels and spectrum of a linear molecule - The rotational and rovibrational energy levels of a linear molecule are separated by $J(J + 1)B$ difference and the corresponding rovibrational spectrum is characterized by the unique $2B$ spacing. Q branch is allowed for perpendicular bands. Figure adapted from Ref. (5)

2.4.1.2 Symmetric Top Molecules

For a prolate symmetric top molecule with $I_{aa}^e < I_{bb}^e = I_{cc}^e$, \hat{H}_{rot} can be re-written as:

$$\hat{H}_{\text{rot}} = \frac{\hat{J}_a^2}{2I_{aa}} + \frac{\hat{J}_b^2 + \hat{J}_c^2}{2I_{bb}} \quad (2.4.1.8)$$

$$= \frac{\hat{J}_a^2}{2I_{aa}} + \frac{\hat{\mathbf{J}}^2 - \hat{J}_a^2}{2I_{bb}} \quad (2.4.1.9)$$

$$= A\hat{J}_a^2 + B[\hat{\mathbf{J}}^2 - J_a^2] \quad (2.4.1.10)$$

which leads to the rotational energy levels:

$$E_{\text{rot}} = AK^2 + B[J(J+1) - K^2] \quad (2.4.1.11)$$

where $\hat{\mathbf{J}}$ is the total angular momentum operator and K is the quantum number corresponding to the projection of the total angular momentum onto the a axis. A similar procedure can be applied to the oblate symmetric top molecule to obtain:

$$E_{\text{rot}} = CK^2 + B[J(J+1) - K^2] \quad (2.4.1.12)$$

The rotational eigenfunctions of all symmetric top, linear, diatomic and spherical top molecules are the *same* – spherical harmonic functions of the Euler angle θ, ϕ, χ given in Sec. C.3 . The spherical harmonic functions are also called the “symmetric top wave function”, $|J, k, m\rangle$, which are the basis set used for the asymmetric top molecules.

2.4.1.3 Asymmetric Top Molecules

Most molecules have three principal moment of inertia that different from each other. The rotational Hamiltonian can be written as:

$$\hat{H}_{\text{rot}} = \frac{1}{2}(B_x + B_y)\mathbf{J}^2 \quad (2.4.1.13)$$

$$+ \frac{1}{2}(2B_z - B_x - B_y)J_z^2 \quad (2.4.1.14)$$

$$+ \frac{1}{4}(B_x - B_y)(J_+^2 + J_-^2) \quad (2.4.1.15)$$

Because the last term is non-diagonal but has $m \pm 2$ off-diagonal terms, E_{rot} of the asymmetric top Hamiltonian cannot be expressed in closed form and has to be obtained by diagonalization of the matrices. The basis set used are the

2.4 Rigid Rotor and Semi-rigid Rotor

symmetric top wave function discussed in Sec. 2.4.1.2. As a result, the asymmetric top rotational eigenfunctions are linear combinations of the symmetric top wave functions that have the same J and m values, with the coefficients that depend on the rotational constants.

To correlate the xyz axes to the abc axes, the convention given in Table 2.1 should be used. Parameter κ is often used to describe the “shape” of the asymmetric molecule.

$$\kappa = \frac{2B - A - C}{A - C} \quad (2.4.1.16)$$

The limiting value $\kappa = -1$ correlates to the prolate top molecules and $\kappa = 1$ correlates to oblate top molecules, with $\kappa = 0$ being the “most” asymmetric when B is halfway between A and C . It can be shown that if the geometry of an asymmetric top molecule is near a prolate top molecule, i.e., $\kappa \approx -1$, then in a type I basis the off-diagonal matrix elements will be small. If the molecule under study is a near oblate top, i.e., $\kappa \approx 1$, then in a type III basis the off-diagonal elements will be small. For asymmetric top molecules with $\kappa \approx 0$, type II representation is usually used.

A detailed derivation of the asymmetric top wave functions shows that each asymmetric top energy level correlates with one prolate and one oblate symmetric top energy level. Therefore, the $2J + 1$ non-degenerate rotational levels of an asymmetric top molecule are labelled $J_{K_a K_c}$, where K_a and K_c indicate the K values of the prolate or oblate top levels with the same value of J that the asymmetric top molecule correlates to, while K_a is associated with a rotation about the a axis and K_c is associated with a rotation about the c axis.

For a given value of J , the values of pseudo-quantum number K_a and K_c runs through $0, 1, 1, 2, 2, \dots, J, J$ in the reverse order. Depending on whether K_a and K_c are even or odd, the asymmetric top levels are labeled as “ee, oe, oo, or eo”. They are associated with the A, B_c, B_b, B_a symmetry of the $D_2(V)$ group, respectively. An example of such correlation for the $J=3$ rotational levels is given in Fig. 2.5.

For the lowest J values, analytical forms of the asymmetric top rotational levels exist. They are given in Table. 2.3. As an example of the rotational energy levels of a semi-rigid asymmetric top molecule, the $J=0,1,2$ rovibrational energy levels of the H_2O molecule in its ground and $\nu_2=1$ excited states are given in Fig. 2.6 and Fig. 5.4. It can be seen the 3_{03} and 3_{13} levels are lower than the closely packed 2_{20} and 2_{12} levels.

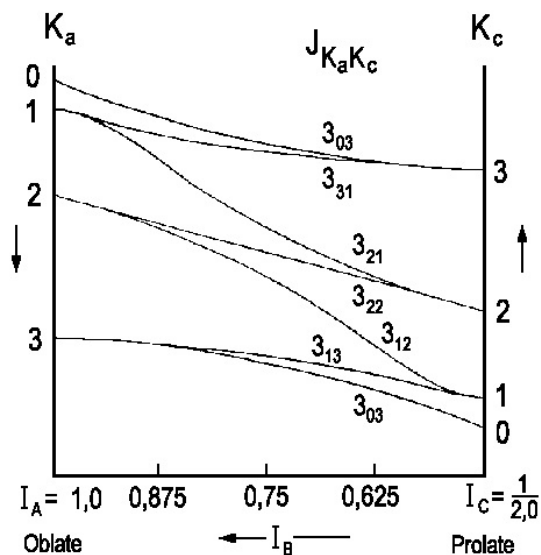


Figure 2.5: Correlation between the asymmetric rotor energy levels and the symmetric top rotor energy levels - Each of the asymmetric rotor energy levels relates to a limiting prolate rotor level and an oblate rotor level. Example of the total angular momentum $J=3$ levels of an asymmetric top molecule is shown. The principal moment of inertia are arbitrarily set to $I_{aa}=1$ and $I_{cc}=2$, and I_{bb} varies between the oblate and the prolate limits. Figure adapted from Gordy & Cook(87).

symmetry	$K_a K_c$	E	Symmetry Operation		
			$C_2(c)$	$C_2(b)$	$C_2(a)$
A	ee	1	1	1	1
B_c	oe	1	1	-1	-1
B_b	oo	1	-1	1	-1
B_a	eo	1	-1	-1	1

Table 2.2: Group characters of the $D_2(V)$ group

2.4 Rigid Rotor and Semi-rigid Rotor

$J_{K_1 K_2}$	$E(A, B, C)$
0_{00}	0
1_{10}	$A + B$
1_{11}	$A + C$
1_{01}	$B + C$
2_{20}	$2A + 2B + 2C + 2[(B - C)^2 + (A - C)(A - B)]^{1/2}$
2_{21}	$4A + B + C$
2_{11}	$A + 4B + C$
2_{12}	$A + B + 4C$
2_{02}	$2A + 2B + 2C - 2[(B - C)^2 + (A - C)(A - B)]^{1/2}$
3_{30}	$5A + 5B + 2C + 2[4(A - B)^2 + (A - C)(B - C)]^{1/2}$
3_{31}	$5A + 2B + 5C + 2[4(A - C)^2 - (A - B)(B - C)]^{1/2}$
3_{21}	$2A + 5B + 5C + 2[4(B - C)^2 + (A - B)(A - C)]^{1/2}$
3_{22}	$4A + 4B + 4C$
3_{12}	$5A + 5B + 2C - 2[4(A - B)^2 + (A - C)(B - C)]^{1/2}$
3_{13}	$5A + 2B + 5C - 2[4(A - C)^2 - (A - B)(B - C)]^{1/2}$
3_{03}	$2A + 5B + 5C - 2[4(B - C)^2 + (A - B)(A - C)]^{1/2}$
4_{40}	—
4_{41}	$10A + 5B + 5C + 2[4(B - C)^2 + 9(A - C)(A - B)]^{1/2}$
4_{31}	$5A + 10B + 5C + 2[4(A - C)^2 - 9(A - B)(B - C)]^{1/2}$
4_{32}	$5A + 5B + 10C + 2[4(A - B)^2 + 9(A - C)(B - C)]^{1/2}$
4_{22}	—
4_{23}	$10A + 5B + 5C - 2[4(B - C)^2 + 9(A - C)(A - B)]^{1/2}$
4_{13}	$5A + 10B + 5C - 2[4(A - C)^2 - 9(A - B)(B - C)]^{1/2}$
4_{14}	$5A + 5B + 10C - 2[4(A - B)^2 + 9(A - C)(B - C)]^{1/2}$
4_{04}	—
5_{42}	$10A + 10B + 10C + 6[(B - C)^2 + (A - B)(A - C)]^{1/2}$
5_{24}	$10A + 10B + 10C - 6[(B - C)^2 + (A - B)(A - C)]^{1/2}$

Table 2.3: Explicit expressions for the rotational energy in terms of rotational constants. Adapted from Table 7.7 of Gordy & Cook(87).

2.4 Rigid Rotor and Semi-rigid Rotor

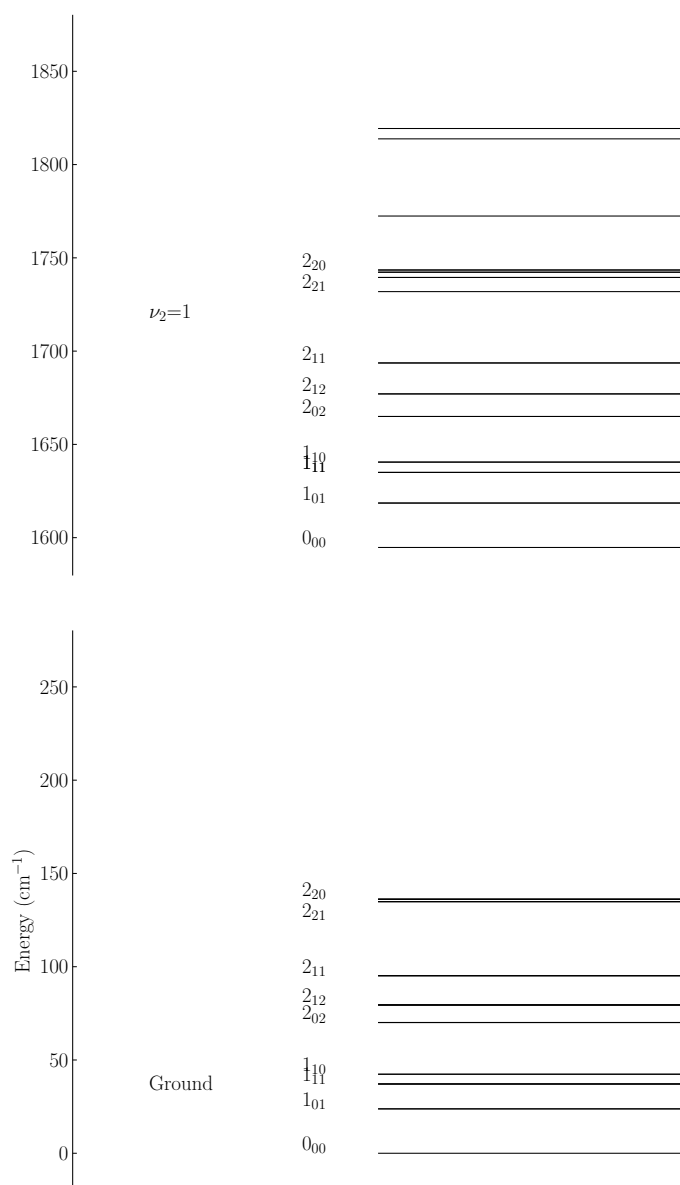


Figure 2.6: Rovibrational energy levels of H_2^{16}O in ground and $\nu_2=1$ bending states - The rovibrational energy levels of $J=0,1,2$ levels. Values are taken from the HITRAN08(216) database. Several $J=3$ levels on the $\nu_2=1$ state are also plotted. Each rovibrational level is labeled by its asymmetric top rotational quantum number $J_{K_a K_c}$ defined in the text.

2.4.2 Centrifugal Distortion Constants

As mentioned in Sec. 2.2.2, the centrifugal distortion constants arise from the non-rigid behavior of the molecule. The bond length and bond angle of the molecule change as the molecule takes different vibrational states. The rotation of the molecule distorts the geometry of the molecule from its equilibrium value. As shown in Eqn. 2.2.1.5, the Hamiltonian term for the centrifugal distortion is:

$$\hat{H}_{\text{dis}} = \sum_{\alpha, \beta} (\hat{J}_\alpha - \hat{\Pi}_\alpha)(\mu_{\alpha, \beta} - \mu_{\alpha\beta}^e)(\hat{J}_\beta - \hat{\Pi}_\beta) \quad (2.4.2.1)$$

where α, β stand for certain rotational axes and \hat{J} and $\hat{\Pi}$ are rotational and vibrational angular momenta. The vibrational angular momentum is usually absorbed into the Coriolis coupling terms. The non-rigidity effect is expanded using perturbation theory which leads to the quartic terms:

$$\hat{H}_{\text{dis}} = \frac{1}{4} \sum \tau_{\alpha\beta\gamma\delta} J_\alpha J_\beta J_\gamma J_\delta \quad (2.4.2.2)$$

with

$$\tau_{\alpha\beta\gamma\delta} = -\frac{1}{2} \sum_{ij} \mu_{\alpha\beta}(f^{-1})\mu_{\gamma\delta} \quad (2.4.2.3)$$

where f is a force constant in the harmonic potential energy defined by

$$V = -\frac{1}{2} \sum_{ij} f_{ij} Q_i Q_j \quad (2.4.2.4)$$

2.4.2.1 Diatomic Molecules and Linear Molecules

The rovibrational energy levels of a diatomic molecule or a linear molecule with centrifugal distortion can be expressed as:

$$E_{v,J} = \omega(v + \frac{d}{2}) - \omega\chi(v + \frac{d}{2})^2 + \dots \\ B_v J(J+1) - D_v [J(J+1)]^2 + H_v [J(J+1)]^3 \dots \quad (2.4.2.5)$$

The rotational constant B_v and centrifugal distortion constants D_v and H_v are subjected to further expansion in terms of vibrational quantum number $(v + \frac{d}{2})$. The centrifugal distortion constant D for a diatomic molecule is:

$$D = \frac{4B^3}{\omega^2} \quad (2.4.2.6)$$

2.4 Rigid Rotor and Semi-rigid Rotor

where ω is the frequency corresponding to the vibrational energy gap. For the weak interaction complex we study, the van der Waals (vdw) stretching force constant (k_s) between the A and B subunits of the complex can be estimated using the pseudo-diatomic approximation:(175)

$$k_s = \frac{\hbar^4 \mu_R}{2Dh} \frac{I_{AB} - I_A - I_B}{I_{AB}^4} \quad (2.4.2.7)$$

where D is the centrifugal distortion constant, μ_R is the reduced mass of the two subunits A and B , I_{AB} , I_A , and I_B are the principle b -inertial moment. If a Lennard-Jones type potential is assumed, the dissociation energy (ΔE_0) could be estimated by the following equation:(26)

$$\Delta E_0 = \frac{1}{72} k_s R_{c.m.}^2 \quad (2.4.2.8)$$

$R_{c.m.}$ is the distance between the center of mass of the two sub-units.

2.4.2.2 Symmetric Top Molecules

The rotational term values from the reduced Hamiltonian of the centrifugal distortion constants for a symmetric top molecule is:

$$\begin{aligned} E(JK) = & BJ(J+1) + (A-B)K^2 \\ & - D_J[J(J+1)]^2 - D_{JK}J(J+1)K^2 - D_K K^4 \quad (2.4.2.9) \\ & + \dots \end{aligned}$$

with

$$A = A^e + \frac{3}{4}\tau_{abab} - \tau_{acac} \quad (2.4.2.10)$$

$$B = B^e - \frac{1}{2}\tau_{abab} + \frac{1}{4}\tau_{acac} \quad (2.4.2.11)$$

$$D_J = -\frac{1}{4}\tau_{aaaa} \quad (2.4.2.12)$$

$$D_{JK} = \frac{1}{2}\tau_{aaaa} - \frac{1}{2}\tau_{aacc} - \tau_{acac} \quad (2.4.2.13)$$

$$D_K = -\frac{1}{4}\tau_{aaaa} - \frac{1}{4}\tau_{cccc} + \frac{1}{2}\tau_{aacc} + \tau_{acac} \quad (2.4.2.14)$$

as the first order correction to the effective rotational constants.

The second order correction gives rise to the sextic terms:

$$E_{\text{dis}}^{(2)} = H_J[J(J+1)]^3 + H_{JK}[J(J+1)]^2 K^2 + H_{KJ}[J(J+1)]K^4 + H_K K^6 \quad (2.4.2.15)$$

2.4.2.3 Asymmetric Top Molecules

The distortable asymmetric top rotor problem was first studied by Kivelson and Wilson.(125) Due to its complexity, microwave spectroscopists had tended to measure a few lines of low angular momentum to minimise the centrifugal distortion on the measured transitions. Otherwise, excess parameters are needed to fit the transitions. For example, 105 sixth-degree terms had been used by Chung and Parker.(52) A large number of phenomenological terms were used to account for the centrifugal distortion constants by Dreizler *et al.*. However, the experimental observed eigenvalues depend on only *certain* linear combination of the parameters. The proper Hamiltonian to fit the experimental data should remove the indeterminate parameters. Watson in his classical works(269, 270, 272, 273) provided a unified treatment of centrifugal distortion effects using the contact transformation method (Sec. 2.2.2). The resulted reduced Hamiltonian, or known as the “Watsonian”, is suitable for fitting of observed spectroscopy transitions because of the following features:

1. In general, there are $n + 1$ centrifugal distortion terms for degree n . There are 5 quadratic terms and 7 sextic terms.
2. Also, it is totally symmetric in the point group $D_2(V)$ regardless of the symmetry of the molecule.
3. Its matrix elements in a symmetric top wave function basis set satisfy the selection rule $\Delta K = 0, \pm 2$, which is the same as the selection rule for the asymmetric top rigid rotor matrix elements introduced in Sec. 2.5.2.2.

The very complex full vibration-rotation problem is beyond the scope of this work and can be found in detail elsewhere.(7, 208)

For a general asymmetric top molecule, Watson’s Asymmetric (A) reduction asymmetric Hamiltonian (276) contains diagonal (capital) and off-diagonal (lower case) quartic terms:

$$\Delta_J, \Delta_{JK}, \Delta_K, \delta_J, \delta_K \tag{2.4.2.16}$$

and sextic terms:

$$\Phi_J, \Phi_{JK}, \Phi_{KJ}, \Phi_K, \phi_J, \phi_{JK}, \phi_K \tag{2.4.2.17}$$

For a number of slightly asymmetric top molecules with near symmetric top structure, the determined off-diagonal terms are usually highly-correlated and the

2.4 Rigid Rotor and Semi-rigid Rotor

matrix are usually ill-conditioned. Symmetric (S) reduction Hamiltonian has to be used, with the quadratic terms:

$$D_J, D_{JK}, D_K, d_2, d_1 \quad (2.4.2.18)$$

and sextic terms:

$$H_J, H_{JK}, H_{KJ}, H_K, h_3, h_2, h_1 \quad (2.4.2.19)$$

It should be noted that in these widely used reduced Hamiltonians, distortion energy terms are absorbed into the rigid rotor Hamiltonian as the symmetric top molecules. Therefore, the determined effective rotational constants in these treatment contain contributions from the centrifugal distortion, in addition to the vibrational angular momentum contribution π in Eqn. 2.2.1.5. Although very small, these effects add in ambiguity into the experimental derivation of the molecular structure.

2.4.3 Coriolis Coupling

The Coriolis coupling arise from the rotation-vibration cross terms that cannot be totally eliminated from the molecular rovibrational Hamiltonian in Eqn. 2.2.1.4:

$$\hat{H}_{\text{Coriolis}} = \mu_{\alpha,\beta} \Pi_\alpha \Pi_\beta - \mu_{\alpha,\beta} (J_\alpha \Pi_\beta + J_\beta \Pi_\alpha) \quad (2.4.3.1)$$

The classical treatment of the rotation-vibration coupling is introduced in Appendix B.4. A general discussion of the Coriolis coupling and intensity perturbation is given by Mills.(180)

The Coriolis constant ζ is defined Eqn. B.4.0.28:

$$\zeta_{rr'}^{(\alpha)} = \sum_n e_{\alpha\beta\gamma} l_{nr}^{(\beta)} l_{nr'}^{(\gamma)}$$

where $\zeta_{rr'}^\alpha$ is the Coriolis coupling constant between the two normal coordinates Q_r and $Q_{r'}$ and it scales the internal angular momentum about the α axis generated by the two normal vibrations. The vibrational angular momentum is defined in Eqn. B.4.0.32:

$$\Pi_\alpha = \sum_r \sum_s \zeta_{rs}^{(\alpha)} Q_r P_s$$

Therefore, the general form of the Coriolis coupling operator is:

$$H_{\text{Coriolis}} = - \sum_{\alpha,r,s} \mu_{\alpha\alpha} \zeta_{r,s}^{(\alpha)} Q_r \hat{P}_s \hat{J}_\alpha \quad (2.4.3.2)$$

2.4 Rigid Rotor and Semi-rigid Rotor

and the $\mu_{\alpha,\beta}\Pi_\alpha\Pi_\beta$ term, which is orders of magnitude smaller, is usually neglected.(45)

Since the Coriolis terms have the forms $\hat{P}_z\hat{J}_x, \hat{P}_x\hat{J}_y, \hat{P}_y\hat{J}_z$, two vibration modes connected by one rotation operator can always be mixed by one of the high order terms, because their direct product contains total symmetry elements. The two vibrational mode with different symmetry have to be close enough in energy. For the degenerate vibration of a linear or symmetric top molecule perpendicular band, we have first-order Coriolis coupling. For the other non-degenerated vibrational modes, the Coriolis coupling is of second order.

2.4.3.1 Perpendicular Band of Linear or Symmetric Top Molecules

The *first order Coriolis coupling* appears in the diagonal terms of the degenerate bending mode of a linear or symmetric top molecule. The degenerate bending mode of such molecules is modeled by the doubly degenerate harmonic oscillator introduced in Sec. 2.3.1.2. A pair of quantum number v, l is used to describe the vibrational momentum and angular momentum, respectively. Therefore, the vibrational angular momentum π from such degenerated vibrations is $\sum_t \zeta_t^{(\alpha)} L_t$. The Coriolis coupling operator is:

$$T_{\text{Coriolis}} = -2\left(\frac{1}{2}\mu_\alpha\hat{J}_\alpha \sum_t \zeta_t^{(\alpha)} L_t\right) \quad (2.4.3.3)$$

The diagonal terms for such operator of the energy expression are easily obtained. For a linear molecule, the rotational energy expression is:

$$E(Jl_t) = B[J(J+1) - l_t^2] \quad (2.4.3.4)$$

This energy expression is essentially the same as the pseudo-diatomic Hamiltonian used for the rare gas water dimer complex such as Ar-H₂O and Ne-H₂O studied in the following Sec. 2.4.4, in which projection of the internal rotating H₂O subunit also contribute angular momentum to the symmetry axis of the axis. Therefore, the Hamiltonian of the Ar-H₂O takes the same form and the internal angular momentum is labelled by K instead of l for clarity as argued by Lascola and Nesbitt.(133). The discussion of this aeration can be find in Sec. 2.4.4.

$$E_{\text{vib-rot}} = B[J(J+1) - K^2] - D[J(J+1) - K^2]^2 + H[J(J+1) - K^2]^3 \quad (2.4.3.5)$$

For a prolate top symmetric top molecule, the rotational energy expression is:

$$E(JKv_t l_t) = BJ(J+1) + (A-B)K^2 - 2AK\zeta_t l_t \quad (2.4.3.6)$$

2.4 Rigid Rotor and Semi-rigid Rotor

Without the Coriolis coupling term, the bending excited rovibrational state of a symmetric top molecule with a non-zero K is 4-fold degenerated as K, l can each take \pm values. With the Coriolis coupling term, the initially 4-fold degenerated levels is split into 2; those two components having K, l with the same sign, and the two components with the different sign. Such splitting is called the *l-type doubling*, analogue to the *Λ -type doubling* in the diatomic molecules with electronic angular momentum contribution. It should be noted that the *l-type doubling* arise purely from the Coriolis coupling, instead of the “asymmetric effect” from the bending vibration as argued by Herzberg(96), which is discussed by Nielsen(190) and summarized by Watson.(274)

2.4.3.2 Second Order Coriolis Coupling

The Coriolis coupling operator is

$$\hat{H}_{\text{Coriolis}} = - \sum_{\alpha, r, s} \mu_{\alpha\alpha} \zeta_{r,s}^{(\alpha)} Q_r \hat{P}_s \hat{J}_\alpha \quad (2.4.3.7)$$

The Coriolis couplings between two non-degenerated vibrational modes v_1 and v_2 have non-vanishing matrix elements under proper symmetry considerations. Generally speaking, the diagonal matrix elements take the form:

$$\langle v_1 \pm 1 v_2 \mp 1 J k | \hat{H}_{\text{Coriolis}} | v_1 v_2 J k \rangle = \pm 2i \frac{1}{2} \mu_{aa} \zeta_{1,2}^{(a)} \Omega k [(v_1 \pm 1)(v_2 \mp 1)]^{1/2} \quad (2.4.3.8)$$

and the off-diagonal terms take the form:

$$\langle v_1 \pm 1 v_2 \mp 1 J k \pm 1 | \hat{H}_{\text{Coriolis}} | v_1 v_2 J k \rangle = \pm 2i \frac{1}{2} \mu_{bb} \zeta_{1,2}^{(b)} \Omega [J(J+1) - k(k \pm 1)]^{1/2} [(v_1 \pm 1)(v_2 \mp 1)]^{1/2} \quad (2.4.3.9)$$

where Ω is the Mills' abbreviation,

$$\Omega = \frac{1}{2} \left[\left(\frac{v_1}{v_2} \right)^{1/2} + \left(\frac{v_2}{v_1} \right)^{1/2} \right] \quad (2.4.3.10)$$

In general, the off-diagonal Coriolis coupling term is J and k dependent, taking the form $G = \beta [J(J+1) - k(k \pm 1)]^{1/2}$. In the atom-asymmetric top van der Waals complex Hamiltonian introduced in Sec. 2.4.4, the Coriolis coupling term is introduced as $G = \beta [J(J+1)]^{1/2}$ in Eqn. 2.4.4.2. This is a simplified version of the general form with k value taken as 0.

2.4.4 Atom-Asymmetric Top van der Waals Complex

The discussion in the previous sections was limited to small semi-rigid molecules with a single deep minimum and small amplitude vibrations, in which the vibrational wave functions of the molecules are localized around the equilibrium position. The amplitude of such vibrations is far less than the dimension of the inter-nuclear distance. The decoupling of rotation and vibration in such cases is therefore valid. This model is not suitable for molecules with large amplitude motions such as internal rotation, and tunnelling inversion motion. The amplitude of vibration is usually on the same order as the dimension of the bond length of the molecule. For such floppy molecules, effective Hamiltonians are often used, with effective spectroscopic constants that can be derived from calculations of the rovibrational wave function or from fitting of spectroscopic data.(189, 241, 201)

Such molecular complexes are spectroscopically stable; although the binding energy of the molecular complex is far less than the infrared radiation energy that it absorbs. For example, the binding energy of Ne-H₂O and Ar-H₂O are 65 and 142 cm⁻¹ respectively. However, it is stable after absorption of mid-IR radiation at 3 and 6 μm. This is because the vibrational lifetime of the infrared mode at 3 and 6 μm are long enough so that the absorbed photon energy is localized to the intra-molecular degree of freedom for a relatively long time before transferring to the low energy intermolecular degree of freedom.

Large amplitude motion (LAM) is also a key feature of the weak interaction molecular complex.(14) With the flat minima and low barriers of the PES, the floppy weakly-bonded molecular complex has large amplitude motions which access portions of the PES far from the equilibrium. The rovibrational wave functions supported on such PES are not localized. Separation of rotation and vibration of such complexes is poor and there are usually strong rovibrational couplings. Measurement of the high resolution infrared spectrum of such complexes probe their rovibrational states that depend in a very sensitive way on the potential energy surface.(188, 177, 178, 186, 185, 110)

As shown by Nesbitt *et al.*, a small number of rovibrational states probed in the low temperature, jet expansion cannot completely specify the potential energy surface. The transitions with low J, K values that are thermally accessible in a supersonic jet cannot distinguish between a relatively floppy or a rigid complex. These transitions can usually be well fit by a rigid or semi-rigid rotor Hamiltonian.

The binary complexes consisting of a rare gas atom and H₂O or NH₃ molecule studied in this thesis have weak interaction energies and low internal rotation

2.4 Rigid Rotor and Semi-rigid Rotor

barriers. The potential energy surface (PES) of the binary complex of rare gas atom-H₂O has been studied by Makarewicz(157) using the CCSD(T)/CBS level of theory, which is so far the most accurate *ab initio* PES. A detailed review of several *ab initio* calculation of the Ar-H₂O PES is given in Sec. 5.1.1. The PES of the Ar-H₂O complex is given in Fig. 5.3, featuring a broad and flat minimum of only 140 cm⁻¹ and two low in-plane rotation barriers.

The rovibrational energy levels of the floppy atom-asymmetric top van der Waals complex is best described by the nearly free internal rotor model suggested by Hutson.(111) The central assumption is that the interacting monomers are not significantly affected by the weak van der Waals forces. The molecular Hamiltonian contains four parts:

1. a pseudo-diatomic rotational term to describe the two rotational degrees of freedom of the complex,
2. an asymmetric top-like term to describe the three degrees of freedom of the hindered internal rotation associated with the motion of the H₂O monomer within the cluster,
3. a term to describe the intermolecular stretching coordinate, and
4. the anisotropic intermolecular potential.

It is convenient to consider the spectroscopic notation in terms of the degree of freedom (DOF) of the system. In the limit of strong anisotropic potential, the Ar-H₂O complex has a well defined “rigid” structure.

- 3 translational DOF ($\mathbf{X}, \mathbf{Y}, \mathbf{Z}$)
- 3 rotational DOF ($\mathbf{J}_{\mathbf{K}_a, \mathbf{K}_c}$)
- 3 H₂O vibrational DOF ($\mathbf{v}_1, \mathbf{v}_2, \mathbf{v}_3$)
- 3 VDW vibrational DOF (stretch, in-plane bend, out-of-plane bend)

In the limit of total isotropic potential, the H₂O subunit is a free internal rotator in the complex.

- 3 translational DOF ($\mathbf{X}, \mathbf{Y}, \mathbf{Z}$)
- 2 end-over-end rotational DOF (\mathbf{J})

2.4 Rigid Rotor and Semi-rigid Rotor

- 3 H₂O vibrational DOF ($\mathbf{v}_1, \mathbf{v}_2, \mathbf{v}_3$)
- 3 free H₂O rotational DOF ($\mathbf{j}_{\mathbf{k}_a, \mathbf{k}_c}$) as VDW vibrational DOF
- 1 VDW stretching DOF (\mathbf{n})

The slightly anisotropic potential of the Ar-H₂O complex leads to the *nearly* free internal rotor model:

- 3 translational DOF ($\mathbf{X}, \mathbf{Y}, \mathbf{Z}$)
- 2 end-over-end rotational DOF (\mathbf{J})
- 3 H₂O vibrational DOF ($\mathbf{v}_1, \mathbf{v}_2, \mathbf{v}_3$)
- 3 hindered H₂O rotational DOF ($\mathbf{J}_{\mathbf{k}_a, \mathbf{k}_c}$) as VDW vibrational DOF
- 1 VDW stretching DOF (\mathbf{n})

Therefore, the rovibrational term values of Ar-H₂O is represented by a pseudo-diatomic molecule:(54)

$$\begin{aligned}
 E_{\text{vib-rot}} = & \quad G(\nu_{\text{H}_2\text{O}}) + G(\nu_{\text{vdW}}) + G(\nu_{j_{k_a k_c}}) \\
 & \quad + B[J(J+1) - K^2] \\
 & \quad - D[J(J+1) - K^2]^2 + H[J(J+1) - K^2]^3
 \end{aligned} \tag{2.4.4.1}$$

The pseudodiatomic rotational term to describe the end-over-end rotation of the complex is essentially the same as that of a linear polyatomic molecule with the vibrational angular momentum contribution, as discussed in Sec. 2.4.3.1. Note that by setting the ratio of the quadratic distortion constants to 1 : -2 : 1, and the sextic distortion constants to 1 : -3 : 3 : -1, the symmetric top distortion constants introduced in Eqn. 2.4.2.10 and Eqn. 2.4.2.15 can be used to simulate the pseudo-diatomic Hamiltonian used in Eqn. 2.4.2.5. This trick is used when fitting the atom-asymmetric top Hamiltonian with the SFFIT program as discussed in Sec. 2.5.4.

The $G(\nu_{\text{H}_2\text{O}})$ term represents the ‘‘intramolecular’’ vibration of the H₂O subunit and the $G(\nu_{\text{vdW}})$ term represents the ‘‘intermolecular’’ van der Waals stretching between the H₂O subunit and the Ar atom. The $G(\nu_{j_{k_a k_c}})$ term represents the nearly free internal rotation of the H₂O subunit in the complex, which are correlated to the free H₂O molecule rovibrational states and are labeled by the corresponding free H₂O rotational energy state $J_{K_a K_c}$. The anisotropy in the

angular PES splits the degeneracy of the internal rotor states into $2j + 1$ components. The internal rotating H₂O subunit contributes an effective moment of inertia and an angular momentum component K along the intermolecular axis of the complex.⁽¹³³⁾ Therefore, the internal rotor states of the complex are further characterized by the magnitude of the projection of this angular momentum, labeled as $\Sigma, \Pi, \Delta, \dots$ states. The slightly anisotropic potential preserves the *ortho/para* nuclear spin classification of the H₂O subunit, i.e., the $\Sigma(0_{00})$ internal rotor state is *para* and the $\Sigma(1_{01})$ and $\Pi(1_{01})$ states are *ortho*. At the ~ 1 K temperature of the supersonic jet expansion, only levels within a few cm^{-1} of the lowest level of each nuclear spin symmetry are populated. Levels of different nuclear spin symmetries are not connected by optical or collisional transitions. Therefore, on the vibrational ground state, the $\Sigma(0_{00})$ level of the *para* manifold is populated, since the lowest excited levels, i.e., the $n = 1, \Sigma(0_{00})$ and the $\Sigma(1_{11})$ states are 30-40 cm^{-1} higher in energy. Among the states of the *ortho* manifold, both the $\Sigma(1_{01})$ and the $\Pi(1_{01})$ levels are populated, which are $\sim 11 \text{ cm}^{-1}$ apart.

Coriolis effects due to large amplitude nature of the H₂O internal rotation mix together states of the same internal rotor states, i.e., the same wave function $\Phi_{j_{k_a k_c}}$. These Coriolis effects are the predominant cause of the K doubling of the nearly degenerate Π^e and Π^f states. A J dependent off-diagonal Coriolis coupling term is introduced:

$$G = \beta[J(J + 1)]^{1/2} \quad (2.4.4.2)$$

This is a simplified version of the general form of the off-diagonal Coriolis coupling term in Eqn. 2.4.3.9, with k value taken as 0. The Coriolis terms mixes the Σ and Π states are introduced in the effective Hamiltonian:

$$\begin{bmatrix} H_{\Sigma} & H_{\text{Coriolis}} \\ H_{\text{Coriolis}} & H_{\Pi} \end{bmatrix} \quad (2.4.4.3)$$

It has been shown that for an internal rotor state dominated by $j = 1$, for example the $(1_{01}), (1_{10})$ states, $\beta = 2B$; while for the $j = 2$ states, for example the (2_{12}) states, $\beta = 2\sqrt{3}B$.⁽⁵⁶⁾

2.5 Rovibrational Transitions

The direct absorption spectra measured in this study are recorded as the attenuation of the laser beam intensity detected by the infrared detector. The infrared photon in the laser beam is absorbed by the molecular complex in the supersonic

2.5 Rovibrational Transitions

free jet expansion through optical transitions between the lower and upper rovibrational states. The energy absorbed is then released through predissociation and radiation-less transitions. With electromagnetic radiation as the “driving force” applied to the molecule, the Hamiltonian can be written as

$$\hat{H} = \hat{H}_1(q) + \hat{H}_2(q, t) \quad (2.5.0.4)$$

The first term gives the time independent “stationary state” $\Phi^{(1)}(q, t)$. The second term is the perturbation from the light: the radiation field $\mathbf{E}(z, t) = \mathbf{E}_0 e^{i(kx - \omega t)}$ dotted with the electric dipole moment μ of the molecule.

$$\begin{aligned} \hat{H}_2(q, t) &= - \sum \mathbf{e}_q \cdot \mathbf{E} & (2.5.0.5) \\ &= -\mu \cdot \mathbf{E} & (2.5.0.6) \end{aligned}$$

Here μ is the molecular dipole moment operator:

$$\mu_q = \sum_j e_j q_j \quad (2.5.0.7)$$

with e_j as the charge and q_j coordinate ($q_j = X, Y, Z$ in space fixed orientation or $q_j = a, b, c$ in molecular fixed orientation) of the j th particle (electrons and nuclei) of the molecule. The two sets of coordinations are transformed by the direction cosine elements in Eqn. B.1.1.2. The electric field \mathbf{E} of the light is oscillating at the frequency of the radiation ω , leading to the oscillating perturbation. It should be noticed that only the electric dipole moment is usually considered. Magnetic dipole and electric quadrupole transitions are also possible but much weaker.

The general approach to solve the time-dependent Schroedinger equation is to expand the total wave function in terms of the time-independent wave function $\Phi_1(q, t)$ with coefficients as a function of time:

$$\Phi = \sum_n C_n(t) \Phi_n^{(1)}(q, t) \quad (2.5.0.8)$$

It is then solved using time dependent perturbation theory and the optical Bloch Equations. Briefly, the transition occurs when the oscillating frequency of the radiation field matches the transition frequency between the upper (v', J') and lower (v'', J'') level. The line strength factor involves the evaluation of the matrix element of the electric dipole operator μ between the wave functions $\phi(v', J')$ and $\phi(v'', J'')$, namely the transition dipole moment between the two states:

$$M = \langle v', J', k', m' | \mu | v'', J'', k'', m'' \rangle \quad (2.5.0.9)$$

In practice the integral itself does not need to be calculated. If the transition moment function $\phi_1^* \mu \phi_2$ is antisymmetric, the integral is zero. A non-vanishing integral requires that the transition moment function spans the total symmetric representation of the group to which the system belongs. The symmetry of the transition moment function is the direct product of the symmetries of its three components. Therefore, a **selection rule**, which is a constraint on the possible transitions of a system from one state to another, can be derived based on symmetry considerations. (45) For pure rotational transitions, this requires exist of a permanent dipole moment on the ground vibrational state. For rovibrational transitions, the requirement is the transition-dipole moment between the upper and lower vibrational state to be non-vanishing.

2.5.1 Vibrational Transitions

The vibrational transition intensity is given by the square of the transition moment:

$$M = \langle v' | \mu | v'' \rangle \quad (2.5.1.1)$$

The dipole moment can be expanded in a Taylor series:

$$\mu = \mu_e + \sum_k \left(\frac{\partial \mu}{\partial Q_k} \right)_e Q_k + \dots \quad (2.5.1.2)$$

So the transition dipole moment becomes:

$$M = \langle v' | \mu_e | v'' \rangle + \langle v' | \sum_k \left(\frac{\partial \mu}{\partial Q_k} \right)_e Q_k | v'' \rangle + \dots \quad (2.5.1.3)$$

$$= \mu_e \langle v' | v'' \rangle + \sum_k \left(\frac{\partial \mu}{\partial Q_k} \right)_e \langle v' | Q_k | v'' \rangle + \dots \quad (2.5.1.4)$$

The first term is zero because of the orthogonality of the Hermite polynomials used as the vibrational wave functions. The second term indicates that the vibrational band intensity is proportional to the derivative of the dipole moment with respect to the change of normal mode coordinates.

If only the harmonic oscillator potential is considered, as shown in Sec. 2.3, $\langle v' | Q_k | v'' \rangle$ is non-vanishing only with the selection rule:

$$\Delta v = \pm 1 \quad (2.5.1.5)$$

2.5 Rovibrational Transitions

When the lower level is the lowest vibrational level $v'' = 0$, the vibrational band is called **fundamental band**. When the lower level is a higher vibrational level $v'' \neq 0$, the vibrational band is called **hot band**.

As shown in Sec. 2.3, if the anharmonic oscillator potential is considered, there are more non-vanishing terms possible. For example, if the V^3 term is considered, the allowed transitions are:

$$\Delta v = \pm 2 \tag{2.5.1.6}$$

Other $\Delta v = \pm 3, 4, \dots$ transitions are also possible. These bands are called **overtones**.

The transition dipole moment containing $\langle v' | Q_k | v'' \rangle$ is non-vanishing if it is total symmetric. Therefore the symmetry representation of the vibrational state and the Cartesian x, y, z components of the μ can be used to determine if a vibrational normal mode is infrared active. For example, H₂O molecule belongs to the C_{2v} group, the character table of which is shown in Table 2.4. The ground vibrational state $|v''\rangle$ has A_1 symmetry. The excited ν_2 bending state $|v'\rangle$ has A_1 symmetry. Therefore the ν_2 bending mode is infrared active through the A_1 symmetry component of the dipole moment that is along the b axis of the molecule.

C_{2v}	E	C_2	$\sigma_v(ab)$	$\sigma_v(bc)$	
A_1	1	1	1	1	b
A_2	1	1	-1	-1	J_b
B_1	1	-1	-1	1	c, J_a
B_2	1	-1	1	-1	a, J_c

Table 2.4: C_{2v} Character Table

For the H₂O molecule all the 3 normal modes are infrared active:

- $\nu_1(a_1)$ symmetric stretch 3657 cm^{-1}
- $\nu_2(a_1)$ bend 1595 cm^{-1}
- $\nu_3(b_2)$ anti-symmetric stretch 3756 cm^{-1}

2.5.2 Rovibrational Transitions

Using the vibrational transition moment from Eqn. 2.5.1.4, the transition dipole moment of a rovibrational transition is:

$$\begin{aligned}
 M &= \langle v' J' k' m' | \mu | v'' J'' k'' m'' \rangle \\
 &= \langle J' k' m' | \sum_k \left(\frac{\partial \mu}{\partial Q_k} \right)_e \langle v' | Q_k | v'' \rangle | J'' k'' m'' \rangle \\
 &= \langle J' k' m' | \sum_k \left(\frac{\partial \mu}{\partial Q_k} \right)_e \sum_{\alpha, \beta, \gamma} \mathbf{R}(\alpha, \beta, \gamma) \langle v' | a | v'' \rangle | J'' k'' m'' \rangle \quad (2.5.2.1)
 \end{aligned}$$

where $\mathbf{R}(\alpha, \beta, \gamma)$ are the direction cosine elements that transform the normal mode coordinates Q_k to the molecular fixed orientation a, b, c . These direction cosine elements are functions of the Euler angles α, β, γ , which brings in the selection rules for rotational wave functions.

2.5.2.1 Linear and Symmetric Top Molecules

The selection rule for the rotational transitions with quantum number J for the linear and symmetric top rotational transitions is:

$$\Delta J = 0, \pm 1 \quad (2.5.2.2)$$

The standard spectroscopic notation for a rotational transitions of a particular vibrational transition band is:

- P branch $\Delta J = J' - J'' = -1$
- Q branch $\Delta J = J' - J'' = 0$
- R branch $\Delta J = J' - J'' = +1$

A simplified diagram showing the P, Q, R branches is given in Fig. 2.7 and a typical linear molecule's perpendicular band is given in Fig. 2.8

The selection rule for the quantum number K of symmetric top molecules is $\Delta K = 0, \pm 1$. The rotational line intensity factors are called Hönl-London factors which are given in Table 2.5. The $\Delta K=0$ transitions are called parallel band, because the transition dipole is parallel to the symmetric axis of the top. From Table 2.5, the approximate intensity is:

$$P(J'') \approx J'' \quad (2.5.2.3)$$

$$Q(J'') \approx 0 \quad (2.5.2.4)$$

$$R(J'') \approx J'' + 1 \quad (2.5.2.5)$$

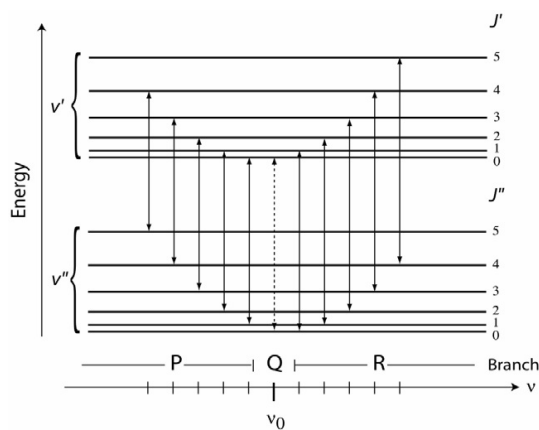


Figure 2.7: Schematic diagram of the P, Q, R branches of a linear molecule - The selection rule is $\Delta J = 0, \pm 1$, Q branch is present for perpendicular band. The position of band origin is given at ν_0 . Figure adapted from thesis by Matthew Dzikowski, University of Alberta.

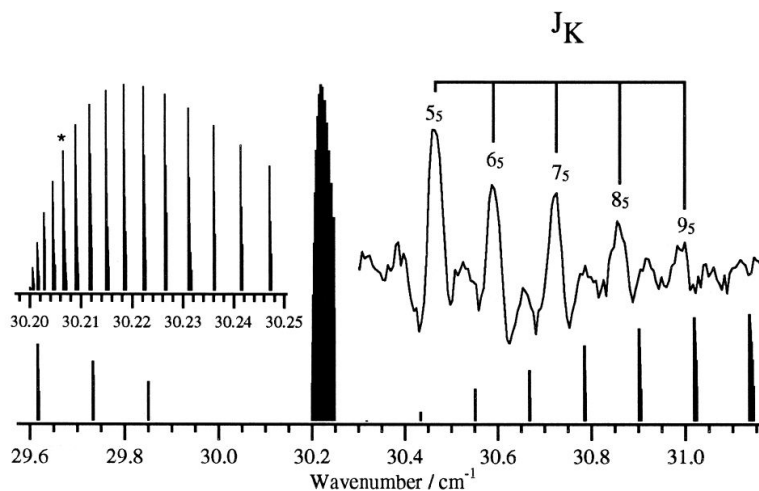


Figure 2.8: A typical spectrum of P, Q, R branches of a linear molecule - The selection rule is $\Delta J = 0, \pm 1$, Q branch is presented for perpendicular band. The position of band origin is given at ν_0 . Figure adapted from Ref. (61).

2.5 Rovibrational Transitions

$\Delta K = +1$	
$P(J'')$	$\frac{(J''-1-K'')(J''-K'')}{4J''}$
$Q(J'')$	$\frac{(J''+1+K'')(J''-K'')(2J''+1)}{4J''(J''+1)}$
$R(J'')$	$\frac{(J''+2+K'')(J''+1+K'')}{4(J''+1)}$
$\Delta K = 0$	
$P(J'')$	$\frac{(J''+K'')(J''-K'')}{J''}$
$Q(J'')$	$\frac{(2J''+1)K''^2}{J''(J''+1)}$
$R(J'')$	$\frac{(J''+1+K'')(J''+1-K'')}{J''+1}$
$\Delta K = -1$	
$P(J'')$	$\frac{(J''-1+K'')(J''+K'')}{4J''}$
$Q(J'')$	$\frac{(J''+1-K'')(J''+K'')(2J''+1)}{4J''(J''+1)}$
$R(J'')$	$\frac{(J''+2-K'')(J''+1-K'')}{4(J''+1)}$

Table 2.5: Hönl-London Factors

That is for P and R branch, they have comparable strength; only the lowest J'' lines of the Q branch have appreciable strength.

The $\Delta K = \pm 1$ transitions are called perpendicular band, because the transition dipole is perpendicular to the symmetric axis of the top. From Table 2.5, the approximate intensity is:

$$P(J'') \approx (J'' - 1)/4 \quad (2.5.2.6)$$

$$Q(J'') \approx (2J'' + 1)/4 \quad (2.5.2.7)$$

$$R(J'') \approx (J'' + 2)/4 \quad (2.5.2.8)$$

This shows that the P branch and R branch of a perpendicular band are of comparable strength and the Q branch is twice as strong. Depending on the different

K'' value, a rovibrational band consists of several sub-bands, each of which belongs to a certain $K' \leftarrow K''$ value. The intensities of the P/R branches of these sub-bands varies as the K'' value changes. When there is a rovibrational coupling mechanism that mix the different vibrational states, the rovibrational intensity of these bands is further complicated. For example, it is noticed that the intensity of the P, Q, R branches of the van der Waals complexes such as the Ar-H₂O and Ne-H₂O complexes do not strictly follow the Hönl-London factor and the perturbed states have drastic intensity changes.

2.5.2.2 Asymmetric Top Molecules

The selection rule for the J quantum number for the asymmetric top rotational transitions is

$$\Delta J = 0, \pm 1 \quad (2.5.2.9)$$

There are in general, non-vanishing permanent or transitional dipole moment along the abc axis: μ_a, μ_b and μ_c , which transform as B_a, B_b , and B_c , under the symmetry operations of the $D_2(V)$ group, respectively. The character table of the $D_2(V)$ group is given in Table 2.2. Therefore, the selection rule for the rotational transitions are:

- a type $\mu_a \neq 0$
 $A \leftrightarrow B_a \quad ee \leftrightarrow eo$
 $B_b \leftrightarrow B_c \quad oo \leftrightarrow oe \quad \Delta K_a = 0, \pm 2, \dots \quad \Delta K_c = \pm 1, \pm 3, \dots$
- b type $\mu_b \neq 0$
 $A \leftrightarrow B_b \quad ee \leftrightarrow oo$
 $B_a \leftrightarrow B_c \quad eo \leftrightarrow oe \quad \Delta K_a = \pm 1, \pm 3, \dots \quad \Delta K_c = \pm 1, \pm 3, \dots$
- c type $\mu_c \neq 0$
 $A \leftrightarrow B_c \quad ee \leftrightarrow oe$
 $B_a \leftrightarrow B_b \quad eo \leftrightarrow oo \quad \Delta K_a = \pm 1, \pm 3, \dots \quad \Delta K_c = 0, \pm 2, \dots$

note that ΔJ and $\Delta K_{a/c}$ cannot be zero at the same time.

Since the rotational wave function for asymmetric top molecule is the linear combination of symmetric top wave functions, calculation of the transitional intensity factor for the asymmetric top wave function involves the combination coefficients of the symmetric top wave function and using the Hönl-London factors in Table 2.5. As an example of the rotational transitions of a semi-rigid

asymmetric top molecule, the $J''=0,1,2$ rovibrational energy levels and the rovibrational transitions of the $\nu_2=1$ bending band of H₂O molecule at 6 μm are given in Fig. 2.9.

2.5.3 Population Distribution of Rovibrational States

The intensity of the observed rovibrational transitions also depends on the number of molecules in the lower state of the transitions at the sample. The population of the lower state is mainly determined by two factors:

- Thermal equilibrium state of the sample
- Spin statistical weights

2.5.3.1 Boltzmann Distortion

Under thermal equilibrium, the population distortion on the rovibrational states of a molecular system, which is represented by a canonical ensemble, follows the Boltzmann distribution.

$$p_i = \frac{1}{Z} e^{-\frac{E_i}{kT}} \quad (2.5.3.1)$$

where

$$Z = \sum_i e^{-\frac{E_i}{kT}} \quad (2.5.3.2)$$

is the partition function. A well defined temperature of the system (T) is given by the heat bath with which the system is in equilibrium. A well defined rotational-vibrational temperature can be fit from the rovibrational transitions.

In the supersonic expansion process, however, the molecular complex generated in the molecular beam is not under thermodynamic equilibrium. The supersonic expansion technique is introduced in Sec. E. The exchange of internal energy of seeded molecules with the cold bath is terminated once the density of the jet is so low that the jet enters the collision-less stage. Since the rotational energy gaps of the seeded molecule is much smaller than the vibrational and conformational energy gap, the internal energy of the rotational degree of freedom is transferred more efficiently to the cold bath. Therefore, the temperature obtained from fitting of the rotational energy levels of a particular vibrational state (T_r), and from different vibrational states (T_v), and between different conformers (T_{con}) are not consistent. Usually the order is $T_r < T_v < T_{con}$.

2.5 Rovibrational Transitions

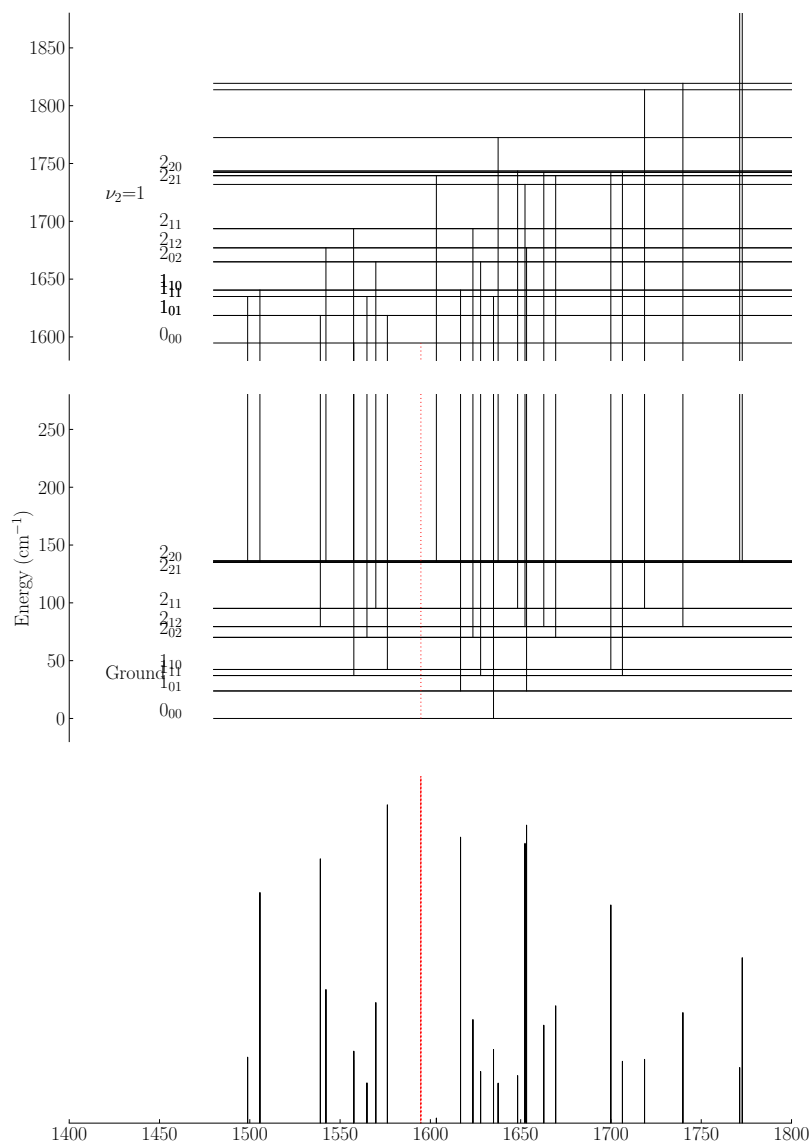


Figure 2.9: Rovibrational transitions of the $\nu_2=1$ bending band of H_2^{16}O - The rovibrational energy levels of $J=0,1,2$ levels are taken from the HITRAN08(216) database as shown in Fig. 2.6. The position of the band origin is shown in red. Since the 0_0 level has zero rotational energy, the band origin is calculated as the difference between the $\nu_2=1,0_{00}$ level and the ground 0_{00} level. Under the supersonic free jet expansion condition, the $1_{11} \leftarrow 0_{00}$, $1_{10} \leftarrow 1_{01}$, and $2_{12} \leftarrow 1_{01}$ are the 3 strongest transitions. The intensity shown is under ambient condition at 273K.

2.5.3.2 Spin Statistical Weights

When the molecule contains certain symmetry, identical nuclei are presented in the molecule. Exchange of one pair of the identical nuclei follows the quantum statistics:

- Bosons
Such as Deuterium, follows Bose-Einstein statistics, that is “the wave function of the system before interchange equals the wave function of the system after interchange”.
- Fermions
Such as Hydrogen, follows Fermi-Dirac statistics, that is “the wave function of the system before interchange is the wave function of the system after interchange, with an overall minus sign”.

Therefore, the overall wave function $|v, J\rangle|\text{spin}\rangle$ needs to be symmetric with Bosons and anti-symmetric with exchange of Fermions. Such requirement leads to the spin statistical weight of the different states of a molecule with symmetry.

For example, the H_2O molecule contains two identical H nucleus, which are Fermions. So the overall wave function of the H_2O molecule should be anti-symmetric. There are four spin wave functions for the two identical H nuclei at position A and B :

$$A(\uparrow)B(\uparrow) \quad (2.5.3.3)$$

$$A(\downarrow)B(\downarrow) \quad (2.5.3.4)$$

$$(A(\uparrow)B(\downarrow) + A(\downarrow)B(\uparrow))/\sqrt{2} \quad (2.5.3.5)$$

$$(A(\uparrow)B(\downarrow) - A(\downarrow)B(\uparrow))/\sqrt{2} \quad (2.5.3.6)$$

The first 3 wave functions are symmetric and the last wave function is anti-symmetric. The symmetric spin wave functions are associated with the anti-symmetric rovibrational wave functions, such as the 1_{01} , 1_{10} rotational levels on the ground or bending excited vibrational states. The anti-symmetric spin wave functions are associated with the symmetric rovibrational wave functions, such as the 0_{00} , 1_{11} states on the ground or bending excited vibrational states. Under the ambient environment and supersonic free jet expansion condition, the mixing and interchange of the two spin modifications are neglected. The spin statistical weight between the two spin modifications are 3:1.

2.5.4 Fitting of Spectroscopic Constants

The measured rovibrational transitions are the energy differences between the stationary rovibrational energy levels introduced in Section 2.2.1 to Section 2.4. The experimental spectroscopists' job is to assign the measured spectra and least squared fit the measured transitions to obtain spectroscopic parameters for the determined rovibrational states. The vibrational frequency ν , anharmonic resonance energy E , and the rotational constants A, B, C , centrifugal distortion constants D, H , Coriolis coupling constants G are often determined from a fitting of the rovibrational transitions with ν, J, K, \dots quantum numbers.

The current working horse for fitting of the rovibrational transitions is Pickett's superb CALPGM/SPFIT/SPCAT package(202). Some post-processing programs to deal with output and data associated with SPFIT/SPCAT are used, such as PIFORM and PICHAM program from Kisiel. AABS software package for Assignment and Analysis of Broadband Spectra(124, 3) is used to aid the assignment and fitting of the spectrum. Use of the AABS package is illustrated in Fig. 6.17.

Pickett's program uses Euler series to fit spectral transitions.(203) For example, the atom-asymmetric top Hamiltonian introduced in Eqn. 2.4.4.1 can be fitted using this program based on a symmetric top Hamiltonian as discussed in Sec. 2.4.4. Input files(.par and .lin files) are taken from the fit the *ortho* Ar-H₂O transitions in Sec. 5.1.2. A typical parameter file (.par) including the Σ ground state (00) and the Π excited states with the unperturbed 01 state and the perturbed 02 state, connecting by the Coriolis coupling term 40000200. The centrifugal distortion constants D, H for the symmetric top Hamiltonian is fixed to $1 : -2 : 1$ and $1 : -3 : 3 : -1$ to generate the linear rotator Hamiltonian.

```

254 523 100 0 0.0000E+000 1.0000E+037 -1.0000E+000 1.0000000000
s -1 4 1 1 0 1 1 1 -1 1 1
s -1 3 1 1 0 1 1 1 -1 1 1
s -1 2 1 1 0 1 1 1 -1 1 1
s -1 1 1 1 0 1 1 1 -1 1 1
s -1 0 0 0 0 1 1 1 0 1 1
10000 3.014792853457038E+003 1.00000000E+037 /(B+C)/2
-100000 -3.014792853457038E+003 1.00000000E-037 /A-(B+C)/2
20000 -7.263567465323843E-002 1.00000000E+037 /-DJ
-110000 1.452713493064727E-001 1.00000000E-037 /-DJK
-200000 -7.263567465323843E-002 1.00000000E-037 /-DK
30000 1.333416930241649E-006 1.00000000E+037 /HJ
-120000 -4.000250790725053E-006 1.00000000E-037 /HJK
-210000 4.000250790725053E-006 1.00000000E-037 /HKJ
-300000 -1.333416930241649E-006 1.00000000E-037 /HK
101 3.426211154276423E+005 1.00000000E+037 /E
-202 3.426211154276423E+005 1.00000000E-037 /E
10101 2.951947576064437E+003 1.00000000E+037 /(B+C)/2
-100101 -2.951947576064437E+003 1.00000000E-037 /A-(B+C)/2
-10202 2.951947576064437E+003 1.00000000E-037 /(B+C)/2
-100202 -2.951947576064437E+003 1.00000000E-037 /A-(B+C)/2
20101 -1.156759093104446E-001 1.00000000E+037 /-DJ
-110101 2.313518186208910E-001 1.00000000E-037 /-DJK
-200101 -1.156759093104446E-001 1.00000000E-037 /-DK
30101 4.123573558744699E-006 1.00000000E+037 /HJ

```

2.5 Rovibrational Transitions

```

-120101 -1.237072067623428E-005 1.00000000E-037 /HJK
-210101 1.237072067623428E-005 1.00000000E-037 /HKJ
-300101 -4.123573558744699E-006 1.00000000E-037 /HK
 20202 -1.356458170301056E-001 1.00000000E+037 /-DJ
-110202 2.712916340602086E-001 1.00000000E-037 /-DJK
-200202 -1.356458170301056E-001 1.00000000E-037 /-DK
40000200 8.346432609802299E+003 1.00000000E+037 /Gb

```

A typical transition file (.lin) including the ground state pure rotational transitions and the infrared transitions. The Coriolis perturbed states are alternatively labeled $K = \pm 1$

```

1 0 0 0 0 0 5824.2523 .0005 /microwave
2 0 0 1 0 0 11647.0474 .0004 / Germann Gutosky 1993
3 0 0 2 0 0 17466.907 .004 / Fraser 1990
4 0 0 3 0 0 23282.332 .005 /
0 0 13 1 0 0 0 0 0 0 0 0 0 0 0 1652.227343 -0.001 1.00000
1 0 13 2 0 0 0 0 0 0 0 0 0 0 0 1651.995863 -0.001 1.00000
2 0 13 3 0 0 0 0 0 0 0 0 0 0 0 1651.732886 -0.001 1.00000
3 0 13 4 0 0 0 0 0 0 0 0 0 0 0 1651.433390 -0.001 1.00000
4 0 13 5 0 0 0 0 0 0 0 0 0 0 0 1651.104663 -0.001 1.00000
5 0 13 6 0 0 0 0 0 0 0 0 0 0 0 1650.745561 -0.001 1.00000
6 0 13 7 0 0 0 0 0 0 0 0 0 0 0 1650.359305 -0.001 1.00000
7 0 13 8 0 0 0 0 0 0 0 0 0 0 0 1649.948930 -0.001 1.00000
8 0 13 9 0 0 0 0 0 0 0 0 0 0 0 1649.517181 -0.001 1.00000
9 0 13 10 0 0 0 0 0 0 0 0 0 0 0 1649.063947 -0.001 1.00000
10 0 13 11 0 0 0 0 0 0 0 0 0 0 0 1648.586775 -0.001 1.00000
11 0 13 12 0 0 0 0 0 0 0 0 0 0 0 1648.093748 -0.001 1.00000
10 0 13 9 0 0 0 0 0 0 0 0 0 0 0 1652.648843 -0.001 1.00000 /R-
9 0 13 8 0 0 0 0 0 0 0 0 0 0 0 1652.740472 -0.001 1.00000
8 0 13 7 0 0 0 0 0 0 0 0 0 0 0 1652.809414 -0.001 1.00000
7 0 13 6 0 0 0 0 0 0 0 0 0 0 0 1652.856215 -0.001 1.00000
5 0 13 4 0 0 0 0 0 0 0 0 0 0 0 1652.879212 -0.001 7.16E+07
6 0 13 5 0 0 0 0 0 0 0 0 0 0 0 1652.879212 -0.001 6.49E+07
6 0 13 5 0 0 0 0 0 0 0 0 0 0 0 1652.879212 -0.005 6.49E+07
4 0 13 3 0 0 0 0 0 0 0 0 0 0 0 1652.851090 -0.001 1.00000
3 0 13 2 0 0 0 0 0 0 0 0 0 0 0 1652.793954 -0.001 1.00000
2 0 13 1 0 0 0 0 0 0 0 0 0 0 0 1652.703981 -0.001 1.00000
1 -1 14 0 0 0 0 0 0 0 0 0 0 0 0 1658.130749 -0.002 1.00000 /R-
2 1 14 1 0 0 0 0 0 0 0 0 0 0 0 1658.320085 -0.002 1.00000
3 -1 14 2 0 0 0 0 0 0 0 0 0 0 0 1658.505430 -0.002 1.00000
4 1 14 3 0 0 0 0 0 0 0 0 0 0 0 1658.674476 -0.002 1.00000
5 -1 14 4 0 0 0 0 0 0 0 0 0 0 0 1658.832471 -0.002 1.00000
6 1 14 5 0 0 0 0 0 0 0 0 0 0 0 1658.968508 -0.002 1.00000
7 -1 14 6 0 0 0 0 0 0 0 0 0 0 0 1659.080643 -0.002 1.00000
8 1 14 7 0 0 0 0 0 0 0 0 0 0 0 1659.165372 -0.002 1.00000
9 -1 14 8 0 0 0 0 0 0 0 0 0 0 0 1659.215613 -0.002 1.00000
10 1 14 9 0 0 0 0 0 0 0 0 0 0 0 1659.228433 -0.002 1.00000
11 -1 14 10 0 0 0 0 0 0 0 0 0 0 0 1659.202363 -0.002 1.00000
12 1 14 11 0 0 0 0 0 0 0 0 0 0 0 1659.136172 -0.002 1.00000
13 -1 14 12 0 0 0 0 0 0 0 0 0 0 0 1659.031541 -0.002 1.00000
14 1 14 13 0 0 0 0 0 0 0 0 0 0 0 1658.892614 -0.002 1.00000
15 -1 14 14 0 0 0 0 0 0 0 0 0 0 0 1658.716518 -0.012 1.00000
1 -1 14 2 0 0 0 0 0 0 0 0 0 0 0 1657.546048 -0.002 1.00000 /P-
2 1 14 3 0 0 0 0 0 0 0 0 0 0 0 1657.348112 -0.002 1.00000
3 -1 14 4 0 0 0 0 0 0 0 0 0 0 0 1657.144117 -0.002 1.00000
4 1 14 5 0 0 0 0 0 0 0 0 0 0 0 1656.929414 -0.002 1.00000
5 -1 14 6 0 0 0 0 0 0 0 0 0 0 0 1656.696950 -0.002 1.00000
6 1 14 7 0 0 0 0 0 0 0 0 0 0 0 1656.446905 -0.002 1.00000
7 -1 14 8 0 0 0 0 0 0 0 0 0 0 0 1656.174283 -0.002 1.00000
8 1 14 9 0 0 0 0 0 0 0 0 0 0 0 1655.873636 -0.002 1.00000
9 -1 14 10 0 0 0 0 0 0 0 0 0 0 0 1655.534744 -0.002 1.00000

```

3

Molecular Self-Recognition: Rotational Spectra of the Dimeric 2-Fluoroethanol Conformers

Fluoroalcohols show competitive formation of intra- and intermolecular hydrogen bonds, a property that may be crucial for the protein-altering process in a fluoroalcohol/water solution. In this study, we examine the intra- and intermolecular interactions of 2-fluoroethanol (FE) in its dimeric conformers by using rotational spectroscopy and ab initio calculations. Three pairs of homo- and heterochiral dimeric FE conformers are predicted to be local minima at the MP2/6-311++G(d,p) level of theory. They are solely made of the slightly distorted most stable G+g-/G-g+ FE monomer units. Jet-cooled rotational spectra of four out of the six predicted dimeric conformers were observed and unambiguously assigned for the first time. All four observed dimeric conformers have compact geometries in which the fluoromethyl group of the acceptor tilts towards the donor and ensures a large contact area. Experimentally, the insertion of the O-H group of one FE subunit into the intramolecular O-H \cdots F bond of the other was found to lead to a higher stabilisation than the pure association through an intermolecular O-H \cdots O \cdots H link. The hetero- and homochiral combinations were observed to be preferred in the inserted and the associated dimeric conformers, respectively. The experimental rotational constants and the stability ordering are compared with the ab initio calculations at the MP2 level with the 6-311++G(d,p) and aug-cc-pVTZ basis sets. The effects of fluorination and the competing inter-and

intramolecular hydrogen bonds on the stability of the dimeric FE conformers are discussed.

3.1 Introduction

Fluoroalcohols can alter the secondary and tertiary substructures of proteins and polypeptides when used as a cosolvent in aqueous solutions.(84, 42) To study the mechanism of the fluoroalcohol intervention in peptide binding, NMR spectroscopy(31), X-ray diffraction(106, 25), circular dichroism spectroscopy(113), FTIR spectroscopy(226) and molecular dynamics approaches(215) have been applied to enrich our understandings. A detailed picture of this important process, on the other hand, is still lacking. A prerequisite for the understanding of protein-ligand interactions is the precise knowledge of the physical properties of the fluoroalcohol solvent and the aqueous solution themselves.(18, 70) It has been proposed that small fluoroalcohol aggregates are crucial for the protein altering process.(211) Suhm and co-workers had recently used a bottom-up approach to tackle the question of intermolecular binding in fluoroalcohol solvents. They investigated small clusters of trifluoroethanol(222, 220) and 2-fluoroethanol (FE)(221) produced in a molecular expansion by means of low-resolution IR and Raman spectroscopy, enhanced by molecular modelling and quantum chemical approaches. In the FE study, they tentatively identified four dimeric FE conformers based on the observed and calculated vibrational contours and the “Argon (Ar) test”,(68) in which a small amount of Ar is added to the free jet expansion of Helium (He) to promote collisional relaxation and to convert the higher-lying conformers to the global minimum structure. The method of broadband jet FTIR spectroscopy has the advantage of providing an overview of the vibrational band contour patterns of the hydrogen-bonded aggregates with good signal-to-noise ratios and high reproducibility. This low-resolution method, on the other hand, does not provide direct structural information. Such information is extracted in an indirect way through the analysis of the vibrational frequencies, together with pressure dependence and isotopic studies and theoretical calculations. It is therefore desirable to probe the fluoroalcohol aggregates by using high-resolution spectroscopic techniques for which each individual conformer can be unambiguously identified with its own set of rotational constants. These small aliphatic systems are inaccessible to the sensitive fluorescence spectroscopic techniques, previously applied in the pioneering work in chiral recognition by Zenhacker and co-workers, because they lack an aromatic chromophore. One suitable method is Fourier

transform microwave (FTMW) spectroscopy, which is known to offer highly accurate structural information. It has been applied in recent years to characterise large and biologically relevant systems such as phenylglycine,(217) the ethanol dimer(93) and molecular lock and key model systems.(32, 34) Furthermore, this technique can profit from the generous dipole moments of the fluoro-containing organic compounds in the excitation and emission detection processes.

In this chapter, we present the assignments and the analyses of rotational spectra of four dimeric FE conformers, by using FTMW spectroscopy, complemented with high-level *ab initio* calculations. The stability ordering of the four coexisting dimeric FE conformers was established by monitoring their transition intensities in a co-expansion of FE and Neon (Ne) and by performing the “Ar test”. The experimental data of the rotational constants, the magnitudes of the electric dipole moment components, and the stability ordering are compared with the *ab initio* predictions. The effects of fluorination and the competing inter- and intramolecular hydrogen bonds on the stability of the conformers of the FE dimer are discussed.

3.2 Methods

3.2.1 Experimental Details

FE (97%, Sigma-Aldrich) was used without further purification. The samples used are 0.3% FE in Ne (99.9990%, Praxair) or mixtures of 20% Argon (99.996%, Praxair) and 80% He (99.996%, Praxair). The samples were expanded through a pulsed jet pinhole nozzle (General Valve Series 9) with a home made cap (0.8 mm diameter opening and 3.0 mm long exit channel) into the vacuum chamber of a Balle-Flygare type(19, 8) FTMW spectrometer. The spectrometer is described in detail elsewhere.(294) FE and Ne were mixed in several gas cylinders with a total volume of 4 L so that the optimum stagnation pressure around 3-4 bar was maintained over the long automated survey scans. Rotational lines in the frequency region of 3.9-10.3 GHz were recorded. The full line width at half maximum is 15 kHz for a well-resolved transition and the accuracy of the frequency determination was estimated to be 2-3 kHz. Each transition appeared as a Doppler doublet, because the propagation direction of the microwave radiation was parallel to the molecular expansion. The central frequency was obtained by unweighted averaging of the frequency pair.

3.2.2 Computational Methods

MP2 geometry optimization of the equilibrium geometries of the 2-fluoroethanol dimer with the 6-311++G(d,p) and the aug-cc-pVTZ(65) basis set were performed using the Gaussian 03 suite of programs.(81) Stationary points were confirmed to be local minima by harmonic frequency analyses. The BSSE corrections were determined using the counterpoise correction methods of Boys and Bernardi(39) in the same way as suggested in reference(287).

3.3 Results

3.3.1 Preliminary Model Calculations

Ab initio geometry predictions of the targeted complexes, although not essential, are of great help for spectral assignments, especially when large numbers of conformers are anticipated. In addition to the rotational constants, the calculations can also provide information about the electric dipole moment components and the preliminary relative stabilities of the possible conformers. *Ab initio* calculations were performed using the second order Møller-Plesset (MP2) perturbation theory(27) with the 6-311++G(d,p) basis set.(128) The MP2/6-311++G(d,p) level of theory was chosen because it provided astonishingly good agreement between the predicted and the experimentally observed geometries for several van der Waals(72) and hydrogen-bonded complexes(244) in a number of previous studies.

The FE monomer has two structurally relevant dihedral angles: $\tau(\text{FCCO})$ and $\tau(\text{CCOH})$. Each can adopt three values of approximately 0° (trans or t/T), $+60^\circ$ (gauche+ or g+/G+), and -60° (gauche- or g-/G-). This leads to nine possible combinations with four mirror image or enantiomeric pairs: G+g-/G-g+, G+g+/G-g-, G+t/G-t, Tg-/Tg+, and Tt. the capital letters represent the conformation of $\tau(\text{FCCO})$ and the lower case that of $\tau(\text{CCOH})$. The Newman projections of these nine combinations are given in Figure S1 of Appendix I and the relative energy ordering of them and the Cartesian coordinates of the G+g- conformer are given in Table S1 and S2 of Appendix I, respectively. The G+g-/G-g+ pair is more stable by 7 kJ/mol compared to the next higher energy conformer. This is consistent with the previous experimental and theoretical studies,(221, 43, 172) showing that the G+g-/G-g+ pair is by far the dominant conformations.

The two species of an enantiomeric pair of FE have the same energy and the same rotational spectrum without considering the possible minute effect of parity violation. However, in a chiral environment, for example, when binding to FE itself, the two chiral forms of FE interact differently, resulting in different binding energies. This subtle chirality recognition is taken into account in the initial search of the dimeric FE conformers. The dimeric FE conformers are expected to be linked by an intermolecular O-H \cdots O-H bond. To identify the low energy dimeric conformers that are relevant in a free jet expansion, Schrage *et al.*(221) carried out initial screening calculations at the HF/3-21G and HF/3-21G* levels and additional calculations at the MP2/6-31+G(d) and MP2/6-311+G(d) levels for the six lowest energy conformers. The nine monomeric conformers are expected to generate 81 dimeric combinations, without considering the more subtle differences in the secondary hydrogen bonds in each combination. Our further exploratory calculations at the MP2/6-311++G(d,p) level point to the same conclusion: the most stable dimeric FE conformers are formed by the G+g-/G-g+ FE monomer subunits, and the next most stable group of dimeric conformers, which are complexes composed of the G+g-/G-g+ and G+g+/G-g- subunits and of the G+g-/G-g+ and Tt subunits, are about 510 kJ/mol higher in energy than the most stable one. The dimeric FE conformers with only an O-H \cdots F intermolecular hydrogen bond have also been surveyed. These are 69 kJ/mol less stable than the global minimum structure.

In the following, we focus on the four combinations formed by the G+g-/G-g+ FE subunits, namely G+g \rightarrow G+g-, G+g \rightarrow G-g+, G-g+ \rightarrow G+g-, and G-g+ \rightarrow G-g+, with the arrow indicating the hydrogen bond-donating direction. These four can be classified as homochiral (hom) or heterochiral (het) complexes based on the chirality of the two binding subunits. The two hom configurations are mirror images to each other, as are the two het ones. Since rotational spectroscopy cannot tell apart the two mirror images, we end up with only two distinguishable conformers: hom and het. For simplicity, we choose to use G+g- as the hydrogen-bond acceptor throughout this paper. When forming the O-H \cdots O-H intermolecular hydrogen bond, the hydroxyl group of the donor can either be inserted into the intramolecular O-H \cdots F five-membered hydrogen-bond ring or simply associated to the hydroxyl group of the acceptor. While the inserted (i) conformers have a seven-membered ring with the consecutive O-H \cdots O and O-H \cdots F hydrogen bonds, the associated (a) conformers leave the intramolecular O-H \cdots F five-membered hydrogen-bond ring of the acceptor intact. A further consideration is that the hydrogen donor can either bind to the right or left hand

lone pair of the oxygen atom of the acceptor. This gives rise to two different relative orientations of the two binding partners. One of them is compact (c), with the fluoromethyl group of the acceptor tilting towards the donor, ensuring a large contact area. The other is open (o), with the fluoromethyl group of the acceptor pointing away from the donor. Therefore, we expect $2^3=8$ conformers. Each conformer is named using the three abbreviations of the structural properties. For example, *ichet* means that the conformer has an inserted intermolecular hydrogen-bond ring, with the two binding partners in the compact relative orientation, and is heterochiral. This labelling scheme is the same as that used in reference(221).

Six out of the eight structures proposed above were confirmed to be true minima by the ab initio calculations, while two of them, namely *aohom* and *aohet*, are saddle points. These conformers are summarised in Figure 3.1 with their important intermolecular distances. Side views of the geometries of the six conformers are given in Figure S2 and their Cartesian coordinates are shown in Table S3 of Appendix I. The side views provide better visual discrimination between the compact and open conformers. The raw, zero-point energy (ZPE), and basis set superposition error (BSSE) corrected energy values are listed in Table 3.1, together with the predicted rotational constants and the dipole moment components of the six conformers.

3.3.2 Assignment of the FE Dimer Rotational Spectra

The energy span among the six dimeric conformers is about 2 kJ/mol at the MP2/6-311++G(d,p) level. Each conformer has at least one substantial dipole-moment component. Therefore, one may expect to observe all six conformers in a supersonic jet expansion. The expansion of 0.3% FE in Ne carrier gas generates many species. Besides the targeted dimeric FE conformers, there are also the conformers of the FE monomer, other small FE oligomers and the FE-Ne_x van der Waals complexes. The rotational spectrum of the dominating G+g-/G-g+ conformations of the FE monomer was reported previously.(43, 172, 41) The known FE transitions were used to monitor its concentration in the sample mixture. Automatic spectral scans were carried out in the frequency region from 3.98-10.2 GHz with 15 cycles and 0.2 MHz step size. Each transition candidate was then measured separately by using an optimised MW excitation pulse length and sufficient averaging cycles for a signal-to-noise ratio better than 10. More than three hundred rotational lines were measured in this frequency region. There

	<i>ichet</i>	<i>ichom</i>	<i>achet</i>	<i>achom</i>	<i>iohet</i>	<i>iohom</i>
MP2/6-311++G(d,p)						
$D_e^{[a]}$ [kJ/mol]	34.81 (22.96)	33.92 (22.14)	34.00 (23.84)	33.75 (23.54)	32.26 (22.77)	33.20 (23.45)
$D_0^{[a]}$ [kJ/mol]	30.00 (18.14)	29.26 (17.48)	29.89 (19.72)	29.60 (19.38)	27.92 (18.43)	28.59 (18.84)
$\mu_a^{[b]}$ [D]	0.54 (0.53)	1.33 (1.35)	0.06 (0.21)	0.67 (1.00)	0.82 (0.71)	0.69 (0.57)
μ_b [D]	0.44 (0.35)	0.77 (0.95)	2.07 (2.27)	1.81 (1.99)	0.33 (0.50)	0.31 (0.47)
μ_c [D]	0.78 (0.96)	0.92 (0.86)	0.09 (0.05)	1.51 (1.61)	1.45 (1.53)	0.31 (0.34)
A [MHz]	2477	2498	2905	2869	3239	3287
B [MHz]	1110	1016	872	880	762	761
C [MHz]	1033	1010	765	785	645	642
MP2/aug-cc-pVTZ//MP2/6-311++G(d,p) ^[c]						
$D_e^{[a]}$ [kJ/mol]	36.33 (30.44)	35.31 (29.70)	33.42 (28.81)	33.53 (28.87)	31.81 (27.37)	32.71 (28.24) a
$\mu_a^{[b]}$ [D]	0.52 (0.51)	1.26 (1.28)	0.10 (0.11)	0.58 (0.83)	0.66 (0.58)	0.79 (0.71)
μ_b [D]	0.40 (0.33)	0.69 (0.83)	1.91 (2.07)	1.67 (1.81)	0.29 (0.42)	0.32 (0.44)
μ_c [D]	0.71 (0.85)	0.84 (0.80)	0.07 (0.04)	1.42 (1.50)	0.29 (0.31)	1.34 (1.40)
MP2/aug-cc-pVTZ						
De [kJ/mol]	37.29	36.27	33.92	34.35		
$\mu_a^{[b]}$ [D]	0.49 (0.48)	1.18 (1.20)	0.13 (0.08)	0.79 (1.05)		
μ_b [D]	0.53 (0.47)	0.88 (1.01)	1.79 (1.94)	1.40 (1.51)		
μ_c [D]	0.72 (0.86)	0.84 (0.79)	0.13 (0.11)	1.29 (1.35)		
A [MHz]	2481	2483	2864	2753		
B [MHz]	1143	1060	895	931		
C [MHz]	1077	1057	779	843		

BSE corrected values are given in parentheses.

b Calculated using the MP2 density; The values calculated using the HF density are given in parentheses.

c Single-point calculation at the MP2/aug-cc-pVTZ level with the optimised geometry at the MP2/6-311++G(d,p), MP2/aug-cc-pVTZ//MP2/6-311++G(d,p), and MP2/aug-cc-pVTZ level of theory.

Table 3.1: Calculated raw (De) and ZPE-corrected (D0) dissociation energies, rotational constants, and the magnitudes of the electric dipole moment components of the six most stable hydrogen bonded dimeric FE conformers at the MP2/6-311++G(d,p), MP2/aug-cc-pVTZ//MP2/6-311++G(d,p), and MP2/aug-cc-pVTZ level of theory.

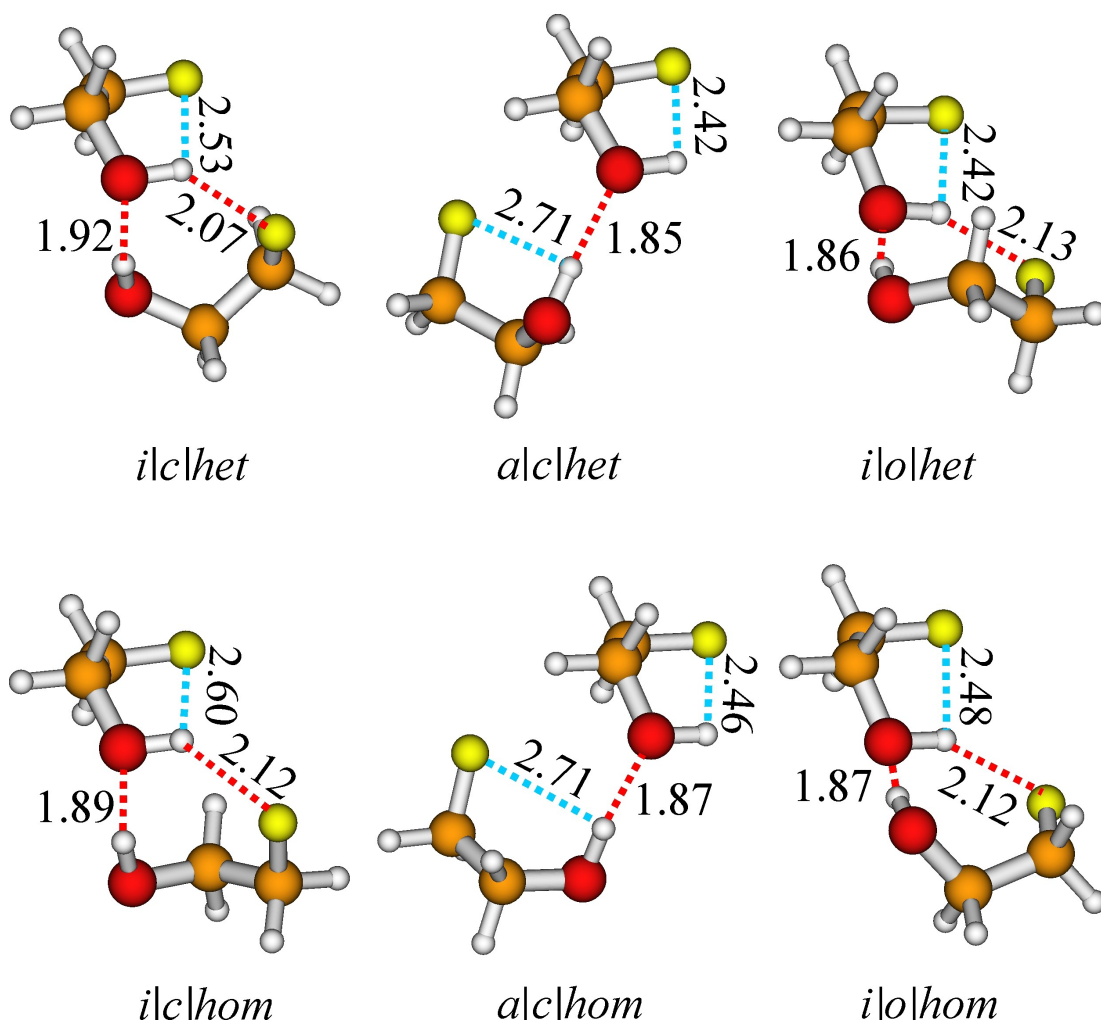


Figure 3.1: Optimized geometries of the six dimeric FE conformers - The geometries are obtained at the MP2/6-311++G(d,p) level of theory. The important intra- and intermolecular bond distances are indicated in units of Å.

are 23 lines which were absent in the expansions of 0.3% FE in He as carrier gas, indicating that they probably originate from the FE-Ne_x complexes. Transitions belonging to the FE monomer (10 lines) and the FE-Ne_x complexes were excluded from further consideration.

The auto-scan spectra exhibit an eye-catching pattern with narrowly spaced triplets around 4024, 6036, 8048 and 10 060 MHz. They are consistent with a-type $J=2\leftarrow 1, 3\leftarrow 2, 4\leftarrow 3, 5\leftarrow 4$, transitions of a near-prolate top. They were tentatively assigned to the conformer *ichom*, which has a predicted basis-corrected (BC) of 6 MHz, whereas all others have the BC values of 77 MHz or larger. Another distinct pattern is a group of transitions observed around 4460 MHz. This corresponds to the Q-branch b- and c-type $K_a=2\leftarrow 1$ transitions with J ranging from 2 to 8. They were also assigned to *ichom*, which was predicted to have b- and c dipole moment components of similar magnitude. The observed spectrum in the 4460 MHz region is depicted in Figure 3.2, together with the simulated spectrum of *ichom* in this frequency region. Besides *ichom*, three additional sets of transitions were assigned. Because the predicted rotational constants differ substantially between the compact and the open conformers, it is relatively straightforward to recognise that the additional three sets of rotational constants determined experimentally belong to the other three compact conformers.

While the correlations of the observed rotational constants to those of the *ichet* and *ichom* predictions were fairly clear, the situation was less evident for *achet* and *achom*, because their predicted rotational constants are more similar. In this case, we also utilised the detailed comparison of the trends of the observed and calculated dipole moment components. For example, the c-type transition intensities of *achet* were optimised experimentally with a much longer MW excitation pulse width than its b-type transitions, while the b- and c-type transitions of *achom* were optimised with similar MW excitation pulse widths. This is consistent with the prediction that *achet* has a c-dipole moment component many times smaller than its b-component, whereas the b- and c-dipole moment components of *achom* are of similar magnitude. In general, the dipole moment information supports the frequency based conformer assignments discussed above.

Altogether, about 200 pure rotational transitions were unambiguously assigned to four dimeric FE conformers, namely *ichet*, *ichom*, *achet*, and *achom*. The measured transitions and their spectroscopic assignments are given in Tables S4-S7 of Appendix I. The spectroscopic constants obtained from spectroscopic fits using Watson's S-reduction(276) semi-rigid rotor model are listed in Table 3.2 for

3.3 Results

	<i>ichet</i>	<i>ichom</i>	<i>achet</i>	<i>achom</i>
A [MHz]	2482.7877(3)[a]	2492.3145(9)	2882.0866(6)	2807.4482(4)
B [MHz]	1091.0870(2)	1006.5733(2)	867.1778(2)	883.9286(2)
C [MHz]	1026.2203(2)	1005.5385(2)	753.2254(2)	788.8082(2)
DJ [kHz]	0.897(9)	0.884(3)	0.609(3)	0.871(3)
DJK [kHz]	0.275(9)	0.946(18)	-2.45(1)	1.38(1)
DK [kHz]	-0.108(37)	-0.378(187)	15.5(1)	5.66(2)
d1 [kHz]	-0.0071(20)	0.0043(18)	0.0303(17)	-0.0113(18)
d2 [kHz]	-0.031(1)	0.023(1)	0.0105(4)	-0.0217(5)
k	-0.9109	-0.9986	-0.8929	-0.9057
N ^[b]	63	49	27	59
σ ^[c] [kHz]	2.3	2.8	1.2	2.9
rel. μ ^[d]	$\mu_c > \mu_a > \mu_b$	$\mu_a > \mu_c > \mu_b$	$\mu_b \gg \mu_c \approx \mu_a$	$\mu_b \approx \mu_c > \mu_a$

a The error given in parenthesis in units of the last digits. b Number of the rotational transitions fitted. c Standard deviation of the fit. d Relative strength of the dipole moment components μ_a, μ_b, μ_c , as estimated from the optimised MW excitation pulse lengths at the $\pi/2$ condition.

Table 3.2: Experimental rotational and centrifugal distortion constants and relative magnitudes of the dipole moment components of the four dimeric FE conformers.

all four conformers observed. Also listed in Table 3.2 are the relative magnitudes of the electric dipole moment components estimated from the experimental optimised MW excitation pulse widths. A spectral simulation and fitting program, Jb95,(206, 205) was used to evaluate the rotational temperatures for these conformers, which are about 1 K.

The relative abundances of the four conformers in the jet expansion were estimated from their experimental transition intensities. For simplicity, we used the same c-type transitions for *ichet* and *ichom*, since these transitions were optimised experimentally at similar MW excitation pulse widths, consistent with the fact that their calculated c-dipole moment components are quite close (0.8 D, see Discussion section for details of dipole moment calculations). Similarly, the b-type transitions were used for *achom* and *achet*. For comparison of the inserted and associated conformers, different rotational transitions that are close in frequency were used and the corresponding transition line strength and dipole moment component were taken into account. We also used Jb95 to simulate the relative intensity patterns of several transitions of the dimeric FE conformers and estimated their relative abundances. The estimated relative stability order-

ing, from the most stable to the least, is *ichet* > *ichom* > *achom* > *achet* and the ratio of the relative population is 17:9:2:1. Assuming a conformational temperature of 60 K as reported for this type of hydrogen-bonded complexes with a similar experimental setup,(33) the relative energy differences with respect to the global minimum are 0.0, 0.3, 1.1 and 1.4 kJ/mol, respectively, assuming a Boltzmann distribution. Another way to establish the relative stability ordering is to perform the “Ar test”,(68) or simply substitute a lighter carrier gas with a heavier one.(242) Both methods promote collisional relaxation and have been shown to effectively convert the higher-lying hydrogen-bonded or van der Waals conformers to the global minimum. The “Ar test” result performed with the FE dimer gave the same energy ordering as reported above.

Considerable efforts were spent to locate the two remaining conformers, namely *iohet* and *iohom* in the 70 unassigned transitions by using Jb95 package. However, no patterns could be assigned to the open conformers. This suggests that only four compact dimeric FE conformers are selectively formed under our experimental condition, and the two open conformers are probably substantially less stable than the four observed ones. This point will be further discussed in the section below. Some of the unassigned lines are likely to belong to higher FE aggregates such as the FE trimer and FE tetramer, since their line intensities increase much faster with increasing backing pressure than the dimeric FE conformers. Further investigations of these larger aggregates are underway.

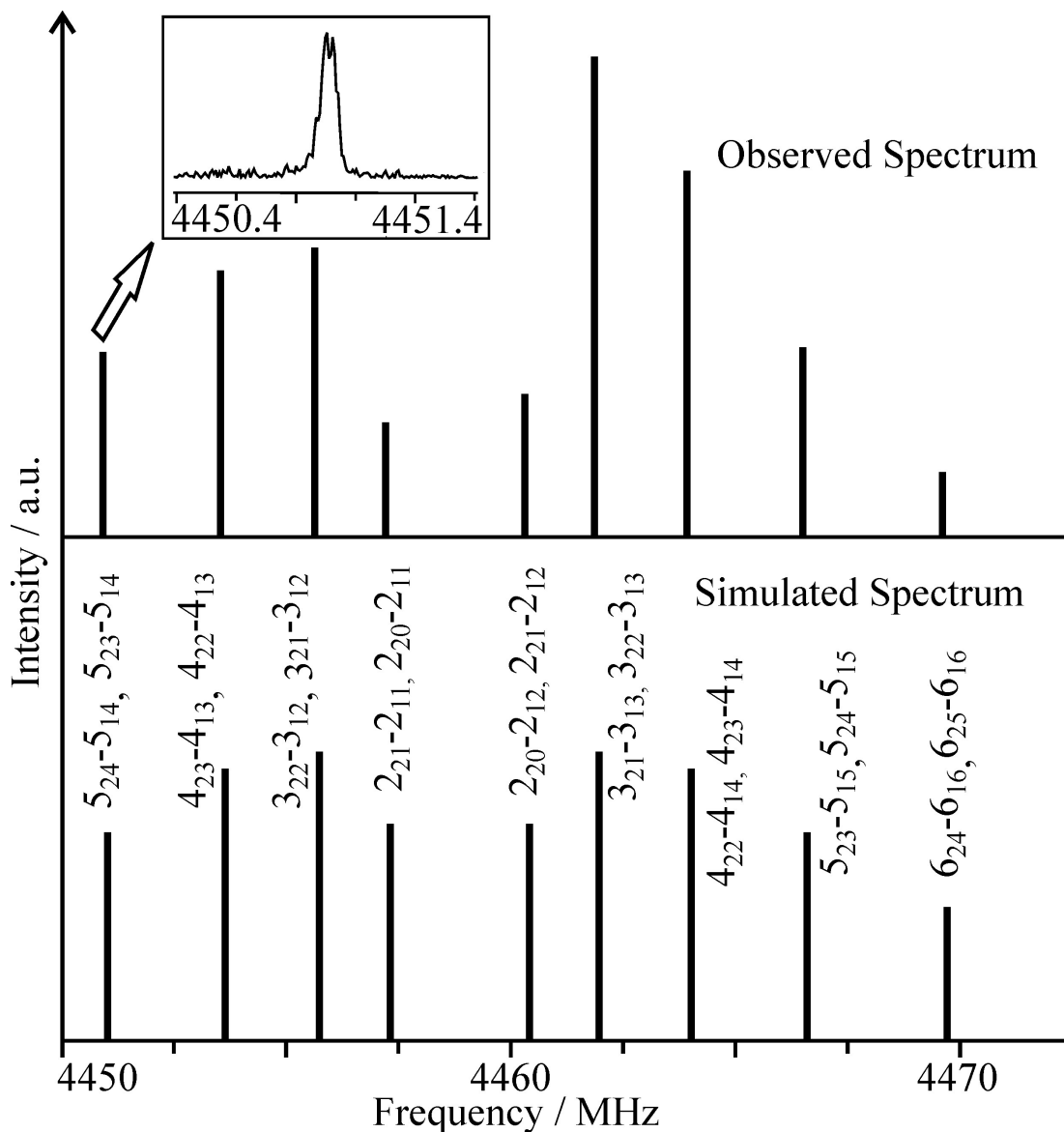


Figure 3.2: Microwave spectrum of the FE dimer - Top: a section of the rotational spectrum of the *ichom* conformer showing the b- and c-type transitions with $K_a=2\leftarrow 1$ and J ranging from 2 to 6. Transitions observed are represented by sticks with the corresponding experimental intensities. An example showing overlapping band c-type transitions with J=5 is given in the insert. Please note that the line width (FWHM) is 30 kHz, twice the usual line width because of the unresolved Doppler splittings and the overlapping b- and c-type lines. Bottom: the spectrum simulated from the experimental rotational and centrifugal constants with a rotational temperature of 1 K. The rotational transitions are labelled with JKaKc quantum numbers.

3.4 Discussions

3.4.1 Stability Order of the Dimeric FE Conformers

One of our goals is to examine the effects of inter- and intramolecular hydrogen bonds on the stability of the dimeric FE conformers. As mentioned before, the energy differences between the conformers of the FE monomer are 8 kJ/mol and higher, based on the MP2/6-311++G(d,p) calculations. The energy differences among the monomeric FE conformers are substantial such that the formation of the dimeric conformers, consisting of the higher lying FE conformers, is energetically and kinetically less favoured. It is therefore not surprising that the most stable dimeric conformers are made of the most stable G+g-/G-g+ FE subunits. A similar conclusion was obtained from the lower level MP2/6-311+ G* calculations.(27)

To understand the more subtle molecular recognition among the dimeric conformers observed is, however, more challenging. The energy span of the six most stable dimeric conformers built out of the G+g-/G-g+ FE subunits is on the order of 2 kJ/mol or about 10% of the total binding energy at the MP2/6-311++G(d,p) level of theory. The experimental data indicate that *ijcjh* is the most stable conformer, followed by *ichom*, *achom*, and *achet*; *ajojhet* and *ajojhom* are bound with even smaller binding energies. The MP2/6-311++G(d,p) calculations without BSSE corrections and with or without ZPE corrections correctly predict that *ichet* is the global minimum, but fail for the rest. Inclusion of BSSE overcorrects the binding energies and wrongly predicts *achet* as the global minimum. This is probably not surprising, since BSSE tends to overcorrect with relatively small basis sets such as the one used here. We therefore performed the MP2 geometry optimisations using Dunning's correlation-consistent triple-zeta basis set augmented with the diffuse functions, namely aug-ccpVTZ,(65) for the four compact dimeric FE conformers observed. For comparison, single-point energy calculations at the MP2/aug-cc-pVTZ level with the MP2/6-311++G(d,p) optimised geometries were also performed for all six dimeric conformers. The resulting dissociation energies, rotational constants, and dipole moment components are collected in Table 3.1. It is gratifying to see that the experimentally observed stability ordering was correctly captured by the MP2/ aug-cc-pVTZ//MP2/6-311++G(d,p) and MP2/aug-cc-pVTZ calculations. Even the more subtle chiral recognition preference observed for the heterochiral conformer in the inserted

conformers (*ichet* over *ichom*) and for the homochiral conformer in the associated conformers (*achom* over *achet*) was correctly predicted. Also the predicted energy ordering stays the same with or without BSSE corrections. The BSSE correction with the aug-cc-pVTZ basis set is much smaller than that with the 6-311++G(d,p) basis set; the former contains 598 basis functions, much larger than the latter with 246 basis functions. It appears that the augcc- pVTZ basis set with rich diffuse functions is essential for capturing the subtle energy differences that drive the molecular recognition process in the FE dimer.

To analyse the stability ordering of the six most stable dimeric conformers made of the same G+g-/G-g+ FE subunits, we divide the contributions to the raw dissociation energy D_e into three parts: E_{distd} , E_{dista} , and E_{int} . Their values are listed in Table 3. Here, E_{distda} is the so called fragment distortion or deformation energy for the hydrogen-bond donor or acceptor, respectively. It corresponds to the energy penalty for distorting the isolated FE conformer from its equilibrium geometry to the optimal geometry in the dimeric FE conformer; E_{int} , the interaction energy of the dimeric complex, is defined in footnote [a] of Table 3, following the notation introduced in references(287). Here, the reference points are the FE donor and acceptor fragments in the dimeric complex. It is clear from Table 3 that the interaction energy is the most significant factor in the relative stability ordering of these six conformers, although the distortion energy term also plays a role. The magnitudes of the donor distortion energy terms are larger than the corresponding acceptor terms in all six cases, implying that the hydrogen bond donors make greater geometry distortions to fit into the intermolecular hydrogen bonds than the acceptors. It is also interesting and somewhat surprising that the magnitudes of E_{distd} are larger in the associated conformers than in the inserted ones, considering that the intramolecular O-H...F interaction has to open up to form the seven-membered intermolecular hydrogen-bond ring in the latter cases. The hydrogen-bond acceptors, on the other hand, show greater distortions in the inserted conformers than in the associated ones. Overall, the inserted conformers are favoured over the associated ones because of their larger interaction energies and smaller distortion penalties.

Geometries of the observed dimeric FE conformers: Good agreement was noted between the calculated and experimental rotational constants with a maximum deviation of 62 MHz or 2% at the MP2/6-311++G(d,p) level. The root mean squares (RMS) of the experimental minus calculated rotational constants for the four observed conformers: *ichet*, *ichom*, *achet*, and *achom*, are 12, 7, 15, and 36 MHz, respectively, at the MP2/6-311++G(d,p) level. From this, we can

	<i>ichet</i>	<i>ichom</i>	<i>achet</i>	<i>achom</i>	<i>iohet</i>	<i>iohom</i>
MP2/aug-cc-pVTZ//MP2/6-311++G(d,p)						
$E_d^{dist[a]}$ [kJ/mol]	-1.61	-1.42	-1.98	-2.23	-1.86	-2.02
$E_a^{dist[a]}$ [kJ/mol]	-0.52	-1.05	-0.36	-0.35	-0.29	-0.26
$E_a^{int[a]}$ [kJ/mol]	38.46	37.78	35.77	36.12	33.97	34.98
$D_e^{[a]}$ [kJ/mol]	36.33	35.31	33.42	33.53	32.71	32.71
MP2/aug-cc-pVTZ						
$E_d^{dist[a]}$ [kJ/mol]	-1.74	-1.54	-2.70	-3.58		
$E_a^{dist[a]}$ [kJ/mol]	-0.41	-0.85	-0.36	-0.39		
$E_a^{int[a]}$ [kJ/mol]	39.44	38.65	36.97	38.32		
$D_e^{[a]}$ [kJ/mol]	37.29	36.27	33.92	34.35		

^a An overview of the different energy terms and their relations is presented in the reaction scheme given in Fig. 3.3. The superscripts “monomer” and “dimer” indicate the usage of the optimised geometries in the corresponding monomer or dimer conformations.

Table 3.3: The calculated donor and acceptor distortion energies and the interaction energies for the six most stable dimeric FE conformers.

infer that the actual geometries of these conformers are very close to the predicted ones given in Figure 1 and in Table S3 of Appendix I. The RMS at the MP2/aug-cc-pVTZ level are 42, 43, 24, and 54 MHz, respectively, slightly worse than those obtained with the 6-311++G(d,p) basis set. The superior performance of 6-311++G(d,p) in geometry predictions had been reported before.(32, 34, 72, 244)

Another quantity obtained from the experiments and the calculations is the electric dipole moment component. It was reported that the MP2 density predicts the electric dipole moment components more accurately than the HF density.(15) For comparison, we applied both the HF and MP2 density to calculate the dipole moments using 6-311++G(d,p) and aug-cc-pVTZ. The HF density is the default setting and the usage of the MP2 density was evoked by adding DENSITY= CURRENT in the route section in Gaussian 03.(81) These values are also summarised in Table 1. The differences in the dipole moment components obtained with different densities and basis sets in Table 1 are small. In particular, the MP2 density calculations with the MP2/6-311++G(d,p) geometries provide the best agreements with the experimental data. For example, the b-component of *ichom* was predicted to be slightly larger than the c-component at the MP2/aug-cc-pVTZ level of theory, while the opposite was observed. The MP2 density calculations at the MP2/6- 311++G(d,p) and MP2/aug-cc-pVTZ//MP2/6-311++G(d,p) level of theory, on the other hand, predicted the same trend as observed experimentally. This may be due to the fact that the MP2/6-311++G(d,p) geometries are closer to the experimental ones. In summary, the comparison of the experimental and calculated dipole components supports the assignment of the four distinct conformers based on the rotational constants discussed previously.

3.4.2 Comparison with the Previous Studies of the FE and Ethanol Dimers

The current high-resolution FTMW experiments provide unambiguous identification of the four dimeric FE conformers, which were tentatively assigned in the previous low-resolution jet-cooled FTIR investigation.(221) The current study also supports the previous conclusion that *ichet* is the most stable dimeric FE conformer. By using the experimentally determined rotational constants of each individual conformer, the corresponding geometries were confirmed directly. Because the rotational transitions of each conformer are well resolved, we can monitor the intensity variations in each conformer separately without the complication of

spectral overlapping reported in reference(221). Additionally, the intensity variation with the “Ar test” is much more dramatic with the pinhole-pulsed FTMW experiments than with the slit-jet FTIR experiments. Therefore minor energy differences that do not cause noticeable changes in the jet FTIR spectra can be detected in a FTMW experiment. This allowed us to establish the stability ordering of the four observed dimeric conformers experimentally.

The related dimeric ethanol conformers were studied previously using FTMW spectroscopy.(93) The fluorination of ethanol increases the number of monomer conformations from three to nine. In addition, the energy span among the monomeric conformers increases from 0.5 kJ/mol for ethanol(307) to 10.3 kJ/mol for FE. This is because fluorination at the α -H position of ethanol enables the strong O-H \cdots F intramolecular hydrogen bond, which provides extra stability for the G+g-/G-g+ conformations. As a result, the dimeric FE conformers display improved conformational selectivity and flexibility. In particular, the most stable dimeric FE conformers are made exclusively of the lowest energy FE monomer subunit, while the lowest energy dimeric ethanol conformers do not show such preference. In other words, the energy differences among the FE conformers are a major factor in determining the stability ordering of the dimeric FE systems. Fluorination also provides an additional binding site for the hydroxyl group of the hydrogen-bond donor and thus enables the more stable inserted intermolecular hydrogen-bond pattern. The ethanol dimer, in contrast, can only form the associated-type intermolecular hydrogen bonds. Such enhancement of molecular recognition ability upon fluorination has also been detected and analysed in other complexes such as the propylene oxide-FE dimer.(34)

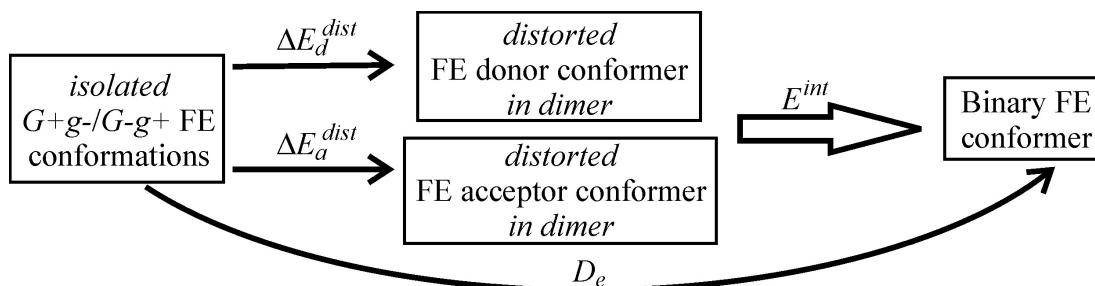


Figure 3.3: Scheme of binding energies -

3.5 Conclusions

The molecular self-recognition in the dimeric FE conformers has been investigated by using FTMW spectroscopy complemented with high-level ab initio calculations. Rotational spectra of four out of the six most stable dimeric conformers predicted have been recorded and unambiguously assigned. The rotational spectra reveal that the transient chiral FE moiety remains in its favoured G+g-/G-g+ conformations in the four dimeric conformers observed. The stability ordering of the dimeric FE conformers has been established experimentally. The heterochiral combination is preferred in the inserted conformers, whereas the homochiral one is favoured in the associated conformers. The trends of the general energy ordering and the subtle chiral recognition were reproduced with MP2 calculations using the augcc- pVTZ basis set. Fluorination of ethanol enhances the molecular recognition ability of FE as compared to ethanol by providing additional binding sites for both intra- and intermolecular hydrogen bonds.

4

Experimental Instrumentation

The instrument used to measure high resolution infrared spectroscopy of jet-cooled molecular complexes studied in this thesis is tunable quantum cascade laser direct absorption spectrometer with an astigmatic multipass cell. Since the molecular complexes of interest are unstable at room temperature.

A continuous wave (cw) liquid nitrogen cooled distributed-feedback QCL at the carbonyl stretch frequency around $5.7\ \mu\text{m}$ and a cw room temperature mode-hop-free external-cavity QCL centered at $6.1\ \mu\text{m}$ water bending region are employed as the light source. Two optical cavities are employed to increase the sensitivity of the measurements. The coupling of quantum cascade lasers (QCL) with an off-axis **cavity enhanced absorption** (CEA) spectrometer and an astigmatic **multiple pass absorption** (MPA) spectrometer are described in this chapter.

For the CEA spectrometer, a pair of 1 inch highly reflective cavity ring-down mirrors ($R=99.98\%$ at $5.2\ \mu\text{m}$) separated by $55\ \text{cm}^{-1}$ is used. The effects of mirror size and laser scan rate are evaluated. One of the cavity mirrors is mounted on a piezoelectric actuator with 1" clear aperture to maximize the effective mirror size. The effects of mirror size, cavity dither frequency, and laser sweep rate are evaluated. A minimum detection sensitivity of $1.8 \times 10^{-8}\ \text{cm}^{-1}$ is achieved. For the MPA spectrometer, a pair of 1.5 inch astigmatic mirrors with a 55 cm mirror distance is aligned to the 366-pass configuration. To automate and to synchronize the timing of the laser scan, the pulsed slit jet molecular expansion, and the data acquisition, two LabVIEW programs are developed to measure the spectra of the short lived molecular complexes. The jet-cooled samples are generated using a homemade pulsed slit jet nozzle assembly. Jet-cooled infrared spectra of methyl lactate and the Ar-*para* H₂O complex and the room temperature infrared spectra of the static N₂O and NH₃ samples are measured using both the rapid scan and

the wavelength modulation methods to evaluate the sensitivity and resolution of the CEA and MPA spectrometer to record the high resolution infrared spectra of the short lived molecular complexes.

Measuring spectra of the same spectral feature from the two spectrometers provided us a good opportunity to compare the effective absorption path provided by the multi-pass resonator and cavity ring down mirrors, as well as their sensitivity and resolution. The combination of the MPA spectrometer with the external-cavity QCL using the rapid scan method has been found to be the most suited combination to measure high resolution jet-cooled infrared spectra.

4.1 Introduction

Tunable Quantum Cascade Laser Absorption Spectroscopy Tunable diode laser absorption spectroscopy (TDLAS) is widely used to measure mid-IR spectra. Lead salt (Pb-salt) diode laser (235) is one of the most common laser sources for mid-infrared high resolution molecular spectroscopy. It is based on the stimulated emission across the band gap between the conduction band and the valance band of the p-n junction formed by a single crystal of the semiconductor materials made of alloys comprised of PbTe, PbSe, PbS, or SnSe, SnTe, CdS and other materials. Direct absorption techniques using different types of multi-pass absorption cells (64, 40, 243) and cw cavity ring-down technique (250) based on lead salt diode lasers have been developed for molecular spectroscopy. Xu group recently reported the design and construction of a lead salt diode laser based mid-infrared cavity ring-down (CRD) spectrometer in combination with a molecular jet expansion for the study of medium size organic molecules and complexes. The high reflectivity (99.98%) of the ring-down cavity mirrors at $3.3\ \mu\text{m}$ provided a very long effective absorption path and a minimum detection limit of $1.4 \times 10^{-6}\ \text{cm}^{-1}$ or $1.5 \times 10^{-8}\ \text{cm}^{-1}$. (250) In addition, the narrow line width of a lead salt diode laser provides the foundation to achieve high resolution spectroscopic measurements. CRD spectroscopy on the other hand, has some shortcomings to carry out jet-cooled spectroscopic studies. For example, it is very tedious to scan over a wide frequency region using CRD technique in combination with a pulsed jet expansion, as compared to the direct absorption technique. Cavity enhanced absorption (CEA) spectroscopy is an ideal alternative that allows one to take advantages of both the high reflective mirrors and the rapid scan capability of a diode laser. Unfortunately, the output power of a lead salt diode laser is simply too low for such experiments.

Quantum Cascade Laser

In recent years, a new type of mid-infrared tunable semiconductor laser, quantum cascade laser (QCL) (71, 105) has attracted much attention because of its superior output power and mode quality as compared to lead salt diode lasers. The first QCL was demonstrated by Capasso *et al.* at Bell Laboratories in 1994.(71) Design of the lasing principle of QCL is based on intersubband transitions in a multiple-quantum-well heterostructure, designed by means of band-structure engineering grown by molecular beam epitaxy. Fig. 4.1 shows the energy diagram and the TEM picture of a QCL emitting at $\lambda=7.5\ \mu\text{m}$.

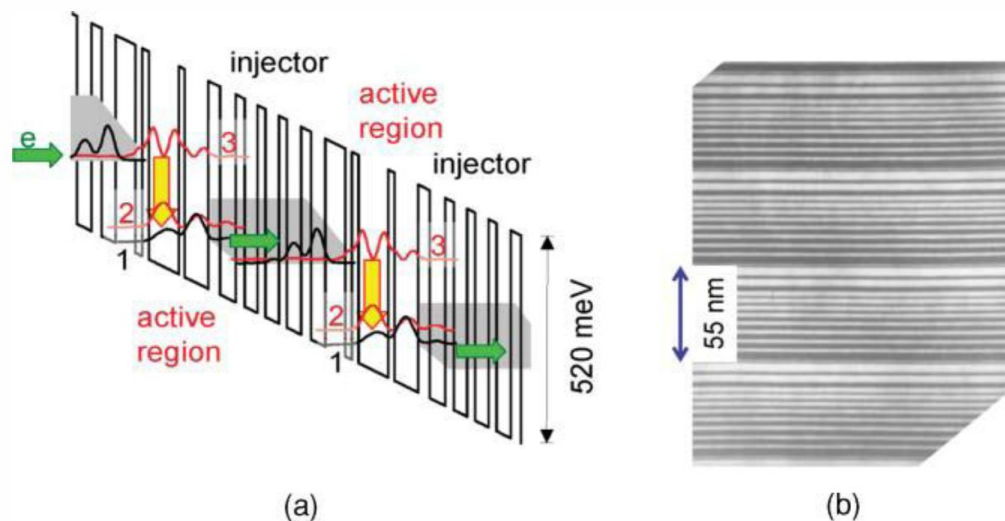


Figure 4.1: Energy diagram and TEM picture of QCL - a) Energy diagram of a quantum cascade laser emitting at $\lambda=7.5\ \mu\text{m}$. The energy levels and the corresponding probability distributions. The energy well and barriers are made of AlInAs and GaInAs alloys lattice-matched to InP, respectively. Each injection-active region is 55 nm thick as shown in b) a transmission electron microscope picture showing a portion of the quantum cascade laser structure. The white and black color on the picture represent the well and barriers. Figure adapted from Ref. (48).

A diffraction grating is used as the frequency selective element in the external cavity. Depending on whether the grating element is movable or fixed, there are the Littrow configuration and the Littman-Metcalf configuration, as shown in Fig. 4.2. The design of the external cavity quantum cascade laser following the Littrow configuration is shown in Fig. 4.3. The QCL substrate is placed attached to a thermoelectric cooler. The highly divergent light is collected and

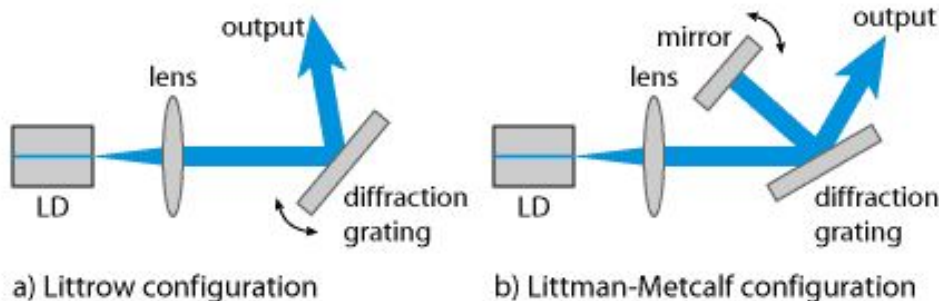


Figure 4.2: Tunable external-cavity diode lasers - a) Littrow configuration; b) Littman-Metcalf configuration. Figure adapted from Encyclopedia of Laser Physics and Technology.

focused by a collimating lens onto a diffraction grating. The grating and output mirror are mounted on a movable stage which allows the angle and the distance of the grating from the QCL to be controlled by piezoelectric transducers. This gives fine control over the external cavity length and wavelength selection of the diffraction grating.

The high sensitivity achievable using this new mid-infrared laser source and the narrow laser line width (usually a few MHz) make it an attractive light source to carry out high resolution molecular spectroscopy. These characteristics are particularly important since we are interested in detecting rotationally resolved infrared spectra of medium size organic molecules and complexes. Such experiments place stringent requirements on the sensitivity and resolution of the infrared spectrometers used. A jet expansion can greatly reduce the spectral congestion and increase the detection sensitivity by transferring almost all the molecular population from the low lying vibrational excited states to a few lowest rotational levels in the ground vibrational state. In the infrared region, a slit nozzle can usually provide a much narrower line width than a pinhole nozzle. Therefore we chose a slit jet combination in designing our infrared spectrometers.

The first Distributed Feedback (DFB) lasers became commercially available in 2004(154) followed closely by broadly-tunable external-cavity QCLs in 2006(152). More recently, significant improvements, such as room temperature operation, wide frequency tunability, and narrow line width, have been achieved for continuous wave (cw) QCL (23). A number of research groups have successfully applied this new laser technology to trace gas sensing. For example, detections of biologically relevant NO using CRD and CEA techniques with excellent sensi-

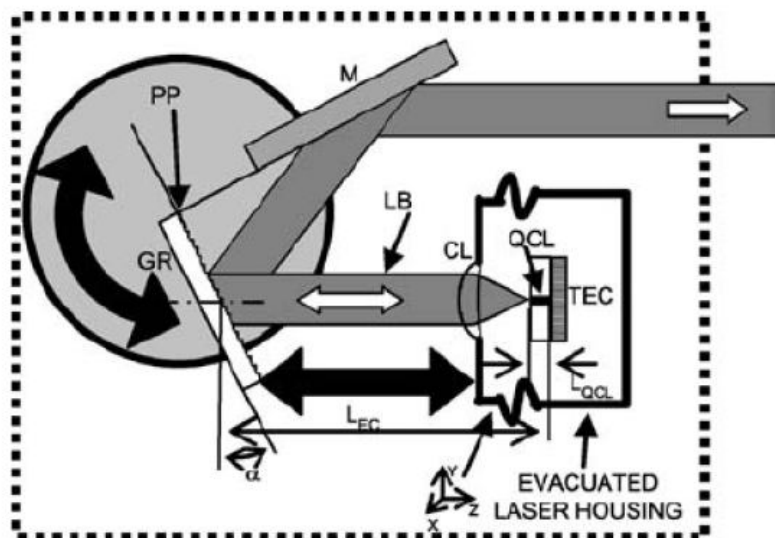


Figure 4.3: Design of the external cavity QCL (EC-QCL) system - QCL - quantum cascade laser substrate, TEC - thermoelectric cooler, CL - collimating lens, LB - laser beam, GR - diffraction grating, M - output mirror, PP - pivot point of rotational movement. Figure adapted from Ref. (286).

tivities have been reported. (174, 127, 17, 285, 16, 164, 165, 126, 256) Quantum cascade lasers have been widely used in trace gas detection of known molecular absorption features, but little work has been done to use QCLs to measure “new spectroscopy” of previously unobserved or unresolved vibrational bands.

In this chapter, the design, construction, and performance of a slit jet off-axis CEA spectrometer based on quantum cascade lasers are described in detail. A continuous wave (cw) liquid nitrogen cooled Distributed-Feedback QCL at $5.7\ \mu\text{m}$ (Alpes Lasers) and a cw room-temperature mode-hop-free External-Cavity QCL at $6.1\ \mu\text{m}$ (Daylight Solutions) were used as light source. Besides the CEA spectrometer, a multiple pass absorption (MPA) spectrometer was constructed for comparison. Jet-cooled sample was generated using a homemade pulsed slit jet nozzle assembly. Room temperature NH_3 and N_2O and the jet-cooled Methyl Lactate and Ar-*para*-water complex were measured with both rapid scan and wavelength modulation (WLM) schemes in which *pseudo-cw jet* and *step-scan* schemes were used to enable the harmonic detection of jet-cooled complex. The sensitivity and resolution of the CEA and MPA spectrometer were evaluated. Based on these comparison, MPA spectrometer with rapid scan method was more

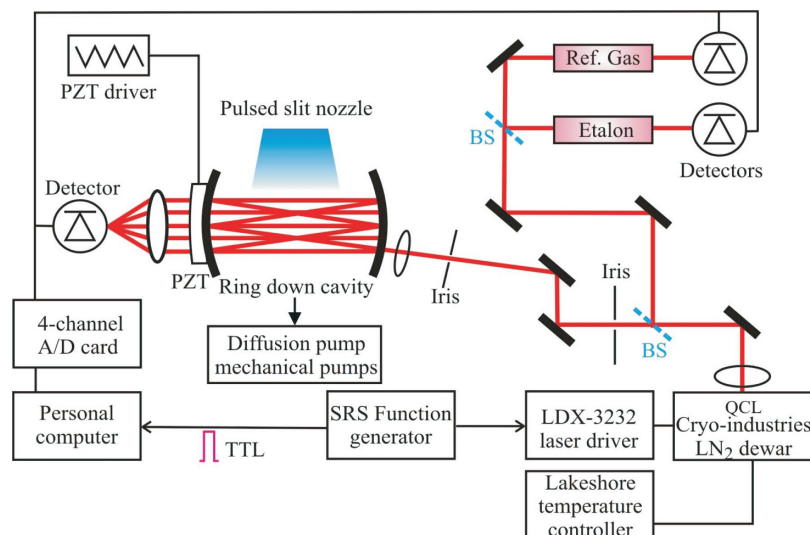


Figure 4.4: Schematic diagram of the slit-jet QCL cavity enhanced absorption (CEA) spectrometer - The apparatus consisted of four main components: (1) a tunable cw QCL as light source, (2) a ring-down optical cavity as optical resonator, (3) a pulse slit jet expansion assembly to produce the jet-cooled sample, and (4) the hardware and software for experiment control and data acquisition.

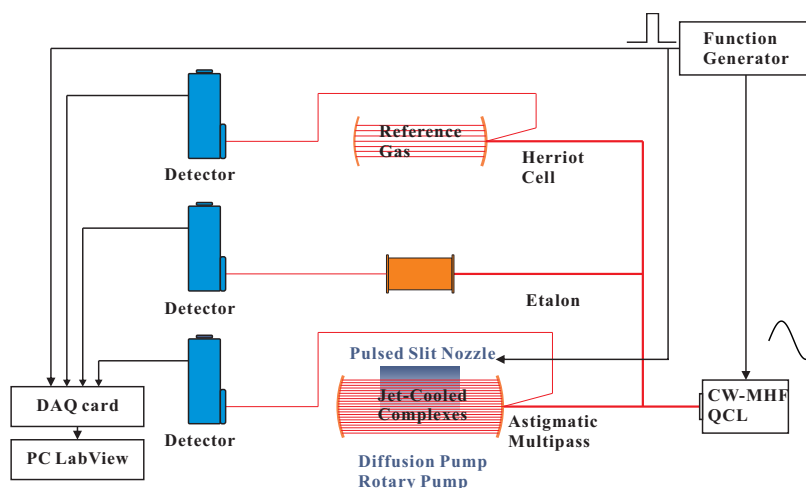


Figure 4.5: Schematic diagram of the slit-jet QCL multipass absorption (MPA) spectrometer - The apparatus consisted of four main components: (1) a tunable cw QCL as light source that is pulsed by the SRS function generator, (2) an astigmatic multipass-cell as optical resonator, (3) a pulse slit jet expansion assembly to produce the jet-cooled sample, and (4) the hardware and software for experiment control and data acquisition.

suitable for the measurement of jet-cooled sample.

A schematic diagram of the slit jet off-axis CEA spectrometer is shown in Fig. 4.4 and a schematic diagram of the slit jet astigmatic MPA spectrometer is shown in Fig. 4.5. Both apparatus consist of four main components: (1) a tunable cw QCL as light source, (2) a ring-down optical cavity or an astigmatic multipass-cell as optical resonator, (3) a pulse slit jet expansion assembly to produce the jet-cooled sample, and (4) the hardware and software for experiment control and data acquisition. A picture of the spectrometer chamber, He-Ne laser beam and optical bench are given in Fig. 4.6 and Fig. 4.7.

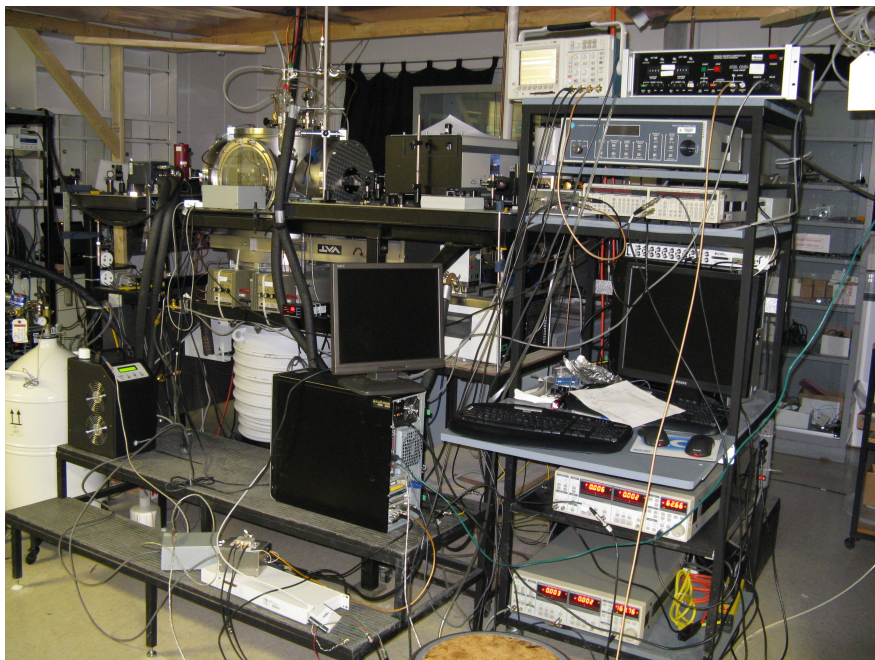


Figure 4.6: Picture of the spectrometer (Side View) - Showing the diffusion pump, the control system and lock-in amplifiers.

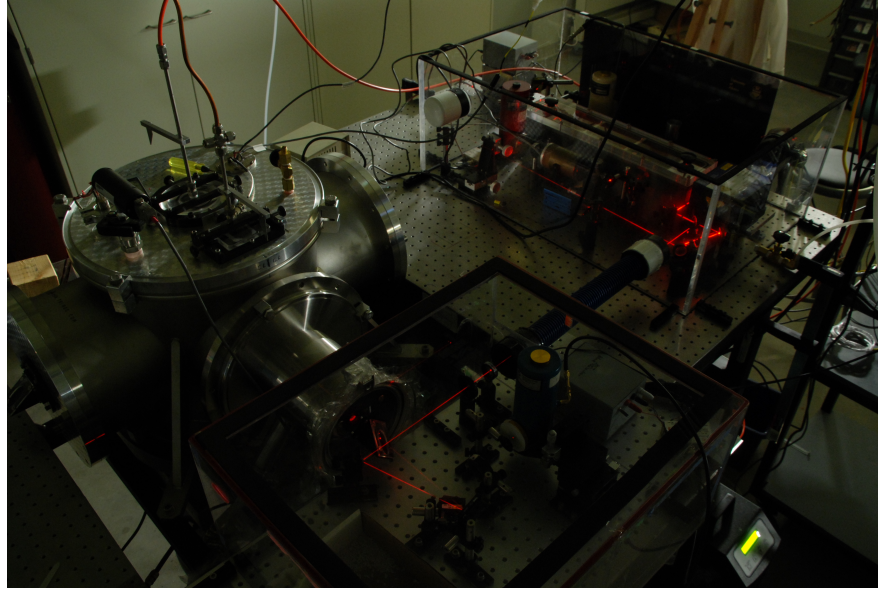


Figure 4.7: Picture of the spectrometer (Top View) - Showing the optical bench, laser head and detectors, the He-Ne laser beam is in red.

4.2 The Light Source

4.2.1 The Distributed-Feedback QCL

The single mode liquid nitrogen cooled Distributed-Feedback QCL at 1760 cm^{-1} (Alpes Lasers, #sbcw27) operated in a temperature range from 80 K to 110 K with a total frequency coverage from 1760 cm^{-1} (110 K) to 1766 cm^{-1} (80 K). The frequency-temperature tuning rate was about $-0.2\text{ cm}^{-1}/\text{K}$. To operate the QCL, one needed a liquid nitrogen dewar that could handle the large amount of heat generated by the QCL operation, while maintaining a satisfactory temperature stability. Fig. 4.8 shows the liquid nitrogen dewar to mount the DFB QCL. This turned out to be a difficult task. Our initial try with a standard liquid nitrogen cooled dewar (Laser Components Instrument Group, L5736), commonly used for a lead salt diode laser was not successful. For a typical operation with a lead salt diode laser, Teflon spacers were inserted between the cold finger and the surface in direct contact with liquid nitrogen, to reduce the heat exchange between the laser head and the liquid nitrogen. This was essential for achieving a wide operating temperature range. It was easy to stabilize the dewar temperature during the operation of a lead salt diode laser since it does not generate much heat in operation.



Figure 4.8: The DFB QCL - Liquid nitrogen dewar and the DFB QCL.

To accommodate the large amount of heat generated by a QCL in operation, it was necessary to remove all the Teflon spacers. This made it not possible to raise the temperature of the dewar to above 83~84 K with the existing heater. To overcome this problem, a liquid nitrogen laser dewar (Cryo Industries of America, DVT-2090-LMN) specially designed with a thermal link was used. The dimension of the thermal link was engineered to fit the narrow passage of the liquid nitrogen dewar. By lowering the thermal link into the narrow passage, one could restrict the liquid nitrogen flow in situ. With the thermal link design, it was possible to bring the dewar to a high temperature such as 100 K by simply lowering the thermal link further into the narrow passage to reduce the amount of liquid nitrogen available to cool the cold finger where the laser was mounted. The temperature stability achieved during laser operation was typically better than 0.01 K at a temperature lower than 100 K, and about 0.01~0.02 K for a higher temperature up to 110 K. In addition, the cold finger was in contact with liquid nitrogen through flexible copper braids and rigidly attached to the bottom frame of the dewar which was directly mounted on a laser table. This improved the laser beam pointing stability as compared to the case of the LCIG liquid nitrogen dewar where the cold finger was in direct mechanical contact with liquid nitrogen. The infrared beam shifted noticeably in this latter case, since the amount of liquid nitrogen reduced gradually during a one day operation. (250) The QCL diode was mounted on a homemade copper laser mount with an additional silicon temperature sensing diode mounted directly underneath to obtain a more reliable laser temperature reading. The laser temperature and current were controlled by a Lakeshore temperature controller (LS340) and a current driver (LDX-3232) from ILX Lightwave Corporation, respectively. The current driver was interfaced with a personal computer using a custom LabVIEW experimental control software program. The laser output power was about a few mW on average. An aspheric lens made of CaF₂ with a focusing length of 11.2 mm was employed to collimate the laser beam. Two irises were inserted into the beam path to remove the unwanted optical fringes by further selecting the center portion of the beam. By placing an infrared camera right before and after the ring-down cavity, we found that the diameter of the collimated beam was about 2~3 mm with a Gaussian like profile.

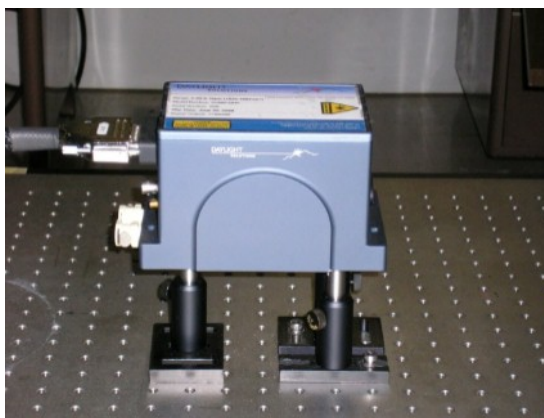


Figure 4.9: Laser head of the External Cavity QCL - The water cooling elements, TEC cooling elements and the external cavity of the QCL are included in the laser head.

4.2.2 The External-Cavity QCL

The External-Cavity room temperature mode-hop-free QCL (TLS-21061-MHF, Daylight Solutions) centered at the water bending band at $6.05\mu\text{m}$ is shown in Fig. 4.9. It utilizes a robust, externally tunable laser cavity to generate a broad continuous frequency tuning range from 1592 cm^{-1} to 1698 cm^{-1} .

This represents a 15 folds improvement in the frequency tuning range as compared to the Distributed-Feedback QCL. The new property made it a very promising mid-infrared laser source for molecular spectroscopy since extensive spectral searches are often required. The laser was compact and turnkey ready. These features made it more user friendly than the liquid nitrogen cooled QCL where several highly specialized items such as a liquid nitrogen dewar, a laser mount, and a temperature controller had to be purchased or constructed before one could operate the system. To ensure a proper operation of the QCL, a water chiller (T255P, ThermoTek) was used to circulate cooling water into the laser case to maintain 18.0°C temperature for the laser case. The actual laser temperature was kept at 18.00°C with a built-in thermo-electric cooler and a PID temperature control unit inside the laser head. Typically, the laser head needed only 15 min to achieve a stable temperature with less than 0.01°C fluctuation while the laser was in operation. The laser beam was factory collimated with a diameter of 1.0 mm. This eliminates the need to purchase a ZnSe aspheric lens as in the case of the liquid nitrogen cooled QCL described above.

The QCL could be scanned coarsely over 40 to 60 cm^{-1} in one second by tuning the grading of the external-cavity using the laser driver provided. Besides the mode hops around 1660 cm^{-1} , a large portion of the gain curve was mode-hop-free (MHF). Fine tuning of the laser frequency over $\sim 1 \text{ cm}^{-1}$ for high resolution spectroscopic applications could be performed by tuning a piezo electric transducer (PZT) attached to the external laser cavity. An external piezo driver (E6-10.00, Polytec PI) was used to drive the PZT with a sinusoidal waveform produced by a function generator (Stanford Research Systems, DS345), which was unipolar, with 100 V maximum amplitude and a maximum frequency of 100 Hz. Fig. 4.10 shows two typical PZT scan of a 3" solid Ge etalon with a free spectrum range (FSR) of $\sim 0.016 \text{ cm}^{-1}$: one MHF and one with several hops. Since the PZT must be driven with a sine wave to ensure the smooth performance of the laser, the etalon fringes were dense where the PZT voltage changed rapidly and sparse where the PZT turned around. Such scan behaviour was different than the linear Distributed-Feedback QCL, making the calibration procedures of the laser frequencies slightly different.

Since the tuning of external-cavity QCL was purely mechanical, it was noted in our experiments that the laser head pick up environmental noise, especially acoustic, during the scanning cycles. The laser frequency started and ended at slightly different position, which lead to frequency shift in the measured spectra. Therefore the laser line width was broadened during repetition of the PZT scan, which could be minimized with the highest possible PZT scan rate (100 Hz) and was severe with PZT scan rate below 10 Hz. When the external-cavity was tuned at very slow PZT scan rate, such as 1 Hz or below, the laser frequency output deviated from a sinusoidal response, which might due to the static friction of the mechanical parts inside the laser head. Better scan quality would be achieved with constantly undergoing manufacturing improvement. Occasionally, mechanical jitter of the external-cavity lead to mode-hop, at which time factory realignment was needed to eliminate it. Overall, to achieve the best tuning performance, the PZT scan rate should be set as high as possible. Such property of the mechanically tuned External-Cavity QCL placed certain limit on our experiments when slow PZT scan rate was favored. Another advantage of high PZT scan rate, as will be shown in the experimental results sections, is the spectra obtained had higher signal to noise ratio (SNR). Since the frequency is mechanically modulated by the PZT elements driven with a sine wave, the frequency drift is *nonlinear*, which we found can be removed by performing frequency calibration after *each* laser sweep before co-adding. During each scan, the signals from the

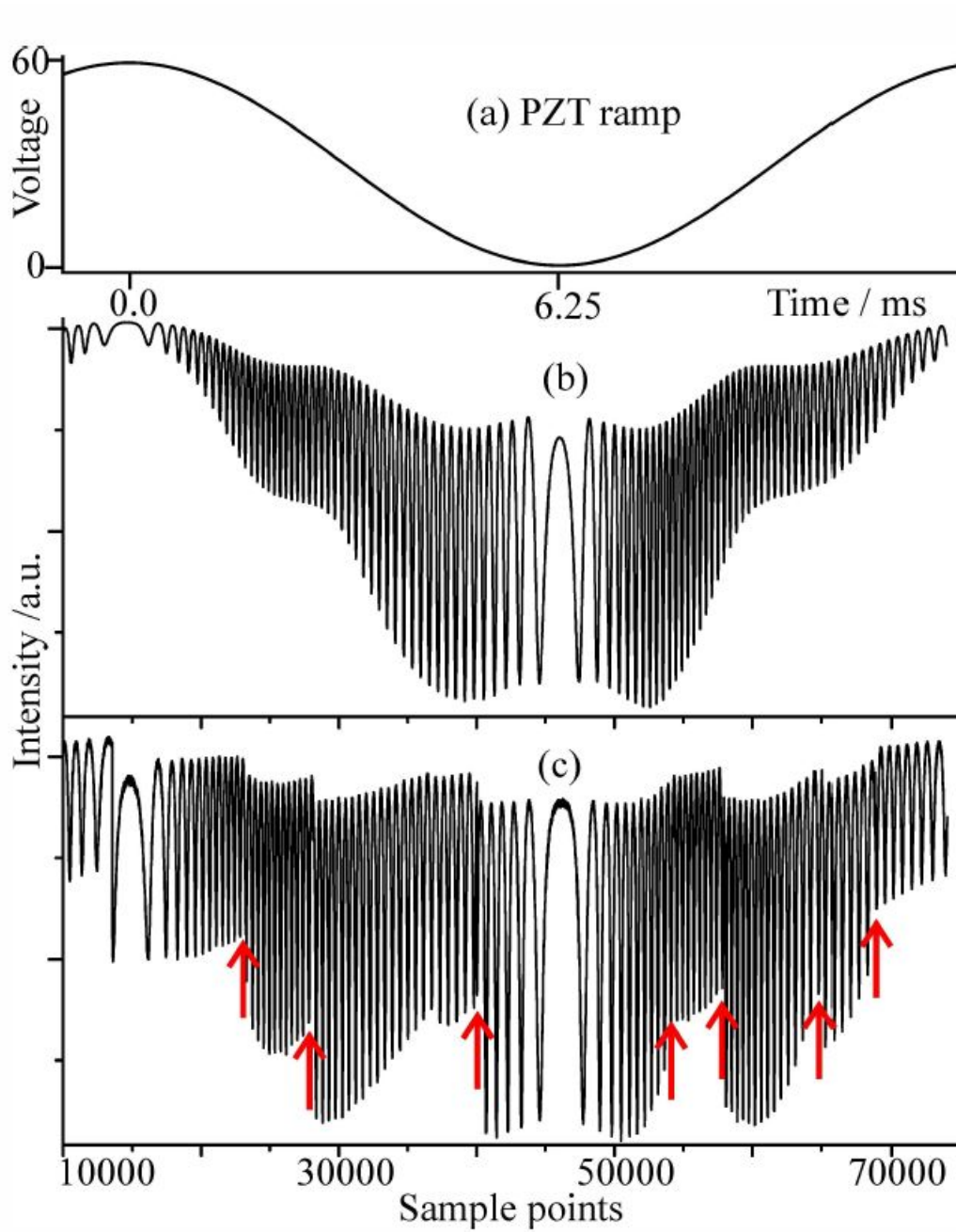


Figure 4.10: PZT scan of the External-Cavity QCL - (a) A typical PZT ramp with an amplitude of 60 V and 80 Hz PZT rate. (b) The corresponding fine PZT tuning at $\sim 1626 \text{ cm}^{-1}$, showing no mode hops in the frequency scan. The etalon spacing was $\sim 0.016 \text{ cm}^{-1}$. The total frequency coverage was $\sim 0.76 \text{ cm}^{-1}$. (c) The corresponding PZT scan at $\sim 1638 \text{ cm}^{-1}$, showing several mode hops with abrupt change of the scanning profile that are indicated with arrows.

supersonic jet, a solid Germanium etalon, and a Herriott multipass reference cell which contained a diluted mixture of NH_3 and H_2O gas are recorded by three Mercury Cadmium Telluride (MCT) detectors simultaneously to allow frequency calibration using the HITRAN08 database.⁽²¹⁶⁾ The accuracy of the frequency calibration is better than 0.001 cm^{-1} . Such a “on the fly” calibration procedure can efficiently remove the noticeable sweep-to-sweep frequency drift to enable averaging of the Doppler limited jet signal without noticeable broadening of the peaks. Details of the frequency calibration procedure are given in Sec. 4.6.3.

The third method to scan the laser frequency was to modulate the injection current of the QCL by external sine wave through an internal bias Tee. The modulation frequency applied should range from 10 kHz to 2 MHz, with the amplitude of the sine wave below 4 V as limited by the protection circuit of the laser head. Modulation of the laser frequency was due to thermal effect, the modulation depth of which depending on the laser frequency and the modulation frequency and amplitude. The interference fringes are discussed in Appendix G. By counting the measured fringes of the Ge etalon when scanning the laser frequency by the current modulation, we estimate the modulation depth was 0.1 cm^{-1} at 1.5 Vpp amplitude and 0.01 cm^{-1} at 0.15 Vpp with 50 kHz modulation frequency. The modulation depth usually varied at different frequency range. The same type of function generator (Stanford Research Systems, DS345) was used to generate the modulation waveform.

4.3 Vacuum Chamber and Slit Jet

A six way vacuum chamber (Trinos Vacuum Systems Inc.) was used to house the CEA assembly and the pulsed slit jet nozzle. The jet-cooled molecules and complexes were generated in the pulsed slit jet expansion. The chamber was evacuated by a 8000 L/s oil diffusion pump (Leybold, DIP8000) backed by a combination of a roots blower (Leybold, Ruvac WAU251) and a rotary pump (Leybold, Trivac D65B). This provides higher pumping capacity compared to a turbopump to quickly pump the vacuum chamber after a pulsed jet expansion is made. The diffusion pump was equipped with a liquid nitrogen baffle, which helped to minimize the back streaming of the oil vapor in order to protect the highly reflective ring-down mirrors and astigmatic multipass mirrors.

In an alternative operation scheme, the liquid nitrogen baffle was removed. As a consequence, the back streaming Silicon oil quickly covers the whole vacuum chamber and the astigmatic multipass mirror mount. To overcome this difficulty,

4.3 Vacuum Chamber and Slit Jet

we heat up the two astigmatic mirrors to prevent the oil condensation on the mirror surface. The Kapton heaters are 120 Ohm for each and for each heater a copper heat spreader is clamped the heater behind the AMAC-100 mirrors. A Teflon isolator is used to stop the heat flow to the mirror mount. The 3" astigmatic mirrors are heated to 60°C to eliminate pump oil deposition on the mirror surface. Since the alignment of the AMAC-100 mirror to the 366-pass configuration is very sensitive to the mirror distance, which varies as the temperature changes, the temperature of the mirrors needs to be kept constant. Two thermocouples are used to read the temperature of each mirror and two PID temperature controllers are used to maintain the temperature of each mirror. With vacuum condition we use 2 Watt power to heat the mirrors to ~60°C. A controller using micrometer screws is installed to allow the fine adjustment of mirror distance under vacuum condition.

Since the molecular complexes of interest has a very weak binding energy, they easily dissociate with thermal collisions in conventional room temperature gas phase. Also the complex is stable only with the few lowest rovibrational states. Therefore, the supersonic free jet expansion techniques is used to produced a cold, collision-less condition for producing the molecular complexes. Since this technique is widely used in high resolution spectroscopy, it is briefly introduced in Appendix E. It should be noted that the jet sample produced is not under thermodynamic equilibrium. The exchange of internal energy of seeded molecules with the cold bath is terminated once the density of the jet is so low that the jet enters the collision-less stage. Since the rotational energy gaps of the seeded molecule is much smaller than the vibrational and conformational energy gap, the internal energy of the rotational degree of freedom is transferred more efficiently to the cold bath. Therefore we have $T_r < T_v < T_{\text{con}}$, as discussed in Sec. 2.5.3.

The pulsed slit nozzle was constructed by modifying a GV series 9 circular nozzle, following the design reported by Maier and co-workers. (28) The design also follows Fig. 2 of Reference(57). Briefly, a homemade nozzle cap was constructed to direct the gas pulse exiting the pinhole nozzle through 6 narrow cylindrical channels in a row. The diameters of the channels are 1.0 mm, 1.5 mm and 2.0 mm, with the small one in the center and big one at the edge to evenly distribute the gas pulse, which was then flow into a 40 mm×2 mm×2 mm groove. The nozzle cap block was then outfitted with two stainless steel plates to form a 40 mm×0.06 mm slit. The slit was aligned parallel to the optical axis of the cavity with proper height to ensure maximum overlap of the slit jet pulse with the IR-beam. The design of the nozzle body and nozzle cap are shown in Fig. 4.11,

4.3 Vacuum Chamber and Slit Jet

Fig. 4.12. We also designed a 7 cm long slit nozzle with 7 channels which is shown in Fig. 4.13, Fig. 4.14.

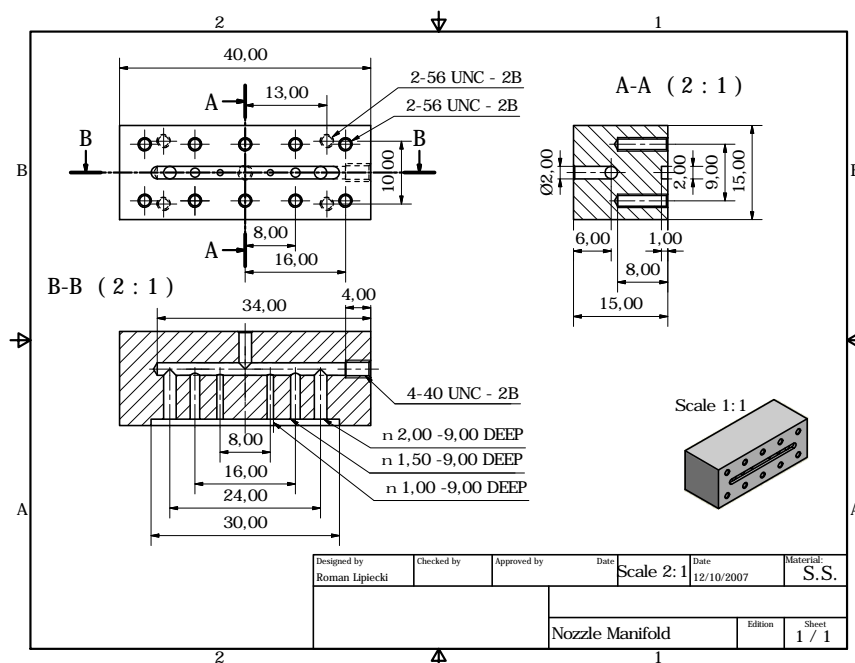


Figure 4.11: Drawing of homemade nozzle body (4 cm) - With 6 narrow cylindrical channels.

The nozzle was operated with an Iota One nozzle driver (Parker Hannifin Corporation). This slit nozzle design provided a longer absorption path and showed better performance compared to a previous slit nozzle design with a 15 mm × 0.06 mm slit. (243) The absorption path can be further extended by using two slit nozzles simultaneously. The two nozzles are mounted on movable flanges to allow fine tune to place them in line with the IR beams in the multipass cell.

Typical backing pressure used for Ar-water complex was 3000~8000 Torr, with 1% water in 300~800 Torr Argon. To measure spectra of room-temperature gas, we simply fill the vacuum chamber with the sample. Typical sample pressure used were 50~150 mTorr or 0.1~1% sample gas in 1~3 Torr noble gas. Since the vacuum chamber were designed without gas-flow and calibration apparatus, measurement of such low sample pressure was not accurate.

4.3 Vacuum Chamber and Slit Jet

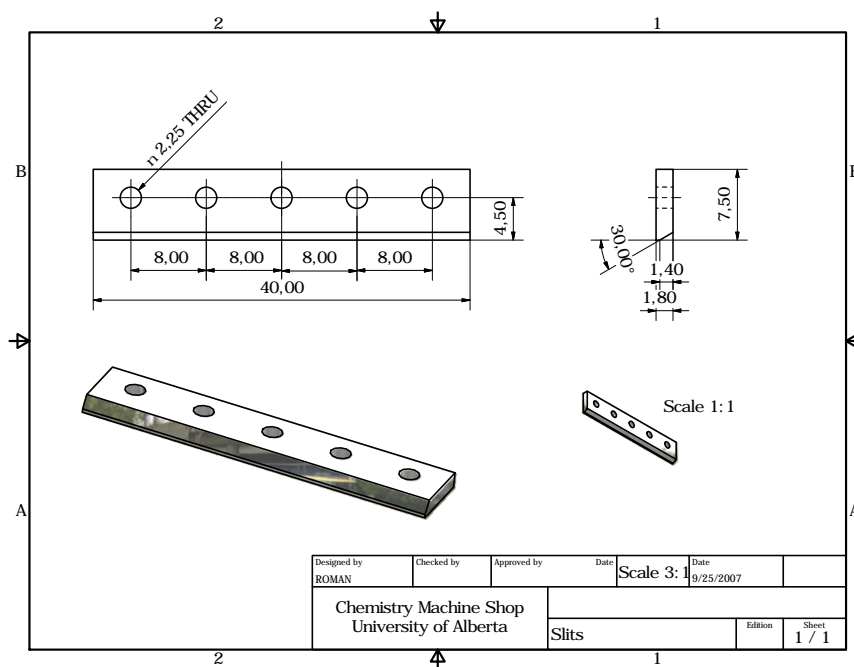


Figure 4.12: Drawing of homemade nozzle caps (4 cm) - The slit is 40 mm × 0.06 mm.

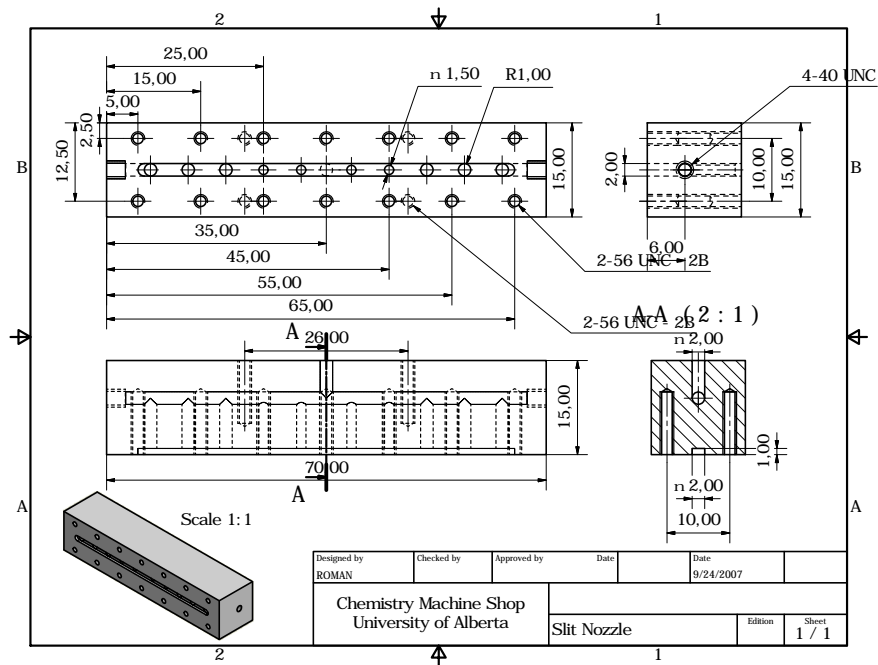


Figure 4.13: Drawing of homemade nozzle body (8 cm) - With 7 narrow cylindrical channels.

4.3 Vacuum Chamber and Slit Jet

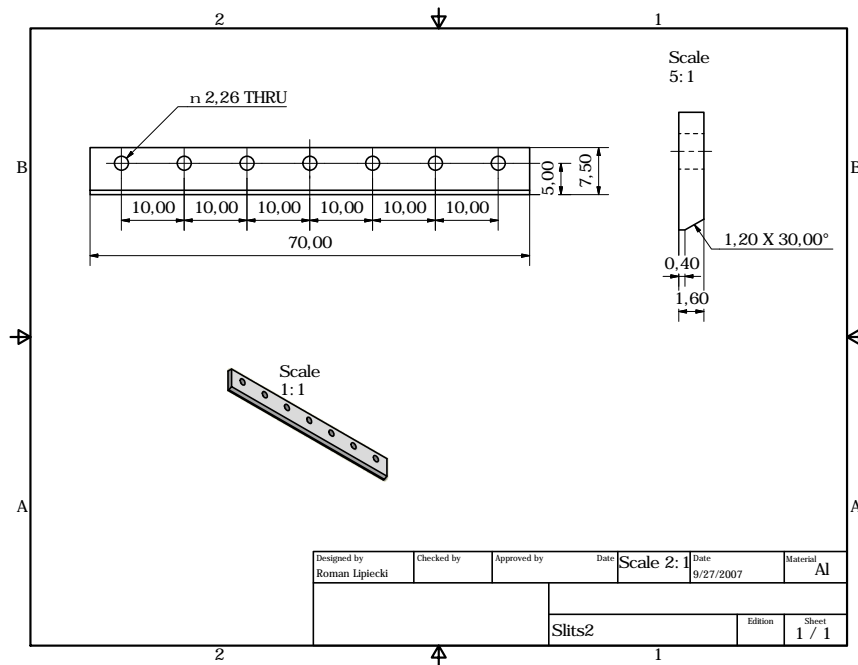


Figure 4.14: Drawing of homemade nozzle caps (8 cm) - The slit is 70 mm × 0.06 mm.

4.4 Ring-Down Cavity

The ring-down cavity is a confocal off-axis cell. The geometric analysis of the beam in such cells are discussed in Appendix F. The ring-down cavity consisted of a pair of ultra-high reflectivity mirrors (Los Gatos Research Inc.) with 1" diameter and 1 m radius of curvature and with R of $\sim 99.98\%$ centered at $5.2\ \mu\text{m}$ or $7.0\ \mu\text{m}$. The entrance mirror was attached to a piezoelectric actuator. The effective aperture of the entrance mirror was 20 mm in diameter. A pair of kinematic mirror holders, which were fixed to a homemade four-rod rigid optical system, provided the tip tilt adjustments for the two mirrors. This was similar to that used in the previous CRD experiments with a lead salt diode laser. (250) The mirror separation was 55 cm, corresponding to a free spectral range (FSR) of 273 MHz with on-axis alignment.

To achieve off-axis CEA alignment in a Herriott cell like this, the advanced angle after each reflection was 63° and the laser beam should make 40 passes of reflection (7 circles) between the ring-down mirrors before tracing itself again. (94) Such alignment was accomplished in the following steps. First, the infrared laser beam was brought to coincide with a visible He-Ne laser beam by overlapping them at the two irises positioned right before and after the ring-down cavity, using an infrared camera (Electrophysics, PV320L). The on-axis pre-alignment was then achieved using the He-Ne laser. We placed two spacers with $2\ \varnothing = 1\ \text{mm}$ holes drilled at angle spacing of 63° on each one. After setting the two spacers normal to each other, the path of the desired off-axis alignment was indicated by the diagonal holes on the two spacers. The visible beam was then aligned to the two points with the entrance ring-down mirror in and out iteratively until the beam hit the entrance spacer at the correct point and, with the entrance ring-down mirror mounted hit the correct point at the rear spacer. In such way, the visible beam, therefore the IR beam was shifted to trace a standard Herriot cell pattern with the sequential spots separated by about 126° on each ring-down mirror. It was very difficult to follow the beam path after the first few round trips because of the low transmission of the mirrors prevents the majority of the visible beam from coupling into the cavity. Only the first few He-Ne laser spots were visible on the mirror surfaces. We found that it was most efficient to perform the final optimization by monitoring the infrared detector output on an oscilloscope directly. Here, the infrared laser alignment was optimized to achieve the best SNR for a known transition of the static gas molecule filled the cavity. (17) The typical infrared intensity patterns for the on- and off-axis alignment are shown

in Fig. 4.15 In the on-axis alignment, there were four strong spikes in each PZT period, corresponding to the fundamental TEM_{00} mode. The smaller spikes were due to the higher order modes. The off-axis alignment, on the other hand, excited many more high order modes than the on-axis case. Therefore in the ideal case, all frequencies were effectively coupled into the cavity and the strong spurious cavity power build-ups were minimized.

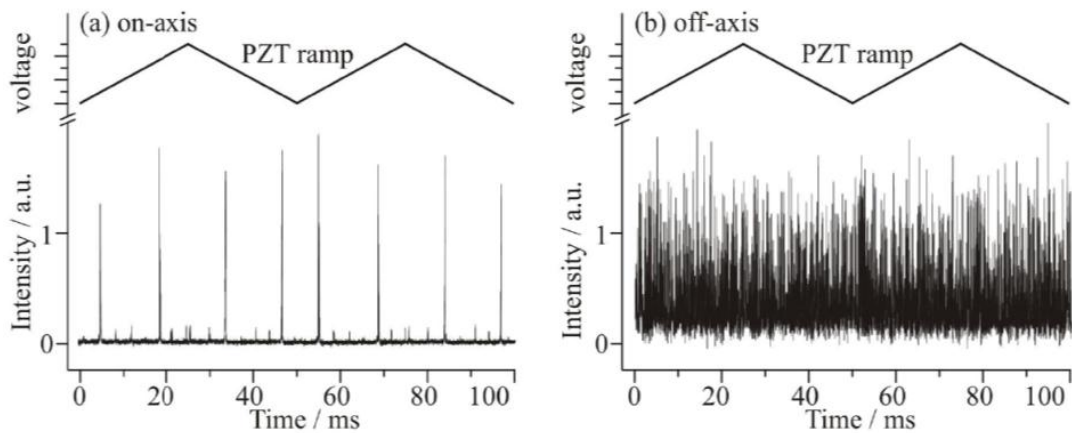


Figure 4.15: On-axis and Off-axis alignment of ring-down cavity - (a) On-axis cavity output pattern, showing eight bigger spikes and the smaller ones due to the TEM_{00} and higher order transverse modes, respectively. (b) Off-axis cavity output pattern. Two consecutive piezo ramping periods are given here and the laser frequency was fixed.

An alternative and more straight forward approach was to deviate from the TEM_{00} mode of the on-axis alignment directly by shifting the mirror in front of the cavity. The procedure was best monitored by placing an IR-camera after the cavity to observe the beam pattern evolve from a uniform spot of TEM_{00} mode to a line and then a circle. (198, 199, 13, 120, 121, 155, 159) We found the alignment achieved by such method could produce very similar degree of mode averaging as shown in Fig. 4.15 but slightly worse than the Herriott cell alignment approach describe before, which might due to the fact that the mode intensity monitored from the IR-camera was very weak because of the strong water absorption at the QCL frequency. An $f = 50$ cm CaF_2 focusing lens was used to couple the laser beam into the ring-down cavity and the infrared beam exiting the ring-down cavity was then focused onto the detector. The IR-beam existing the ring-down cavity was focused onto a liquid nitrogen cooled MCT

4.5 Astigmatic Multipass Absorption Cavity

detector (Fermionics Corporation, PV-6-1) with a matching preamplifier (PV MCT-1000) from Infrared Systems Development. The typical preamplifier output was adjusted to less than two volts by varying the amplification factor of the preamplifier. The voltage limit of 2 volts was imposed by the analog-to-digital card used for the data acquisition.

4.5 Astigmatic Multipass Absorption Cavity

Multiple pass absorption using off-axis resonator absorption cells (94, 95, 170, 167, 169) is a widely used method to increase the effective absorption path in a compact volume. (6, 122, 80, 305, 171, 184, 168)

The astigmatic multipass cell is similar to the Herriott reference gas cell used in the experiment. They are both confocal off-axis cell consisting of two spherical mirrors separated by nearly their radius of curvature, and hence the name confocal. The basic geometric analysis of an off-axis multipass cell is given in Appendix F. An optical beam is injected through a hole in one mirror in an off-axis direction, and it recirculates a number of times before exiting through the coupling hole. For the Herriott reference cell use, the beam reflects 48 times.

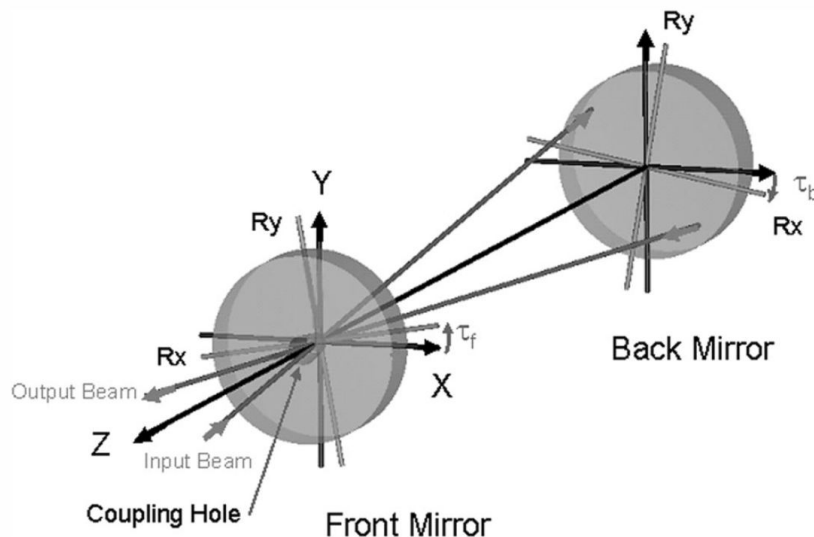


Figure 4.16: Geometry of the astigmatic cell - adapted from Ref. (169).

The basic geometry of the astigmatic multipass cell is shown in Fig. 4.16, which is an astigmatic variation based on the basic Horriotte cell. The main

4.5 Astigmatic Multipass Absorption Cavity

difficulty to use astigmatic off-axis resonator is in the error of X and Y axis from manufacturing. McManus(167) showed that one can compensate the error by rotation of once of the mirrors. Matrix analysis of the ray optics is provided, leading to “space map” of the reentrant solutions as shown in Fig. 4.17. Rotation and Translation of the movable mirror can explore the space map to meet a various of reentrant solutions. So it is possible to locate a certain pattern, for example 182 pass by first finding an easily recognizable pattern and then move on the phi space map by rotation and translation.

The optical resonator used in the MPA spectrometer was an astigmatic multiple pass absorption cell from Aerodyne research. The IR beam entering the optical resonator through the central hole of the front mirror traced out Lissajous pattern with a rectangular outer boundary and exists the absorption cell through the same coupling hole of the front mirror after many passes. The MPA spectrometer with $\varnothing=3.8$ cm astigmatic mirrors (AMAC-36) had been reported previously. (243) A set of $\varnothing=7.6$ cm astigmatic mirrors (AMAC-100) was installed in the vacuum chamber of the CEA spectrometer described above. To suit the vacuum chamber, homemade mirrors mounts were used to hold the mirrors 55 cm apart.

The reentrant condition was met with proper combination of mirror distance and rotation angle of the astigmatic axes. Alignment of the astigmatic multipass cell was aided by calculated pattern map of the cell. We usually first locate the reentrant condition that are easily reached and confirmed, like the 86-pass or 90-pass, then move to the desired reentrant condition on the pattern map by changing the mirror distance and rotation. Typical reentrant condition we locate was 182-pass or 366-pass, which was confirmed by following the pattern of the visible laser spots with calculated one. Follow the pattern map of the AMAC-100 astigmatic mirrors, we could translate the 182-pass reentrant condition to 366-pass by simply decreasing the mirror distance by 5.1 mm. Comparison of the absorption spectra measured from the 182-and 366-pass reentrant condition are shown in section 4.7.1.1. Furthermore, since the Lissajous pattern of certain reentrant condition is determined by the angle of the entrance beam, we aligned the spot pattern to be a vertical rectangular, as shown in Fig. 4.18, to favor the overlap of IR beam and the jet-cooled sample produced from the slit jet.

Since heaters are used to prevent the oil condensation on the mirror surface, thermal expansion of the mirror body needs to be considered. The astigmatic mirrors are first aligned to the 366-pass configuration outside the vacuum chamber. After the mirrors are transferred into the vacuum chamber, the multipass

4.5 Astigmatic Multipass Absorption Cavity

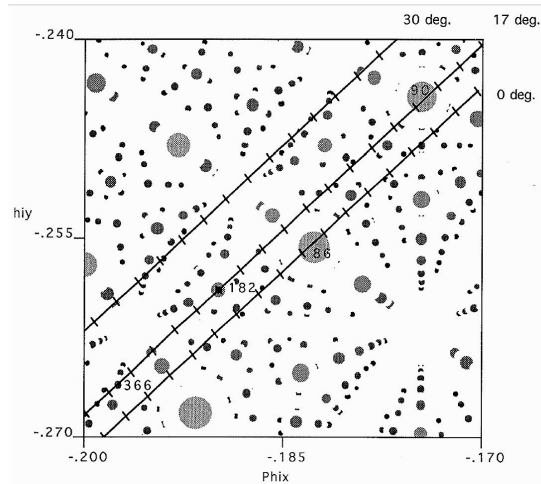


Figure 4.17: “Space Map” of the AMAC-100 astigmatic cell - Each spot on the map represents a reentrant condition that the alignment of the beam has to meet. The size of the spot represents the error tolerance of the alignment. Each line on the map represents the same rotation of the movable mirror with different mirror distance. Figure taken from user manual of the cell from Aerodyne Research.

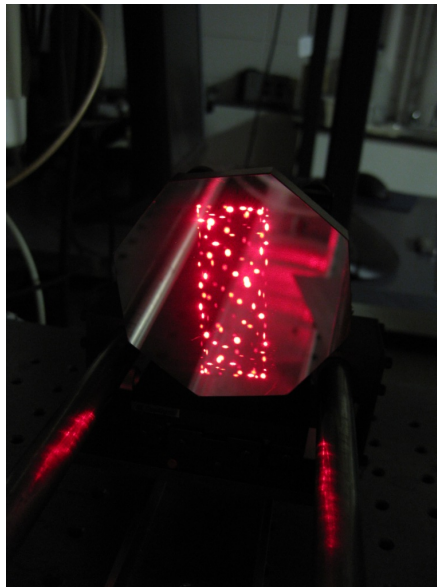


Figure 4.18: Astigmatic multipass absorption cavity - photograph of the He-Ne spots pattern in 366-pass vertical rectangular configuration.

alignment has slight variation, because it is very sensitive to the mirror condition. Therefore, we use two temperature controllers to stabilize the temperature of each mirror at 60°C and an external controller using micrometer screws is installed through a feed through on the flange to allow the fine adjustment of mirror distance under vacuum condition.

4.6 Data Acquisition and Control

Two data acquisition scheme are used to retrieve the spectral features from the measurement. The first method is the “Rapid scan” data acquisition technique with signal averaging and simultaneous background subtraction scheme as described by McKellar *et al.*(40) Our rapid scan scheme was similar to those of Buelow, (64) Sharpe, (230, 108) and Nesbitt. (149, 227) The second method is the wavelength modulation (WLM) method when the current modulation is applied to the EC-QCL.

4.6.1 Rapid Scan Method

Controlled by the IOTA nozzle driver, the supersonic jet pulse usually last 1~3 ms. Measurement of the transient jet sample was therefore not so straight forward as the static room temperature sample. Successful measurement of the jet-cooled sample relied on precise control of the laser frequency to scan at exact time when the jet-cooled sample was produced. To carry out such experiments with the CEA spectrometer *RapidScan* and *RapidOScope*, two LabVIEW control programs, were developed using NI LabVIEW software. They facilitate the execution of the pulse sequences given in Fig. 4.19 and Fig. 4.20.

The previous software program for the rapid scan experiments with a lead salt diode laser (243) was modified substantially to perform the necessary tasks in *RapidScan* and *RapidOScope*. The radiation source control part of the software was modified to allow the switch between a lead salt diode laser and a QCL controller. Briefly, the QCL was ramped continuously using a composed saw tooth waveform (Fig. 4.19) which was generated using a function generator (Stanford Research Systems, DS345). The duration of each ramp was about 1.6 ms with a built-in 0.4 ms recovery period at the end of each ramp. The built-in recovery feature alleviates the frequency nonlinearity of the laser scan somewhat and allow the measurement of zero level of the laser power. The sawtooth and triangular waveforms available on the functional generator were also used directly. The

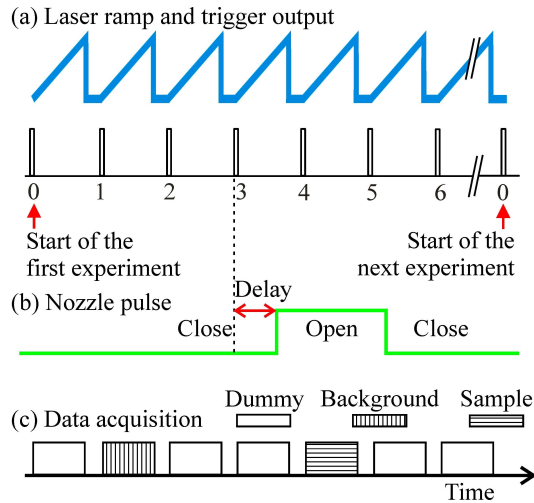


Figure 4.19: Rapid Scan - The pulse sequence of the *RapidScan* program. See text for details.

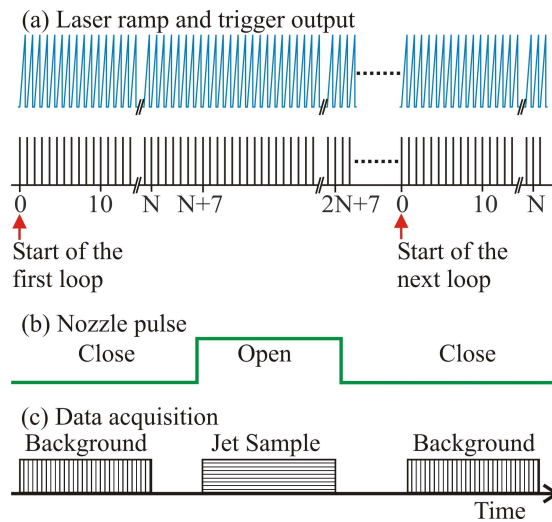


Figure 4.20: Rapid Scope - The pulse sequence of the *RapidScope* program. See text for details.

corresponding TTL triggers from the function generator were put into the NI PCI-6251 multifunctional card, which was used to count the number of triggers. In a normal jet expansion experiment, a background signal was recorded at trigger number 1 (Fig. 4.19). The nozzle was then open at trigger number 3 plus an adjustable delay time to insure the molecular jet expansion encompass the next laser scan starting at trigger number 4, in which the molecular spectrum was recorded. The pure molecular spectrum was then obtained by subtracting the background signal from the signal with a molecular pulse. Both the nozzle delay time and the nozzle opening duration could be optimized experimentally to ensure the best SNR of the molecular spectrum measured. A typical laser scan for the distracted-feedback covered 0.7 cm^{-1} , dictated by the mode character of the particular QCL and for the external-cavity laser the range is 1 cm^{-1} controlled by the applied sine wave voltage. The infrared detector signal was digitized using a 14 bit, four channel analog-to-digital card (GageCompuScope 8340) with a 10 MS/s sample rate for each channel, and was then stored in a PC. To account for the small laser drift during one data collection period, the subsequent laser scans were locked to the first scan of the reference spectrum. The improvements made in the new *RapidScan* LabVIEW program and the implementation of the four-channel fast digitizer board have increased the measurement repetition rate from a few Hz (243) to about 50 Hz.

RapidOScope was developed for even faster, real time data collections, with the same experimental setup and the same computer hardware for static gas sample measurements. Up to $\sim 1\text{ kHz}$ repetition rate was achieved. *RapidOScope* also enabled fast data collections with a pseudo-cw jet expansion with corresponding pulse sequence illustrated in Fig. 4.20. In this case, the program rapidly collected tens to hundreds of laser ramps which overlapped with one pseudo-cw jet expansion nozzle pulse. To achieve a pseudo-cw jet expansion, the nozzle was held open for 200 to 500 ms. The same number of background scans was collected shortly before the nozzle opening. The molecular signal was obtained by subtraction of the two spectra. This procedure could be done in a loop fashion to obtain the desired number of averaging. *RapidOScope* therefore allowed us to explore different operation conditions of a slit jet expansion.

Parameters that should be optimized in a rapid scan measurement were 1) the laser frequency ramp rate: we found the SNR increased with high ramp rate; 2) timing parameter of the nozzle control to produce the jet-cooled sample at the optimum time point when the laser frequency was scanned. Details of the optimization are shown in the experimental results.

4.6.2 Wavelength Modulation (WLM) Method

Wavelength-modulation method is a well known technique to improve the SNR of spectral measurement. (59, 85, 232, 246, 229, 89, 249, 301–303) Recently it has been applied to IR absorption spectroscopy with QCL and CEA spectroscopy. (17, 16, 311) To implement Wavelength Modulation (WLM) method in our experiments with the External-Cavity QCL, the QCL frequency was varied by modulation of the injection current as described in Sec. 4.2.2. The signal from the MCT detector was fed into a lock-in amplifier (Stanford Research Systems, SR830) locked to the modulation frequency. Second order harmonic detection was usually used (the $2f$ signal). Signal from the lock-in amplifier was recorded using the data acquisition (DAQ) cards and the same *RapidScan* program was used with modified DAQ rate and timing parameters. Since main noise source in our experiments was $1/f$ noise from the QCL, harmonic detection obtained in this way greatly reduced the noise picked up at low frequency region.

Four parameters need to be properly optimized for our WLM measurement: 1) the modulation frequency (Ω); 2) the QCL frequency scan rate (ω); 3) the modulation depth; 4) time constant (τ) used in the lock-in amplifier. Our measurements followed the general trend of WLM measurement that the difference between the modulation frequency and the laser frequency ramp rate should be large enough ($\Omega \gg \omega$). The maximum modulation frequency could be used was $\Omega = 50$ kHz, limited by the lock-in-amplifier we used with the $2f$ detection. Increasing the modulation frequency up to 2 MHz might increase the SNR. Typical laser frequency rate we used were $\omega < 10$ Hz to ensure a large difference in order to obtain the harmonic signal. The modulation depth was controlled by the amplitude of the sinusoidal modulation waveform. Increasing the modulation depth would increase the line intensity of the $2f$ signal but enlarge the line width. Therefore the optimized modulation depth for individual transition depended on its line width. Typical value of the amplitude of the modulation waveform was 0.3 Vpp for room temperature gas and 0.15 Vpp for jet-cooled sample. The time constant (τ) was usually adjust according to different scan rate (ω) to optimize the SNR of spectra. Typical values were $\tau = 1$ ms or $\tau = 0.3$ ms.

Special efforts were made to measure the WLM spectra of jet-cooled sample. Unlike the rapid scan scheme, (64, 230, 108, 149, 227) there have been *cw-jet* and *fast-repetition* schemes to achieve harmonic detection of transient jet-cooled sample signal.

In the *cw-jet* approach, the laser frequency is tuned slowly over spectral region of interest while WLM being applied, during which time the jet is operated continuously. (268, 297, 289, 290) Unlike the transient nature of pulsed jet, the *cw-jet* displays continuous existence. Since the background pressure in the vacuum is as high as several tens of mTorr, the jet temperature is higher than a typical pulsed jet. Moreover, the continuous opening of the nozzle resulted in a large gas consumption in comparison with pulsed jet, limiting the sample employed in this method to commercially available gaseous molecule in cylinder.

In the *step-scan* approach, fast nozzle repetition rate as high as 60-100 Hz is used to produce pulsed jet at such frequency to mimic *cw-jet*. Therefor a concentration modulation scheme is often implemented with a boxcar integrator or frequency filter to extract jet signal at certain repetition rate, (63) and a concentration-frequency double modulation scheme can also be realized with the addition of a lock-in amplifier to extract laser signal at modulation frequency. (92, 194) In such approaches, high repetition rate is needed to increase the duty cycle of data acquisition process. Assuming a typical jet transition of 30 MHz FWHM needs a minimum of 10 data points, therefore 10 pulsed per line shape, 10,000 data points are needed to scan 1 cm^{-1} in this manner. With 100 Hz, 10 Hz, and 1 Hz jet repetition rate, the total DAQ time are 100 s, 1,000 s, and 10,000 s respectively; with a 1 ms jet duration, the cycle duty of each scenario are 10%, 1%, and 0.1%. Specially designed nozzles are needed to produce highly reliable pulsed jet at high repetition speed. Fluctuation of the concentration of the jet-cooled sample would lead to shot-to-shot noise in the measured spectra.

We implemented both method with the External-Cavity QCL to measure the $2f$ line shape of pulsed signal. In our *step-scan* approach, the nozzle repetition rate was set to 1 Hz to 0.1 Hz, as optimized to produce the jet-cooled Ar-*para*-water complex. The laser frequency scan rate (ω) was set to $10^{-4} \sim 10^{-5}$ Hz to ensure enough data points are measured to achieve high resolution measurement. Typical jet duration was 3 ms as shown in Fig. 4.21 Modulated laser signal from the detector (black line) was feed into a lock-in amplifier (Stanford Research Systems, SR830) locked to the modulation frequency (Ω) to get the harmonic signal with improved SNR (red line). Instead of using a boxcar integrator or frequency filter to extract the jet signal, we simply picked the average of 1 ms data around the peak maximum with the subtraction of the average of 1 ms data that were 10 ms ahead as the data point to plot the spectrum. As will be discussed in section 4.7.2.2 the shot-to-shot noise dominated the spectra measured using such scheme since our slit-nozzle was not specially designed to produce the same

amount of jet-cooled complex at each pulse. Another drawback was that the External-Cavity QCL gave poor scan performance when operated at such low scan rate and this method was highly resource and time consuming.

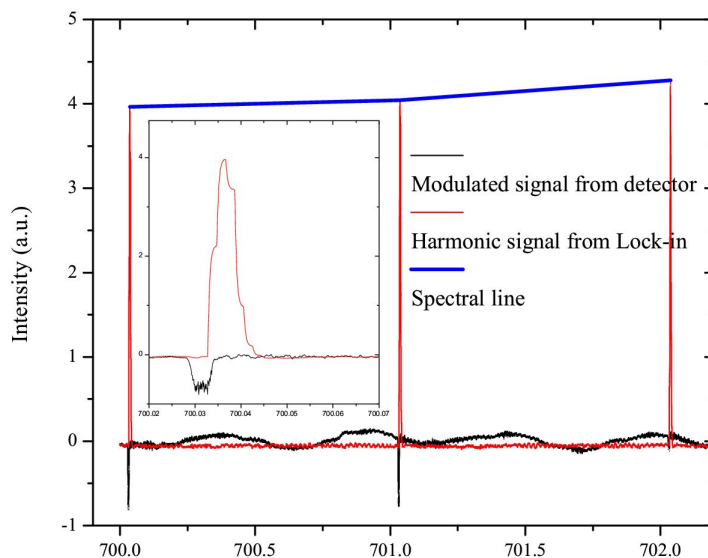


Figure 4.21: *step-scan* WLM scheme - Data acquisition of 3 data points in a typical *step-scan* WLM scheme. The horizontal axis represents time in the unit of second.

In the *pseudo-cw-jet* WLM approach, we extended the slit nozzle opening time long enough to allow harmonic detection of the jet signal within one pulsed expansion. Similar to the *cw-jet* method, the jet signal was available for detection during the whole DAQ rime period. The longest opening time we could use was 70 ms with 3000-7000 Torr backing pressure. With the pumping speed of the diffusion pump to be 8000 L/s, this produced ~ 100 mTorr background pressure in the multi-pass absorption cell that lasted ~ 0.1 second. We observed that the existence of jet-cooled sample could last for as long as 50 ms. Such time period allowed us to perform WLM measurement of the jet signal with $\Omega = 50$ kHz modulation rate and $\omega = 10$ Hz to $\omega = 1$ Hz laser frequency scan rate. The whole measurement process was finished within single long-lasting jet expansion, with the concentration of jet sample gradually decreasing. Thus there was no shot-to-shot noise from concentration fluctuation. The SNR obtained by this method was much better than the *step-scan* scheme. In addition, the External-Cavity QCL was operated at reasonable scan rate and this scheme was almost at the same cost as the rapid scan method.

Further improvement of the WLM method relies on using a lock-in amplifier with high analog-to-digital rate that can operate with high modulation frequency amenable for the current modulation mode of the external-cavity QCL. One of the commercial available module is the SR844 from Stanford Research Systems with 200 MHz bandwidth. This time scale would then be short enough to accompany the short lived supersonic free jet expansion experiment.

4.6.3 Frequency Calibration

Since the scan of the laser frequency of the diode laser cannot be perfectly linear, frequency calibration of the measured spectrum is always crucial to accurately determine the transition frequency for the spectroscopic fitting procedures. To convert the current scan into the frequency scale and account for the scan-to-scan shift of the QCL frequency, we used a frequency calibration procedure to calibrate the measured supersonic free jet signal. Briefly, two beam splitters were used to intercept the laser beam. The first portion of the beam was directed through a 3" solid Ge etalon with an FSR of $\sim 0.016 \text{ cm}^{-1}$ and then focused onto an MCT detector. The second portion was directed through a Herriott multi-pass reference cell with two 1.5" spherical mirrors aligned for 48 passes and separated by 20 cm. Less than 3 Torr of room temperature gas was used as the reference. The main portion of the beam was used to probe the jet expansion. For the near-linear Distributed-Feedback QCL, the etalon fringes were fitted to a polynomial, typically second or third order to establish the relative frequency scale, and the known NH_3 , N_2O and H_2O frequencies in HITRAN08 database (216) were used to determine the FSR of the etalon and the absolute frequencies.

The frequency scale for the External-Cavity QCL was driven by a sine wave, which could not be satisfactorily fitted to a low order polynomial. Typically only part of the laser frequency scan, which was almost monotonic, is used to achieve the same degree of accuracy as the DFB QCL. We use a temperature controlled Germanium Fabry-Pérot interferometer (etalon) to provide higher accuracy calibration. The details of the interference fringes are discussed in Appendix G. The etalon fringes are interpolated to establish the relative frequency scale for calibration. We assume the Free Spectral Range (FSR) of the etalon is a constant in each sweep of the laser frequency. This is a good assumption that each sweep lasts for less than 5 ms long and additionally, the Ge etalon is equipped with a temperature controller to keep its temperature slightly higher than room

temperature at 27°C. Therefore, the etalon peak provide us additional “frequency tickers” that can be used to “measure” the transition frequencies.

Here we show the calibration procedure of a portion of the Propylene Oxide (PO) H₂O spectrum as an example to demonstrate the principle of the calibration and evaluate the accuracy of several numerical methods. If we simply add the collected raw data of the jet signal, scan-to-scan shift completely smear the peaks in the jet signal, as shown in Fig. 4.22 a). Dramatic QCL frequency drifts from the mechanical jitter of the external cavity prevent us from directly averaging the measurement and increase the SNR. Therefore, each scan of the QCL measurement need to calibrated to wavenumber unit by the following procedures separately before averaging. As a result of the frequency calibration, the data collected on each laser scan can be averaged on the wavenumber scale to increase the SNR of the measured spectrum.

The first step of the frequency calibration is to convert the measured transition signal from a sequence of running number to the etalon free spectral range (FSR) scale. Fig. 4.23 a) shows the raw data of the jet-cooled complex, reference gas and etalon signal that are simultaneously obtained from one scan. In the graph, a portion of the raw data of absorption spectrum obtained by simultaneously measurement of 3 channels. The X axis shows the running index of time. Here, we record the data at 10 MS/s. So the spacing between each data point is 0.1 μ s. The blue trace is the signal of the jet-cooled complex need to be calibrated. The green trace is the reference gas signal from the Herriott cell. The total attenuation of the laser power around index 10000 is due to the absorption from a strong transition of the trace amount of water in the laser path way in air. The same transition in the jet-cooled water monomer can also be seen in the upper trace. The red trace is the etalon signal.

We then determine the peak position indices in both the reference and the etalon trace. The peak index is determined by locating the minimum/maximum index and fitting the adjacent data points to a **parabola**. Instead of an integer index, the least-squared fitted center of the parabola is then used as the peak position. This method proved to be more accurate than the simple minimum/maximum method in case of noising data. The difference between the integer index running number and the fitted peak center are usually less than a few unit as shown in Table 4.1 and Table 4.2. A portion of the raw data showing the peak finding procedure is shown in Fig. 4.23 b). The red trace and the blue trace are the etalon and reference gas signal respectively. Blue curve show the

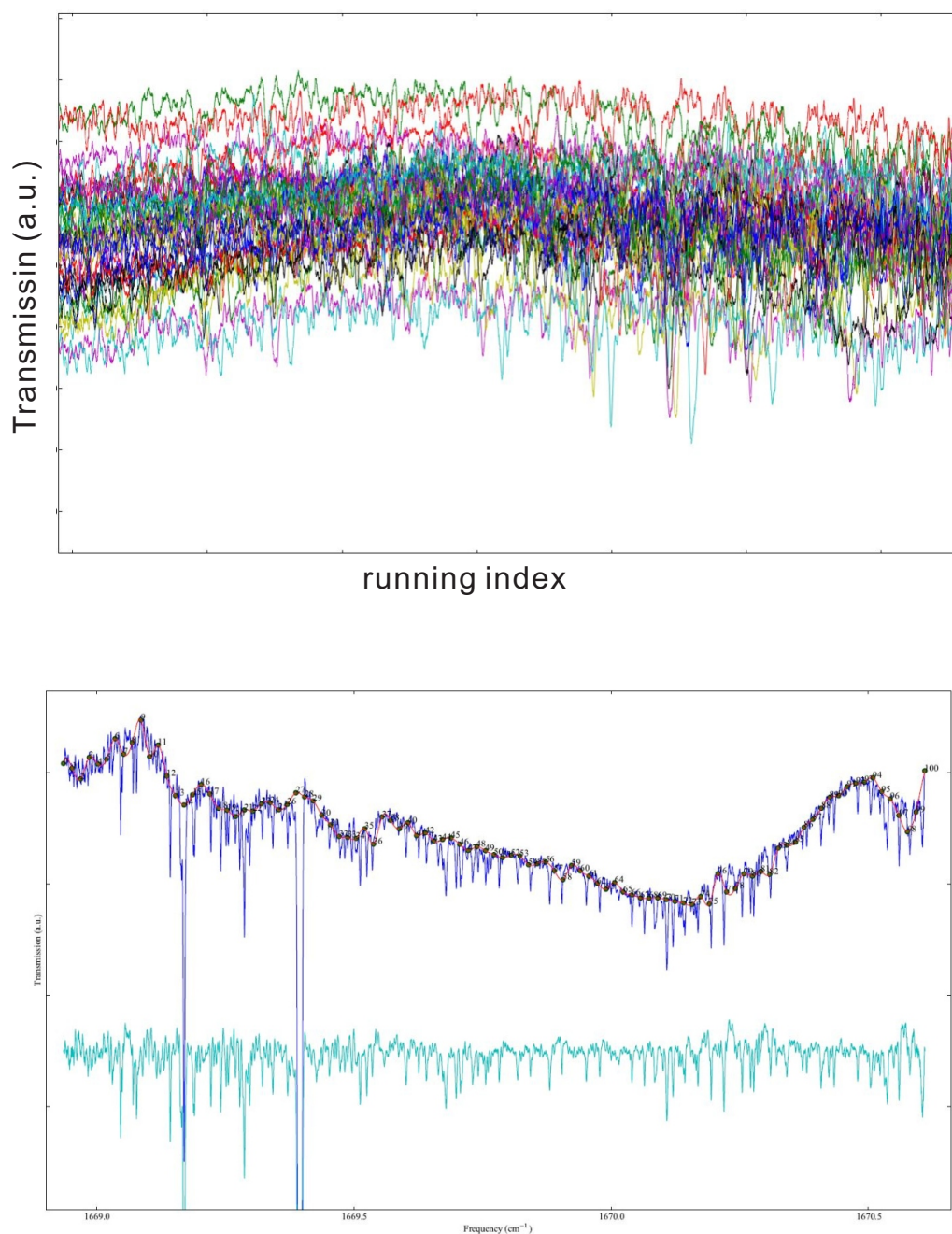


Figure 4.22: Averaging of raw data - a) Portion of the raw data from supersonic free jet expansion of the PO-H₂O spectrum in time scale; b) averaging of the raw data on frequency scale after frequency calibration of each scan with baseline removal.

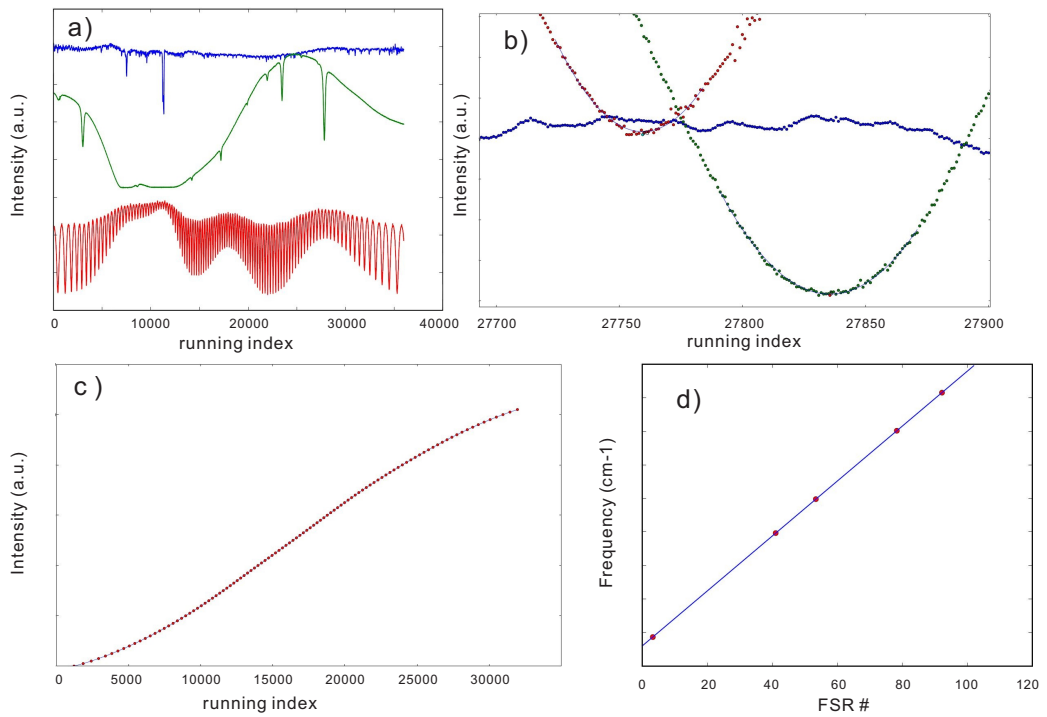


Figure 4.23: Procedure of frequency calibration - a) Raw data collected from supersonic free jet expansion; reference gas and etalon; b) Peak finder; c) Interpolation of the etalon peaks; d) Least-square fit of FSR value.

minimum index	fitted peak center	assigned FSR unit
1203	1205.1172	0
1842	1839.2955	1
2399	2399.2376	2
2902	2909.9162	3
3382	3383.8279	4
3829	3828.0283	5
4250	4250.7128	6
4653	4654.5417	7
5041	5043.2376	8
5425	5422.5353	9
5793	5791.5033	10
6146	6148.0459	11
6489	6493.0676	12
6824	6825.3318	13
7149	7147.7071	14
7463	7463.5702	15
7772	7772.4677	16
8078	8076.5576	17

Table 4.1: Portion of the etalon trace peak center and assigned FSR unit used in the calibration. Comparison between the raw minima and the peak center from the parabola fit.

fitting of the data points to a parabola and the peak is determined as the symmetry axis of the parabola. It can be seen that although the minimum point is not always at the center of the peak, it gives a reasonably good estimation of the range of the peak to allow the parabola fit to capture the peak center accurately.

The etalon peaks are then assigned to indices 0,1,2,..., meaning that the running indices are corresponding to the FSR unit. As an example, part of these values are shown in Table 4.1. The column 2 of Table 4.1 are then interpolated to column 3 as shown in Fig. 4.23 c), which shows interpolation of the index running number to FSR unit. Interpolation of the etalon peak running index in Table 4.1 column 2 and 3. In the index range of 32000, there are 100 etalon peaks in the scan, so the FSR unit range from 0 to 100. This provide us the function (the blue curve in Fig. 4.23 c)) to convert the running index to FSR unit. Previously, we used a polynomial fitting method to convert the running index to FSR unit. The interpolation method proved to give much smaller error in the conversion from running index to FSR units. The function to convert the running index to FSR

4.6 Data Acquisition and Control

index	peak center	FSR unit	ν ($\text{cm}^{-1}10^{-5}$)	error ($\text{cm}^{-1}10^{-5}$)
3021	3019.40450	32.2482	166897404	38.967
14221	14216.5678	41.0315	166959340	35.755
17212	17205.6018	53.3889	166979560	35.969
23488	23488.2820	78.3108	167020320	17.334
27831	27835.5470	92.2161	167043005	50.092

Table 4.2: The etalon trace peak center and assigned FSR unit used in the calibration. The line frequency from HITRAN database is taken as integer number to avoid numerical error. The error of the calibration is on the order of 10^{-4} cm^{-1} .

unit from Fig. 4.23 c) is then used to convert the reference peak center indices to FSR units as shown in column 3 of Table 4.2. Each of the peak center FSR units are assigned to the corresponding HITRAN transition values as shown in column 4 of Table 4.2. A numerical trick is to use the HITRAN frequencies as integer data type instead of float number to allow fast and accurate calculation in the following steps.

Finally, the assigned reference line frequency and the FSR unit number in Tab. 4.2 is fitted wrt Eqn. 4.6.3.1, which are the column 3 and 4 of Table 4.2 are least squared fitted to:

$$v = v_0 + n \times FSR \quad (4.6.3.1)$$

with n as the FSR unit and v as the HITRAN frequency. Fitting of the data in Table 4.2 is shown in Fig. 4.23 d), which gives $v_0=1668.92166 \text{ cm}^{-1}$ and the FSR is $0.0163625168 \text{ cm}^{-1}$. The FSR determined from the fit is a good indicator of the quality of the fit and is around 0.0163 cm^{-1} . The error of the fit indicates the uncertainties of our frequency calibration procedure. As can be seen in column 5 of Table 4.2, the uncertainty is below 0.001 cm^{-1} .

The calibrated jet signal can be averaged on the frequency domain where the scan-to-scan drift is moved by the frequency calibration. Usually the spectrum obtained contains the laser profile as baseline. A number of points from the baseline are used to interpolate the baseline function to be removed from the spectrum. The averaged and baseline removed jet spectra are shown in Fig. 4.22 b). Comparing with Fig. 4.22 a) where the jet spectra are added directly, the effect of the ‘‘on the fly’’ calibration method is obvious. The calibrated jet signal are averaged on the frequency domain where the scan-to-scan shift is removed.

4.7 Experimental Results with MPA Spectrometer

The interpolation method can be used again to minimize the error but this method leads to large shift of the calibrated jet-cooled signal that prevent averaging. To use the interpolation method, one assume that the FSR is not always constant and can vary slightly. Although this is true in the physical scenario of our experiments, in practice, this method won't allow us to remove the frequency drifts. The main reasons why the least-squared fitting procedure performs better than the interpolation method is that:

- Measurement of the reference peak is less accurate than the etalon peak position due to the large line width. So we assume the FSR is constant during the time of each scan and use the fitting procedure to account for the slight error in the determination of the peak position.
- the FSR would change from time to time, so the relative phase between the etalon channel and reference channel always change

Also we cannot use a single peak method in which one peak is measured and the rest of the spectrum is simply calculated using a known FSR value. This method is often used in MW and millimeter wave spectroscopy, in which the FSR of a etalon cavity can be accurately calculated. In our experiments, the FSR cannot be accurately calculated and is assumed to be kept constant from scan to scan.

4.7 Experimental Results with MPA Spectrometer

The External-Cavity QCL covered 1592 cm^{-1} to 1698 cm^{-1} , which allowed us to investigate the high resolution mid-IR transitions of water bending vibration in water-containing complexes. Ar-*para*-water complex investigated by Weida et al.(277) is used as an example to test the performance of the spectrometer. The Q(1) to Q(14) line of Ar-*para*-water $\Pi(1_{11}) \leftarrow \Sigma(0_{00})$ band lies between 1634.02 cm^{-1} to 1634.09 cm^{-1} , which provides us a touchstone for the sensitivity and resolution of the CEA and MPA spectrometer. By measuring these lines we could calibrate and optimize the MPA and CEA spectrometers. The band center of nitrous oxide $\text{N}_2\text{O } 0001 \leftarrow 0110$ mode lies at 1635 cm^{-1} , thus its Q-branch was chosen as the reference in the CEA and MPA spectrometer to calibrate the frequency. Furthermore, the laser line width and detection limit of the spectrometer could be obtained by investigating the N_2O spectra.

4.7.1 Room-Temperature Nitrous Oxide Spectra (N_2O)

4.7.1.1 Rapid Scan Spectra of N_2O

The whole laser frequency coverage could be roughly scanned by the laser controller. Fig. 4.24 shows the scan of 40 m dilute laboratory air without the beam splitters in the optical path. Several water bands could be identified. There was only 1 mode hop region at 1660 cm^{-1} .

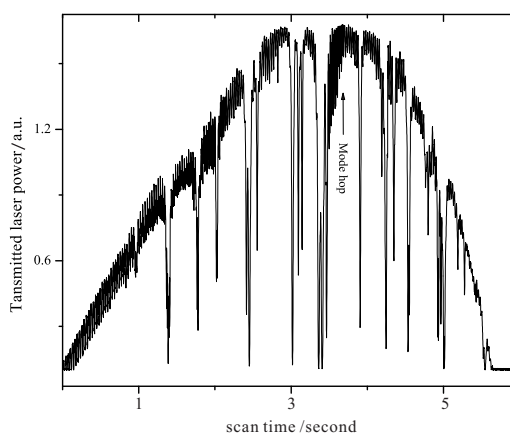


Figure 4.24: Rough scan of the QCL - Transmitted intensity of the External-Cavity QCL after 40 m dilute laboratory air using a multi-pass absorption cell. The laser profile is scanned by motor in ~ 6 seconds. The full range is from 1640 cm^{-1} to 1670 cm^{-1} .

Tuning the laser to certain frequency and applying the scanning waveform to the PZT elements on the external-cavity allowed fine scan of $\sim 1\text{ cm}^{-1}$ above the controller set frequency. By varying the frequency and amplitude of the scanning waveform applied, the scan region and rate of the laser frequency could be controlled. The maximum laser frequency scan rate were $\omega = 100\text{ Hz}$ over 1 cm^{-1} , determined by the PZT elements.

The upper part of Fig. 4.25 shows one cycle scan of the N_2O Q(9) line with the laser frequency scanned 1 cm^{-1} at 100, 10, and 1 Hz, i.e. 0.1 , 0.01 , and $0.001\text{ cm}^{-1}/\text{ms}$. It is obvious that the signal to noise ratio (SNR) increases with faster scan rate since there was less background noise ($1/f$) at higher frequency. It was noticed that the line width increased significantly as the laser frequency scan rate decrease. The line width was $\sim 0.003\text{ cm}^{-1}$ with 100 Hz scan rate, which was close to the Doppler line width of the thermal N_2O gas, and increased to $\sim 0.004\text{ cm}^{-1}$ with 1 Hz scan rate. The middle part of Figure 3 shows the 100

4.7 Experimental Results with MPA Spectrometer

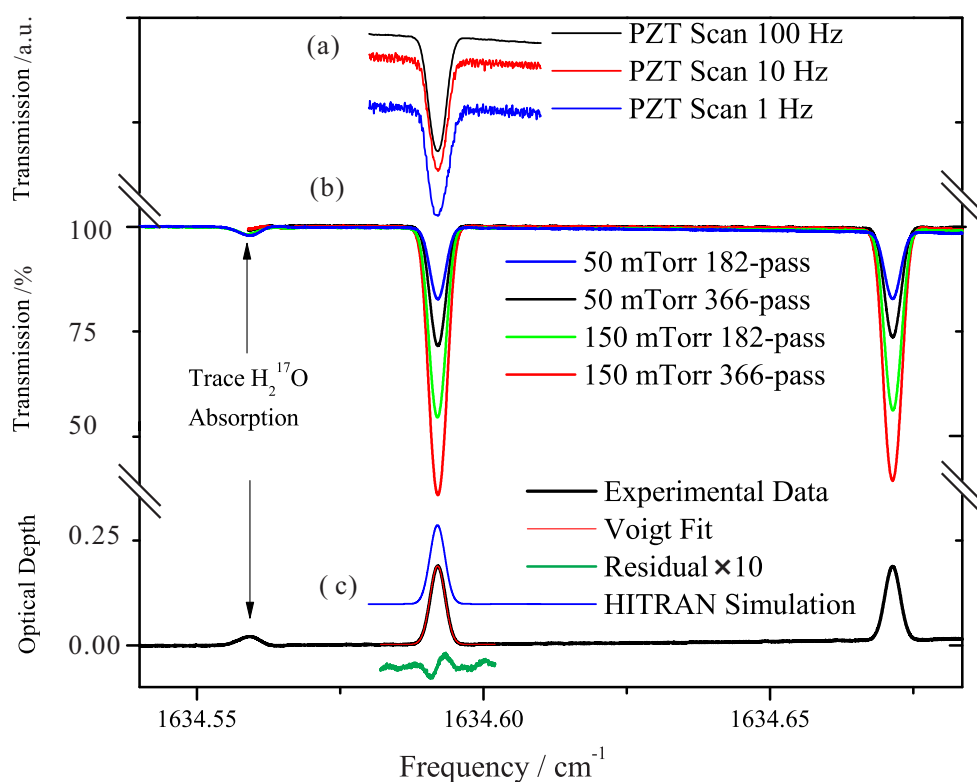


Figure 4.25: Room temperature N_2O spectrum - Laser absorption of 50 or 150 mTorr N_2O with different absorption path length, together with experimental and simulated optical depth from HITRAN08(216).

4.7 Experimental Results with MPA Spectrometer

cycle sum of N₂O Q(9) and Q(8) line with background H₂¹⁷O absorption with 188-pass or 366-pass alignment and different sample pressure. It should be noticed that without gas-flow and calibration procedure, our measurement of the N₂O pressure is not very accurate. Generally, Beer-Lambert law was followed that larger optical depth could be achieved by increasing the sample concentration and absorption path. Thus in the following experiments with the astigmatic mirrors we choose the 366-pass alignment.

The line shape of the measured transition was the convolution of the laser line width with Lorentzian shape pressure broadening and Gaussian shape Doppler broadening. The pressure broadening (FWHM) at experimental condition was $4.7 \times 10^{-5} \text{ cm}^{-1}$, calculated from the N₂O line list data from Toth (257) that had been adapted in HITRAN08 (216) database. The Doppler broadening (FWHM) of the thermal N₂O sample is 0.00303 cm^{-1} . We assume the laser line width could be represented by a Gaussian profile. Therefore the overall line shape could be fitted into to a Voigt line shape, which is shown in the bottom part of Fig. 4.25. With fixed Lorentzian component (FWHM) to be the pressure broadening value, the Gaussian component (FWHM) was 0.00308 cm^{-1} from the fit. Recall that the convolution of two Gaussian profile was a Gaussian profile with line width to be the geometric sum of the two, the laser line width was then determined to be $5.5 \times 10^{-4} \text{ cm}^{-1}$. Similarly, we could estimate the laser line width with 1 Hz slow PZT scan rate to be $2.5 \times 10^{-3} \text{ cm}^{-1}$, which was ~ 4 times larger. The broadening placed limits on the line width we obtained with slower laser frequency scan rate, especially with wavelength modulation method in which slow scan rate was used. It was also noticed that the accuracy of the polynomial fit was worse as the PZT rate decreased, which indicated the laser frequency becomes more non-linear as PZT rate get slower, aside from the laser line width increase. Also shown in Fig. 4.25 are the simulated optical depth from HITRAN and the residual of the Voigt fit. Without additional polynomial fit of the baseline, the standard deviation of the baseline for 182-pass spectra was 1.19×10^{-4} , which gave the minimum detection limit (3σ) to be $3.56 \times 10^{-8} \text{ cm}^{-1}$ with 182-pass absorption path. The calculation of detection sensitivity is introduced in Appendix A.4.

As could be clearly observed from the residual, the line shape was asymmetric, which was due to the rapid passage. (151, 231, 66) The asymmetric line shape and even more unusual, an emission spike following the absorption line could be better observed in the jet-cooled sample signal in Section 4.7.2.1, in which the sample pressure is small and the transition line width is narrow. In another rapid scan scheme in which the laser frequency was scanned at 10 kHz over 0.1 cm^{-1} purely

4.7 Experimental Results with MPA Spectrometer

by the current modulation, the asymmetric, hook line shape was observed more cleanly since the scan rate was higher (Supplementary Materials). Previously the rapid passage signal was usually observed with very low pressure sample (1 mTorr) and very high laser frequency chirp rate (~ 100 MHz/ns) (163) with pulsed mode QCL. (184) It was very interesting to observe such phenomenon in our experiments with large amount of molecules and relatively slow scan rate using cw QCL. This demonstrated the efficient QCL power to carry out non-linear spectroscopy. And the observation of rapid passage signal in jet-cooled sample opened the door to a new type of coherent population transfer in jet-cooled molecules and weak interaction complexes.

4.7.1.2 Wavelength-Modulation Spectra of N_2O

As described in Section 4.2.2, the wavelength modulation (WLM) method was applied to very weak static gas signal to enhance its SNR, with the purpose to optimize the WLM parameters that should be used for very weak jet-cooled signal.

The modulation frequency was fixed to the highest allowed value $\Omega = 50$ kHz. We found that the laser scan rate had to be set to below 10 Hz to see the $2f$ signal. Fig. 4.26 shows the $2f$ signal of very weak trace H_2^{17}O absorption at $1634.55892\text{ cm}^{-1}$, the rapid scan spectra of which have been depicted in Fig. 4.25. The PZT scan rate was varied from 1 Hz to 1×10^{-4} Hz. As discussed in Section 4.2.2, the scan performance deteriorated as we went to such low scan rate. The line width gradually increased and the laser frequency jittered. Therefore the PZT scan rate was often set between 10 Hz to 0.1 Hz, typically 1 Hz. The poor scan quality at low PZT rate limited the application of the External-Cavity QCL in the WLM method compared to laser source that operates more stable at such low scan rate.

The time constant (τ) was usually adjusted according to different scan rate (ω) to optimize the SNR of spectra. Proper combination of the laser scan rate (ω) and lock-in amplifier time constant (τ) would produce $2f$ signal with good SNR. Typical values used in our experiments were $\tau = 1$ ms or $\tau = 0.3$ ms.

The optimized modulation depth for individual transition depended on its line width. Fig. 4.27 shows how increasing the modulation depth would increase the $2f$ line SNR and line width of Q(9) line of 50 mTorr N_2O measured from the Herriott reference cell. Typical value of the amplitude of the modulation waveform was 0.3 Vpp for room temperature gas and 0.15 Vpp for jet-cooled sample.

4.7 Experimental Results with MPA Spectrometer

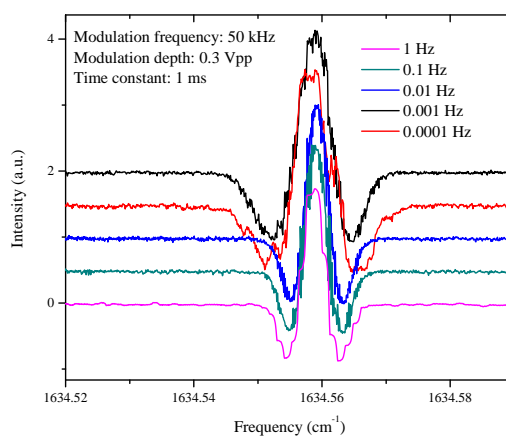


Figure 4.26: WLM spectra of room temperature H_2^{17}O - WLM spectra of H_2^{17}O with different laser frequency scan rate.

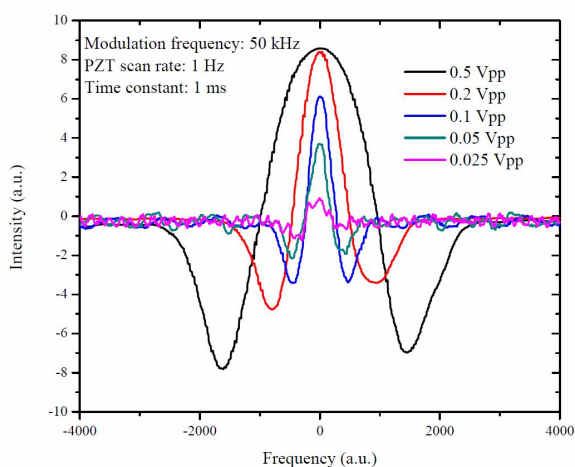


Figure 4.27: WLM spectra of N_2O - The spectra are measured with different modulation depth.

4.7 Experimental Results with MPA Spectrometer

Fig. 4.28 shows the case in which small modulation depth (0.10 Vpp) was used in order not to over-modulate the very weak 3 mTorr N₂O Q(14) line at 1634.062899 cm⁻¹ (0.1% N₂O in 3 Torr Ar). It should be noticed that there was severe fringes in the rapid scan spectrum, which was slightly depressed in the WLM spectrum since the modulation depth was not big enough to improve the SNR a lot. But signal averaging 100 cycles did not improve the SNR of WLM spectrum significantly.

Overall, the limiting factor in the rapid scan and WLM spectra of room temperature N₂O measured from the MPA spectrometer was the interference fringes from optical components and the multi-pass cell, which could not be satisfactory depressed by cycling. The interference fringes are discussed in Appendix G.

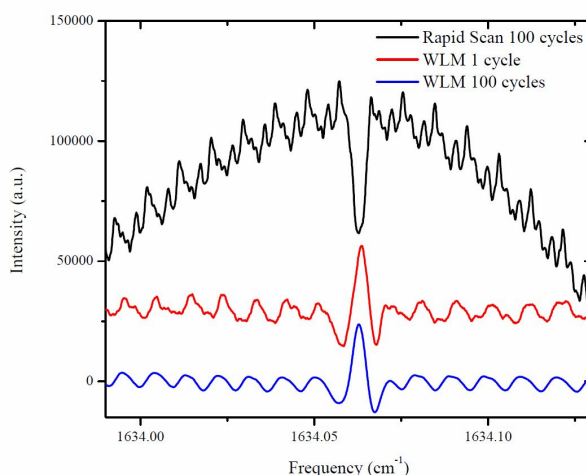


Figure 4.28: Rapid scan and WLM spectra of N₂O - The spectra are measured with different cycles of data accumulation.

4.7.2 Jet-cooled Ar-*para*-water Spectra

4.7.2.1 Rapid Scan Spectra of Jet-Cooled Ar-*para*-water

A typical spectrum of jet-cooled Ar-*para*-water produced in single pulse supersonic expansion is shown in Fig. 4.29 with the Q-branch and R(1) R(2) line clearly recorded with hook shape rapid passage signal. The SNR obtained from the single scan was quite good due to the high QCL power and long absorption path. Procedure to calibrate the transition frequencies are discussed in Section 4.6.3 and the details of which is listed in the Supplementary Materials. Basically, the precision

4.7 Experimental Results with MPA Spectrometer

the calibrated frequencies was 0.001 cm^{-1} with the same order of accuracy as the reference lines listed in HITRAN08 database.

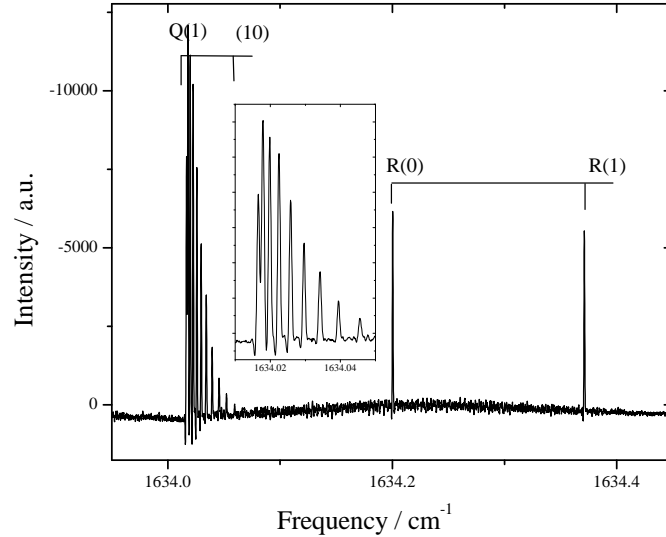


Figure 4.29: Rapid scan spectrum of Ar-*para*-water - The spectrum is measured from one shot with 366-pass.

Measurement of the Q-branch offered us an unique opportunity to monitor the temperature of the jet-cooled sample. The well known trend of temperature raise during the jet fly time was observed and typical rotational temperature was $0.7 \sim 1 \text{ K}$. Such rotational temperature obtained from the 5000 Torr stagnation pressure was lower than the 6.42 K value that obtained from the 0.4 bar stagnation pressure used by Weida et al. (277) and same as the value we obtained before using similar experimental condition as described in Appendix 3. Assuming rapid equilibration of translational and rotational temperature in the slit jet, the Doppler broadening of the Ar-*para*-water was 5 MHz . Fig. 4.30 shows 1-cycle and 50-cycle spectra of the single R(1) line recorded at 3 s cycling period. Fitted to Gaussian line shape, the line width (FWHM) for the 1-cycle and 50-cycle peaks are 0.0013 cm^{-1} and 0.0022 cm^{-1} respectively, i.e., 40 MHz and 65 MHz . The broadening was mainly due to the excited state life time, the nonorthogonal crossing of the beam, and most significantly, the QCL line width.

As discussed in Section 4.7.1.1, the QCL line width increased with signal averaging. In our experiment, 1 second or longer recovery time was needed to

4.7 Experimental Results with MPA Spectrometer

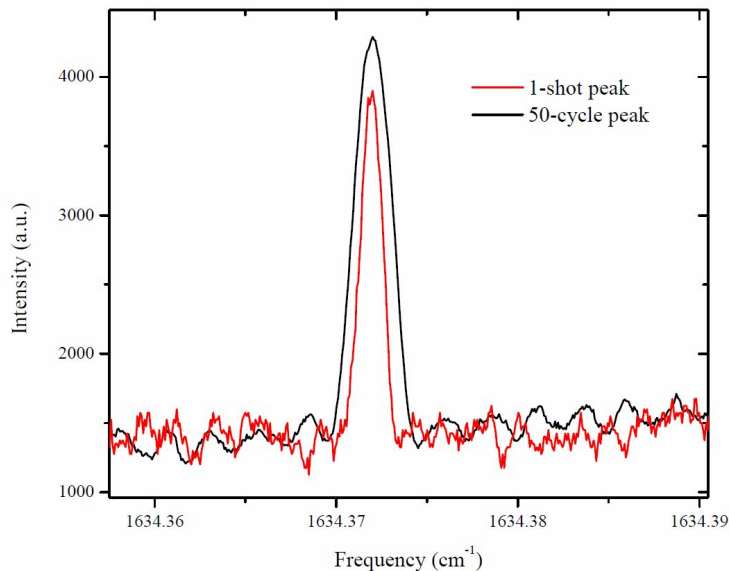


Figure 4.30: Rapid scan spectrum of Ar-*para*-water - The spectra are measured with 1-cycle and 50-cycle.

pump down the chamber to proper vacuum level. Recording many cycles for the jet-cooled sample took substantially longer time than for the room-temperature sample. Thus large line width broadening due to laser line width was expected. The broadening from one-shot peak to 50-cycle peak was due to the QCL line width during the cycling, which was estimated to be 0.0017 cm^{-1} , the same order of magnitude as the jet signal line width. This line width was greater than the 0.00055 cm^{-1} broadening estimated from the N_2O spectrum in Section 4.7.1.1 since the DAQ time for 50 cycles of the jet experiments was 150 second, much longer than the 1 second cycling time for rapid scan experiments. It was also noticed that the interference fringe limit the SNR one could get by accumulating many cycles, the same was observed for the room temperature N_2O sample. As shown in the 50-cycle spectrum, the SNR did not follow the \sqrt{N} rule due to the interference fringes. Because accumulating many cycles increased the spectral line width substantially and did not increase SNR significantly, we tried to achieve the best SNR we could get in one shot instead of cycling, such as increase the backing pressure and jet duration to produce as much jet-cooled sample as possible.

4.7 Experimental Results with MPA Spectrometer

4.7.2.2 Wavelength-Modulation Spectra of Ar-*para*-water

As described in Section 4.6.2, both the *step-scan* and *pseudo-cw-jet* scheme were implemented to measure the $2f$ signal of transient jet cooled sample. Fig. 4.31 shows a typical spectrum obtained from the *step-scan* approach with 1 Hz jet repetition rate and 5×10^{-4} Hz laser scan rate over 1 cm^{-1} , in which combining 2000 data points were measured per wavenumber. The SNR of the spectrum obtained was limited by the shot-to-shot intensity fluctuation indicating the amount of jet-cooled sample produced by the slit nozzle varies. To overcome shot-to-shot noise, we used the boxcar averaging method by averaging of 10 data points to plot the spectrum, which eliminated the shot-to-shot noise efficiently as shown in Fig. 4.31. However, the external-cavity QCL scanned at such low PZT rate couldn't provide smooth frequency scan quality and mod-hop appeared. Long data acquisition time and large amount of gas sample was needed to perform such a measurement, which was quite unaffordable.

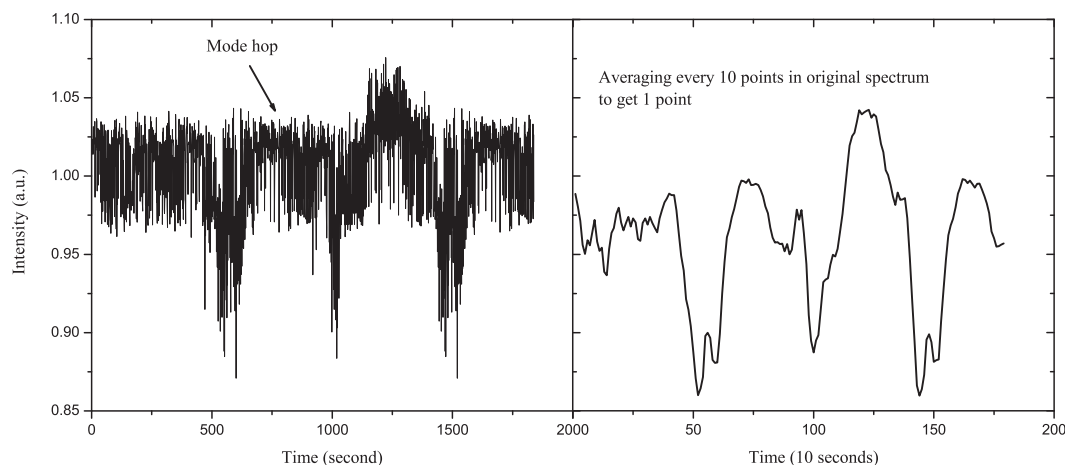


Figure 4.31: step scan WLM spectrum of N_2O R(1) line - The spectrum is obtained with *step-scan* scheme plotted directly and use boxcar averaging. See text for details.

On the other hand, the *pseudo-cw-jet* scheme enabled the measurement of decent $2f$ signal within one long expansion that lasted 30~70 ms. Such time period allowed us to perform the WLM measurement (modulation frequency $\Omega = 50 \text{ kHz}$, depth 0.15 Vpp, lock-in time constant $\tau = 0.3 \text{ ms}$) of the R(2) line of the Ar-*para*-water complex as shown in Fig. 4.32 Compared with the rapid scan spectrum measured at $\omega = 10 \text{ Hz}$, the WLM spectrum measured at the same laser scan rate

4.7 Experimental Results with MPA Spectrometer

shows ~ 10 fold improvement of SNR. Scanning the laser frequency at lower rate ($\omega = 1$ Hz, $\tau = 1$ ms) increased the difference between modulation frequency and laser scan rate ($\Omega \gg \omega$), thus an even better SNR was obtained. The SNR of the WLM spectrum obtained at $\omega = 1$ Hz was slightly better than the best SNR obtained from the rapid scan spectrum at $\omega = 100$ Hz.

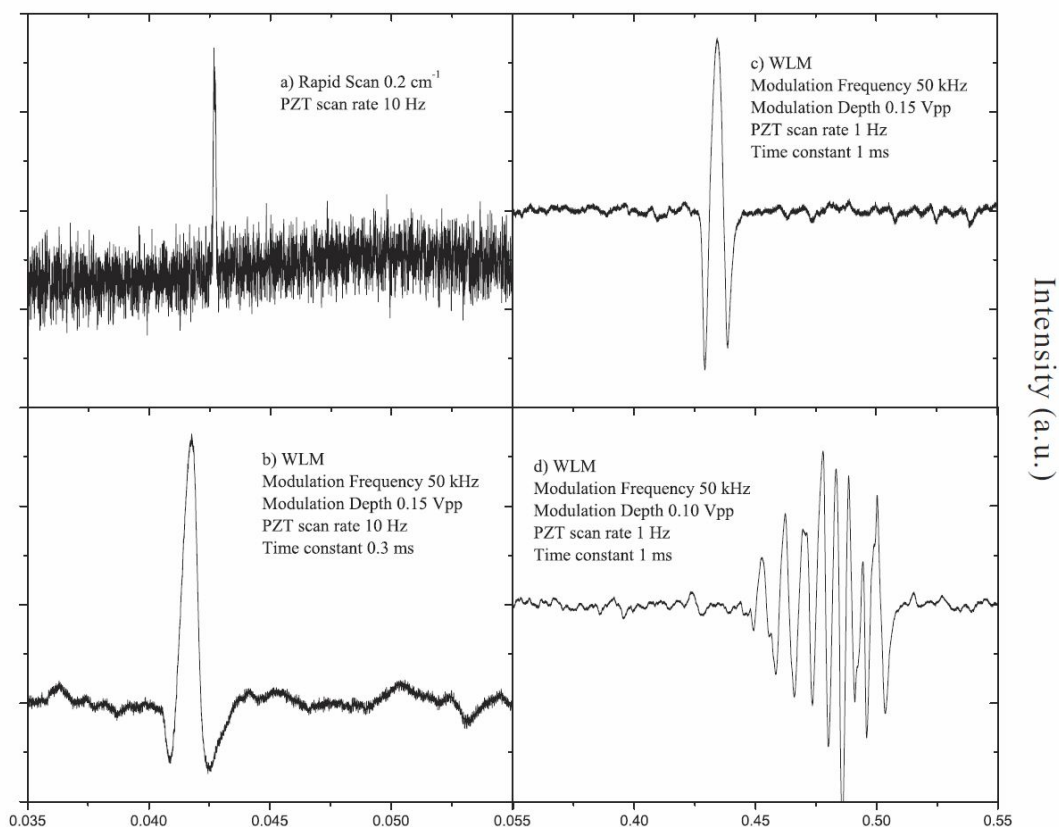


Figure 4.32: Rapid scan and WLM spectra of N_2O R(1) line - The spectra are obtained with *pseudo-cw-jet* scheme. a) rapid scan spectrum obtained at 10 Hz PZT rate; b) WLM spectrum obtained at the same laser scan rate; c) WLM spectrum obtained at lower laser scan rate; d) Q-branch spectrum obtained at 1 Hz PZT rate.

Careful consideration had to be made to ensure the synchronization of the production of jet-cooled sample during the jet expansion and the laser frequency scan. With $\omega = 10$ Hz laser scan rate, we needed to have the nozzle opening time greater than 20 ms to ensure *good* WLM measurement of the jet signal, which lasted 5 ms. For example to measure the spectra in Fig. 4.32, the nozzle open point for the rapid scan and WLM scheme were both at 0.039 second, ~ 5 ms

4.7 Experimental Results with MPA Spectrometer

ahead of the jet signal. With the $\omega = 1$ Hz laser scan rate, we needed at least 30 ms nozzle opening time to cover the time needed for the laser frequency to sweep the signal. In the spectrum shown in Fig. 4.33, the nozzle opening time was varied with 10 ms interval. The asymmetric line shape of the WLM signal was due to the change of jet cooled sample concentration originated from the different nozzle open point. Consider the mechanical response delay time of the slit nozzle, the first 10 ms section of the expansion had stronger signal intensity than the following time. Decrease of the jet cooled sample concentration might due to the increase of the sample temperature and pumping. Fig. 4.32 shows our attempt to measure the Q-branch with the laser frequency scanned from high frequency to low frequency. The nozzle open point was at 0.44 second. The whole Q-branch lasted 50 ms time period, which could not be perfectly covered by one pseudo-cw-jet.

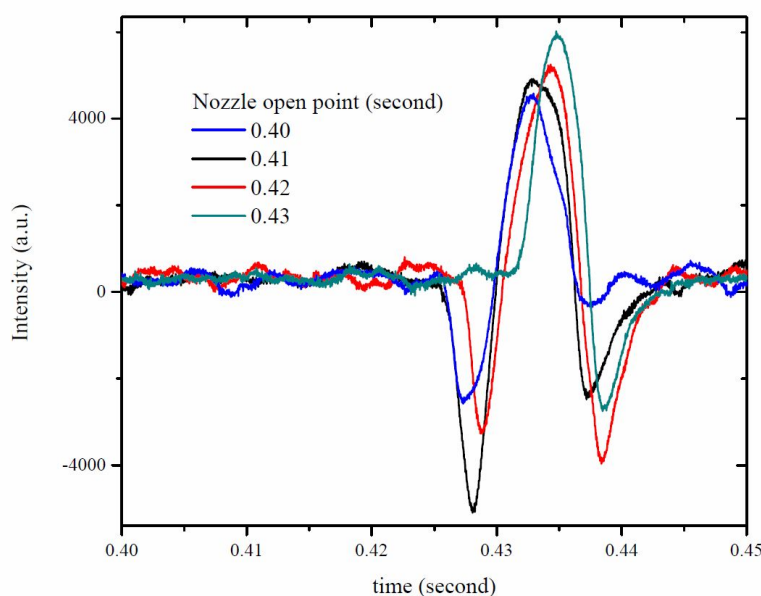


Figure 4.33: *Pseudo-cw-jet* WLM spectra of Ar-*para*-water - The R(2) is line measured using *pseudo-cw-jet* scheme with different nozzle opening point.

Another parameter we optimized was the modulation depth. Typical modulation depth we used broadened the line width of the superiority jet signal. Fig. 4.34 shows the direct measured signal from the detector and the WLM signal with different modulation depth. When the modulation depth was below 0.100 Vpp, the SNR was usually poor; when it's above 0.200 Vpp, the line width

4.7 Experimental Results with MPA Spectrometer

broadening was more severe. Thus in our attempt to measure the Q-branch WLM signal, 0.100 Vpp modulation depth was used. Considering the broadening due to modulation and the laser scan quality at low laser scan rate, the resolution of the *pseudo-cw-jet* WLM method might be as large as 0.01 cm^{-1} .

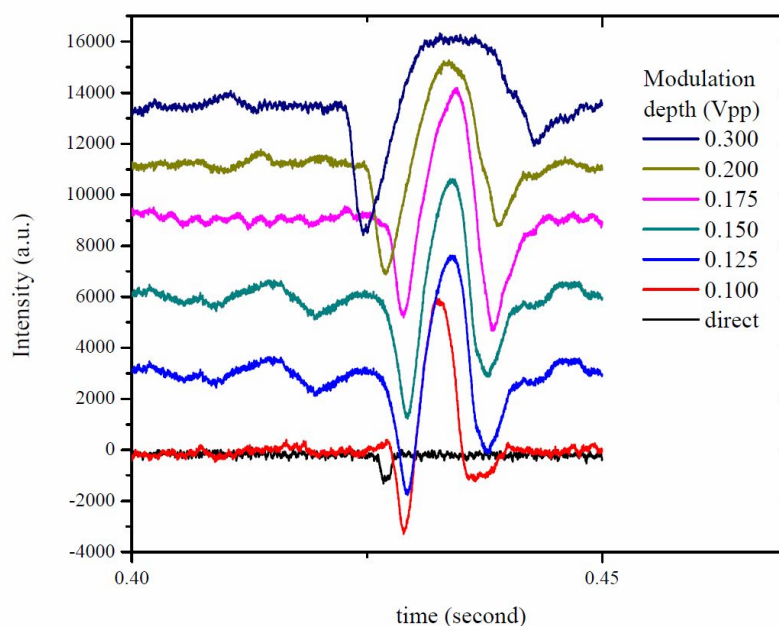


Figure 4.34: Effects of modulation depth - WLM spectra of Ar-*para*-water R(2) line measured using *pseudo-cw-jet* scheme with different modulation depth.

We found calibration of the WLM signal was not as precise as the rapid scan spectrum, which might due to the inherent limit of the resolution, the frequency shift due to jet cooled sample concentration change, and the fact that harmonic measurement of the reference and etalon channel were done with different type of lock-in amplifier. In principle one could piece up a number of spectra with sequential nozzle open point to get the whole profile of the spectrum after calibrate each one. We found this approach not practical to produce very dense spectral profile such as the Ar-*para*-water Q-branch since its resolution is not good. The line broadening and shift prevented us from identify and overlap each peak of the Q-branch. Yet for a single peak such as the R(2) line, piecing up like Fig. 4.32 was still possible. It could be anticipated that laser source capable to perform stable high resolution scan at low scan rate around 1 Hz would be more suitable to be implemented with the *pseudo-cw-jet* approach.

4.8 Experimental Results with CEA Spectrometer

Both the External-Cavity and Distributed-Feedback QCL were implemented in the CEA spectrometer with ring-down mirrors designed at corresponding wavelength. As clearly shown in Fig. 4.15, the spurious coupling to optical resonances within the cavity was the dominating noise source in CEA experiments. The advantages of an off-axis coupling in minimizing such noise had been demonstrated and discussed by Anderson and co-workers using a near infrared diode at $1.55\ \mu\text{m}$. (69) Other methods had also been explored to minimize such noise. For example, Vasudev (265) and Tittle et al. (17) had reported that wavelength modulation was a very effective way to remove the residual etalon fringes in the CEA spectra, in addition to the off-axis coupling. Cheung and co-workers (51) had showed that one could achieve a significantly higher SNR by recording only the highest light intensity signal at each scan interval instead of the usual time-integrated averaged signal. The latter techniques require scanning the laser slowly, making it difficult to couple the CEA technique to a pulse jet expansion as discussed in the previous section of the MPA spectrometer. We therefore focused our efforts on optimizing the off-axis CEA setup.

4.8.1 Room-Temperature Molecules

4.8.1.1 NH_3 Measured with Distributed-Feedback QCL

In the early CEA experiments with the Distributed-Feedback QCL, one ring-down mirrors was mounted on a PZT (Polytec PI S-314.10) with a 10 mm clear aperture, which was used in the previous CRD experiments. (250) To increase the effective mirror size from 10 mm to 20 mm, a new PZT (PiezoMechanik, HPSt 150/35-25/40TPVS45) was acquired. The new PZT has a 25 mm diameter clear aperture and a maximum stroke of $40\ \mu\text{m}$. To maximize the surface usage of the existing 1" ring-down mirrors, a homemade mirror mount with a clear aperture of 20 mm in diameter was machined. In Fig. 4.35, we compare the CEA measurements obtained with the two different effective mirror surfaces, with the same experimental setup. The effect was significant! With the 10 mm effective mirror size, the fringes due to the spurious laser build-ups inside the ring-down cavity were quite prominent, even after 1000 averaging cycles. With the 20 mm effective mirror size, such noise was of similar magnitude as the detector noise. It was also noted that the IR power reached the MCT detector is much higher

4.8 Experimental Results with CEA Spectrometer

with the 10 mm effective mirror size than the 20 mm one, presumably because of the much longer effective absorption path achieved with the latter. As a result 20 Torr of NH_3 was needed with the 10 mm mirror setup in order to observe the NH_3 transitions with good SNR (Fig. 4.35 (a) top trace), while only 2 mTorr of NH_3 was used to achieve much better SNR with the 20 mm one (Fig. 4.35 (a) bottom trace and Fig. 4.35 (c)).

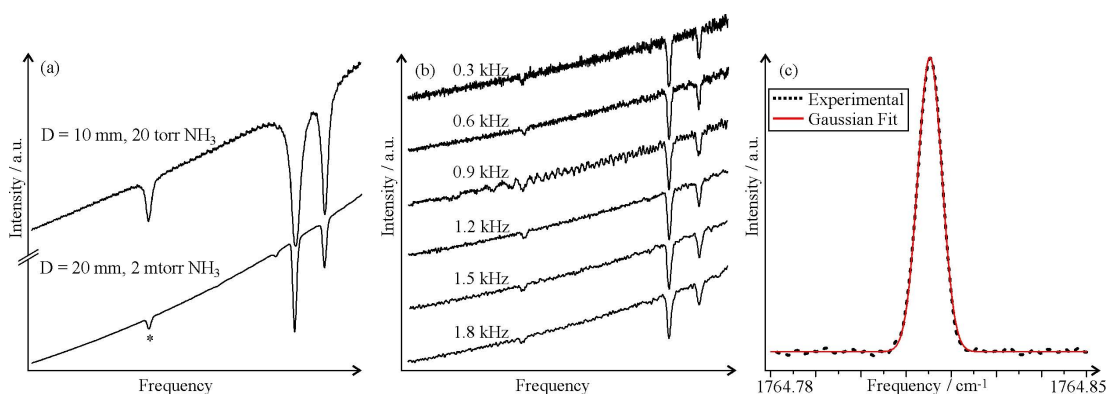


Figure 4.35: Room temperature NH_3 spectra measure with CEA spectrometer - (a) Upper trace was recorded with an effective mirror diameter of 10 mm and 20 Torr of NH_3 in the CEA cavity; lower trace with an effective mirror diameter of 20 mm and 0.5% NH_3 in Ne with a total pressure of 400 mTorr. 1000 averaging cycles and a laser scan rate of 1.2 kHz were used for each spectrum. (b) The NH_3 spectra were recorded using six different laser scan rates ranging from 0.3 kHz to 1.8 kHz, with a sample mixture of 0.5% NH_3 in Ne with a total pressure of 400 mTorr and one experimental cycle. (c) The NH_3 line at $1764.8155 \text{ cm}^{-1}$, indicated with * in (a), after baseline correction and frequency calibration. The dotted curve shows a Gaussian fit with a FWHM of $5.33 \times 10^{-3} \text{ cm}^{-1}$. The signal-to-noise ratio, defined as the ratio of $A/\delta A$ where A is the area under the absorption line and δA the deviation of A in the fit, is 653.

Another possible way to reduce spurious laser build-ups inside the ring-down cavity was to increase the laser scan rate (ω) so that there was not enough time at each frequency interval to get a significant laser power build-up. As a result, one would have more evenly distributed mode intensities besides the advantage reducing the $1/f$ noise the laser and optical system would pick up from the environment. On the other hand, this reduces the output infrared power to the detector and may result in a lower SNR. It was therefore necessary to optimize laser scan rate experimentally. To illustrate the effects of varying laser scan rate, a small section of the NH_3 spectrum was recorded with the laser scan rates arranging from $\omega = 0.3 \text{ kHz}$ to $\omega = 1.8 \text{ kHz}$ for a sample mixture of 0.5% NH_3

4.8 Experimental Results with CEA Spectrometer

in Ne with a total pressure of 400 mTorr. The baseline noise was considerably smaller with a scan rate of $\omega = 1.2$ kHz and higher. Not much further improvement was detected above 1.2 kHz since other noise sources such as detector noise also became important. Furthermore, the observed NH_3 transitions were broadened at higher scan rates. Therefore, laser scan rate of 0.7~1.2 kHz was typically used in our experiments. Note that this was much higher than the 100 Hz scan rate used with the External-Cavity QCL, indicating a great potential to improve the SNR that could be obtained from the External-Cavity QCL with higher PZT scan rate. Although current modulation to the External-Cavity QCL allowed scanning up to 0.1 cm^{-1} at 10 kHz~2 MHz, it was not an applicable method to measure the rapid scan spectrum because 1) the region it covered was too small to allow frequency calibration procedure; 2) similar line width broadening was observed at high laser scan frequency.

Fig. 4.35 (c) shows the NH_3 line at $1764.81555 \text{ cm}^{-1}$ recorded with 1000 averaging cycles, i.e. about 1 s data acquisition time. The experimental data points were fitted to a Gaussian profile. The experimental full width at half maximum (FWHM) was $5.33 \times 10^{-3} \text{ cm}^{-1}$, slightly bigger than the $5.27 \times 10^{-3} \text{ cm}^{-1}$ Doppler line width of NH_3 at 296 K. The Distributed-Feedback QCL line width could thus be estimated as $8 \times 10^{-4} \text{ cm}^{-1}$, i.e. 24 MHz, which was bigger than the 15 MHz value estimated for External-Cavity QCL.

The line strength of the NH_3 line was $1.109 \times 10^{-21} \text{ cm}^{-1}/(\text{molecule} \times \text{cm}^{-2})$ from HITRAN08. From the SNR achieved, the minimum detection limit was calculated to be $1.77 \times 10^{-8} \text{ cm}^{-1}$. This corresponds to a similar NH_3 detection limit reported previously. (265) It should be mentioned that no special effort was made to use the pre-calibrated NH_3 samples since the spectrometer was designed to perform pulsed molecular jet experiments rather than to carry out quantitative trace gas measurements.

4.8.1.2 N_2O Measured with External-Cavity QCL

Fig. 4.36 shows the rapid scan and WLM spectra of 150 mTorr N_2O . The rapid scan method used 100 Hz PZT scan rate and 1 second DAQ time to take 100-cycle data accumulation while only 1 cycle was taken in the WLM method with 1 Hz PZT scan rate and 50 kHz modulation frequency and 0.200 Vpp modulation depth. Within the same DAQ time, the SNR obtained by the WLM method was ~ 4 times better than the rapid scan method. Based on the optical depth obtained, the effective absorption path was $\sim 400 \text{ m}$, which was twice as much as

4.8 Experimental Results with CEA Spectrometer

the absorption path obtained from the MPA spectrometer. However, the standard deviation obtained was 0.019, leading to a minimum detection limit (3σ) to be $1.5 \times 10^{-6} \text{ cm}^{-1}$, which was ~ 40 times bigger than with the MPA spectrometer. The detection limit calculation is introduced in Appendix A.4. As discussed in the previous sections, such big noise came from the incomplete averaging of the cavity transmission resonances. As found with the Distributed-Feedback QCL, the mode averaging would be much more efficient at a higher laser scanning rate, e.g. Bakhirkin et al. (16) achieved $\sim 700 \text{ m}$ effective absorption path and sub-ppbv level sensitivity with $\omega = 1 \text{ kHz}$ laser scan rate. It could be well anticipated that a similar degree of sensitivity would be achieved from the External-Cavity QCL with higher PZT scan rate. It should be noticed that the intensity of the WLM spectrum was proportional to the laser scan rate (ω) and the comparison of intensity of different lines was not straight forward.

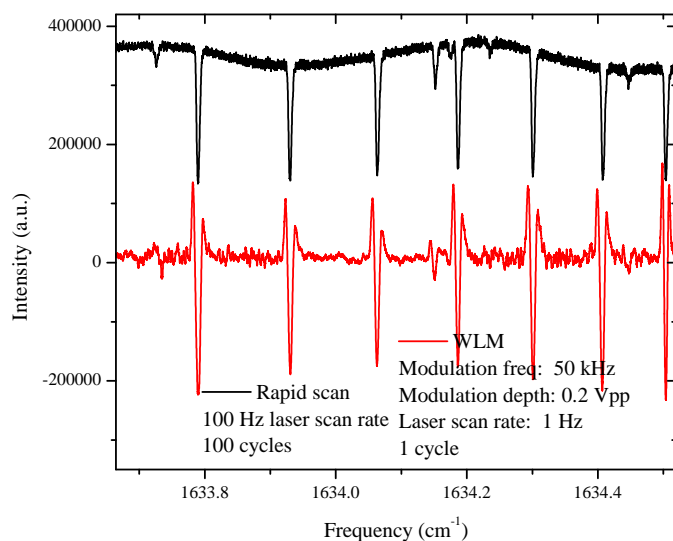


Figure 4.36: Rapid Scan and WLM spectra of N_2O - Comparison of the rapid scan and WLM spectra of 150 mTorr N_2O measured with 1 s DAQ time from the CEA spectrometer.

We noticed that accumulating many scan cycles could efficiently suppress the noise coming from incomplete mode averaging. Fig. 4.37 shows the comparison of WLM spectra obtained with 10-cycle 1 Hz laser scan and 1-cycle 0.1 Hz scan. With the same DAQ time, the 10-cycle scan displays much better noise-depression

4.8 Experimental Results with CEA Spectrometer

and SNR. The lock-in amplifier time constant was optimized to get large SNR without severe distortion of the line shape. Typical value used was 1.0 ms. As shown in Fig. 4.37 (c), the 10-cycle SNR of the N₂O Q(10) line increased as the modulation depth increased from 0.15 V_{pp}, the typical value for narrow jet-cooled sample lines, to 0.4 V_{pp} where the $2f$ line shape was apparently over-modulated. Thus the optimized modulation depth for the N₂O lines was 0.3 V_{pp}. Since there was no obvious interference fringes in the spectra measured, increasing the number of cycles of measurement could suppress noise level. As shown in Fig. 4.37 (d), the SNR obtained increased from 47 to 113 and 238 with the number of cycles accumulated increasing from 10 to 100 and 650, following the \sqrt{N} rule.

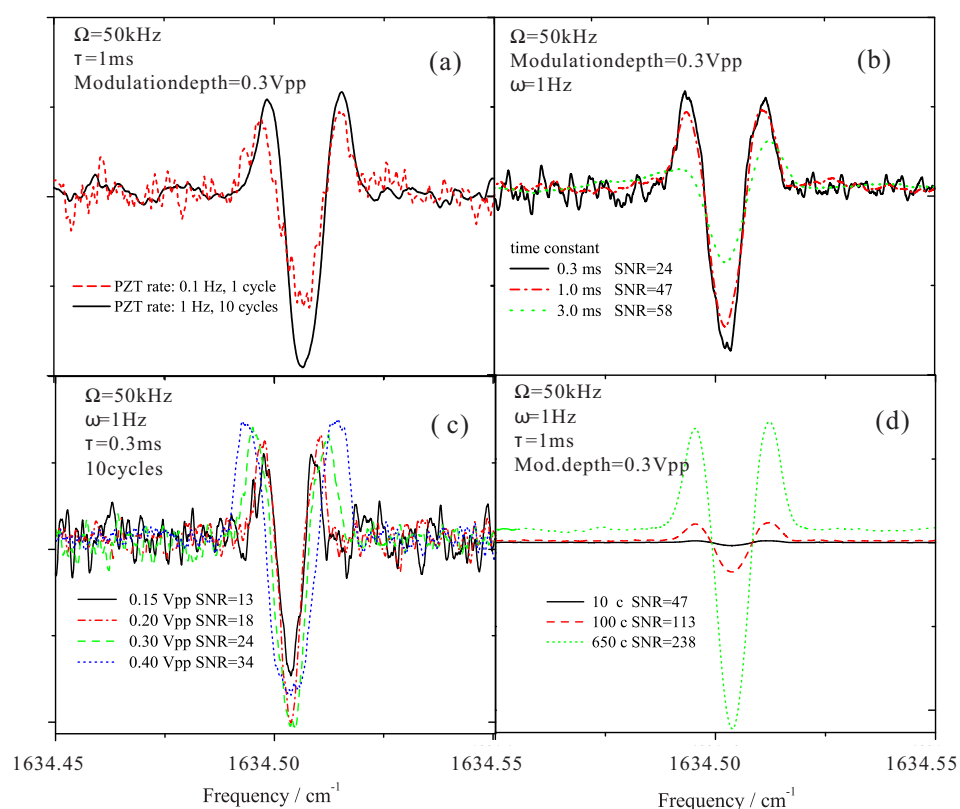


Figure 4.37: WLM spectra of N₂O measured with CEA spectrometer - WLM spectra of N₂O Q(10) line measured with different PZT rate, lock-in amplifier time constant, modulation depth, and cycle numbers.

As a large cycle number was needed to get decent SNR with CEA spectrometer, the data acquisition (DAQ) time was usually much longer than with MPA

spectrometer.

4.8.2 Jet-Cooled Complex

4.8.2.1 Methyl Lactate Measured with Distributed-Feedback QCL

To demonstrate the performance of the Distributed-Feedback QCL CEA spectrometer with a jet expansion, it was best to have a test molecule with its vibrational band origin in the frequency region of $1760\text{--}1766\text{ cm}^{-1}$ provided by the particular QCL. It was difficult to find an ideal candidate. The best candidate identified was methyl lactate ($\text{CH}_3\text{OCOCH}(\text{OH})\text{CH}_3$). Methyl lactate, an α -hydroxyester, had been characterized in the microwave region with a pulsed jet Fourier transform microwave spectrometer. (37) It is a model molecular to study delicate competition between intra- and inter-molecular hydrogen bonds in a chiral recognition process, using low resolution Fourier transform infrared spectroscopy. (228, 35) But no high resolution infrared spectrum was available for this molecule. To get an overview of the vibrational band of interest, a room temperature gas phase spectrum of was recorded with a Bomem DA8.002 spectrometer with the multi-pass sample cell was 0.3 m long and set for 4 passes. The sample pressure was 250 mTorr and the resolution was set at 0.0026 cm^{-1} . S-methyl lactate (97% purity, Acros) was used without further purification. The spectrum in the range from $1710\text{ to }1800\text{ cm}^{-1}$ is given in Fig. 4.38. The strong sharp lines were due to water vapor mostly in the evacuated spectrometer itself. These lines had an unusual shape, resembling a second derivative line shape because the background was taken at a lower resolution than the sample. There were some interference fringes from the cell windows, especially around 1780 cm^{-1} , with a period of about 1.2 cm^{-1} . No rotational structure was resolved, which was most likely due to the fact that there were many low lying vibrational excited states and the RT spectrum was too crowded for individual rovibrational lines to be resolved. The C=O stretching band origin was estimated to be $\sim 1754.4\text{ cm}^{-1}$.

To obtain a jet-cooled spectrum, methyl lactate was placed in a bubbler with a water jacket kept at a temperature of 12°C . The Argon carrier gas with a backing pressure of $200\text{--}600\text{ Torr}$ was forced through a molecular sieve inside the bubble. The molecular sieve was used to ensure that the vapour of methyl lactate was mixed efficiently with Ar to be brought to the nozzle. The infrared beam intercepted the jet expansion about 1.0 cm below the nozzle slit. With the rapid scan method, the repetition rate of the nozzle pulse was 5 Hz . Typical chamber

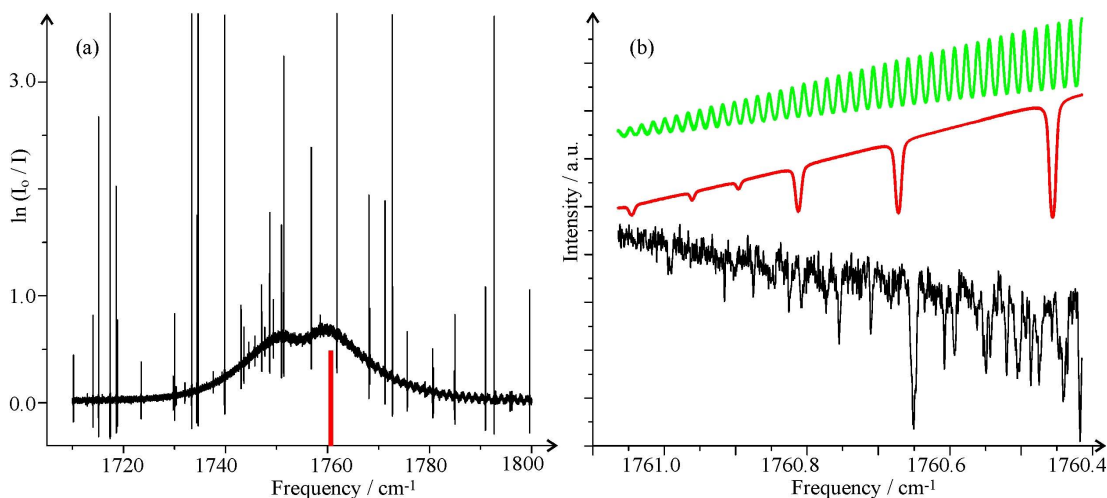


Figure 4.38: Room temperature and jet spectra of methyl lactate - (a) A room temperature gas phase spectrum of methyl lactate in the frequency region from 1710 to 1800 cm^{-1} . This is an absorbance plot on $\ln \frac{I_0}{I}$, where I is the spectrum with sample and I_0 is the background. The strong sharp lines are due to water vapor. The targeted frequency region for the laser experiments is indicated with a red stick. (b) A calibrated jet-cooled ro-vibrational spectrum of methyl lactate, together with the etalon and the reference scans.

pressures were less than 0.1 mTorr during the experiments. The rotational temperature achieved with such a jet expansion was estimated to be 2~5 K. (250) This meant that the ro-vibrational transitions in the 1760.4~1766.0 cm^{-1} region, about 6~12 cm^{-1} away from the band origin, would have diminishing intensity because these higher rovibrational levels were hardly populated at such a low rotational temperature. Indeed, no transitions were observed except at the low end of the frequency region with the temperature of the QCL at its highest. The jet-cooled molecular spectrum was obtained by subtracting the background, i.e. jet-off, spectrum recorded right before the jet expansion, from the jet-on spectrum. The etalon fringes and the reference lines of water and ammonia were recorded simultaneously. An example jet-cooled spectrum of methyl lactate is given in Fig. 4.38 (b), together with the etalon and the reference scans.

4.8.2.2 Ar-water Measured with External-Cavity QCL

Considering the low sensitivity of the CEA spectrometer with the External-Cavity QCL compared to the MPA spectrometer, it was not surprising that more cycles were needed to record the weak jet-cooled sample spectra with the CEA

4.8 Experimental Results with CEA Spectrometer

spectrometer. As discussed in Section 4.8.1.2, taking many cycles to average the transmission modes of the CEA cavity was also inherently required by the CEA spectroscopy. Fig. 4.39 shows the 1000-cycle rapid scan spectra of the Ar-*para*-water Q-branch, R(2) and R(3) line signal with PZT rate to be 100 Hz. Due to the many cycles of data acquisition needed, laser line broadening was severe. The rapid scan spectra line width was 0.002 cm^{-1} , which is twice as large as that in 1-shot jet-cooled spectra with MPA spectrometer. Using the WLM as described in the previous sections, WLM spectrum of R(2) line could be obtained with 1000-cycle data accumulation. Note that the modulation depth used here was $0.300\text{ V}_{\text{pp}}$, much larger than the typical value for jet-cooled sample in order to get a stronger signal. As found in the MPA spectrometer, the SNR obtained with the WLM method with $\omega = 1\text{ Hz}$ laser scan rate was slightly better than that obtained with $\omega = 100\text{ Hz}$ rapid scan method.

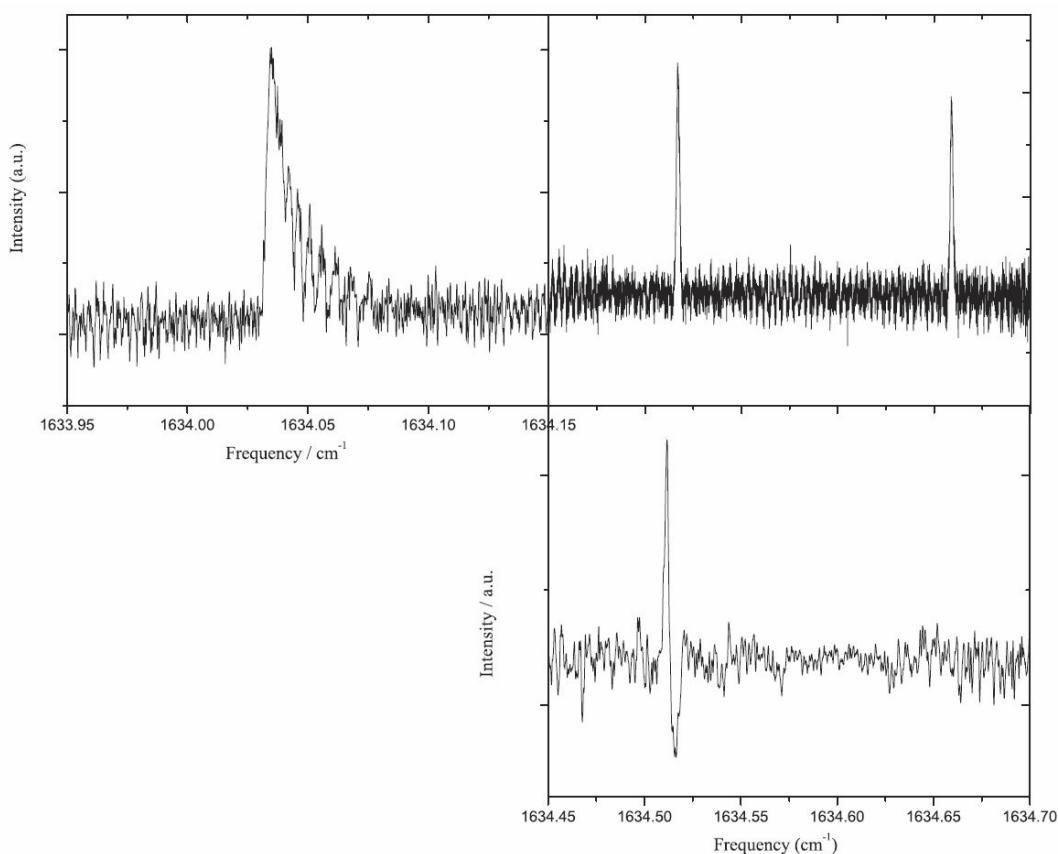


Figure 4.39: Rapid scan and WLM spectra of Ar-*para*-water - The spectra are measured with 1000 cycling from CEA spectrometer.

4.9 Conclusion

In this chapter, the design, construction, and evaluation of an off-axis CEA spectrometer and an astigmatic multi-pass absorption spectrometer based on a cw liquid nitrogen cooled Distributed-Feedback QCL and a cw room-temperature External-Cavity QCL for jet-cooled spectroscopic studies are reported. The External-Cavity QCL is more suitable for the high resolution IR spectroscopic measurement with its wide frequency coverage and mode-hop-free quality. Two LabVIEW computer programs are developed to automate the pulsed jet and fast static gas measurements. The slit jet CEA and MPA spectrometers are well studied to carry out high resolution infrared spectroscopic measurements of medium size organic molecules and complexes. In addition, the setup is robust, relatively easy to align and to maintain.

The sensitivity achieved was considerably better than that of a conventional direct absorption technique. With the Distributed-Feedback QCL, the minimum detection limit is $1.8 \times 10^{-8} \text{ cm}^{-1}$ from the CEA spectrometer. For the MPA spectrometer, the effective absorption path is 200 m. Using the External-Cavity QCL, the minimum detection limit is $3.56 \times 10^{-8} \text{ cm}^{-1}$, limited by the interference fringes that could not be satisfactorily removed by \sqrt{N} rule. Using the External-Cavity QCL, the effective absorption path is ~ 400 m for the CEA spectrometer and the minimum detection limit is $1.5 \times 10^{-6} \text{ cm}^{-1}$, limited by the incomplete averaging of the cavity transmission resonance. Therefore only one cycle is usually needed to get spectrum with decent SNR from MPA spectrometer while many cycles were needed from the CEA spectrometer. Such superior performance is also found by Menzel et al. (174), where although an effective absorption path of 670 m is achieved with on-axis CEAS configuration, the minimum detection limit is 1% of that from a corresponding MPA spectrometer with 100 m absorption path. For both cases, the SNR can be improved by increasing the QCL scan rate from 100 Hz to ~ 1 kHz, which limits the application of the External-Cavity QCL to achieve higher SNR. The laser line width is also minimized at high scan rate with typical value of 10 \sim 20 MHz. The laser line width is severely broadened to > 50 MHz when at scan rate lower than 1 Hz. The absorption line width of jet sample is 30 \sim 40 MHz. Wavelength modulation technique can generally improve the SNR of room temperature sample achieved by 2 \sim 6 times. When applying the WLM to supersonic jet sample, *pseudo-cw jet* method can be used to achieve slightly better SNR compared to rapid scan method. Rapid scan method combined with MPA spectrometer is most suitable for the high resolution spectroscopic study using

the EC-QCL in this study. Results based on this chapter have been published in Ref. (296, 140).

5

High Resolution Infrared Spectra of Binary Molecular Complexes of A Rare gas atom and Water or Ammonia

The binary complex of H₂O with a rare gas atom is the simplest molecular complex and a good starting point to study the rovibrational structures of molecular complexes containing H₂O molecules. In this chapter, high resolution infrared spectra of Ar-H₂O and Ne-H₂O are measured using the multipass direct absorption spectrometer based on the external cavity quantum cascade laser at 6 μm . This region is the ν_2 bending region of H₂O and the ν_4 bending region of NH₂. The rovibrational transitions of H₂O at 6 μm is given in Fig. 2.9. Under the supersonic free jet expansion condition, the $1_{11} \leftarrow 0_{00}$, $1_{10} \leftarrow 1_{01}$, and $2_{12} \leftarrow 1_{01}$ are the 3 strongest transitions since only the para- 0_{00} and the ortho- 1_{01} levels are significantly populated. This chapter describes the studies of these 3 transitions with the perturbation of a rare gas atom. Specifically, the high resolution infrared spectra of Ar-H₂O and Ne-H₂O complexes are measured, which can be viewed as the perturbed pure H₂O transitions based on the $1_{11} \leftarrow 0_{00}$, $1_{10} \leftarrow 1_{01}$, and $2_{12} \leftarrow 1_{01}$ lines. Preliminary study of the Ar/Ne-NH₃ complexes in the same region is also presented.

5.1 High Resolution Infrared Spectra of Ar-H₂O Complex

Ar-H₂O and Ne-H₂O complexes are prototypes to study weak interaction molecular complexes containing water. The study of Ar-H₂O complex is presented first. After introducing of the study of Ar-H₂O complex in Section 5.1.1, the measured spectrum of the Ar-H₂O complex is presented in Section 5.1.2. In the measured spectrum, five bands can be unambiguously assigned to the internal rotor states of the *ortho* Ar-H₂O spin modification. Information derived from these bands is presented in Section 5.1.3. There are several bands that cannot be unambiguously assigned and tentatively “labeled”. These bands are also presented in Section 5.1.2.3. The potential energy surface and the spectrum of the Ne-H₂O complex is very similar to the Ar-H₂O complex. The high resolution spectra of the Ne-H₂O complex is measured in the vicinity of the Ar-H₂O complex and preliminary analysis and fit of the spectrum is presented in Sec. 5.2.

5.1.1 Introduction

Water is a universal solvent. Due to its large polarity, water is a good solvent for ionic and polar substances. Water molecules in solution form a dynamic three-dimensional hydrogen-bond network, with each water molecule serving as the hydrogen bond donor and acceptor as well. When the hydrogen-bond network is disrupted by large non-polar solutes, the water molecules reorients to minimize the disruption and thus leads to a structured water “cage” around the self aggregating non-polar substances.(50) Such tendency of non-polar substances to aggregate in an aqueous medium is known as the hydrophobic effect, which is the main mechanism for biological processes such as membrane formation and protein folding.(153) Small non-polar molecules can dissolve in water. They are accommodated in the hydrogen-bond network of water introducing minor perturbations. The water molecules can reorganize near the small non-polar molecules without sacrificing hydrogen bonds. The density fluctuations in pure water and an enhanced structuring of water in the immediate vicinity of non-polar molecules leads to a large entropic cost of the solvation of small non-polar species in water and a consequently low solubility.(83, 219)

Noble gas has substantial solubility in water. At 20°C, the solubility of Xenon is 108 cm³/kg and that of Krypton is 60 cm³/kg. This decreases to 34 cm³/kg for

5.1 High Resolution Infrared Spectra of Ar-H₂O Complex

Argon, which is still substantially higher than hydrogen, nitrogen, carbon monoxide, methane, and is similar to oxygen.(67) One should note that Argon makes up 0.93% of the earth's atmosphere, making it the third most abundant gas after N₂ and O₂. The hyper-polarized noble gases are used as contrast agent in magnetic resonance imaging (MRI) of lung for distinction between hydrophobic and hydrophilic surfaces.(4) A molecular dynamic study(112) shows that reordering of the water molecules around the rare gas (Rg) atom leads to the non-polar hydration of noble gases in water and the hydrophobic entropy loss is mainly from the water orientation terms. Therefore, a molecular level understanding of the hydration of Rg atoms requires detailed knowledge of the multidimensional intermolecular PES of the binary complexes composed of a water molecule and a Rg atom. This is a prototypical model of hydrophobic interactions and is prerequisite to a clear understanding of more complicated interactions in biological systems.

5.1.1.1 Potential Energy Surface of the binary complex of a rare gas atom and water

Detailed knowledge on the interactions of rare gas atom with water is mainly from spectroscopic study and *ab initio* calculations. The Xe-H₂O(278) and Kr-H₂O(262) complexes were studied in the microwave region. The lowest ground states of these complexes were identified, from which the effective structures have been derived. The *ab initio* potential energy surfaces of the Rg-H₂O binary complexes(9, 157) show that the Xe-H₂O and Kr-H₂O complexes take the linear O-H...Rg hydrogen bond structure. For the Ar-H₂O complex, *ab initio* calculation shows that the PES gets more anisotropic as the weaker dispersion attraction reduce the barrier height. The Ar atom is no longer linearly bounded to the O-H bond in water but takes a slightly anti-hydrogen-bond position due to the subtle balance between the attractive and repulsive intermolecular forces.(9, 157) Experimentally, the Ar-H₂O complex has been extensively studied by far-IR,(53, 54, 248, 310, 56) microwave,(77, 86) near-IR(133, 187) and mid-IR(277, 266, 130) spectroscopy.

The information about the structure and dynamics of the complex can be extracted from the empirical PES derived from the spectroscopic data.(111, 55, 56) The most accurate one is the latest AW2 surface constructed by Cohen and Saykally.(58) It reveals a strong radial variation in the anisotropic interaction, which may be loosely described as variations in the position of the radial minimum

5.1 High Resolution Infrared Spectra of Ar-H₂O Complex

as a function of the relative orientation of the two subunits.(56) The geometry of the Ar-H₂O complex is shown in Fig. 5.1. Equilibrium configuration from the AW2 potential shows a planar structure with a distance from Ar atom to the center of mass of H₂O to be $R = 3.636 \text{ \AA}$ and the polar angle $\theta = 74.3^\circ$. The polar angle $\theta = 0^\circ$ corresponds to the C_{2v} geometry where the Ar points to the hydrogen atoms; $\theta = 180^\circ$ corresponds to Ar pointing to oxygen atom, and $\theta = 55^\circ$ corresponds to the linear O-H...Ar geometry. The floppy complex has two extended and shallow minima with a depth of 142.98 cm^{-1} on each side of the H₂O molecule. Barriers to in-plane rotation have been determined to be 26.29 cm^{-1} at $\theta = 0^\circ$ configuration (V_1) and 17.18 cm^{-1} at $\theta = 180^\circ$ configuration (V_2) from the AW2 surface. The empirical AW2 PES is shown in Fig. 5.2.

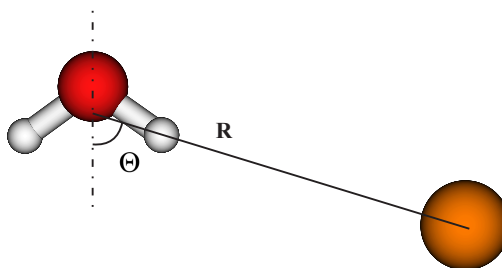


Figure 5.1: Geometry of the Ar-H₂O complex - The relative position of the Ar atom to the H₂O subunit is characterized by the distant from Ar atom to the center of mass of H₂O and the polar angle θ from the center of mass of H₂O to the Ar atom to the C_2 axis of H₂O.

The *ab initio* calculation of the PES of Ar-H₂O has been carried out by Bulski *et al.*,(44) Chalasinski *et al.*,(49) Tao *et al.*,(253) Hodges *et al.*,(104) and Makarewicz(157). Comparison of the *ab initio* PES with the empirical AW2 PES from spectroscopic data provides stringent test for the physics required to calculate the weak interaction between Ar atom and water. In the *ab initio* calculation of the Ar-H₂O PES performed by Chalański *et al.* using the second-order Møller-Plesset perturbation theory (MP2), although the radial anisotropy of the potential was qualitatively predicted, the potential was too flat and the binding energy was too low. Therefore, it was impossible to differentiate the hydrophobic anti-hydrogen bond structure ($\theta = 100^\circ$) with the hydrophilic hydrogen-bonded

5.1 High Resolution Infrared Spectra of Ar-H₂O Complex

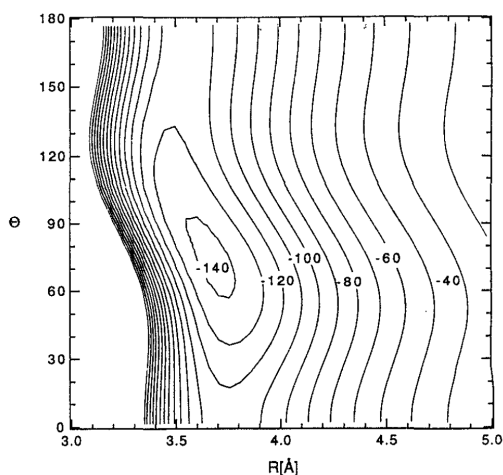


Figure 5.2: The AW2 Potential Energy Surface - This PES is from a fitting of the far-IR VRT spectroscopic data by Cohen and Saykally.

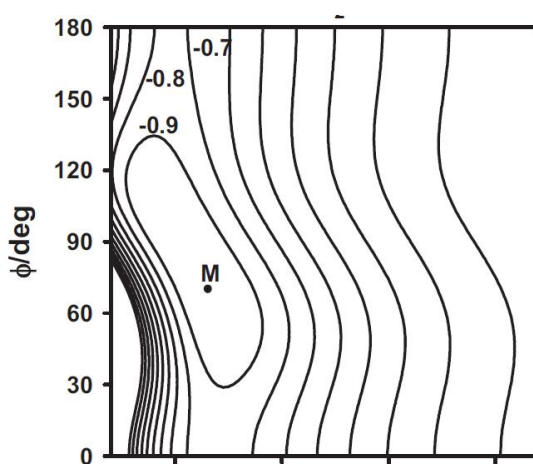


Figure 5.3: The *ab initio* Potential Energy Surface of Ar-H₂O - This PES taken from Ref. (157) is a highly accurate analytical Ar-H₂O PES on the CCSD(T)/CBS level of theory, which is so far the most accurate *ab initio* PES.

5.1 High Resolution Infrared Spectra of Ar-H₂O Complex

structure ($\theta = 80^\circ$).⁽⁴⁹⁾ Similar conclusion was found by the semi-empirical potential constructed by Bulski *et al.* which estimated the depth of the equilibrium configuration to be 129.5 cm^{-1} .⁽⁴⁴⁾ Tao *et al.* carried out a more accurate calculation of the Ar-H₂O potential on the MP4 level of theory.⁽²⁵³⁾ The equilibrium geometry was correctly predicted to be near linear hydrogen-bonded structure with $\theta = 75^\circ$, but the depth of the potential minimum was predicted 130.2 cm^{-1} , which is more than 10 cm^{-1} smaller than the value from the AW2 potential. The barriers to in-plane rotation was $V_1=22.6 \text{ cm}^{-1}$ and $V_2=26.6 \text{ cm}^{-1}$. Hodges *et al.* carried out a scaled perturbation theory study, in which the depth of the potential was correctly calculated to be 142.7 cm^{-1} and the barriers to the in-plane rotation $V_1=27.0 \text{ cm}^{-1}$ and $V_2=13.7 \text{ cm}^{-1}$. A parallel CCSD(T)/SP-AVQZ calculation showed the depth of potential to be 137.7 cm^{-1} with $V_1=21.3 \text{ cm}^{-1}$ and $V_2=26.3 \text{ cm}^{-1}$.⁽¹⁰⁴⁾ Makarewicz⁽¹⁵⁷⁾ constructed a highly accurate analytical Ar-H₂O PES on the CCSD(T)/CBS level of theory, which is so far the most accurate *ab initio* PES. The depth of the equilibrium geometry from this calculation is 141.8 cm^{-1} , which is very close to the experimental fitted value of 142.98 cm^{-1} from the AW2 potential. The barriers to the in-plane rotation are $V_1=20.5 \text{ cm}^{-1}$ and $V_2=26.4 \text{ cm}^{-1}$, which is consistent with the previous *ab initio* study and the PES of other Rg-H₂O systems such as Xe-H₂O, Kr-H₂O. Therefore, the author has suggested that the V_1 and V_2 barriers of the AW2 potential were mis-assigned from the fit. Clearly, a larger set of spectroscopic data is needed to construct a more accurate potential energy surface to test this statement. The high resolution rovibrational transitions would provide a stringent test for theoretical calculation of PES and rovibrational states, which is crucial to understand the structure and dynamic of the weakly-bonded molecular systems.

5.1.1.2 Nearly free internal rotor model of Ar-H₂O complex

With the flat minima and low barriers of the PES, the floppy weakly-bonded Ar-H₂O complex has large amplitude motions (LAM) which access portions of the PES far from the equilibrium.⁽¹⁴⁾ The bound states of the complex depend in a very sensitive way on the intermolecular PES. The bound “static” rovibrational states of such floppy PES are not “rigid” and the molecular structure cannot be derived from the semi-rigid rotor model based on a single deep minimum. “The canonical view of the molecular structure in terms of single deep minimum in the electronic potential energy surface, and the associated embedding of space- and body-fixed coordinate system through the Eckhart conditions, is entirely

5.1 High Resolution Infrared Spectra of Ar-H₂O Complex

abandoned.”(56) Measurement of the high resolution infrared spectrum of such complexes probe their rovibrational states which depend in a very sensitive way on the intermolecular PES.(188, 177, 178, 186, 185, 110) Separation of rotations and vibrations of such complexes is poor and there are usually strong rovibrational couplings.

Before introducing the nearly free internal rotor model, we briefly review the rotational structure of H₂O. The H₂O monomer is an asymmetric top with rotational constants $a=27.88\text{ cm}^{-1}$, $b=14.51\text{ cm}^{-1}$, $c=9.28\text{ cm}^{-1}$. Its rotational states are labeled by $J_{K_a K_c}$, in which K_a, K_c correlate to the K quantum numbers in the prolate and oblate limits. Because of its two equivalent hydrogen atoms ($I = \frac{1}{2}$), the H₂O molecule has two kinds of nuclear spin function by the Fermi-Dirac statistics which require that the total wave function be antisymmetric with respect to the exchange of two identical hydrogen atom. As a result, the antisymmetric state ($(-)^{K_a+K_c} = -1$, like 1_{01}) requires a symmetric spin function (*ortho* $I_H = 1$); and the symmetric ($(-)^{K_a+K_c} = +1$, like 0_{00}) state requires an antisymmetric spin function (*para* $I_H = 0$). An energy level diagram of H₂O is shown in Fig. 5.4.

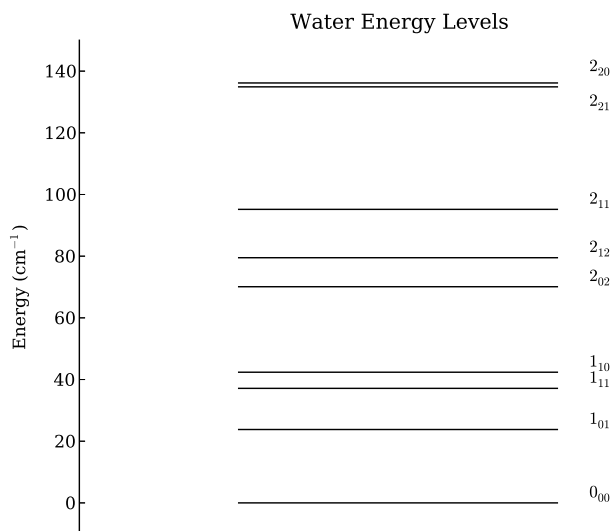


Figure 5.4: The lowest rotational energy levels of H₂O. - The $J = 0, 1, 2$ rotational energy levels are plotted. Values of the rotational energies are taken from Ref. (216).

The Hamiltonian of the nearly free internal rotor model has been introduced

5.1 High Resolution Infrared Spectra of Ar-H₂O Complex

in Sec. 2.4.4. The rovibrational energy levels of the floppy Ar-H₂O complex are best described by the nearly free internal rotor model suggested by Hutson.(111) The central assumption is that the interacting monomers are not significantly affected by the weak van der Waals forces, in words, separability of the angular and the radial coordinates. Therefore, analysis of the rotational term values of Ar-H₂O in terms of an asymmetric rotor formalism is inappropriate, and the rotational energy level structure of the molecule in this regime of anisotropy is better represented by a pseudo-diatomic molecule Hamiltonian. Therefore the rovibrational term values of Ar-H₂O is represented by a pseudo-diatomic molecule Hamiltonian:(54)

$$\begin{aligned}
 E_{vr} = & \quad G(\nu_{\text{H}_2\text{O}}) + G(\nu_{\text{vdW}}) + G(\nu_{j_{k_a k_c}}) \\
 & \quad + B[J(J+1) - K^2] \\
 & \quad - D[J(J+1) - K^2]^2 + H[J(J+1) - K^2]^3
 \end{aligned}
 \tag{5.1.1.1}$$

The pseudodiatomic rotational term to describe the end-over-end rotation of the complex is essentially the same as that of a linear polyatomic molecule. The $G(\nu_{\text{H}_2\text{O}})$ term represents the ‘‘intramolecular’’ vibration of the H₂O subunit and the $G(\nu_{\text{vdW}})$ term represents the ‘‘intermolecular’’ van der Waals stretching between the H₂O subunit and the Ar atom. The $G(\nu_{j_{k_a k_c}})$ term represents the nearly free internal rotation of the H₂O subunit in the complex, which is correlated to the free H₂O molecule rovibrational states and are labeled by the corresponding free H₂O rotational energy state $J_{K_a K_c}$. The anisotropy in the angular PES splits the degeneracy of the internal rotor states into $2j + 1$ components. The internal rotating H₂O subunit contributes an effective moment of inertia and a angular momentum component K along the intermolecular axis of the complex.(133) Therefore, the internal rotor states of the complex is further characterized by the magnitude of the projection of this angular momentum, labeled as $\Sigma, \Pi, \Delta, \dots$ states. The slightly anisotropic potential preserves the *ortho/para* nuclear spin classification of the H₂O subunit, i.e., the $\Sigma(0_{00})$ internal rotor state is *para* and the $\Sigma(1_{01})$ and $\Pi(1_{01})$ states are *ortho*. At the ~ 1 K temperature of the supersonic jet expansion, only levels within a few cm^{-1} of the lowest level of each nuclear spin symmetry are populated. Levels of different nuclear spin symmetries are not connected by optical or collisional transitions. Thus a typical notation of the energy state of the complex is *ortho*, $J = 5, v_2 = 1, \Pi(1_{10}), n = 0$, meaning the two identical hydrogen atom of the H₂O subunit are antisymmetric, the total angular momentum of the complex has 5 quanta, the H₂O subunit is excited on

5.1 High Resolution Infrared Spectra of Ar-H₂O Complex

its ν_2 mode by 1 quanta, and the van der Waals vibrational modes correlate to the 1_{10} state of the free H_2O rotation, whose projection on the intermolecular axis is ± 1 , and the intermolecular stretching van der Waals mode is excited by 1 quanta. The floppy nature of the potential transfers one rotational DOF to van der Waals vibrational DOF. See Fig. 5.5 for examples.

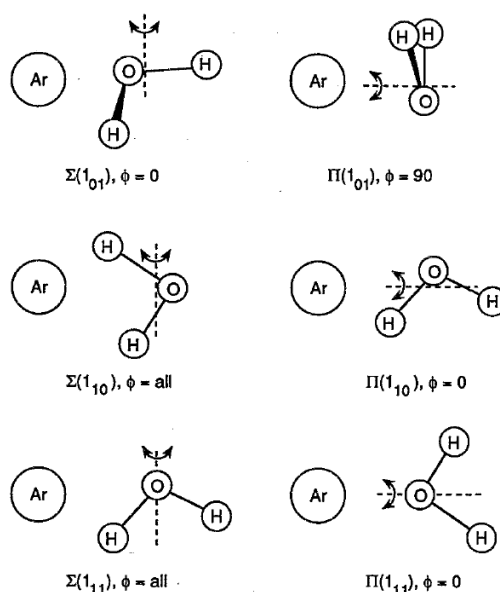


Figure 5.5: Classical depiction of the internal rotor states of Ar-H₂O - A pictorial representation of the $J = 1$ internal rotor states of Ar-H₂O, reproduced from Ref. (277).

Coriolis effects due to large amplitude nature of the H_2O internal rotation mix together states of the same internal rotor states, i.e., the same wave function $\Phi_{j k_a k_c}$. These Coriolis effects are the predominant cause of the K doubling of the nearly degenerate Π^e and Π^f states. A J dependent off-diagonal Coriolis coupling term $\beta[J(J+1)]^{1/2}$ that mix the Σ and Π states is introduced in the effective Hamiltonian:

$$\begin{bmatrix} H_{\Sigma} & H_{\text{Coriolis}} \\ H_{\text{Coriolis}} & H_{\Pi} \end{bmatrix} \quad (5.1.1.2)$$

It has been shown that for an internal rotor state dominated by $j = 1$, for example the (1_{01}) , (1_{10}) states, $\beta = 2B$; while for the $j = 2$ states, for example the (2_{12}) states, $\beta = 2\sqrt{3}B$.(56)

5.1 High Resolution Infrared Spectra of Ar-H₂O Complex

5.1.1.3 Previous Measurement

In the previous measurements on the vibrational ground state, the $\Sigma(0_{00})$ level of the *para* manifold is populated, since the lowest excited levels, i.e., the $n = 1, \Sigma(0_{00})$ and the $\Sigma(1_{11})$ states are 30-40 cm^{-1} higher in energy. Among the states of the *ortho* manifold, both the $\Sigma(1_{01})$ and the $\Pi(1_{01})$ levels are populated, which are $\sim 11 \text{ cm}^{-1}$ apart. The observed relative intensity of about 25:1 for the bands originating in these two levels is consistent with this estimation.

In the microwave region, the rotational spectra of the $\Sigma(0_{00})$, $\Sigma(1_{01})$, and $\Pi(1_{01})$ states of Ar-H₂O were first measured by Fraser *et al.*(77) Gernann and Gutowsky(86) later measured these transitions with higher resolution and analysed the H-H spin-spin hyperfine structures for Ar-H₂O and the nuclear quadrupole hyperfine structures for the Ar-D₂O and Ar-HDO isotopomers.

Coriolis coupling that mix the Σ and Π states of the same $\Phi_{j_k a k_c}$ have been observed in the internal rotor states first observed using far-IR vibration-rotation-tunneling (VRT) spectroscopy on the vibrational ground state of the H₂O subunit.(53, 54, 248, 310, 56) Transitions of the following bands have been measured for *ortho*-Ar-H₂O: $\Pi(1_{01}) \leftarrow \Sigma(1_{01})$, $\Pi(1_{10}) \leftarrow \Sigma(1_{01})$, $n = 1, \Sigma(1_{01}) \leftarrow \Sigma(1_{01})$, $n = 1, \Pi(1_{10}) \leftarrow \Sigma(1_{01})$, $\Sigma(2_{12}) \leftarrow \Sigma(1_{01})$, $\Pi(2_{12}) \leftarrow \Sigma(1_{01})$, $\Sigma(1_{10}) \leftarrow \Pi(1_{01})$. Also the following transitions had been measured for *para*-Ar-H₂O: $n = 1, \Sigma(0_{00}) \leftarrow \Sigma(0_{00})$, $\Pi(1_{11}) \leftarrow \Sigma(0_{00})$, $\Sigma(1_{11}) \leftarrow \Sigma(0_{00})$

In the near infrared region, the asymmetric $\nu_3=1$ excitation of the H₂O subunit has been observe by Lascola *et al.*(133) and Nesbitt *et al.*(187). For the *ortho* species, the $\nu_3=1, \Sigma(0_{00}) \leftarrow \Sigma(1_{01})$ and $\nu_3=1, \Sigma(0_{00}) \leftarrow \Pi(1_{01})$ bands have been measured.(133) For the *para* species, it has been shown that $\Pi(1_{01}) \leftarrow \Sigma(0_{00})$ band transitions suffer from avoided crossing with another vibrational level leading to the $\nu_1 = 1$ dissociation continuum.(187) In the same region, the *para* $\Pi(1_{01})$, $\Sigma(1_{01})$ states and the *ortho* $\Pi(2_{02})$, $\Sigma(2_{02})$, $\Sigma(0_{00})$ states have also been observed by helium nano-droplet spectroscopy.(130)

The $\nu_2=1$ bending excitation of the H₂O subunit has a transition moment lies along the C_{2v} symmetry axis of H₂O, thus the Ar-H₂O complex has strong mid-IR transitions corresponding to *b*-type transitions of H₂O monomer. These transitions were extensively studied by Weida and Nesbitt in the frequency region from 1595 cm^{-1} to 1626 cm^{-1} and 1631 cm^{-1} to 1640 cm^{-1} .(277) The $\Sigma(1_{01})$ and $\Pi(1_{01})$ states of *ortho* species and the $\Sigma(1_{11})$, $\Pi(1_{11})$, $n = 1, \Sigma(0_{00})$ levels of the *para* species have been accurately determined. Although the *ortho* transitions could be fitted by a Hamiltonian with Coriolis coupling terms mixing the Σ and

5.1 High Resolution Infrared Spectra of Ar-H₂O Complex

Π states of the same $\Phi_{j_{k_a k_c}}$, the satisfactory interpretation of the transitions of *para* species needed to introduce a J independent off-diagonal angular-radial coupling term to account for the Fermi interaction that couples states with different internal rotation states $j_{k_a k_c}$. These previously determined internal rotor states of the *ortho* and the *para* spin modification are shown in Fig. 5.6 and Fig. 5.7 respectively.

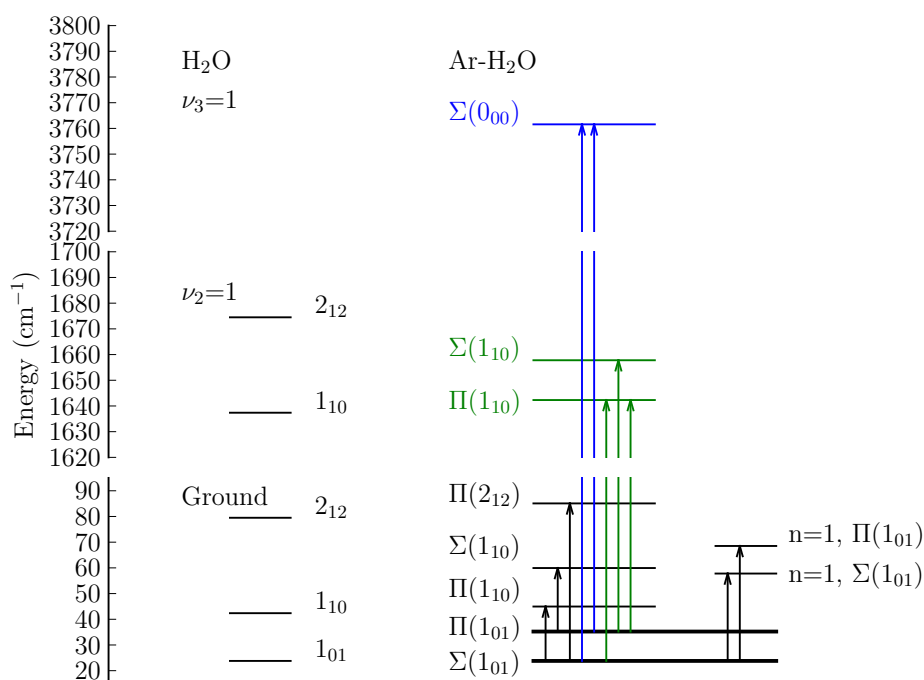


Figure 5.6: Internal rotor states of *ortho* Ar-H₂O complex. - Previously observed Ar-H₂O bands are determined from the microwave (thick black), far-IR (black), near-IR (blue), and mid-IR (green) measurements.

It should be noted that preliminary measurements of the $\nu_2=1$ bending excitation of *para* Ar-D₂O complex was reported by Stewart *et al.*(238, 239) and Li *et al.* assigned and analyzed the $\Sigma(1_{11}) \leftarrow \Sigma(0_{00})$, $\Pi(1_{11}) \leftarrow \Sigma(0_{00})$, and $\Pi(1_{10}) \leftarrow \Sigma(1_{01})$ bands of the Ar-D₂O complex in the 1190-1200 cm⁻¹ region.(139)

In the previous study,(277) the $n = 1, \Pi(1_{01}) \leftarrow \Sigma(1_{01})$ band was not observed around the predicted 1639.5 cm⁻¹ region. However, in our experiments using a quantum cascade laser at 6 μm , this band is measured exactly at the predicted

5.1 High Resolution Infrared Spectra of Ar-H₂O Complex

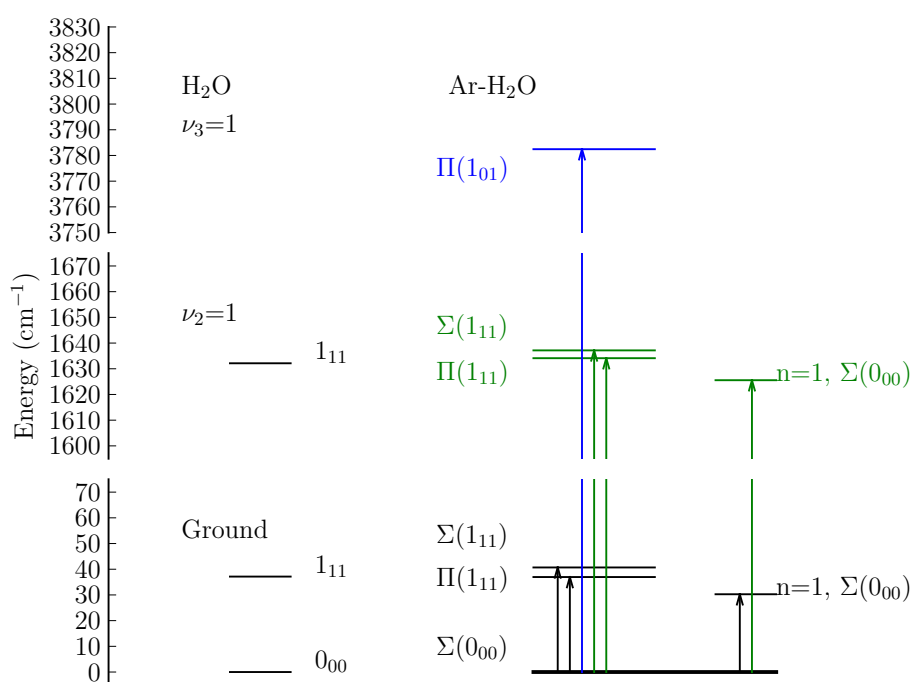


Figure 5.7: Internal rotor states of *para* Ar-H₂O complex. - Previously observed Ar-H₂O bands are determined from the microwave (thick black), far-IR (black), near-IR (blue), and mid-IR (green) measurements.

5.1 High Resolution Infrared Spectra of Ar-H₂O Complex

position. Recently, the $\Pi(2_{12}) \leftarrow \Sigma(1_{01})$ band was observed by Verdes *et al.* at 1658.03 cm^{-1} .(266) In the far-IR study, the $\Pi(2_{12})$ level has been shown to strongly mix with $n = 1, \Pi(1_{10})$ and $n = 2, \Pi(1_{01})$ levels. None of the perturbing states has been observed and only four lines in the $\Sigma(2_{12}) \leftarrow \Sigma(1_{01})$ band have been assigned. This leading to a non-satisfactory fit of the $\Sigma(2_{12})$ and $\Pi(2_{12})$ levels in the far-IR region.(56) We report our measurement of the bands of the $\Sigma(2_{12})$ and $\Pi(2_{12})$ levels in the $\nu_2=1$ region which could be satisfactorily fitted by the Hamiltonian with Coriolis coupling term. These new internal rotor levels are shown in Fig. 5.16.

The transitions of Ar-H₂O are prerequisite to perform supersonic jet expansion experiments of other water containing complexes. Our measurements extend the high resolution mid-IR data of the Ar-H₂O complex and provide more information about the structure and dynamic of this complex. It can shed new light on the understanding of the weak interaction intermolecular PES of this prototypical system.

5.1.2 Results and Discussion

To measure the high resolution mid-IR spectrum of Ar-H₂O complex, we use the pulsed slit-nozzle multipass direct absorption spectrometer with a quantum cascade laser (QCL) to investigate the frequency region of interest. The experimental setup was reported in details in Chapter 4. The Ar-H₂O complex is generated in a supersonic jet expansion with approximately 0.2% of H₂O and 3% of Ar in 8 Bar of Neon (Praxair) backing gas through a homemade 0.025 mm \times 40 mm slit-nozzle.

In total, ten new internal rotation bands related to new internal rotor states of Ar-H₂O are observed. The carrier of these bands can be confidently attributed to the Ar-H₂O complex based on the experimental condition employed to measure these bands and the distinct diatomic like band structure with unique B values about 0.1 cm^{-1} . The measurement is also aided by checking the bands of Ar-H₂O from the previous measurements by Weida and Nesbitt.(277) The lower level of these bands are from the $\Sigma(1_{01})$ or $\Pi(1_{01})$ states of the *ortho* Ar-H₂O or the $\Sigma(0_{00})$ level of the *para* Ar-H₂O, which are the low lying states populated in the supersonic jet expansion. First we consider the bands with the upper state unambiguously assigned by associating these new internal rotor states to those that have been observed in the far-IR region. The upper levels of these bands are unambiguously assigned to the Σ and Π levels of the (2_{12}) and $n = 1, (1_{01})$

5.1 High Resolution Infrared Spectra of Ar-H₂O Complex

states. The upper levels of the other new bands are ambiguous. They have not been measured in the far-IR region and cannot be properly associated to internal rotor states that correlates to H₂O rotational states. We tentatively “label” these states to the Σ and Π levels of the $n = 1, (2_{12})$ and $n = 1, (1_{10})$ states.

5.1.2.1 $n = 1, (1_{01})$ states

According to the previous study, the van der Waals excitation level, i.e. the $n = 1, \Sigma(1_{01}) \leftarrow \Sigma(1_{01})$ and $n = 1, \Pi(1_{01}) \leftarrow \Sigma(1_{01})$ transitions were not found, which are predicted around 1629 cm^{-1} and 1639.5 cm^{-1} , respectively.(277) In our experiments with the QCL spectrometer, we observe a weak band precisely at this position next to the $\Sigma(1_{11}) \leftarrow \Sigma(0_{00})$ band that has been previously measured. The spectrum of this band is shown in Fig. 5.8, which is a typical $\Pi \leftarrow \Sigma$ band with strong Q -branch and presence of $R(0)$ transition and absence of $P(1)$ transition. The position of this band is almost the same as the prediction from the far-IR data, which makes the assignment of this band to the $n = 1, \Pi(1_{01}) \leftarrow \Sigma(1_{01})$ unambiguous. This means that the $n = 1, \Pi(1_{01})$ internal rotor state is not significantly affected by the high frequency H₂O bending vibration.

The same assumption can be applied to the $n = 1, \Sigma(1_{01})$ state. At the predicted 1629 cm^{-1} region, a rich array of spectral feature as shown in Fig. 5.9 is observed. Besides several unassigned transitions between 1628.5 cm^{-1} and 1629.5 cm^{-1} , we can identify a $\Sigma \leftarrow \Sigma$ band at 1629.3 cm^{-1} in addition to two $\Pi \leftarrow \Sigma$ bands around 1630 cm^{-1} . The assignment of the two $\Pi \leftarrow \Sigma$ bands at 1630 cm^{-1} are ambiguous and we tentatively *labeled* them to “ $n = 1, \Pi^{1,2}(1_{10})$ ” states. But the $\Sigma \leftarrow \Sigma$ band at 1629.3 cm^{-1} can be unambiguously assigned to the van der Waals stretching $n = 1, \Sigma(1_{01}) \leftarrow \Sigma(1_{01})$ band based on the fact that the position of this band can be perfectly predicted from the internal rotor state determined from far-IR region. Transition frequencies and the residuals from least square fit of the $n = 1, \Sigma(1_{01}) \leftarrow \Sigma(1_{01})$ and $n = 1, \Pi(1_{01}) \leftarrow \Sigma(1_{01})$ bands are listed in Table 5.1.

Further characterization of these bands can be accessed by checking the $n = 1, \Pi(1_{01}) \leftarrow \Pi(1_{01})$ and $n = 1, \Sigma(1_{01}) \leftarrow \Pi(1_{01})$ bands, which are predicted around 1628 cm^{-1} and 1618 cm^{-1} . The doublet high J transitions of the R -branch of the former band might extend to the 1628.5 cm^{-1} region that account for the unassigned lines in Fig. 5.9. Since these bands are from the less populated $\Pi(1_{01})$ level, their intensity are weak under the jet-cooled condition. Therefore, these bands have not been observed in the far-IR region.

5.1 High Resolution Infrared Spectra of Ar-H₂O Complex

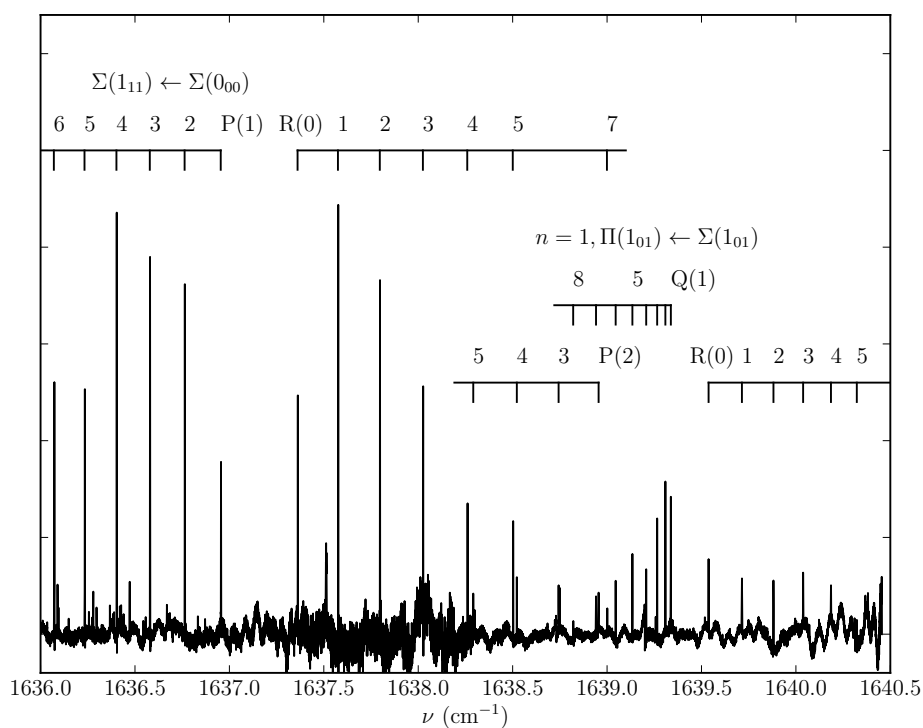


Figure 5.8: The $n = 1, \Pi(1_{01}) \leftarrow \Sigma(1_{01})$ band of *ortho* Ar-H₂O - This band was missing from the previous measurement. We observe this band at the expected position next to the $\Sigma(1_{11}) \leftarrow \Sigma(0_{00})$ band of *para* Ar-H₂O.

5.1 High Resolution Infrared Spectra of Ar-H₂O Complex

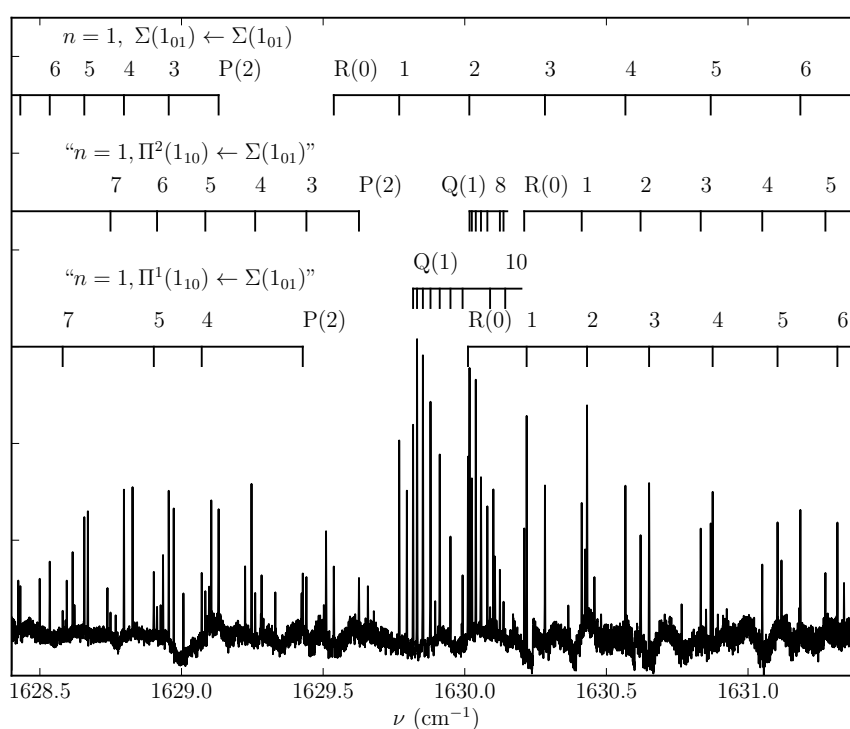


Figure 5.9: The complicated spectral feature of Ar-H₂O at 1630 cm⁻¹
 - The spectral features are from $n = 1, \Sigma(1_{01}) \leftarrow \Sigma(1_{01})$ band, together with two overlapping $\Pi \leftarrow \Sigma$ bands around 1630 cm⁻¹. The $n = 1, \Sigma(1_{01}) \leftarrow \Sigma(1_{01})$ can be unambiguously assigned. The upper states of the two $\Pi \leftarrow \Sigma$ bands are tentatively labeled to the “ $n = 1, \Pi^{1,2}(1_{10})$ ” states. The unassigned transitions red to 1629.0 cm⁻¹ are probably high J transitions of the $n = 1, \Pi(1_{01}) \leftarrow \Pi(1_{01})$ band.

5.1 High Resolution Infrared Spectra of Ar-H₂O Complex

$J' \leftarrow J''$	$n = 1, \Sigma(1_{01}) \leftarrow \Sigma(1_{01})$	$n = 1, \Pi(1_{01}) \leftarrow \Sigma(1_{01})$
0 \leftarrow 1	1629.1310(4)	
1 \leftarrow 2	1628.9548(0)	1638.9552(3)
2 \leftarrow 3	1628.7968(3)	1638.7433(4)
3 \leftarrow 4	1628.6568(4)	1638.5221(2)
4 \leftarrow 5	1628.5348(3)	1638.2914(1)
5 \leftarrow 6	1628.4309(16)	
1 \leftarrow 1		1639.3378(1)
2 \leftarrow 2		1639.3088(2)
3 \leftarrow 3		1639.2653(3)
4 \leftarrow 4		1639.2072(1)
5 \leftarrow 5		1639.1341(1)
6 \leftarrow 6		1639.0455(1)
7 \leftarrow 7		1638.9415(3)
8 \leftarrow 8		1638.8205(2)
1 \leftarrow 0	1629.5377(0)	1639.5376(1)
2 \leftarrow 1	1629.7686(10)	1639.7141(1)
3 \leftarrow 2	1630.0161(4)	1639.8811(0)
4 \leftarrow 3	1630.2831(9)	1640.0382(3)
5 \leftarrow 4	1630.5671(3)	1640.1856(1)
6 \leftarrow 5	1630.8683(1)	1640.3225(1)
7 \leftarrow 6	1631.1848(7)	
8 \leftarrow 7	1631.5089(2)	

Table 5.1: Observed *ortho* ArH₂O transitions of the $n = 1, (1_{01})$ internal rotor states (in cm⁻¹). Residuals (observed-predicted) from least squares fit in least significant digit.

5.1 High Resolution Infrared Spectra of Ar-H₂O Complex

5.1.2.2 (2₁₂) states

The 2₁₂ ← 1₀₁ transition of water monomer is at 55.702 cm⁻¹ on the vibrational ground state and at 1653.267 cm⁻¹ with the $\nu_2 = 1$ excitation in the mid-IR region. In the previous far-IR measurement, Cohen *et al.* were able to record the $\Pi(2_{12}) \leftarrow \Sigma(1_{10})$ and the $\Sigma(2_{12}) \leftarrow \Sigma(1_{01})$ band.(56) Unlike the $j = 1$ levels, analysing and fitting of these bands proved difficult, indicating strong mixing of these levels with probably $n = 1, \Pi(1_{10}), n = 2, \Pi(1_{01})$ or other internal rotor states. But none of these perturbing states has been observed and only 4 lines in the $\Sigma(2_{12}) \leftarrow \Sigma(1_{01})$ band had been assigned.

In our search of the (2₁₂) internal rotor states, we first observe a band structure at 1646.5 cm⁻¹ which is shown in Fig. 5.10. Clearly, this is a $\Pi \leftarrow \Pi$ band with a weak Q -branch and strong P and R -branches starting from $R(1)$ and $P(2)$ respectively. All the transitions are split to doublets due to the doubling of the degenerated Π states in both the upper and lower levels. This band is unambiguously assigned to the $\Pi(2_{12}) \leftarrow \Pi(1_{01})$ band.

Since the other ground state of the *ortho* species, the $\Sigma(1_{01})$ state, is 11.5 cm⁻¹ lower than the $\Pi(1_{01})$ state, we expect to observe the $\Pi(2_{12}) \leftarrow \Sigma(1_{01})$ band that with the same upper state as the $\Pi(2_{12}) \leftarrow \Pi(1_{01})$ band to be 11.5 cm⁻¹ to the blue. A typical $\Pi \leftarrow \Sigma$ band with a strong Q branch is readily observed at 1658 cm⁻¹, which is unambiguously assigned to the $\Pi(2_{12}) \leftarrow \Sigma(1_{01})$ band. As can be seen from the spectrum shown in Fig. 5.11, the P and R -branches are severely perturbed, which are associated with the $\Pi(2_{12})$ level mixed with the $\Sigma(2_{12})$ level through Coriolis coupling. To determine the position of the $\Sigma(2_{12})$ level, the e and f symmetry level of the $\Pi(2_{12})$ state were preliminarily fit as two distinct levels with different band origins. It turned out that the perturbed e symmetry $\Pi(2_{12})$ level is higher than the f symmetry one. Therefore, the perturbing $\Sigma(2_{12})$ state should be lower than the $\Pi(2_{12})$ levels. This is in agreement with the far-infrared observation that the $\Sigma(2_{12})$ level is around 6.5 cm⁻¹ lower in energy than the $\Pi(2_{12})$ level.(56) Around 6.5 cm⁻¹ to the lower frequency side of the $\Pi(2_{12}) \leftarrow \Sigma(1_{01})$ band, we observe a typical $\Sigma \leftarrow \Sigma$ band at 1652 cm⁻¹ with similar intensity. The spectrum of the $\Sigma \leftarrow \Sigma$ band is shown in Fig. 5.12, which is unambiguously assigned to the $\Sigma(2_{12}) \leftarrow \Sigma(1_{01})$ band. Transition frequencies and the residuals from least square fit of the $\Sigma(2_{12}) \leftarrow \Sigma(1_{01})$, $\Pi(2_{12}) \leftarrow \Sigma(1_{01})$ and $\Pi(1_{01}) \leftarrow \Pi(1_{01})$ bands are listed in Table 5.2.

5.1 High Resolution Infrared Spectra of Ar-H₂O Complex

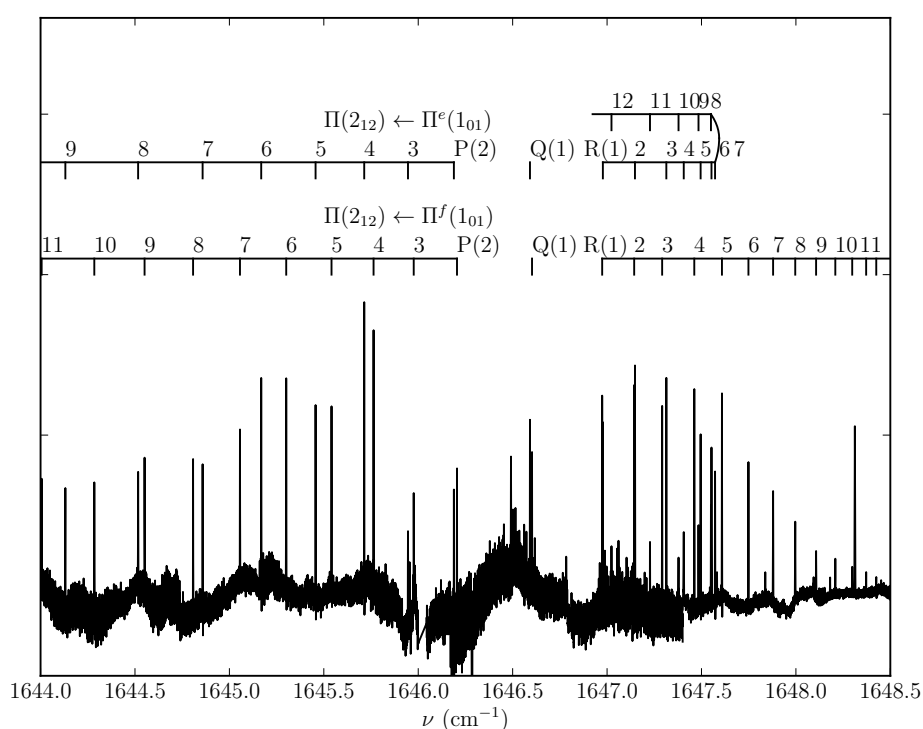


Figure 5.10: The $\Pi(2_{12}) \leftarrow \Pi(1_{01})$ band - With a weak Q -branch, strong P and R -branches starting from $R(1)$ and $P(2)$ and doublet structure, this band can be identified as a $\Pi \leftarrow \Pi$ band. Although this band was not measured in the far-IR region, ground state combination differences confirm the assignment.

5.1 High Resolution Infrared Spectra of Ar-H₂O Complex

$J' \leftarrow J''$	$\Sigma(2_{12}) \leftarrow \Sigma(1_{01})$	$\Pi(2_{12}) \leftarrow \Sigma(1_{01})$	$\Pi(2_{12}) \leftarrow \Pi^f(1_{01})$	$\Pi(2_{12}) \leftarrow \Pi^e(1_{01})$
0 \leftarrow 1	1652.2273(5)			
1 \leftarrow 2	1651.9959(11)	1657.5461(11)	1646.2053(3)	1646.1888(2)
2 \leftarrow 3	1651.7329(7)	1657.3481(5)	1645.9761(150)	1645.9458(151)
3 \leftarrow 4	1651.4334(5)	1657.1441(20)	1645.7634(56)	1645.7140(40)
4 \leftarrow 5	1651.1047(4)	1656.9294(28)	1645.5408(16)	1645.4564(1)
5 \leftarrow 6	1650.7456(3)	1656.6970(3)	1645.3009(10)	1645.1685(34)
6 \leftarrow 7	1650.3593(2)	1656.4469(2)	1645.0560(16)	1644.8582(15)
7 \leftarrow 8	1649.9489(4)	1656.1743(10)	1644.8077(14)	1644.5166(13)
8 \leftarrow 9	1649.5172(5)	1655.8736(32)	1644.5508(29)	1644.1313(36)
9 \leftarrow 10	1649.0640(9)	1655.5347(4)	1644.2846(23)	1643.7229(77)
10 \leftarrow 11	1648.5868(20)		1644.0057(32)	
11 \leftarrow 12	1648.0938(6)			
1 \leftarrow 1		1657.9326(10)	1646.6026(2)	1646.5917(2)
2 \leftarrow 2		1657.9208(13)		
3 \leftarrow 3		1657.9031(14)		
4 \leftarrow 4		1657.8793(12)		
5 \leftarrow 5		1657.8495(7)		
6 \leftarrow 6		1657.8144(6)		
7 \leftarrow 7		1657.7736(6)		
8 \leftarrow 8		1657.7264(3)		
9 \leftarrow 9		1657.6719(3)		
10 \leftarrow 10		1657.6099(6)		
11 \leftarrow 11		1657.5391(3)		
12 \leftarrow 12		1657.4573(3)		
13 \leftarrow 13		1657.3623(14)		
14 \leftarrow 14		1657.2488(6)		
1 \leftarrow 0		1658.1308(8)		
2 \leftarrow 1	1652.7040(7)	1658.3201(13)	1646.9741(12)	1646.9778(14)
3 \leftarrow 2	1652.7940(8)	1658.5054(41)	1647.1436(27)	1647.1477(50)
4 \leftarrow 3	1652.8511(1)	1658.6745(8)	1647.2917(172)	1647.3139(270)
5 \leftarrow 4	1652.8792(14)	1658.8325(15)	1647.4619(13)	1647.4061(8)
6 \leftarrow 5	1652.8792(4)	1658.9685(3)	1647.6084(9)	1647.4954(26)
7 \leftarrow 6	1652.8562(3)	1659.0806(3)	1647.7486(13)	1647.5529(27)
8 \leftarrow 7	1652.8094(3)	1659.1654(25)	1647.8792(23)	1647.5719(35)
9 \leftarrow 8	1652.7405(7)	1659.2156(38)	1647.9965(13)	1647.5501(38)
10 \leftarrow 9	1652.6488(1)	1659.2284(39)	1648.1069(22)	1647.4842(48)
11 \leftarrow 10		1659.2024(31)	1648.2087(8)	1647.3784(10)

5.1 High Resolution Infrared Spectra of Ar-H₂O Complex

12 ← 11	1659.1362(8)	1648.2982(6)	1647.2273(23)
13 ← 12	1659.0315(14)	1648.3720(10)	1647.0233(30)
14 ← 13	1658.8926(10)	1648.4255(18)	
15 ← 14	1658.7165(63)		

Table 5.2: Observed *ortho* Ar-H₂O transitions of the (2₁₂) internal rotor states (in cm⁻¹). Residuals (observed-predicted) from least squares fit in least significant digit.

We failed to observe the corresponding $\Sigma(2_{12}) \leftarrow \Pi(1_{01})$ band, which should be at 1641 cm⁻¹ from the combination difference analysis. The $\Pi(2_{12}) \leftarrow \Pi(1_{01})$ band is observed at 1646.5 cm⁻¹.

The $\Sigma(2_{12})$ and $\Pi(2_{12})$ internal rotor states which were determined can be satisfactorily analysed using a Hamiltonian with Coriolis coupling term mixing the Σ and Π levels with the same $\Phi_{j k_a k_c}$. This is in contrast to the far-IR measurements in which additional fitting parameters were used to achieve a satisfactory fit.(56)

Fitting of the rovibrational transitions is performed with Pickett’s CALPGM/SPFIT program(202). The AABS software package for Assignment and Analysis of Broadband Spectra(124, 3) is used to aid the assignment and fitting of the spectrum. A global fit is performed to include the current measurement with the previous measurements of the microwave(77, 86), far-infrared(53, 54, 56), near-infrared(133, 187), and previous mid-infrared data(277) to fit the (2₁₂) and $n = 1, (1_{01})$ bands to the pseudodiatomic Hamiltonian with Coriolis coupling terms mixing the Σ and Π levels. Since these Coriolis effects vanish for $J = 0$, the origins and B rotational constants are constrained to be equal for the e and f symmetry states in the spectroscopic fitting procedure while the higher-order centrifugal distortion constants D and H are allowed to vary independently to account for any additional couplings that are not included in the effective Hamiltonian. We note that the previous measurement of the far-infrared transitions indicates that the $\Sigma(2_{12})$ and $\Pi(2_{12})$ levels are affected by strong Coriolis coupling and lead to large error in the fit, so in our analysis of the *ortho* transitions, the $\Sigma(2_{12})$ and $\Pi(2_{12})$ levels are not included. The transitions are weighted according to the square reciprocal of the experimental uncertainty: 5 kHz for the microwave data, 0.7 MHz for the far-IR measurements, 0.0005 cm⁻¹ for the near-IR data, 0.00025 cm⁻¹ for the previous mid-IR measurements and 0.001 cm⁻¹ for our current measurements. In total, 423 transitions are included in the fit. The input

5.1 High Resolution Infrared Spectra of Ar-H₂O Complex

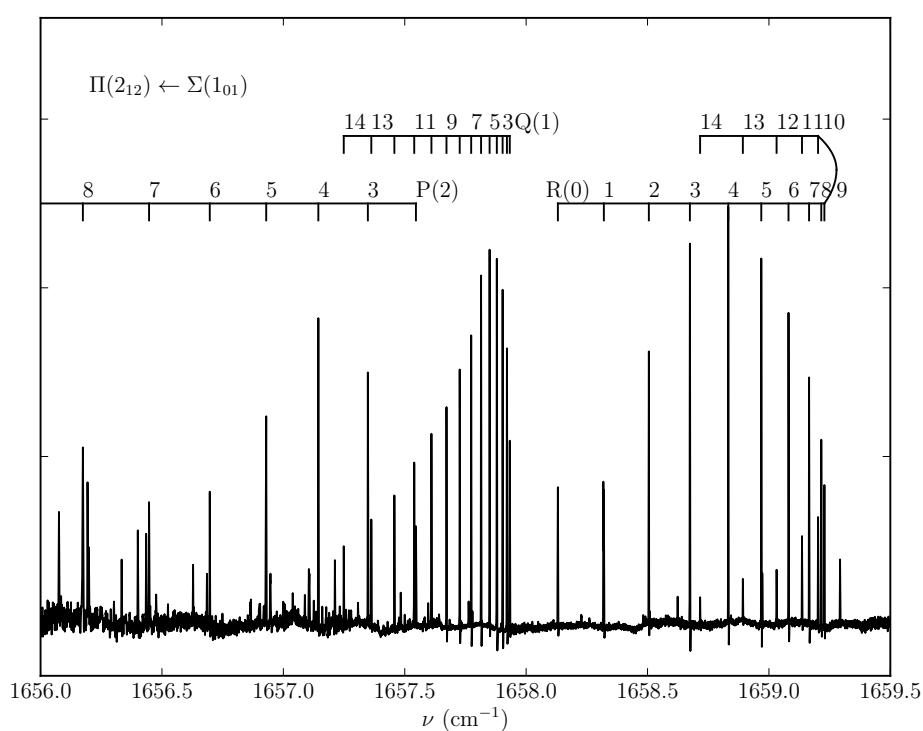


Figure 5.11: The $\Pi(2_{12}) \leftarrow \Sigma(1_{01})$ band - This is a typical $\Pi \leftarrow \Sigma$ band with strong Q -branch and absence of $P(1)$ transition. Position of this band is close to that measured in the far-IR region with H₂O subunit in its vibrational ground state.

5.1 High Resolution Infrared Spectra of Ar-H₂O Complex

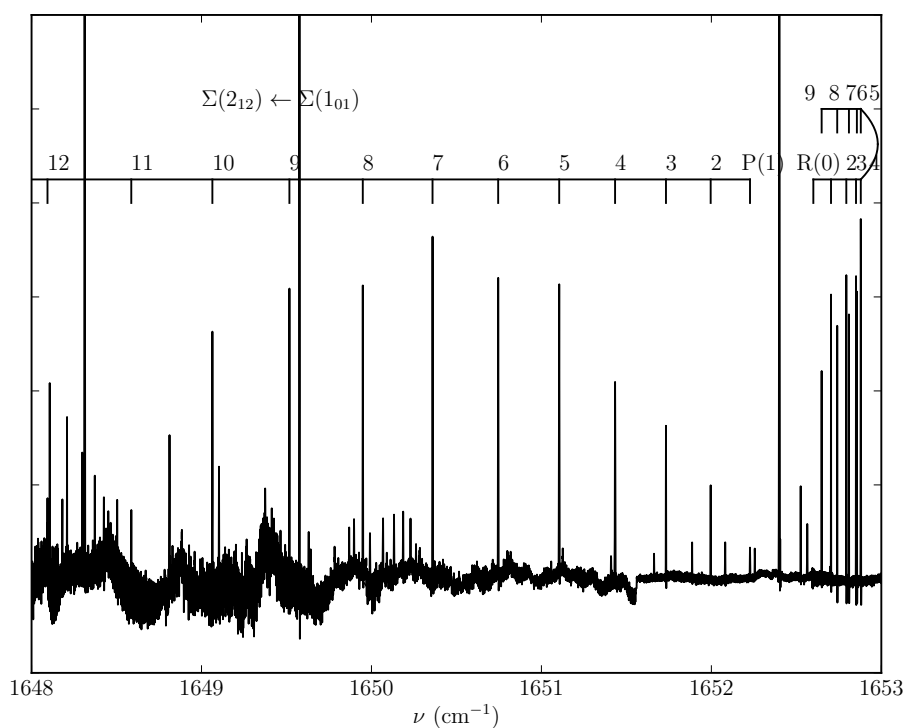


Figure 5.12: The $\Sigma(2_{12}) \leftarrow \Sigma(1_{01})$ band - This band was measured in the far-IR region, but only 4 lines were assigned. The condensed *R*-branch is due to large difference between the perturbed upper and lower state rotational energy levels.

5.1 High Resolution Infrared Spectra of Ar-H₂O Complex

.lin and .par files for the SPFIT program are included in appendix Section 2.5.4. The root-mean-square (RMS) error of the microwave and far-IR transitions is 0.6 MHz and the RMS error is 0.003 cm⁻¹ for the infrared data, which is consistent with experimental uncertainty. The fitted spectroscopic constants are listed in Table 5.3.

5.1.2.3 Ambiguous bands

In addition to the bands associated with the $\Sigma(2_{12})$, $\Pi(2_{12})$, $n = 1, \Sigma(1_{01})$, $n = 1, \Pi(1_{01})$ states that are unambiguously determined, there are at least 5 additional bands observed in our measurements that can also be attributed to the Ar-H₂O complex. An example of the unassigned bands is shown in Fig. 5.9. The two $\Pi \leftarrow \Sigma$ bands overlapping around 1630 cm⁻¹ can be identified and the distinct P , Q , R -branches can be assigned. They can be successfully fit as other unambiguously assigned Ar-H₂O bands to clearly determined two Π levels with B rotational constants very close to the other internal rotor state. These two Π levels are just 1 cm⁻¹ to the blue of the $n = 1, \Sigma(1_{01})$ level, yet they were not reported by the far-IR measurements and cannot be properly associated to any internal rotor states of the Ar-H₂O complex. We tentatively *labeled* these two levels as “ $n = 1, \Pi^2(1_{10})$ ”. It should be noted that these two $\Pi \leftarrow \Sigma$ bands structure are also observed in the spectrum of Ar-D₂O complex in the D₂O bending region at 1192 cm⁻¹ with a continuous-wave cavity ring-down spectrometer (cw-CRDS) using a similar quantum cascade laser (QCL) light source.(238, 239) Therefore, elucidation of these bands would be crucial to understand the spectra of both Ar-H₂O and Ar-D₂O.

In total, five unassigned bands are tentatively *labeled* to the “ $n = 1, (1_{10})$ ” and “ $n = 1, (2_{12})$ ” states of the *ortho* species and the “ $n = 1, \Pi(1_{11})$ ” state of the *para* species. Carrier of these bands can be confidently attribute to the Ar-H₂O complex, because in the global fit including these transitions the rotational constants determined for the upper states are very close to the other unambiguously assigned internal rotor states. But assignment of these bands cannot be made, because the upper states of these bands cannot be properly associated to the rotational energy levels of the nearly free rotating H₂O subunit. Therefore, they are only tentatively *labeled* to the “ $n = 1, (1_{10})$ ” and “ $n = 1, (2_{12})$ ” states of the *ortho* species and the “ $n = 1, \Pi(1_{11})$ ” state of the *para* species. We assume there is strong coupling between the high frequency H₂O vibration and low frequency

5.1 High Resolution Infrared Spectra of Ar-H₂O Complex

	$\nu(\text{cm}^{-1})$	$B(\text{MHz})$	$D(\text{kHz})$	$H(\text{Hz})$	$\beta(\text{MHz})$
Ground					
$\Sigma^e(1_{01})$		3014.788(28)	72.637(27)	1.341(98)	
$\Pi_f^e(1_{01})$	11.428610(73)	2951.956(50)	115.84(75) 135.67(25)	4.9(35) 0 ^a	5901.65(78)
$\Sigma^f(1_{10})$	36.145679(73)	2953.247(44)	112.32(57)	-21.7(21)	
$\Pi_e^f(1_{10})$	21.162294(9)	3037.5951(90)	51.327(97) 60.379(71)	-12.55(24) -21.43(15)	5762.31(42)
$\Pi_f^e(2_{12})$	61.3(16)	3184(9711) 2821(2564)	0 ^a 0 ^a	0 ^a 0 ^a	
Ground, $n=1$					
$\Sigma^e(1_{01})$	33.998168(15)	2731.055(47)	115.5(11)	-32.0(68)	
$\Pi^f(1_{01})$	44.728064(19)	2693.965(35)	149.44(44)	-10.1(14)	
$v_3=1$					
$\Sigma^e(0_{00})$	3737.8070(2)	2975.21(40)	68.3(64)	-136(27)	
$v_2=1$					
$\Sigma^f(1_{10})$	1633.9962(2)	2951.66(34)	118.4(54)	-49(24)	
$\Pi_f^e(1_{10})$	1618.5117(1)	3033.16(11)	64.9(12) 57.3(14)	-26.7(35) -7.5(39)	5667(5)
$\Sigma^e(2_{12})$	1652.4213(7)	2422.6(19)	-727(32)	-1798(166)	
$\Pi_f^e(2_{12})$	1658.0307(6)	2831.03(55)	1593(15) 142.3(29)	2569(55) 0 ^a	2799(30)
$v_2=1, n=1$					
$\Sigma^e(1_{01})$	1629.3257(7)	3259.7(42)	-413(134)	-4640(1280)	
$\Pi_f^e(1_{01})$	1639.4422(6)	2696.2(16)	345(71) 140(24)	0 ^a 0 ^a	4985(66)

^a Zero within uncertainty, and set to zero in final fit.

Table 5.3: Fitted spectroscopic constants from a global fit of the previously measured data with the unambiguously determined (2₁₂) and $n = 1, (1_{01})$ bands from current measurement. Uncertainties (1σ) from least squares fit is in least significant digit.

5.1 High Resolution Infrared Spectra of Ar-H₂O Complex

internal rotation and the van der Waals stretching of the complex that combination states of these vibrational modes are completely shifted from the sum of the individual term values corresponding to the corresponding internal rotor states on the vibrational ground state of H₂O in the far-IR region. The energy of these states cannot be properly associated with the rotational energy levels of the free rotating water molecule. These internal rotor states have not been observed on the vibrational ground state of H₂O in the far-IR measurements. Transition frequencies of these unassigned bands are listed in Table 5.4 and Table 5.5.

The two overlapping $\Pi \leftarrow \Sigma$ bands observed around 1630 cm⁻¹ are shown in Fig. 5.9. Therefore, the upper level of these two bands must be two Π states around 1630 cm⁻¹. Based on the energy difference of these two levels with other tentatively assigned levels, they are assigned to candidates for the $\Pi(1_{10})$ states and labeled $\Pi^1(1_{10})$ and $\Pi^2(1_{10})$ levels. It is also possible that the $\Pi(1_{10})$ level interact with another level, e.g., the $\Sigma(1_{01})$ level, and further splits to two Π levels. However, the band structure of the two $\Pi \leftarrow \Sigma$ bands are not identical. These two bands are labeled as the $\Pi^1(1_{10}) \leftarrow \Sigma(1_{01})$ and $\Pi^2(1_{10}) \leftarrow \Sigma(1_{01})$ bands. The unassigned lines in the 1628.5 cm⁻¹ to 1629.5 cm⁻¹ region might belong to the doublet high J transitions of the $n = 1, \Pi(1_{01}) \leftarrow \Pi(1_{01})$ band.

We observed a $\Pi \leftarrow \Pi$ band at 1664 cm⁻¹ are shown in Fig. 5.13. The structure of the spectral feature cannot be easily identified. The most reasonable assignment is the doublet P -branch of a $\Pi \leftarrow \Pi$ band, although the corresponding Q - and R -branch were missing from the measurement. This $\Pi \leftarrow \Pi$ band is labeled to the “ $n = 1, \Pi(2_{12} \leftarrow \Pi(1_{01}))$ ” band. We observed a clear Q and R -branch at 1655 cm⁻¹ as shown in Fig. 5.14. The P -branch of this band is not measured very well. If this is assigned to a band from the $\Sigma(1_{01})$ level, the upper level is a Π level between the $\Sigma(2_{12})$ and $\Pi(2_{12})$ levels. One possible assignment is the $n = 1, \Pi(1_{10})$, but the difference with the $\Pi(1_{10})$ level is 37.13 cm⁻¹, which is too large compared to the stretching mode on the vibrational ground state 33.5 cm⁻¹. We then assign to a band from the $\Pi(1_{10})$ level to a single Σ state that is 32.87 cm⁻¹ higher than the $\Sigma(1_{10})$ level. This band is assigned to the “ $n = 1, \Sigma(2_{12}) \leftarrow \Pi(1_{01})$ ” band to form the Σ - Π split of the “ $n = 1, (2_{12})$ ” state.

For the *para* Ar-H₂O species, we observed the $\Sigma \leftarrow \Sigma$ band at 1660 cm⁻¹ as shown in Fig. 5.15. Based on the relative energy, this band is assigned to the “ $n = 1, \Sigma(1_{11}) \leftarrow \Sigma(0_{00})$ ” band. However, the R branch of this band is severely perturbed. A satisfactory fit can be achieved by fixing the band origin and fitting the B, D, H constants of the P and R branch of this band separately. Apparently,

5.1 High Resolution Infrared Spectra of Ar-H₂O Complex

$J' \leftarrow J''$	“ $n = 1, \Pi^1(1_{10})$ $\leftarrow \Sigma(1_{01})$ ”	“ $n = 1, \Pi^2(1_{10})$ $\leftarrow \Pi(1_{01})$ ”	“ $n = 1, \Sigma(2_{12})$ $\leftarrow \Pi(1_{01})$ ”	“ $n = 1, \Pi(2_{12})$ $\leftarrow \Pi(1_{10})$ ”
0 \leftarrow 1				
1 \leftarrow 2	1629.4281(3)	1629.6265(6)		1664.8419(41) 1664.8578(120)
2 \leftarrow 3		1629.4409(5)		1664.5903(4) 1664.6054(4)
3 \leftarrow 4	1629.0714(2)	1629.2600(6)		1664.3061(4) 1664.3406(13)
4 \leftarrow 5	1628.9022(15)	1629.0841(9)		1663.9989(4) 1664.0364(13)
5 \leftarrow 6		1628.9136(12)		1663.6692(1) 1663.6928(4)
6 \leftarrow 7	1628.5804(5)	1628.7493(14)		
7 \leftarrow 8				
8 \leftarrow 9				
9 \leftarrow 10				
1 \leftarrow 1	1629.8175(7)	1630.0168(9)		
2 \leftarrow 2	1629.8315(5)	1630.0249(2)	1655.5474(2)	
3 \leftarrow 3	1629.8522(1)	1630.0389(1)	1655.5627(1)	
4 \leftarrow 4	1629.8790(1)	1630.0572(2)	1655.5814(3)	
5 \leftarrow 5	1629.9116(1)	1630.0797(3)	1655.6026(3)	
6 \leftarrow 6	1629.9495(1)		1655.6260(0)	
7 \leftarrow 7	1629.9923(2)	1630.1240(1)	1655.6511(4)	
8 \leftarrow 8		1630.1368(0)	1655.6774(2)	
9 \leftarrow 9	1630.0894(2)		1655.7051(2)	
10 \leftarrow 10	1630.1428(1)		1655.7341(5)	
11 \leftarrow 11			1655.7641(5)	
12 \leftarrow 12			1655.7956(1)	
1 \leftarrow 0	1630.0114(2)	1630.2098(0)		
2 \leftarrow 1	1630.2184(12)	1630.4128(2)	1655.9565(223)	
3 \leftarrow 2	1630.4316(12)	1630.6206(8)	1656.1725(398)	
4 \leftarrow 3	1630.6507(0)	1630.8330(10)	1656.4006(731)	
5 \leftarrow 4	1630.8751(13)	1631.0503(11)	1656.6281(1104)	
6 \leftarrow 5	1631.1042(22)	1631.2732(15)		
7 \leftarrow 6	1631.3156(4)			
8 \leftarrow 7	1631.3156(4)			
9 \leftarrow 8	1631.3156(4)			
10 \leftarrow 9	1631.3156(4)			
11 \leftarrow 10	1631.3156(4)			
12 \leftarrow 11	1631.3156(4)			

Table 5.4: Observed *ortho* Ar-H₂O transitions (in cm⁻¹) that cannot be unambiguously assigned. They are “labeled” to internal rotor states with van der Waals stretch $n = 1$. Residuals (observed-predicted) from least squares fit in least significant digit.

5.1 High Resolution Infrared Spectra of Ar-H₂O Complex

$J' \leftarrow J''$	“ $n = 1, \Sigma(1_{11}) \leftarrow \Sigma(0_{00})$ ”
0 \leftarrow 1	1661.4307(21)
1 \leftarrow 2	1661.2279(6)
2 \leftarrow 3	1661.0172(16)
3 \leftarrow 4	1660.7983(10)
4 \leftarrow 5	1660.5715(2)
5 \leftarrow 6	1660.3371(8)
6 \leftarrow 7	1660.0937(8)
7 \leftarrow 8	1659.8399(1)
8 \leftarrow 9	1659.5721(9)
9 \leftarrow 10	1659.2853(4)
1 \leftarrow 0	1661.8104(5)
2 \leftarrow 1	1661.9877(7)
3 \leftarrow 2	1662.1567(6)
4 \leftarrow 3	1662.3178(1)
5 \leftarrow 4	1662.4706(8)
6 \leftarrow 5	1662.6141(7)
7 \leftarrow 6	1662.7472(4)
8 \leftarrow 7	1662.8649(12)
9 \leftarrow 8	1662.9624(18)
10 \leftarrow 9	1663.0318(20)
11 \leftarrow 10	
12 \leftarrow 11	1662.9908(3)

Table 5.5: Observed *para* Ar-H₂O transitions (in cm⁻¹) that cannot be unambiguously assigned. They are “labeled” to internal rotor states with van der Waals stretch “ $n = 1, \Sigma(1_{11}) \leftarrow \Sigma(0_{00})$ ”. Residuals (observed-predicted) from least squares fit in least significant digit.

5.1 High Resolution Infrared Spectra of Ar-H₂O Complex

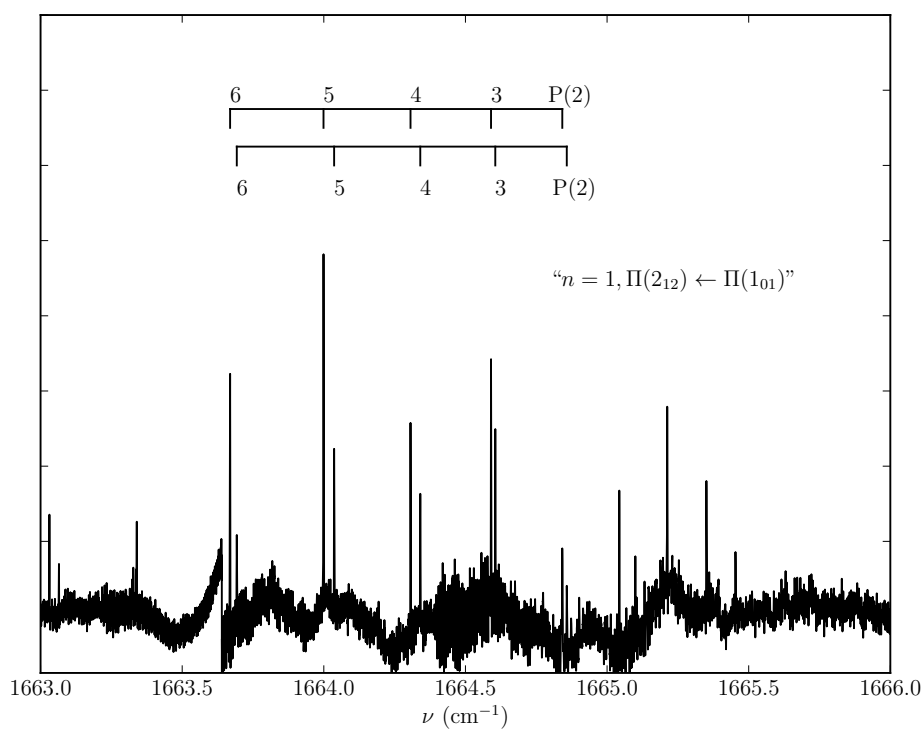


Figure 5.13: The " $n = 1, \Pi(2_{12}) \leftarrow \Pi(1_{01})$ " band at 1664 cm⁻¹ - Only P branch of this band is measured.

5.1 High Resolution Infrared Spectra of Ar-H₂O Complex

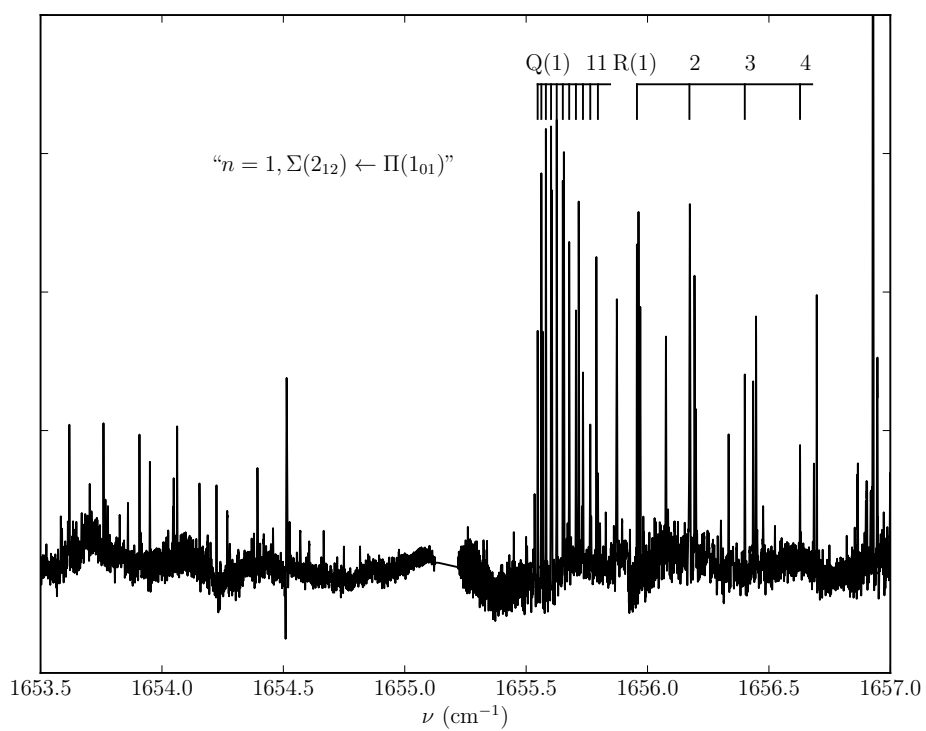


Figure 5.14: The “ $n = 1, \Sigma(212) \leftarrow \Pi(101)$ ” band at 1655 cm^{-1} - Only P and Q branches of this band are measured.

5.1 High Resolution Infrared Spectra of Ar-H₂O Complex

perturbation from other internal rotor states, probably the $n = 1, \Pi(1_{11})$ state, should be included to satisfactorily fit and analysis this band.

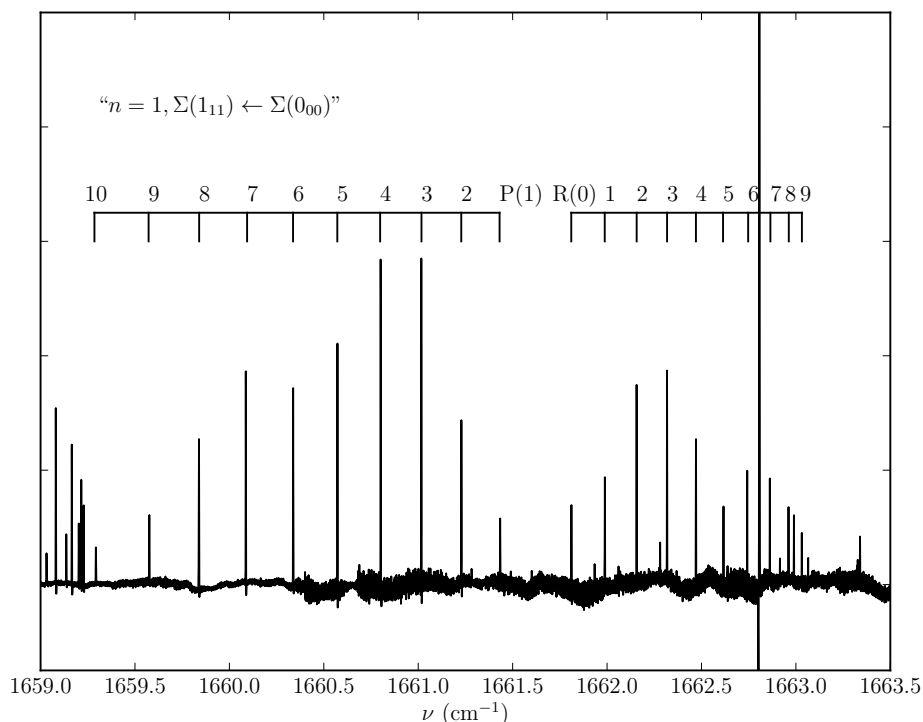


Figure 5.15: The “ $n = 1, \Sigma(1_{11}) \leftarrow \Sigma(0_{00})$ ” band of *para* Ar-H₂O - The B , D , H constants of the P and R branch of this band are fitted separately. See text for details.

Transitions of these new bands are listed in Table 5.4 and Table 5.5. These transitions are included to the global fit and the fitted spectroscopic constants are listed in Table 5.6. A global fit including these transitions which had 522 transitions is performed with the parameters in Table 5.6 fixed to the previous determined values. The RMS error of the microwave and far-IR data was 78 MHz and 0.006 cm^{-1} for the infrared data. The new internal rotor states determined from these bands are shown in Fig. 5.16.

5.1 High Resolution Infrared Spectra of Ar-H₂O Complex

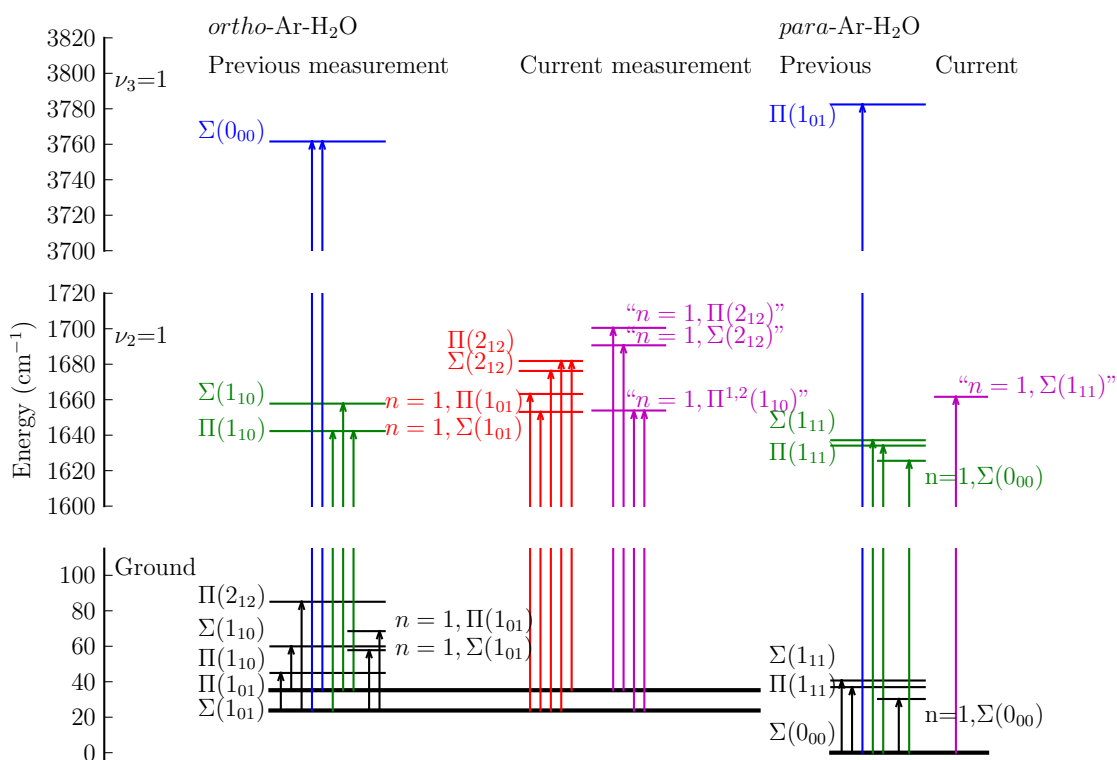


Figure 5.16: Internal rotor states of Ar-H₂O complex - Previously observed Ar-H₂O bands are determined from the microwave (thick black), far-IR (black), near-IR (blue), and mid-IR (green) measurements. We report new measurement that unambiguously determine $\Sigma(2_{12})$, $\Pi(2_{12})$, $n = 1, \Sigma(1_{01})$, $n = 1, \Pi(1_{01})$ states shown in red in the mid-IR region. The internal rotor states determined from the new measurements that cannot be properly assigned are shown in magenta.

5.1 High Resolution Infrared Spectra of Ar-H₂O Complex

	v(cm ⁻¹)	B(MHz)	D(kHz)	H(Hz)	β(MHz)
$v_2=1, n=1$					
$\Sigma^f(1_{10})$	1646.1364(12)	3037.0(66)	162(181)	0 ^a	
${}^1\Pi_e^f(1_{10})$	1629.9135(5)	3016.07(97)	-645(101) 187.7(92)	-15400(1380) 0 ^a	2692(146)
${}^2\Pi_e^f(1_{10})$	1630.1102(4)	2992.2(12)	446.(18) 0 ^a	0 ^a 0 ^a	
$\Sigma^e(2_{12})$	1666.8605(14)	3346.2(60)	198(80)	10360(700)	
$\Pi_f^e(2_{12})$	1676.6834(13)	2500.1(59)	5406(229) -951(184)	18030(930) 0 ^a	9455(67)
$\Sigma^P(1_{11})$		2909.4(36)	664(107)	1220(820)	
$\Sigma^R(1_{11})$	1661.6273(8)	2817.2(20)	-676(35)	-5873(154)	

^a Zero within uncertainty, and set to zero in the final fit.

Table 5.6: Fitted spectroscopic constants of the bands that cannot be unambiguously assigned.

5.1.3 Discussion

As discussed in the previous mid-IR study, presence of the Ar atom has little perturbation on the bending mode of the H₂O monomer.⁽²⁷⁷⁾ This assumption is confirmed by our study of the $n = 1, (1_{01})$ and (2_{12}) internal rotor states. The position of all the bands associated with these states can be accurately predicted by mapping the corresponding far-IR states directly to the $\nu_2 = 1$ excitation of H₂O. This means that the internal rotor states on the vibrational ground and excited states of H₂O subunit have basically the same structure. For these internal rotor states, the coupling of the high frequency H₂O subunit bending with the low frequency internal rotation and intramolecular van der Waals stretching is small. In addition, no predissociation broadening from the measurements is observed, suggesting very little coupling between the H₂O bend and intermolecular coordinates which would lead to predissociation of the complex.

As mentioned above, splitting of the Σ and Π level of the internal rotor states is a direct indicator of the anisotropy of the PES. In Table 5.7, we list the splittings of the internal rotor states observed in the far-infrared region where the water subunit is on the vibrational ground state and in our current mid-IR measurements with the bending excitation of water.

Comparing the splittings in the (1_{10}) state on the ground and ν_2 excitation

5.1 High Resolution Infrared Spectra of Ar-H₂O Complex

states, there is 0.5 cm^{-1} increase of the splitting, which indicates stronger Coriolis and angular-radial coupling among the vibrational excited states of H₂O. This is in agreement with the Ar-D₂O complex(139) where the (1₁₁) internal rotor state shows a similar increase of the splitting upon water bending excitation. On the other hand, the splitting of the 1₀₁ state shows monotonic decrease upon the $n = 1$ van der Waals stretching and ν_2 excitation. This is a result of the small change in the angular anisotropy of the PES in the excited state. It is also quite interesting to note that the splitting for the (2₁₂) state is significantly smaller than that of the (1₁₀) and (1₀₁) states. As discussed later, the abnormal decrease of the splitting might be due to a perturbing state that mix with the $\Pi(2_{12})$ level that pushes the $\Pi(2_{12})$ state to lower energy. However, taking into account of the perturbation, we can still estimate that the splitting of the (2₁₂) internal rotor state is several wavenumber smaller than the $j = 1$ states.

As shown in Table 5.3, although the off-diagonal Coriolis terms determined for the *ortho* $j = 1$ levels are very close to the prediction of $2B$ value, the β value of the (2₁₂) and $n = 1, (1_{01})$ states don't agree with the prediction. This suggests that additional coupling states should be considered, which are probably the unassigned states shown in Fig. 5.16 or states which have not yet been measured. There should be significant mixing with the monomer internal rotor state or van der Waals stretching states that further mix the (2₁₂) states with these unidentified states. This shows that the approximations made in the nearly free internal rotor model starts to fail as the internal rotor states move to higher energy. The inadequacy of this model is more evident when we consider the measured unassigned bands that cannot be properly correlated to the internal rotor states, such at the two overlapping $\Pi \leftarrow \Sigma$ bands at 1630 cm^{-1} shown in Fig. 5.9. Further theoretical calculation of the rovibrational bound states of the Ar-H₂O complex is crucial to resolve the ambiguities of the assignments. A clear assignment of these bands to the new internal rotor states would elucidate the coupling mechanism between the internal rotor states with van der Waals stretching and H₂O bending states.

It is interesting to analyses how the attachment of Ar atom affects the nearly free internal rotation of H₂O. As suggested by Weida and Nesbitt,(277) the “center of gravity” of the split Σ and Π levels for a particular internal rotor state represents the energy of the unperturbed internal rotation energy level from the first order perturbation theory. The average of the split Σ and Π states of the internal rotor states in both the ground and ν_2 excited states of the H₂O subunit

5.1 High Resolution Infrared Spectra of Ar-H₂O Complex

are listed in Table 5.8 and plotted in Fig. 5.17, together with the corresponding values of free H₂O monomer.

We arbitrarily fix the ground state (1₁₀) level of the Ar-H₂O complex to the corresponding value of free H₂O monomer to demonstrate the effect of the Ar atom attachment to the H₂O rotational energy levels. Clearly, the energy difference between the (2₁₂) and (1₁₀) states in the $\nu_2=1$ excitation state greatly decreases upon complexation with the Ar atom while that between the (1₁₀) and (1₀₁) states increases on the H₂O ground state. The abnormal decrease of the energy of the (2₁₂) state indicates that it is very likely that the $\Pi(2_{12})$ level is “pushed down” by mixing with another state. We estimate that the unperturbed $\Pi(2_{12})$ level and consequently the averaged (2₁₂) state should be several wavenumber higher in energy. Yet, this cannot completely explain the abnormally small gap between the (2₁₂) and (1₁₀) internal rotor state. So in the following discussion, we take the value of the “perturbed” $\Pi(2_{12})$ level as it is. Since the $\nu_2=1$ excitation has little effect on the internal rotor states, as shown by the almost identical energy gap between the ground and the H₂O bending excitation of the (1₁₀) states, we could assume that these trends are the same on the ground and excitation state of H₂O subunit.

The rotational energy of the (2₁₂) and (1₁₀) states in terms of the rotational constants of the nearly free rotation of the H₂O subunit are $A+B+4C$ and $A+B$, respectively. Neglecting the centrifugal distortion constants, decrease of the (2₁₂)-(1₁₀) gap can be attributed to a decreased C rotational constant estimated to be 7.243 cm^{-1} , which is 2 cm^{-1} smaller than the free H₂O value. The decrease of the C rotational constant indicates that the in-plane rotation of the H₂O subunit, which is subjected to the V_1 and V_2 barriers, is hindered. The same argument can be applied to the increase of the (1₁₀)-(1₀₁) gap, which is $A - C$ in terms of the rotational constants. Using the value of the C rotational constant determined from the ν_2 excitation state and assume that the C rotational constant is the same for both states, the A rotational constant is roughly estimated to be 30 cm^{-1} , which is $\sim 2\text{ cm}^{-1}$ larger than the free monomer value. It should be noted that the energy gap upon ν_2 excitation for the Ar-H₂O complex is 0.58 cm^{-1} smaller than free H₂O, which was attributed to a red-shift of the H₂O subunit bending origin.(277) With a large change of the A and C constants as discussed in this study, determination of the band origin needs direct measurements of the other internal rotor states such as the $\Sigma(0_{00})$ level.

5.1 High Resolution Infrared Spectra of Ar-H₂O Complex

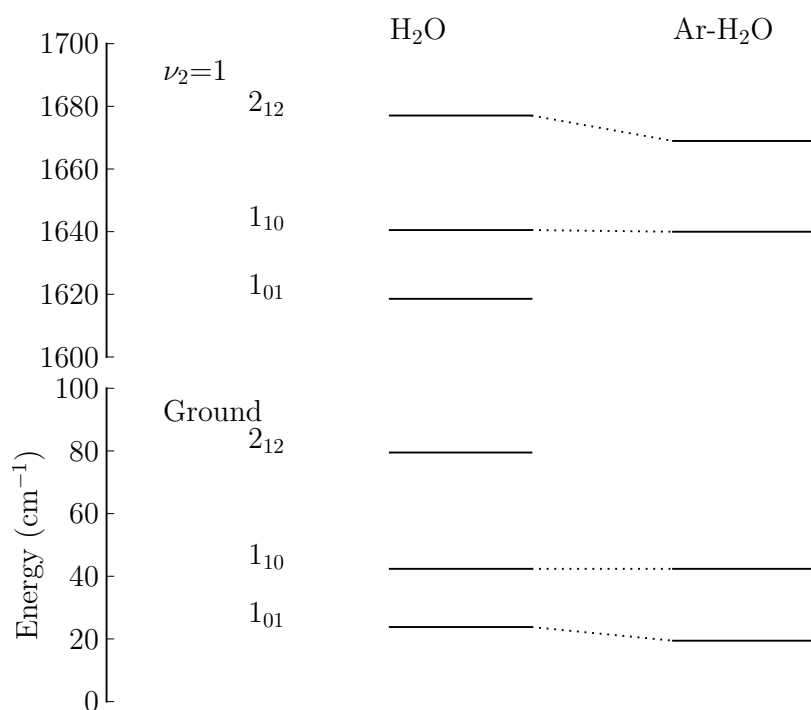


Figure 5.17: The rovibrational energy levels of H₂O and H₂O subunit in Ar-H₂O - The H₂O in the ground and ν_2 excitation state and the internal rotor states, which are taken as the average of the split Σ and Π level of a particular internal rotor state, of the nearly free rotating H₂O subunit in the Ar-H₂O complex. The ground (1_{01}) internal rotor state of the complex is arbitrarily fixed to the 1_{01} state of H₂O. The (1_{10})-(1_{01}) gap increases and the (2_{12})-(1_{10}) gap greatly decreases upon complexation with Ar atom.

5.1.4 Conclusion

Five new rovibrational bands of the Ar-H₂O complex are measured and unambiguously assigned. The $\Sigma(2_{12})$, $\Pi(2_{12})$, $n = 1, \Sigma(1_{01})$, $n = 1, \Pi(1_{01})$ internal rotor states have been accurately determined. The position of these internal rotor states agree with the prediction from the far-IR study, indicating that the bending excitation of H₂O subunit in the complex has small effect on these internal rotor states. The decrease of the C rotational constant of the nearly free rotation of H₂O unit is attributed to the hindered in-plane rotation of H₂O upon complexation with Ar atom. The new measurement provide more information for the study of the rovibrational states and potential energy surface of the Ar-H₂O complex with the nearly free internal rotor model. On the other hand, there are a number of new van der Waals vibrational states of the Ar-H₂O complex determined from this measurements that cannot be properly associated to the internal rotor states of the complex. The assignment of these bands requires considering more complicated rovibrational couplings that have not been included in the previous model.

5.1 High Resolution Infrared Spectra of Ar-H₂O Complex

	$n = 0$	$n = 1$
Ground		
(1 ₀₁)	11.428610	10.729896
(1 ₁₀)	14.983385	
$v_2=1$		
(1 ₀₁)		10.1165
(1 ₁₀)	15.4845	
(2 ₁₂)	5.6094	

Table 5.7: Energy difference between the Σ and Π levels of the internal rotor states with the water subunit on its vibrational ground state and bending excitation $\nu_2 = 1$. Note the splitting of the (2₁₂) state is substantially small compared to the other states.

	H ₂ O ^a	Ar-H ₂ O ^b	
		$n = 0$	$n = 1$
Ground			
1 ₀₁	0	0	33.648811
1 ₁₀	18.5773	22.939681	
2 ₁₂	55.7020		
$v_2=1$			
1 ₀₁	1594.7629		1634.38395
1 ₁₀	1616.7115	1620.539695	
2 ₁₂	1653.2670	1649.511695	

^a set to zero at 23.7944 cm⁻¹

^b set to zero at 5.714305 cm⁻¹

Table 5.8: The Ar-H₂O internal rotor states determined from this study together with the corresponding free H₂O monomer values taken from Ref (?). The internal rotor state energy is calculated as the average of the Σ and Π levels.

5.2 High Resolution Infrared Spectra of Ne-H₂O

5.2.1 Introduction

The PES and rovibrational energy levels of the Ne-H₂O complex is similar to the Ar-H₂O complex. Therefore, the high resolution infrared spectra of the Ne-H₂O complex resemble those of the Ar-H₂O complex. However there are some important differences between the two complexes. The PES of Rg-H₂O complexes including He, Ne, Ar, and Kr have been studied by Makarewicz(157). The highly accurate analytical Ar-H₂O PES on the CCSD(T)/CBS level of theory is so far the most accurate *ab initio* PES. In Fig. 5.18, the equilibrium geometries of the four binary complexes are shown. The MRCI (multi-reference configuration interaction) calculation shows that the 2nd and the 4th highest occupied molecular orbitals of the Ar-H₂O and Kr-H₂O complexes are covalent bonds, i.e., for a certain molecular orbital obtained from the calculation, the electron density distribution is populated on both the H₂O sub-unit and the Kr/Ar atom. However, there is no such covalent bond formed in the Ne-H₂O and He-H₂O complexes. The interaction between the two sub-units is pure dispersion interaction. As a consequence of lack of strong nuclear charge and high electron density, the potential well depth of the Ne-H₂O complex is only 64.7 cm⁻¹ and the depth of the He-H₂O is 34.76 cm⁻¹. The in-plane rotation barriers are $V_1=15$ cm⁻¹, $V_2=16.8$ cm⁻¹ for Ne-H₂O and $V_1=12.26$ cm⁻¹, $V_2=12.67$ cm⁻¹ for He-H₂O. Due to the shallow binding energy and low internal rotational barriers, even greater large amplitude motion and rovibrational coupling are anticipated in the Ne-H₂O and He-H₂O complexes.

Neither of the two weakly dispersion complexes has been measured by rotational or rovibrational spectroscopy. The only isotopologue that has been measured by high resolution spectroscopy is the Ne-D₂O complex studied by Li *et al.*(138). Due to the spin statistical weight of the 2 identical Deuterium nuclei of D₂O, the lowest $\Sigma(0_{00})$ level belongs to the ortho spin modification. The $\Pi(1_{11}) \leftarrow \Sigma(0_{00})$, $\Sigma(1_{11}) \leftarrow \Sigma(0_{00})$, and $n = 1, \Sigma(0_{00}) \leftarrow \Sigma(0_{00})$ bands were measured at 1120 cm⁻¹. Assignment and fit of these three bands is similar to the same three bands of the Ar-H₂O complexes. A J dependent Coriolis coupling term mixing the $\Pi(1_{11})$ e parity and $\Sigma(1_{11})$ state and a Fermi resonance term mixing the $\Sigma(1_{11})$ and $n = 1, \Sigma(0_{00})$ state are needed to satisfactorily fit the 3 bands. In addition to these two coupling terms that have been found in both the Ne-H₂O and the Ar-H₂O complexes, avoid level crossing is found between

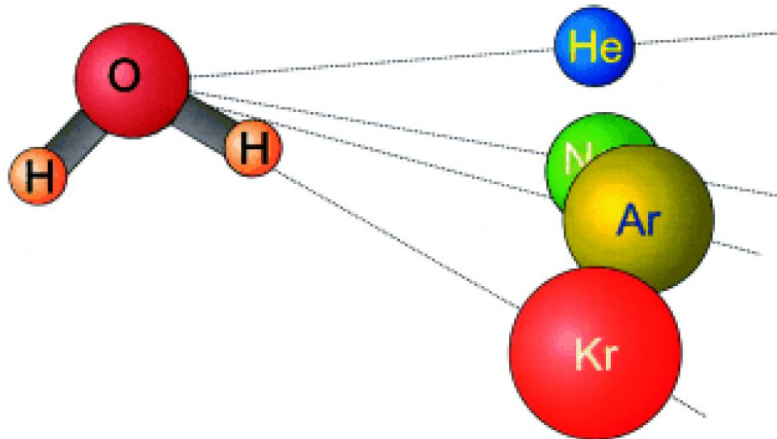


Figure 5.18: Equilibrium geometries of Rg-H₂O complexes - MRCI calculation of the equilibrium geometries and incipient covalence bonds of Rare gas H₂O complex from Ref. (9).

the $\Pi(1_{11})$ e parity and the $n = 1, \Sigma(0_{00})$ state. In the fitting procedure, the $J' > 5$ transitions of the R branches of these two bands at the “band head” are exchanged. The avoided level crossing indicates even stronger rovibrational coupling in the Ne-H₂O complex. The weak transitions due to ²²Ne-D₂O were observed but have not been assigned and analysed.

5.2.2 Results

For the Ne-H₂O complex, the $\Sigma(1_{01})$ and $\Pi(1_{01})$ belong to the ortho spin modification and significantly populated. So the rovibrational bands of Ne-H₂O with the lower level from these two bands are anticipated in the vicinity of the same bands of Ar-H₂O complex. The high resolution rovibrational spectrum of Ne-H₂O complex is investigated using the multipass direct absorption QCL spectrometer. Indeed, at least four rovibrational bands have been observed. The assignment of these bands are made through correlation to the associated Ar-H₂O bands. Since the presence of Ne atom exerts a weaker perturbation compared to the Ar atom, the shift of the Ne-H₂O bands to the pure H₂O transitions is smaller than the Ar-H₂O bands. The $\Pi(1_{10}) \leftarrow \Sigma(1_{01})$ band assigned is shown in Fig. 5.19. The closely packed Q branch and regular P and R branches are assigned and fit to two separate f and e parity of the $\Pi(1_{10})$ state. The transition frequencies of this band are given in Table 5.9. The spectroscopic constants determined for the

5.2 High Resolution Infrared Spectra of Ne-H₂O

ground and $\nu_2=1$ state of the Ne-H₂O complex are given in Table 5.10.

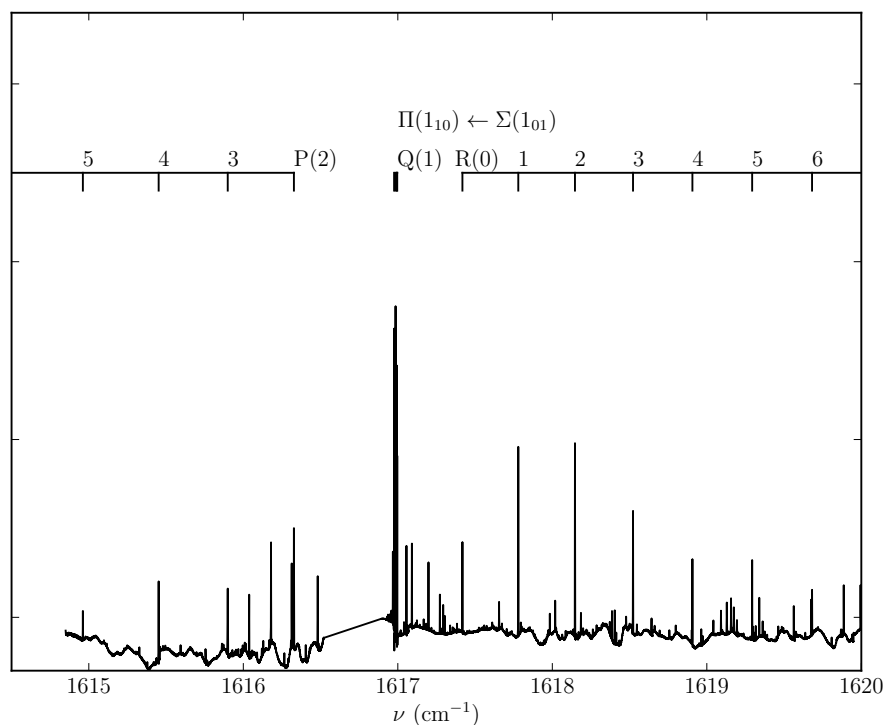


Figure 5.19: The $\Pi(1_{10}) \leftarrow \Sigma(1_{01})$ band of Ne-H₂O - The Q and P and R branches are identified and fit with pseudo-diatomic Hamiltonian.

The B rotational constant determined is 5349(30) MHz for the $\Sigma(1_{01})$ state, which is considerably larger than that of the Ne-D₂O $\Sigma(0_{00})$ state, indicating a larger rotational energy gap due to the lighter Hydrogen nucleus and delocalized wave function. The predicted $J = 1 \leftarrow 0$ pure rotational transition is 10.778(126) GHz in the microwave region. The band origin from the fit is at 1617 cm⁻¹, which is between the pure $1_{10} \leftarrow 1_{01}$ rovibrational transition of H₂O is at 1616.71149 cm⁻¹ and the band origin of the corresponding $\Pi(1_{10}) \leftarrow \Sigma(1_{01})$ band of the Ar-H₂O complex at 1618.51169(7) cm⁻¹, suggesting that the perturbation of the Ne atom to the H₂O rovibrational transition is weaker than that of Ar atom.

Another band from the ortho modification is identified among the R branch of the $\Pi(1_{10}) \leftarrow \Sigma(1_{01})$ band as shown in Fig. 5.20. Due to its weaker intensity and $\Sigma(1_{10}) \leftarrow \Pi(1_{01})$ band of the ortho modification. The Q branch of this band is

5.2 High Resolution Infrared Spectra of Ne-H₂O

$J' \leftarrow J''$	$\Pi(1_{10}) \leftarrow \Sigma(1_{01})$	$“n = 1, \Sigma(0_{00}) \leftarrow \Sigma(0_{00})”$
<i>P</i> -branch		
0 \leftarrow 1		1620.7787(2)
1 \leftarrow 2	1616.3275(9)	1620.5617(289)
2 \leftarrow 3	1615.8992(114)	1620.3852(19)
3 \leftarrow 4	1615.4521(7)	1620.1605(31)
4 \leftarrow 5	1614.9616(2)	1619.8862(19)
5 \leftarrow 6	1614.9616(2)	1619.5628(04)
<i>Q</i> -branch		
1 \leftarrow 1	1616.9962(5)	
2 \leftarrow 2	1616.9935(6)	
3 \leftarrow 3	1616.9854(3)	
4 \leftarrow 4	1616.9760(7)	
5 \leftarrow 5	1616.9875(2)	
<i>R</i> -branch		
1 \leftarrow 0	1617.4181(22)	1621.0653(2)
2 \leftarrow 1	1617.7797(18)	1621.2926(5)
3 \leftarrow 2	1618.1466(9)	1621.4999(2)
4 \leftarrow 3	1618.5223(10)	1621.6816(3)
5 \leftarrow 4	1618.9067(4)	1621.8309(3)
6 \leftarrow 5	1619.2934(7)	1621.9407(0)
7 \leftarrow 6	1619.6811(2)	

Table 5.9: Observed *ortho* Ne-H₂O transitions (in cm⁻¹). The *e* and *f* parity of the $\Pi(1_{10}) \leftarrow \Sigma(1_{01})$ are fit separately. The *P* and *R* branch of the band at 1621 cm⁻¹ are fit separately, which is “labeled” as the “ $n = 1, \Sigma(0_{00}) \leftarrow \Sigma(0_{00})$ ” band. Residuals (observed-predicted) from least squares fit in least significant digit.

	$v(\text{cm}^{-1})$	$B(\text{MHz})$	$D(\text{MHz})$	$H(\text{kHz})$
Ground				
$\Sigma(1_{01})$	0	5349(30)	-19.55(2.06)	-173(43)
$v_2=1$				
$\Pi^e(1_{10})$	1617.2434(31)	5292(24)	-14.41(1.32)	-90.3(20.8)
$\Pi^f(1_{10})$	1617.1748(43)	5411(26)	-13.12(0.82)	0 ^a
R-“ $n = 1, \Sigma(0_{00})$ ”	1620.9587(50)	2684(40)	8.98(122)	40.1(149)
P-“ $n = 1, \Sigma(0_{00})$ ”	1620.8297(37)	3559(38)	11.84(109)	17.7(133)

^a Zero within uncertainty, and set to zero in final fit.

Table 5.10: Band origin and rotational constants of Ne-H₂ from the fit. The *e* and *f* parity of the $\Pi(1_{10}) \leftarrow \Sigma(1_{01})$ are fit separately. The *P* and *R* branch of the band at 1621 cm⁻¹ are fit separately, which is “labeled” as the “ $n = 1, \Sigma(0_{00}) \leftarrow \Sigma(0_{00})$ ” band.

5.2 High Resolution Infrared Spectra of Ne-H₂O

clearly identified, but the *P* and *R* branches are not clearly identified due to the weak intensity of this band. In summary the two internal rotor state belong to

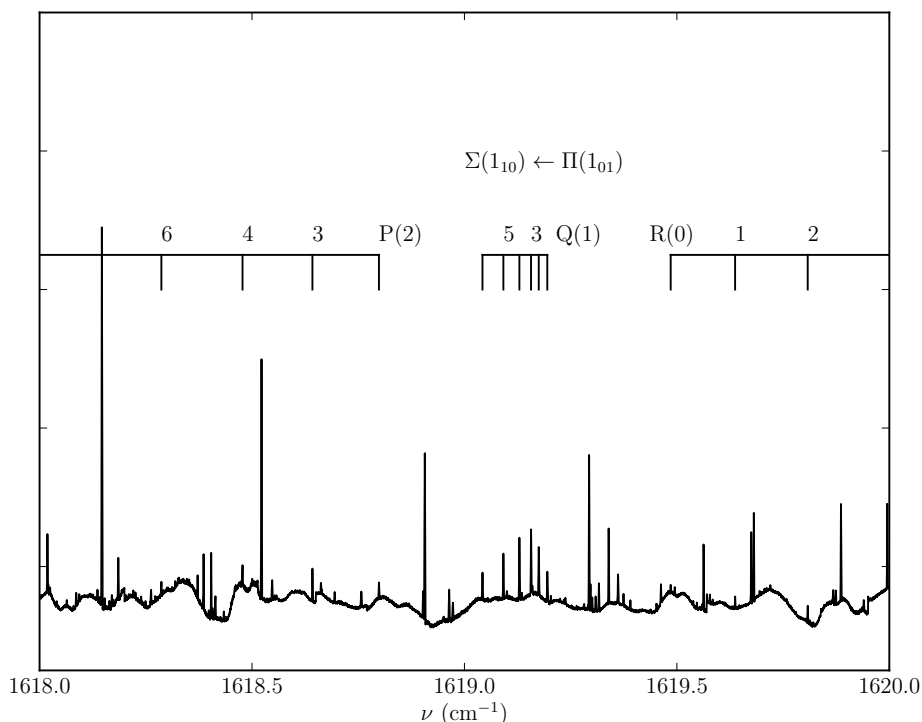


Figure 5.20: The $\Sigma(1_{10}) \leftarrow \Pi(1_{01})$ band of Ne-H₂O - Only the *Q* branch is clearly observed, the *P* and *R* branches are not clearly identified due to the weak intensity of this band.

the *ortho* spin modification identified from these two bands is plotted in Fig. 5.21 together with the corresponding internal rotor states of the Ar-H₂O complex.

The rovibrational bands from the *para* spin modification are also identified. The most prominent feature of the *para* Ne-H₂O band is the $\Pi(1_{11}) \leftarrow \Sigma(0_{00})$ band shown in Fig. 5.22. The position of this band is very close to the $1_{11} \leftarrow 0_{00}$ rovibrational transition of the H₂O monomer and the corresponding band of the Ar-H₂O complex. The *Q* branch of this band is very strong, together with the *Q* branch transitions of the unassigned ²²Ne-H₂O complex. But the *P* and *R* branch of this band is surprisingly weak, so the assignment of the *P* and *R* branch transitions cannot be unambiguously made. The reason for the drastic intensity difference might due to the mixing and intensity borrowing from the *e*

5.2 High Resolution Infrared Spectra of Ne-H₂O

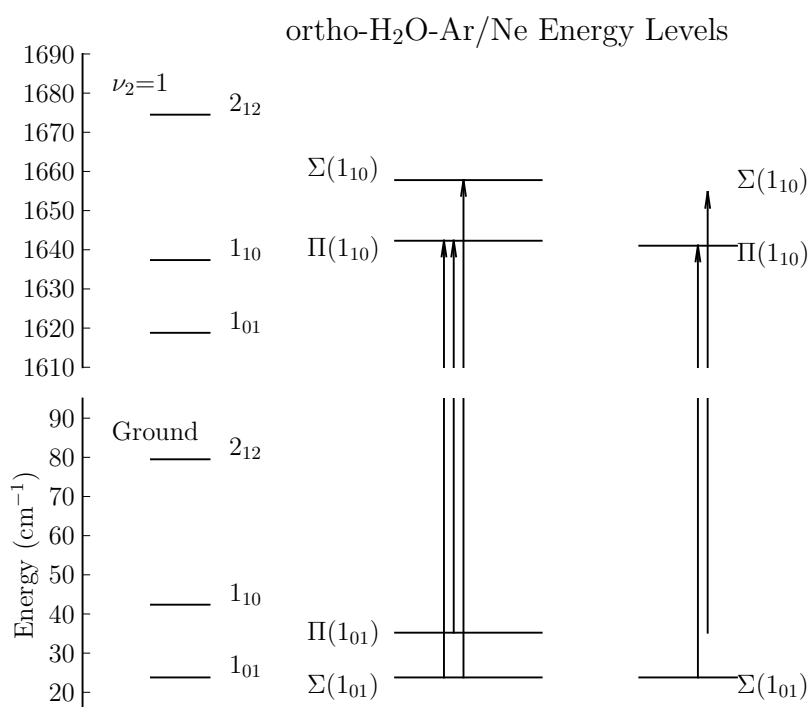


Figure 5.21: The internal rotor states of *ortho* Ne-H₂O - The $\Pi(1_{10})$ and $\Sigma(1_{10})$ internal rotor states of the *ortho* Ne-H₂O complex together with the corresponding internal rotor states of the Ar-H₂O complex.

5.2 High Resolution Infrared Spectra of Ne-H₂O

parity level of the $\Pi(1_{11})$ level, which is the upper level of the P and R branches, to another internal rotor state.

This mixing state is tentatively assigned to the “ $n = 1, \Sigma(0_{00})$ ” state. The “ $n = 1, \Sigma(0_{00})$ ” $\leftarrow \Sigma(0_{00})$ band at 1621 cm^{-1} is shown in Fig. 5.23. This is a $\Sigma \leftarrow \Sigma$ band with P and R branch. Transitions of this band is given in Table 5.9. Judging from the spacing of the transitions, there is large perturbation on this band, probably due to the Fermi resonance between the “ $n = 1, \Sigma(0_{00})$ ” state and the $\Sigma(1_{11})$ level that has not been measured, in a similar way as the *para* spin modification of the Ar-H₂O complex and the *ortho* spin modification of the Ne-H₂O complex. The spectroscopic consequent from the fit are given in Table 5.10. The two internal rotor state belong to the *para* spin modification identified from these two bands is plotted in Fig. 5.24 together with the corresponding internal rotor states of the Ar-H₂O complex. Note that since the well depth on the Ne-H₂O PES is 64.7 cm^{-1} , the $j=2$ internal rotor states cannot exist.

5.2.3 The He-H₂O complex

An attempt to record the rovibrational transitions of He-H₂O complex was also made in the 1634 cm^{-1} region where strong Q branch transitions of the $\Pi(1_{11}) \leftarrow \Sigma(0_{00})$ are measured for both Ne-H₂O and Ar-H₂O complexes. No absorption spectrum of He-H₂O was measured in this region and down to 1620 cm^{-1} region.

Based on the *ab initio* calculation, the binding energy of the He-H₂O complex is $D_e=34.76 \text{ cm}^{-1}$ and $D_0=6.90 \text{ cm}^{-1}$ which is significantly weaker than the other complexes. A full dimensional rovibrational wave function calculation shows that there are only 4 rovibrational wave functions supported on the PES of the He-H₂O complex.(288) They can be labelled as the $\Sigma(0_{00})$ internal rotor state with $J=0-4$. The transition dipole moment between the $\nu_2=1, \Sigma(0_{00})$ and the ground $\Sigma(0_{00})$ state is indeed negligible. Therefore, the experimental finding confirmed the theoretical calculation that no other rovibrational state can be detected.

5.2 High Resolution Infrared Spectra of Ne-H₂O

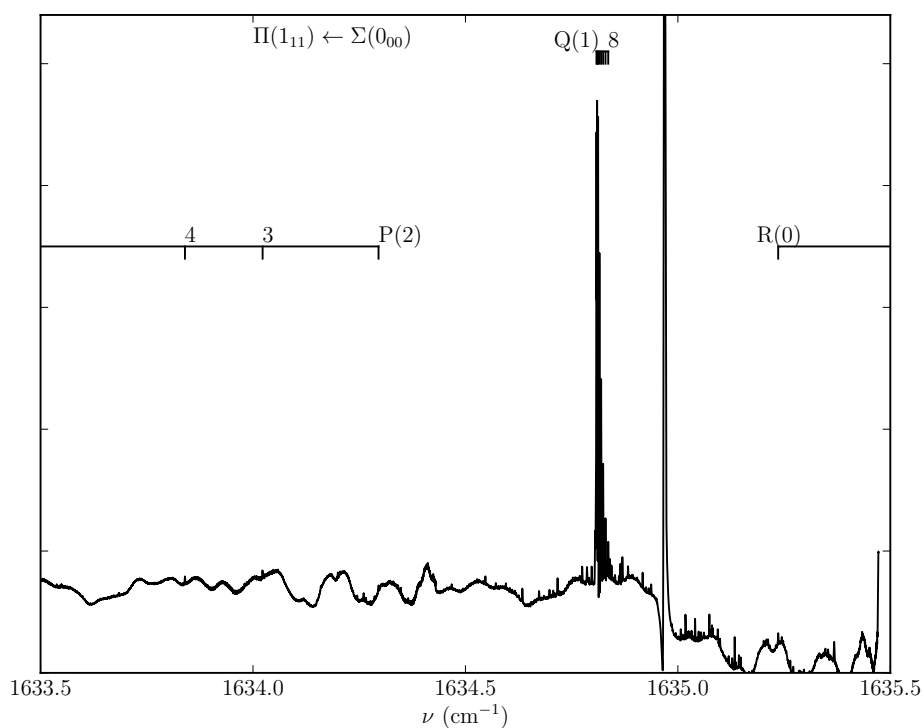


Figure 5.22: The $\Pi(1_{11}) \leftarrow \Sigma(0_{00})$ band of Ne-H₂O - Only the Q branch is clearly observed, the P and R branches are not clearly identified due to the weak intensity of this band.

5.2 High Resolution Infrared Spectra of Ne-H₂O

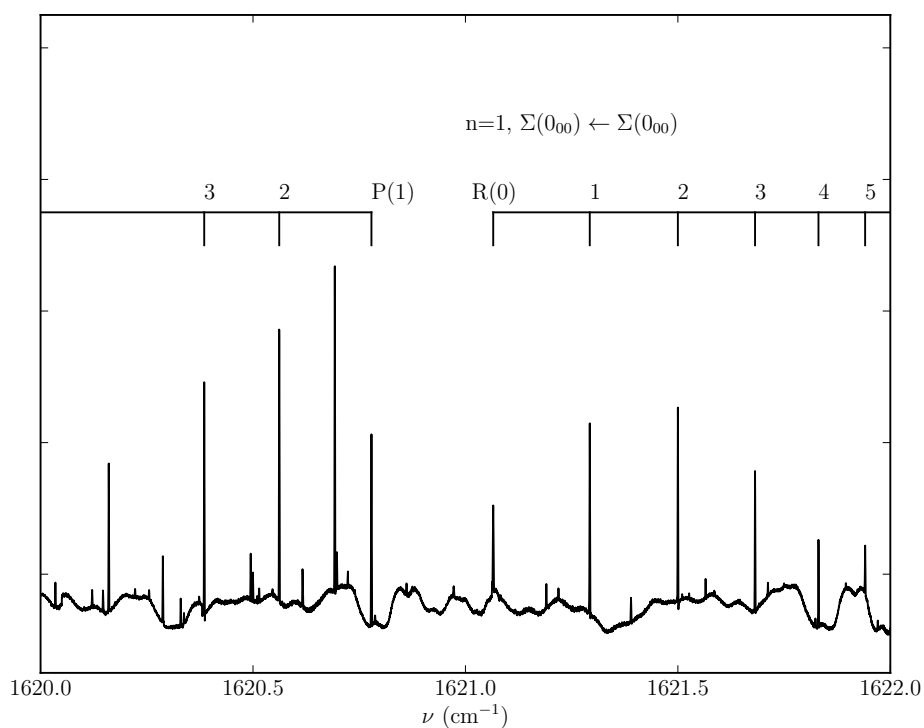


Figure 5.23: The “ $n = 1, \Sigma(0_{00})$ ” $\leftarrow \Sigma(0_{00})$ band of Ne-H₂O - The *P* and *R* branch of the band at 1621 cm⁻¹ are fit separately, which is “labeled” as the “ $n = 1, \Sigma(0_{00}) \leftarrow \Sigma(0_{00})$ ” band.

5.2 High Resolution Infrared Spectra of Ne-H₂O

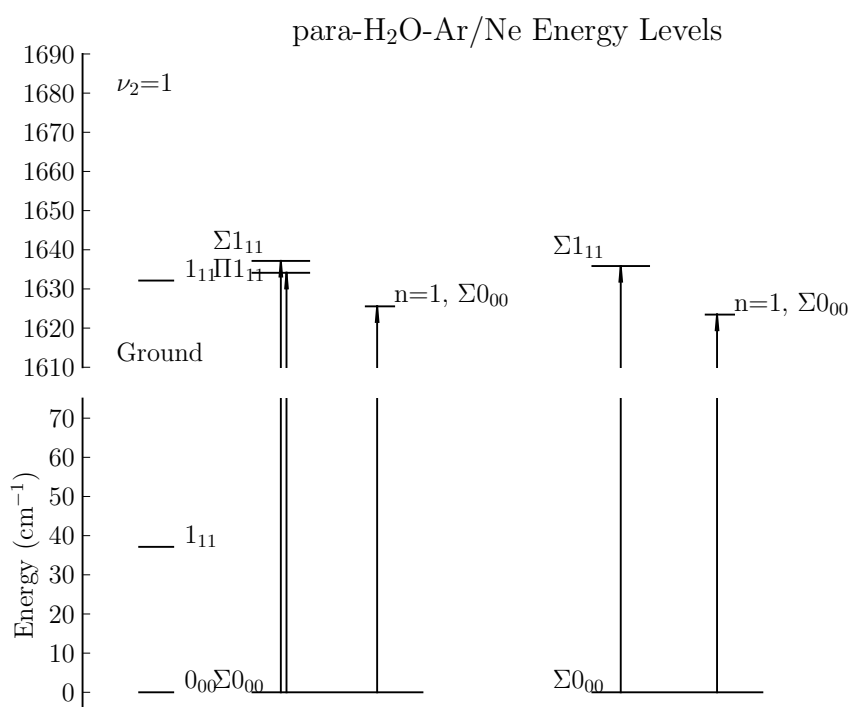


Figure 5.24: The internal rotor states of *para* Ne-H₂O - The Π(1₁₁) and “n = 1, Σ(0₀₀)” internal rotor states of the *para* Ne-H₂O complex together with the corresponding internal rotor states of the Ar-H₂O complex.

5.3 High Resolution Infrared Spectra of “Ar+NH₃” and Ne-NH₃

5.3.1 “Ar+NH₃” Complex

The $1_1 \leftarrow 0_0$ transition of the ν_4 bending band of NH₃ is at $1646.49109\text{ cm}^{-1}$. It is therefore reasonable to postulate that the presence of Ne or Ar atom perturbs this transition and internal rotor bands are anticipated around this position for the binary complexes, which has been observed for the Ar/Ne-H₂O complex. However, the mid-IR transition of Ar-NH₃ cannot be interpreted in this way.

The vibrational ground state of the Ar-NH₃ complex has been well studied by microwave spectroscopy(78, 183) and the vibration-rotation-tunneling spectroscopy has been used to study its internal rotor states(88, 223, 310, 57, 224, 225). The Ar-ND₃ complex has been studied using microwave spectroscopy(263), and sub-millimeter wave spectroscopy(173). The only infrared study has been carried out by Farser *et al.*(79) at the ν_2 vibration of NH₃ at 950 cm^{-1} . Similar to the Ar-H₂O complex, the internal rotor states of the Ar-NH₃ complex are correlated to the free monomer rovibrational states and split to Σ and Π levels due to the projection of the sub-unit angular momentum. The ground vibrational state transition for NH₃ is $1_0 \leftarrow 0_0$ transition. So the internal rotor states correlate to the 1_0 level have been identified. The internal rotor states of the *A* symmetry *ortho* spin modification and *E* symmetry *para* spin modifications of Ar-NH₃ complex on the vibrational ground state of NH₃ is shown in Fig. 5.25 and Fig. 5.26, respectively. In mid-IR transition for NH₃ is the $1_1 \leftarrow 0_0$ transition, so for the *ortho* spin modification, the $\Sigma(1_1) \leftarrow \Sigma(0_0)$ and the $\Pi(1_1) \leftarrow \Sigma(0_0)$ band are expected.

The experimental procedure is similar to the study of Ar/Ne-H₂O complex. The high-resolution mid-IR spectrum of Ar-H₂O complex is measured using the multipass direct absorption spectrometer based on the $6\text{ }\mu\text{m}$ quantum cascade laser. The concentration of NH₃ and Ar gas are set to 1:1 ratio with backing gas Ne pressure around 10 atm.

Strong spectra features are observed in the 1643 cm^{-1} as shown in Fig. 5.27. The carrier of this band is named as “Ar-NH₃”. Since this band is to the red of the monomer transition at 1647 cm^{-1} , the upper level of this band is lower than the monomer 1_1 level. If we assume that the internal rotor states of the complex are not severely coupled with the intra-molecular vibration of the NH₃ sub-unit, in other words, that the internal rotor states of the ground and $\nu_4=1$ states of

5.3 High Resolution Infrared Spectra of “Ar+NH₃” and Ne-NH₃

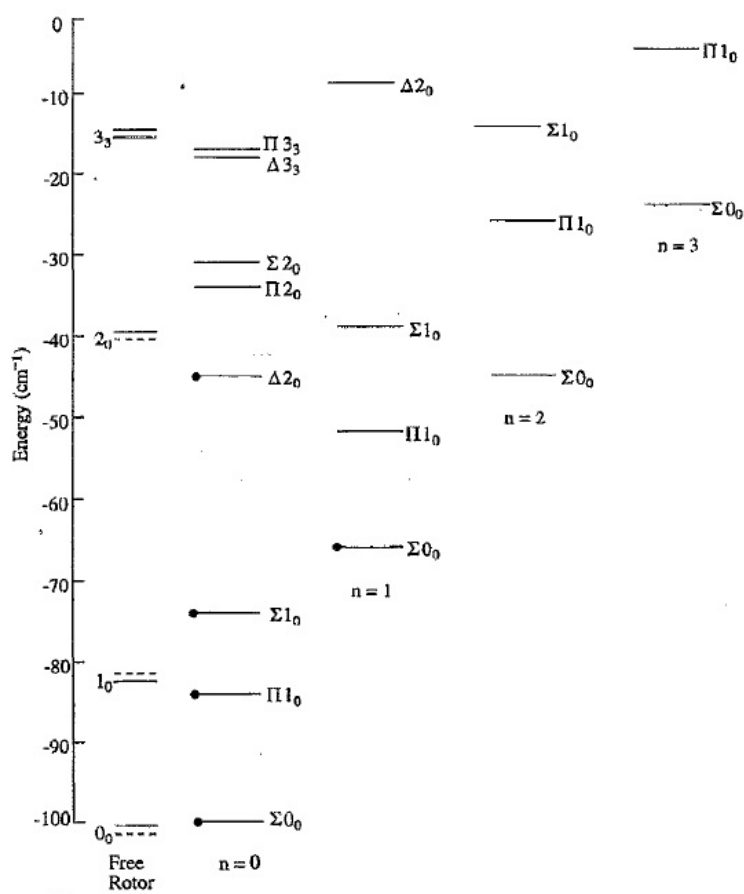


Figure 5.25: Internal rotor states of the ortho *spin* modification of the Ar-NH₃ complex - The internal rotor states of the Ar-NH₃ complex are correlated to the free monomer rovibrational states of NH₃ and split to Σ and Π levels. For the *ortho* spin modification, the Σ(0₀) state is the only lower state significantly populated in the supersonic free jet expansion. Figure taken from Ref. (224).

5.3 High Resolution Infrared Spectra of “Ar+NH₃” and Ne-NH₃

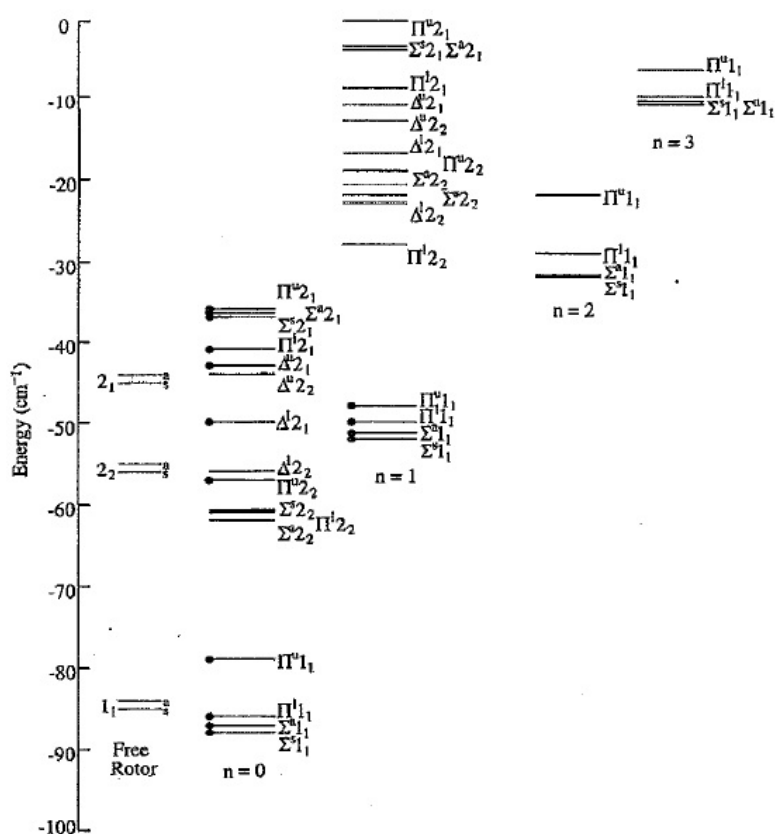


Figure 5.26: Internal rotor states of the *para* spin modification of the Ar-NH₃ complex - The internal rotor states of the Ar-NH₃ complex are correlated to the free monomer rovibrational states of NH₃ and split to Σ and Π levels. For the *para* spin modification, the Σ(1₁) state is the only lower state significantly populated in the supersonic free jet expansion. Figure taken from Ref. (224).

5.3 High Resolution Infrared Spectra of “Ar+NH₃” and Ne-NH₃

the NH₃ sub-unit are the same, the upper level should be the $\Pi(1_1)$ level and a $\Pi \leftarrow \Sigma$ band is expected. However, the Q branch of this band is not observed and close inspection turns out that this band is an $\Sigma \leftarrow \Sigma$ band as shown in Fig. 5.27. Therefore the upper level of this band is the $\Sigma(1_1)$ level, indicating that the ν_4 excitation of NH₃ greatly coupled with other internal rotor states. It should be noted that there are several un-assigned lines in the P and Q branches of the band which are likely belong to the ²²Ne-NH₃ isotopologue.

Another rovibrational band observed is shown in Fig. 5.28. This is clearly the Q and R branches of a $\Pi \leftarrow \Sigma$ band which is assigned to the $\Pi(1_1) \leftarrow \Sigma(0_0)$ band. The upper level $\Pi(1_1)$ is coupled with the $\Sigma(1_1)$ state through a Coriolis coupling term. The transition frequencies of the $\Sigma(1_1) \leftarrow \Sigma(0_0)$ and $\Pi(1_1) \leftarrow \Sigma(0_0)$ bands are listed in Table 5.11. The transitions are fit with the pseudodiatomic Hamiltonian Pickett’s SPFIT program and the spectroscopic constants are given in Table 5.12. The quality of the fit is satisfactory, with the root mean square of the transition errors as 0.0006 cm⁻¹.

Surprisingly, the B rotational constants from the fit are different from those of the Ar-NH₃ complex determined by microwave and far-IR spectroscopy, which is 2876.849(2) MHz for the $K=0$ state.(183). This indicating that the observed spectra does not belong to the binary complex containing Ar and NH₃ subunits. The carrier of these two band contains Ar and NH₃, so that it is named as “Ar-NH₃”. The possibility of ammonia dimer can be eliminated since although the ammonia dimer is also of pseudodiatomic Hamiltonian, the B rotational of its A state is $B=5136$ MHz and E state is $B=5110$ MHz. The possibility of ternary complex Ar₂-NH₃ can also be eliminated since its structure has been determined to be asymmetric top.

5.3.2 Ne-NH₃ Complex

The high resolution infrared spectrum of Ne-NH₃ complex is measured using the multipass direct absorption spectrometer in similar procedure as the Ar-NH₃ complex.

As mentioned above, the $\Pi(1_1) \leftarrow \Sigma(0_0)$ band of the ν_4 bending band of NH₃ is anticipated around 1647 cm⁻¹. Although for the Ar-NH₃ complex a $\Sigma \leftarrow \Sigma$ band instead of a $\Pi \leftarrow \Sigma$ band is observed, the predicted $\Pi \leftarrow \Sigma$ band is observed at 1647 cm⁻¹ for the Ne-NH₃ complex as shown in Fig. 5.29. A strong Q branch and the $P(2)$, $P(3)$, $R(0)$, $R(1)$ transition can be unambiguously determined. Unlike the “Ar-NH₃” complex that has a much larger moment of inertia than

5.3 High Resolution Infrared Spectra of “Ar+NH₃” and Ne-NH₃

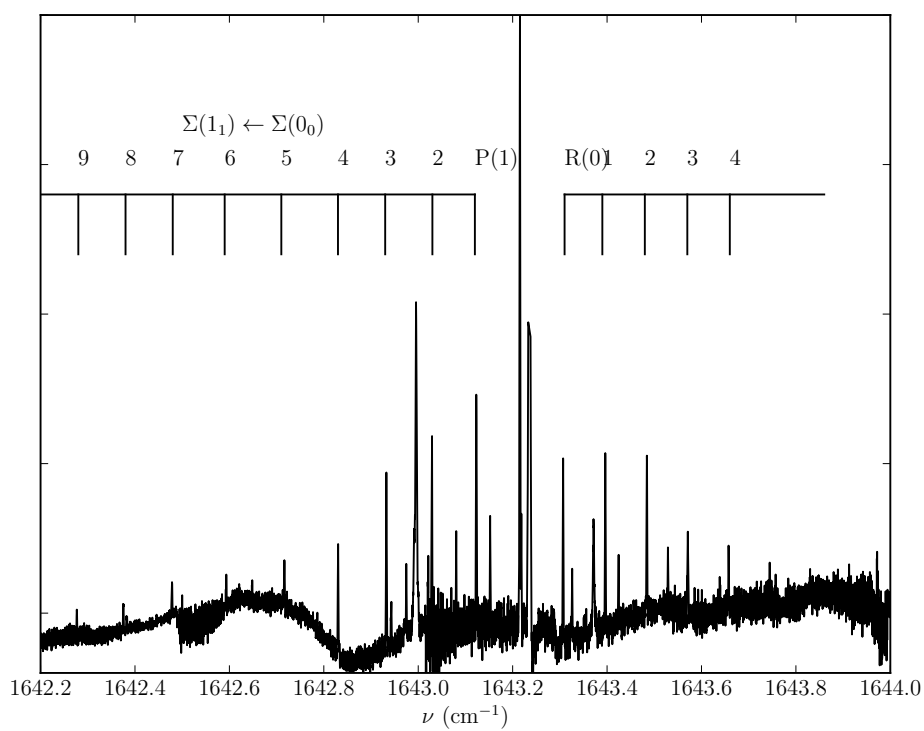


Figure 5.27: $\Sigma(1_1) \leftarrow \Sigma(0_0)$ band of *ortho* “Ar+NH₃” - There are two $\Sigma \leftarrow \Sigma$ overlapped. The weaker band belongs to the ²²Ne-NH₃ isotopologue.

5.3 High Resolution Infrared Spectra of “Ar+NH₃” and Ne-NH₃

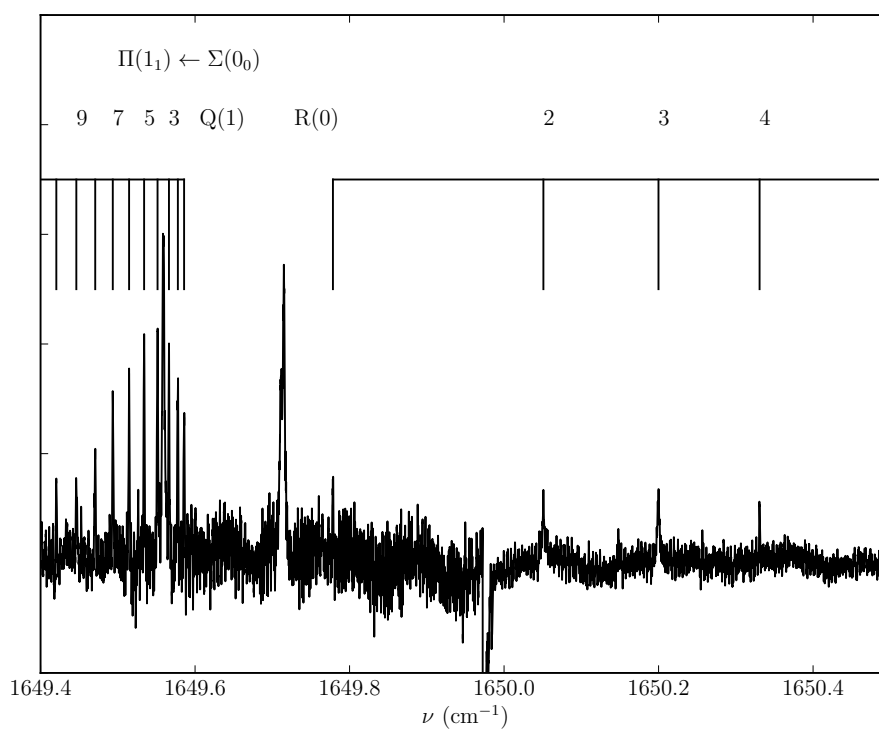


Figure 5.28: $\Pi(1_1) \leftarrow \Sigma(0_0)$ band of *ortho* “Ar-NH₃” - Assignment of the band is based on correlation with the Ar-H₂O spectra.

5.3 High Resolution Infrared Spectra of “Ar+NH₃” and Ne-NH₃

$J' \leftarrow J''$	$\Pi(1_1) \leftarrow \Sigma(0_0)$	$\Sigma(1_1) \leftarrow \Sigma(0_0)$
<i>P</i> -branch		
0 \leftarrow 1		1643.1230(7)
1 \leftarrow 2	1616.3275(9)	1643.0290(8)
2 \leftarrow 3	1615.8992(114)	1642.9324(10)
3 \leftarrow 4	1615.4521(7)	1642.8302(10)
4 \leftarrow 5	1614.9616(2)	1642.7164(10)
5 \leftarrow 6	1614.9616(2)	1642.5934(16)
6 \leftarrow 7	1614.9616(2)	1642.4785(7)
7 \leftarrow 8	1614.9616(2)	1642.3753(1)
8 \leftarrow 9	1614.9616(2)	1642.2758(0)
<i>Q</i> -branch		
1 \leftarrow 1	1649.5858(6)	
2 \leftarrow 2	1649.5777(2)	
3 \leftarrow 3	1649.5662(1)	
4 \leftarrow 4	1649.5514(5)	
5 \leftarrow 5	1649.5340(8)	
6 \leftarrow 6	1649.5146(0)	
7 \leftarrow 7	1649.4935(12)	
8 \leftarrow 8	1649.4708(8)	
9 \leftarrow 9	1649.4463(18)	
10 \leftarrow 10	1649.4204(6)	
<i>R</i> -branch		
1 \leftarrow 0		1643.3068(8)
2 \leftarrow 1		1643.3962(7)
3 \leftarrow 2		1643.4843(6)
4 \leftarrow 3		1643.5711(9)
5 \leftarrow 4		1643.6574(3)
6 \leftarrow 5		
7 \leftarrow 6		

Table 5.11: Observed *ortho* Ar-NH₃ transitions (in cm⁻¹) of the $\Pi(1_1) \leftarrow \Sigma(0_0)$ and $\Sigma(1_1) \leftarrow \Sigma(0_0)$ band.

5.3 High Resolution Infrared Spectra of “Ar+NH₃” and Ne-NH₃

	$v(\text{cm}^{-1})$	$B(\text{MHz})$	$D(\text{MHz})$	$H(\text{kHz})$
Ground				
$\Sigma(0_0)$	0	1372.5(27)	-1.218(55)	0 ^a
$v_4=1$				
$\Sigma(1_1)$	1643.2140(5)	1778(57)	1.861(214)	66.500(5100)
$\Pi^e(1_1)$	1649.7102(6)	1253(45)	-0.490(1290)	-99.800(23700)
$\Pi^f(1_1)$	1649.6336(25)	1314(3.3)	-1.429(71)	-0.677(272)
β	0.29(2)			

^a Zero within uncertainty, and set to zero in final fit.

Table 5.12: Band origin and rotational constants of Ar-NH₃ from the fit. The $\Sigma(1_1)$ level and the e parity of the $\Pi(1_1)$ level are mixed by a Coriolis coupling term β .

the binary Ar-NH₃ complex, the spacing between the $P(2)$, $P(3)$, $R(0)$, $R(1)$ transitions are in good agreement with the binary Ne-NH₃ complex. The P and R branch transitions of the corresponding ²²Ne-NH₃ isotopologue can also be clearly identified as shown in Fig. 5.29. Therefore, the Q branch of the ²⁰Ne and ²²Ne bands are overlapped. It is interesting to notice some pre-dissociation broadening of the Q branch transitions.

Surprisingly, $P(2)$, $P(3)$, $R(0)$, $R(1)$ are the only strong P and R branch transitions that can be observed. Based on the intensity of the $P(2)$, $P(3)$, $R(0)$, $R(1)$ transitions, transitions such as $P(3)$ and $R(2)$ should be easily measured. However, the intensity of the band suddenly disappeared. One possible explanation is that the f parity of the $\Pi(1_1)$ level is strongly mixed with other internal rotor states and probably avoided level crossing occurs that shifts the other P and R branch transitions.

The other rovibrational bands observed for the Ne-NH₃ are shown in Fig. 5.30. Based on the intensity of the spectral feature, the complicated rovibrational transitions should belong to the Ne-NH₃ complex. But the structure of the spectrum shows features of an asymmetric semi-rigid rotor. Another region of the measured spectrum shown in Fig. 5.31 also shows clear evidence that larger clusters are formed in the experiment. The intensity of this band is ~ 10 times weaker than the bands of Ne-NH₃, indicating that they are probably larger clusters such as Ne₂-NH₃. Assignment of the band is needed to elucidate the rovibrational energy levels of the Ne-NH₃ complex in this region.

The other Rg-H₂O/NH₃ complexes including the Kr-H₂O/NH₃ and Xe-H₂O/NH₃ complexes can be expected to have similar rovibrational transitions. However, as

5.3 High Resolution Infrared Spectra of “Ar+NH₃” and Ne-NH₃

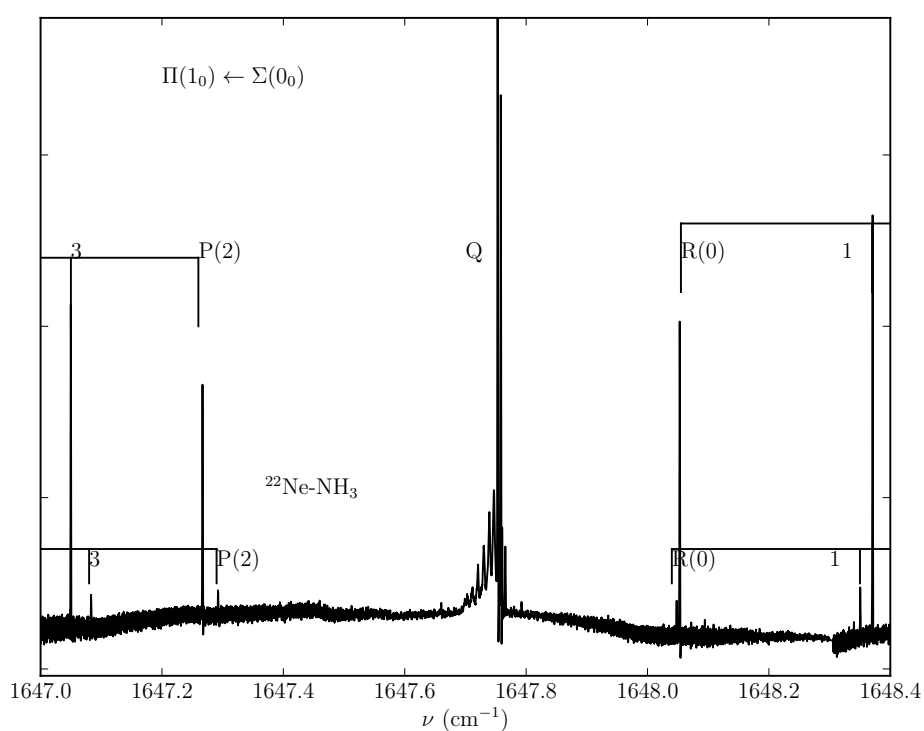


Figure 5.29: The $\Pi(1_1) \leftarrow \Sigma(0_0)$ band of Ne-NH₃ - Both the ²⁰Ne and ²²Ne isotopologue are presented in the spectrum. The Q branches of the two bands are overlapped is very dense. Pre-dissociation of the Q branch transitions can also be seen.

5.3 High Resolution Infrared Spectra of “Ar+NH₃” and Ne-NH₃

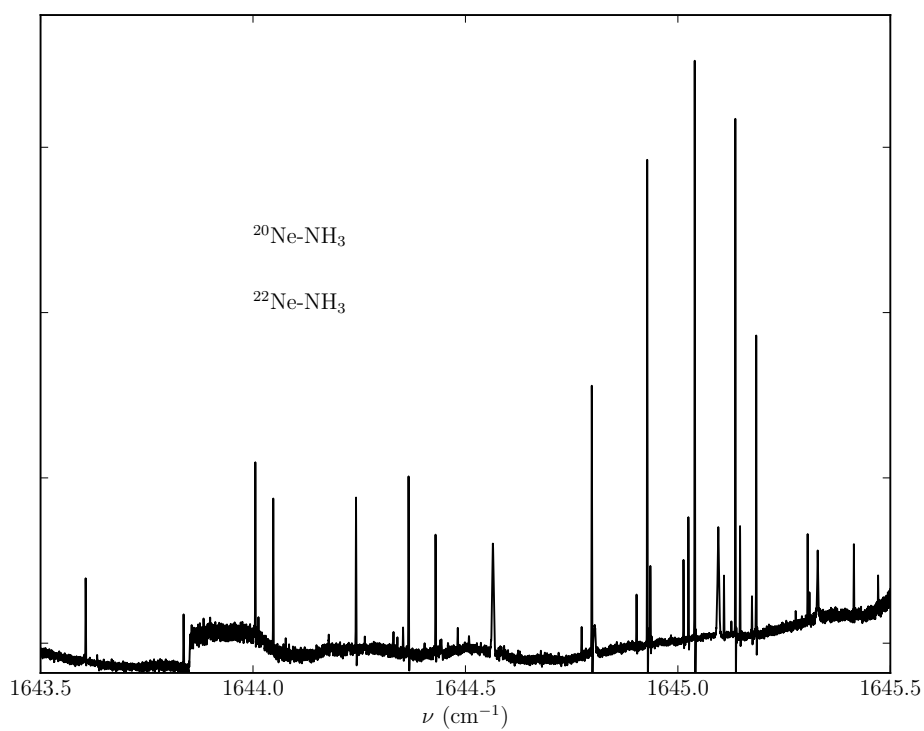


Figure 5.30: Ne-NH₃ spectrum - The strong transitions displayed belong to the Ne-NH₃ complex.

5.3 High Resolution Infrared Spectra of “Ar+NH₃” and Ne-NH₃

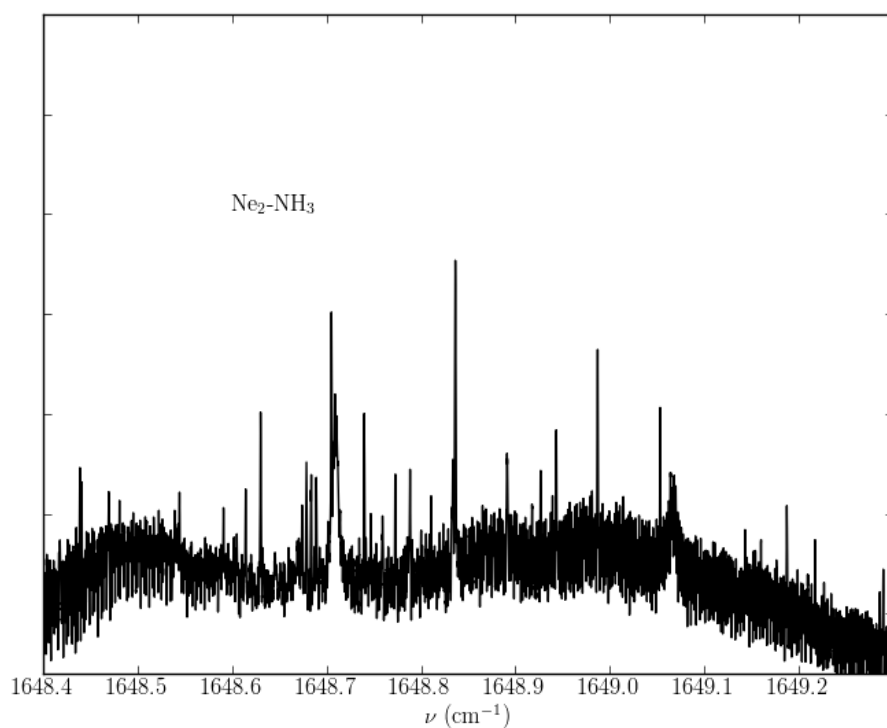


Figure 5.31: Spectrum of larger clusters of Ne and NH₃ - Intensity of this band is much weaker than the Ne-NH₃ dimer spectrum. The carrier of this band is temporarily assigned to the Ne₂-NH₃.

5.3 High Resolution Infrared Spectra of “Ar+NH₃” and Ne-NH₃

the binding energy increase for Rg atoms with larger susceptibility, deviation from the pseudo-diatomic approximation is expected. Future work is needed to confirm this postulate. Also larger clusters such as Ar₂-H₂O and Ne₂-H₂O, and the Ar₂-NH₃ and Ne₂-NH₃ complexes can also be generated in the supersonic free jet expansion. They are anticipated to be regular asymmetric top rotors based on their equilibrium geometry. The high resolution rovibrational spectroscopy measured in the region of the ν_2 mode of H₂O or the ν_4 mode of NH₃ can confirm their structures.

6

Infrared and microwave spectra of the acetylene-ammonia and carbonyl sulfide-ammonia complexes

In this chapter the combined high resolution infrared and microwave spectroscopic investigation of the acetylene-ammonia and carbonyl sulfide-ammonia complexes is presented. The high-resolution infrared spectra presented are measured using the pulsed slit-nozzle multipass absorption spectrometer based on the external cavity quantum cascade laser introduced in Sec. 4.2.2 The pure rotational spectra are measured using a pulsed nozzle beam Fourier transform microwave spectrometer.(294)

The rovibrational transitions of the acetylene-ammonia complex are measured at $6\ \mu\text{m}$ in the vicinity of the ν_4 band of ammonia. The two bands measured are assigned to the perpendicular $K=0\leftarrow-1$ and $K=2\leftarrow-1$ sub-band. The previously reported pure rotational transitions have been extended to higher J and K values with ^{14}N nuclear quadrupole hyperfine components detected and analyzed. The spectral analysis reveals that acetylene binds to ammonia through a $\text{C-H}\cdots\text{N}$ weak hydrogen bond to form a C_{3v} symmetric top, consistent with the previous microwave(75) and infrared spectroscopic study at $3\ \mu\text{m}$ (100).

A parallel study has also been carried out for the carbonyl sulfide-ammonia complex whose pure rotational and rovibrational spectrum at $6\ \mu\text{m}$ have been detected and analyzed for the first time. The band measured is assigned to the perpendicular $K=1\leftarrow 0$ sub-band. The spectral and the subsequent structural analyses, in conjunction with the corresponding *ab initio* calculation, indicate

that the OCS-NH₃ complex assumes C_{3v} symmetry with S atom pointing to N atom of NH₃, in contrast with the “T-shaped” geometries obtained for the isoelectronic N₂O-NH₃ and CO₂-NH₃ complexes. The intermolecular interaction in OCS-NH₃ is mainly governed by the electric dipole-dipole interaction. The strength of the weak C-H···N hydrogen bond of HCCH-NH₃ was found to be much greater than the S···N bond in the OCS-NH₃ complex.

Both of these complexes are C_{3v} symmetric, thus although separated by a large energy gap of $\sim (A - B)$, the ground state $K = 0$ and $K = 1$ levels are equally populated, because the $K=0$ and 1 levels are associated with an A -symmetry *ortho* spin function and an E -symmetry *para* spin function, respectively, with a spin statistical weight ratio of 1 : 1. The *ortho* and *para* species cool down separately in a supersonic jet expansion, resulting in a similar intensity for the observed $K=0$ and $K=1$ rotational transitions.

6.1 Introduction

Inter(intra) molecular interactions govern the physical and biological properties of matter. One of the strongest and most important types of interaction is the hydrogen bond X-H···Y, in which the electropositive H atom bonded with the more electronegative X species is attracted to electron rich Y (typically a nitrogen, oxygen, or fluorine atom) of another molecule or at another site of the same molecule.(10) Although the interaction may consist of contributions from electrostatic interactions, polarization or induction interactions, dispersion, charge transfer induced covalence, and exchange correlation effects,(116, 240, 82) electrostatic interactions between electric dipoles are often a major component, distinctively characterized by linear directionality.

Vibrational spectroscopy is an important method to identify hydrogen bonds.(181, 12, 308, 20, 156) Usually the vibrational band corresponding to the X-H stretch gets broader, gains intensity, and is red shifted upon formation of a X-H···Y hydrogen bond. High resolution infrared spectroscopy can reveal detailed information of weakly bound complexes and nature of the intermolecular interactions.(177, 186, 218, 178, 185, 22) But there are relatively few experimental high resolution spectroscopic studies of the C-H···Y weak hydrogen bonds,(21) which have been identified in a large number of crystallographic data(236) and a few gas phase studies.(261, 212, 103) Most of these studies have been concentrated on complexes with subunits that both have large permanent electric dipole moments and the C-H bond connecting to electronegative species, such as chloroform and

HCN (102). Therefore the C-H bond length usually decreases upon complexation, leading to the unusual blue-shifted C-H stretching frequency that gives name to the interactions in such complexes, “improper hydrogen bonds”. Besides these strongly dipolar systems, it is of significant interest to study C-H \cdots Y weak hydrogen bond consisting of a non-polar partner.

One such model systems is the acetylene-ammonia (HCCH-NH₃) complex. The rotational spectrum of HCCH-NH₃ has been studied by Fraser *et al.*,⁽⁷⁵⁾ and the high resolution infrared spectrum in the vicinity of the C-H stretching vibration has also been measured.⁽¹⁰⁰⁾ These studies indicate that HCCH-NH₃ is a C_{3v} symmetric top complex with a C-H \cdots N weak hydrogen bond. Although there have been previous attempts to detect the infrared spectrum of this complex in the 6 μ m region of ammonia *E*-symmetry ν_4 deformation, no spectral feature had been conclusively identified.^(142, 197)

Carbonyl sulfide-ammonia (OCS-NH₃) complex also consists of ammonia with a linear molecule, but with a permanent dipole moment. Modest resolution infrared spectra of this complex had been measured at 10 μ m upon excitation of the OCS $2\nu_2$ bending overtone and NH₃ ν_2 umbrella motion.⁽⁷⁸⁾ Both bands display homogeneous broadening due to photo dissociation. No detailed spectroscopic assignments has been reported and therefore no direct structural information has been obtained. Microwave spectroscopic studies of the isoelectronic complexes, CO₂-NH₃ and N₂O-NH₃, showed that these complexes are “T-shaped”, with N of NH₃ pointing to the middle atom of the linear subunit.⁽⁷⁸⁾ The authors speculated that OCS-NH₃ may have a T-shaped structure as well. On the other hand, one may argue that with a much larger dipole moment (0.7 Debye) compared to N₂O (0.2 Debye) and CO₂ (no permanent dipole), it is feasible for OCS to bind to NH₃ through electric dipole-dipole interaction and form a C_{3v} symmetric structure with S atom pointing to ammonia, similar to that of the HCCH-NH₃ complex. So far, no microwave or high resolution infrared spectroscopic study has been reported for this complex to support either one of the proposed structures. Therefore, the OCS-NH₃ complex which has a larger dipolar subunit will provide interesting comparisons to the weak hydrogen bonded HCCH-NH₃ and the van der Waals N₂O-NH₃ and CO₂-NH₃ complexes.

In this chapter, we report the combined high resolution infrared and microwave spectroscopic studies and *ab initio* calculations of the HCCH-NH₃ and OCS-NH₃ complexes. From the spectral and subsequent structural analyses, together with the associated *ab initio* calculations, the structures and the nature

of the intermolecular forces at play in these two prototype complexes have been investigated in detail.

6.2 Microwave and Infrared Experiments

HCCH-NH₃ and OCS-NH₃ complexes were generated in a supersonic jet expansion with 0.5% of HCCH/ OCS and 0.5% of NH₃ mixture in Helium (Praxair) backing gas at room temperature. For the microwave measurements, a pulsed molecular beam Fourier transform microwave spectrometer based on the free induction decay of the pulsed excited sample in a microwave cavity was used to measure the rotational transitions of both complexes between 5 and 18 GHz.⁽²⁹⁴⁾ The bandwidth of the microwave cavity is around 1 MHz. The full line width at half maximum (FWHM) of a well resolved peak is about 30 kHz and the corresponding uncertainty is estimated to be around 2 kHz. The sample gas with a stagnation pressure around 4 Bar was expanded through a General Valve (Series 9) pulsed nozzle of 0.8 mm orifice diameter.

For the infrared measurements, the pulsed slit-jet multipass absorption spectrometer with an external-cavity quantum cascade laser described in Chapter 4 was used to record the rovibrational transition of the complexes at 6 μm . The sample gas with a stagnation pressure around 10 Bar was expanded through a homemade pulsed slit-jet nozzle with 40 mm \times 0.04 mm slit. The astigmatic multipass absorption cell was aligned with the 366-pass configuration. The full frequency coverage of the laser is from 1634 to 1680 cm^{-1} .

6.3 Results

6.3.1 *Ab initio* Calculations

To aid and to complement the spectroscopic study, *ab initio* calculations using the Gaussian03 program⁽⁸¹⁾ have been performed. *Ab initio* calculations of both the C_{3v} symmetric and T-shaped conformers as well as the NH \cdots O binding pair had been performed. The NH \cdots O conformer was found to be much less stable. In fact, this is not a minimum at the MP2 level of theory and was not further considered. Equilibrium geometries for both T-shaped and C_{3v} symmetric conformers of OCS-NH₃ have been obtained at the MP2/aug-cc-pVTZ level of theory. (An)harmonic frequency calculation have also been performed to obtain the spectroscopic constants and vibrational frequencies. Although theoretical

6.3 Results

study of HCCH-NH₃(91) with emphasis on the dissociation energy had been reported previously, we have also performed the parallel *ab initio* calculations for HCCH-NH₃ for comparison. The corresponding equilibrium structures, single point energies, with basis set super position errors (BSSEs)(38) and harmonic and anharmonic zero-point energy (anh-ZPE) corrections have been calculated and are summarized in Table 6.1. Calculation details are listed below: Harmonic and anharmonic vibrational frequencies and zero-point energies of the complexes and the monomer subunits at the MP2/aug-cc-pVTZ level of theory. HCCH-NH₃:

Mode(Quanta)	E(harm)	E(anharm)	Aa(z)	Ba(x)	Ca(y)
Fundamental Bands (DE w.r.t. Ground State)					
1(1)	3496.371	3384.925	0.180750	-0.001946	-0.001946
2(1)	3494.521	3361.181	0.161732	-0.001980	-0.001980
3(1)	3335.407	3259.993	0.189251	-0.000978	-0.000978
4(1)	1949.820	1924.933	0.193146	-0.002007	-0.002007
5(1)	1076.846	1014.298	0.147592	-0.002292	-0.002292
6(1)	130.982	136.235	0.193765	-0.003977	-0.003977
7(1)	3639.281	3471.484	0.183533	-0.002027	-0.002027
8(1)	3639.281	3471.639	0.183533	-0.002027	-0.002027
9(1)	1669.153	1626.978	0.136596	-0.001978	-0.002004
10(1)	1669.153	1627.728	0.136596	-0.002004	-0.001978
11(1)	868.800	773.318	0.197668	-0.003414	-0.003388
12(1)	868.800	774.761	0.197668	-0.003388	-0.003414
13(1)	640.486	644.191	0.194749	-0.002215	-0.002246
14(1)	640.486	646.389	0.194750	-0.002246	-0.002215
15(1)	213.692	223.212	0.540488	-0.002460	-0.002516
16(1)	213.692	217.098	0.540487	-0.002516	-0.002460
17(1)	90.760	151.613	0.150804	-0.001465	-0.001682
18(1)	90.760	156.274	0.150804	-0.001682	-0.001465
ZPE(harm) = 0.16585D+03 kJ/mol			ZPE(anh)= 0.16338D+03 kJ/mol		

OCS-NH₃:

Mode(Quanta)	E(harm)	E(anharm)	Aa(z)	Ba(x)	Ca(y)
Fundamental Bands (DE w.r.t. Ground State)					
1(1)	3496.905	3352.323	0.310162	-0.000321	-0.000321
2(1)	2069.121	2044.655	0.352849	-0.000399	-0.000399
3(1)	1061.474	986.344	0.300634	-0.000466	-0.000466
4(1)	878.034	865.696	0.352474	-0.000318	-0.000318
5(1)	86.661	69.156	0.352690	-0.001312	-0.001312
6(1)	3642.217	3474.483	0.344760	-0.000326	-0.000326

6.3 Results

7(1)	3642.217	3474.412	0.344760	-0.000326	-0.000326
8(1)	1668.642	1621.773	0.295348	-0.000351	-0.000347
9(1)	1668.642	1622.226	0.295348	-0.000347	-0.000351
10(1)	534.858	542.887	0.353333	-0.000430	-0.000439
11(1)	534.858	537.535	0.353333	-0.000439	-0.000430
12(1)	123.310	111.301	0.842806	-0.000338	-0.000353
13(1)	123.310	114.526	0.842811	-0.000353	-0.000338
14(1)	33.234	41.209	0.328577	-0.000293	-0.000388
15(1)	33.234	51.612	0.328575	-0.000388	-0.000293
ZPE(harm) = 0.11721D+03 kJ/mol			ZPE(anh)= 0.11519D+03 kJ/mol		

NH₃:

Mode(Quanta)	E(harm)	E(anharm)	Aa(z)	Ba(x)	Ca(y)
Fundamental Bands (DE w.r.t. Ground State)					
1(1)	3503.370	3360.670	-0.217151	-0.217197	-0.154949
2(1)	1039.089	961.134	-0.149187	-0.149168	-0.174113
3(1)	3650.040	3484.095	-0.241515	-0.240649	-0.120067
4(1)	3650.040	3484.114	-0.240613	-0.241551	-0.120067
5(1)	1668.900	1621.450	0.300007	0.016024	-0.172464
6(1)	1668.900	1621.453	0.016029	0.300003	-0.172464
ZPE(harm) = 0.90799D+02 kJ/mol			ZPE(anh)= 0.89335D+02 kJ/mol		

HCCH:

Frequencies --	601.3897	601.3897	753.9250
Frequencies --	753.9250	1967.8846	3431.6016
Frequencies --	3533.6350		
Zero-point correction=			0.026526 (Hartree/Particle)

OCS:

Frequencies --	522.6526	522.6526	888.0232
Frequencies --	2083.7994		
Zero-point correction=			0.009152 (Hartree/Particle)

6.3.2 The HCCH-NH₃ Complex

We assume the band origin of the ν_4 *E*-symmetry deformation of NH₃ monomer to be 1626.825(2) cm⁻¹, which is the average of its two ν_4 fundamentals centered at 1626.276(1) cm⁻¹ (*s* ← *s*) and 1627.375(2) cm⁻¹ (*a* ← *a*), where *s* and *a* are the symmetry labels of the two inversion tunneling states.(60) The umbrella

tunnelling motion of NH_3 in the complex is expected to be quenched because of the weak hydrogen bonding. Indeed, no tunnelling splitting was observed in the previous high resolution infrared study at $3\ \mu\text{m}$.(100) Based on the anharmonic frequency calculations of the NH_3 monomer and the HCCH-NH_3 complex,(91) one expects that the $\text{NH}_3\ \nu_4$ band to be blue shifted by $\sim 5\ \text{cm}^{-1}$ when NH_3 binds to HCCH through a weak $\text{C-H}\cdots\text{N}$ hydrogen bond. In the initial search from $1634\ \text{cm}^{-1}$ to $1680\ \text{cm}^{-1}$, the full frequency region covered by the quantum cascade laser in use, only one infrared band was observed. This is shown in Fig. 6.1. This band was confirmed to belong to HCCH-NH_3 by omitting either HCCH and NH_3 from the sample mixture. Since the transition dipole moment of $\text{NH}_3\ \nu_4$ deformation is perpendicular to the a -axis of HCCH-NH_3 , one expects to see a perpendicular band. Indeed, the band observed is consistent with a typical symmetric top perpendicular band. A closer examination reveals that $R(0)$, $P(1)$, $P(2)$ transitions ($\Delta J(J'')$) are missing. Therefore this band was assigned to the $K = 2 \leftarrow 1$ subband. The frequencies of the observed transitions are listed in Table 6.3.

As A'' rotational constant was estimated to be about 196 GHz from the *ab initio* calculation, one would expect the $K=1$ levels not to be substantially populated in a jet expansion in general. The observation of the $K = 2 \leftarrow 1$ subband is a consequence of nuclear spin statistics. Since HCCH-NH_3 is of C_{3v} symmetry with three identical hydrogen nuclei, the $K=0$ and $K=1$ levels are associated with A and E spin functions, respectively, with a 1:1 spin statistical weight ratio. In the jet expansion, the meta-stable $K=1$ levels cool down separately from the $K=0$ levels. As a result, the $K = 2 \leftarrow 1$ subband is of similar intensity as the $K = 1 \leftarrow 0$ subband under jet expansion.

The $K=1\leftarrow 0$ sub-band, that should have similar intensity, was not observed in the full laser range from $1634\ \text{cm}^{-1}$ to $1670\ \text{cm}^{-1}$. It was postulated that a large first-order Coriolis perturbation likely shifts the $K=1\leftarrow 0$ sub-band out of the laser frequency range. Later on, we acquired a new quantum cascade laser which provides a frequency coverage down to $1610\ \text{cm}^{-1}$. Searches for the $K=1\leftarrow 0$ and other new sub-bands were carried out.

The full frequency range from $1680\ \text{cm}^{-1}$ down to $1610\ \text{cm}^{-1}$ was scanned. While the $K=2\leftarrow 1$ sub-band was observed again, the only other spectral feature detected was a sub-band with slightly less intensity centered at $1622\ \text{cm}^{-1}$. This is shown in Fig. 6.2. Clearly this is a typical perpendicular sub-band of a symmetric top molecule, with a strong Q -branch and regular P - and R -branch structures. A number of strong transitions of the NH_3 monomer are also present

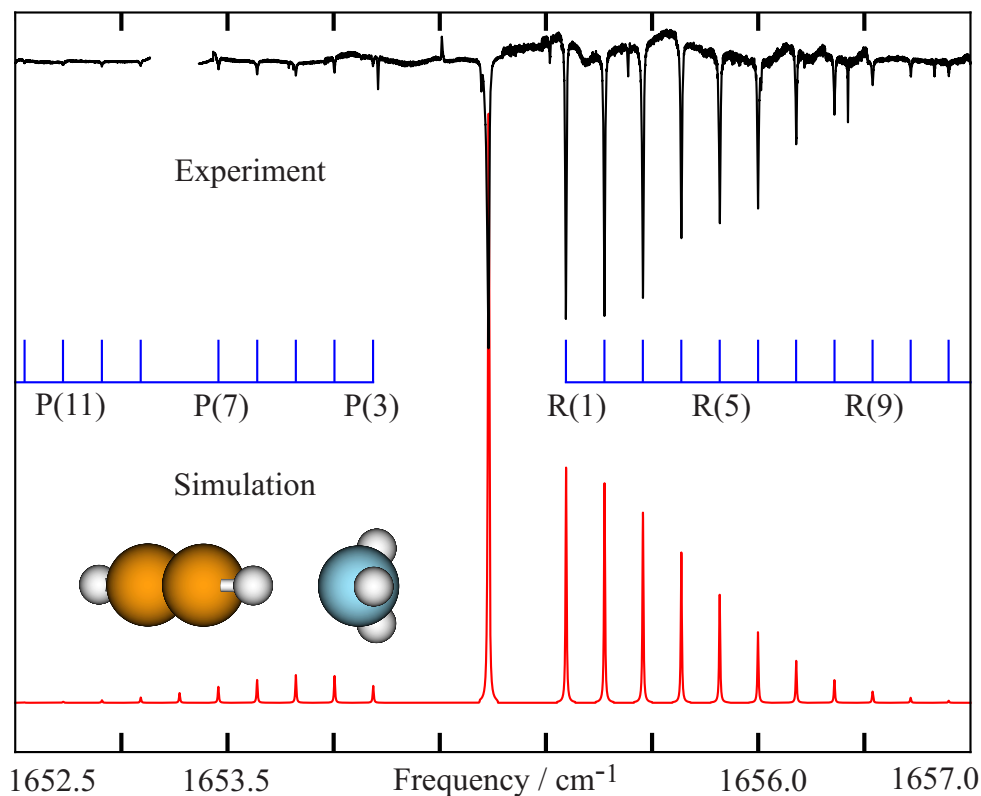


Figure 6.1: Experimental high resolution infrared spectrum of the $K = 2 \leftarrow 1$ sub-band of HCCH-NH₃, with the calculated spectrum based on the constants in Table 6.4. The spectrum consists of several frequency scans. Each scan has 50 averaging sweeps to increase the signal-to-noise ratio. The gap around the $P(8)$ transition was due to a strong ammonia peak.

in the spectrum. A closer examination revealed that while the $P(1)$ transition was presented, the $R(0)$ transition was noticeably missing in the spectrum. This indicates that the observed band must belong to the $K=0 \leftarrow 1$ sub-band, rather than the $K=1 \leftarrow 0$ sub-band initially expected. The transitions observed for the new band exhibit a broader line width of $\sim 0.005 \text{ cm}^{-1}$ (FWHM), due to vibrational predissociation. This width is the same as what was observed previously for the $K=2 \leftarrow 1$ sub-band.

The observed infrared transitions are listed in Table 6.3. A global fit of the current measurement and the previous measurement of the $K=2 \leftarrow 1$ sub-band, together with the pure rotational transitions with the ^{14}N nuclear quadrupole splittings was performed using the standard prolate top Hamiltonian using Pick-

ett's CALPGM/SPFIT/SPCAT program.(202) Each of the infrared transitions was treated as a blend of nuclear hyperfine structures due to the ^{14}N nuclear quadrupole coupling, weighted with their respective intensity. The A rotational constant and the sextic centrifugal distortion constants of the excited and ground vibrational states were fixed to the same value in the fitting procedure. The resulting spectroscopic parameters are listed in Table 6.4. The quality of the fit was good with the infrared rms deviation of 0.00064 cm^{-1} comparable to the experimental uncertainty of our infrared measurement of about 0.001 cm^{-1} . The rotational constants of the ground vibrational state are almost identical to those previously fitted by the microwave transitions, since they are essentially determined by the highly accurate microwave measurements. The observation of two sub-bands allowed us to determine the A rotational constant to be $8.18301(7)\text{ cm}^{-1}$, which was greater than the 6.228 cm^{-1} value of NH_3 monomer.(259) The decreased moment of inertia might be due to shrinking of the 3 identical hydrogen nuclei about the symmetric axis upon formation of the HCCH-NH_3 complex. It is also partly as a result of the quenching of the inversion motion of the NH_3 molecule. The ν_0 term was correctly determined to be $1630.4548(2)\text{ cm}^{-1}$, which indicates the band origin of the ν_4 E -symmetry deformation of NH_3 in the complex is more than 4 cm^{-1} blue shifted from the band origin of NH_3 at $1626.825(2)\text{ cm}^{-1}$.(60) This experimentally observed blue shift was predicted by the *ab initio* calculation at the MP2/aug-cc-pVTZ level of theory, in which the ν_4 deformation of NH_3 is calculated to be 1627.35 cm^{-1} in the HCCH-NH_3 complex and 1621.47 cm^{-1} in the NH_3 monomer. The B rotational constant of the excited state decreased slightly compared to the ground state value while the centrifugal distortion constant D_J increases, indicating that the $\text{C-H}\cdots\text{N}$ hydrogen bond gets weaker and the corresponding bond length gets slightly longer upon the deformation excitation of NH_3 .

But where is the $K=1\leftarrow 0$ sub-band? One would expect the $K=1\leftarrow 0$ sub-band lies approximately in the middle of the $K=0\leftarrow 1$ (1622 cm^{-1}) and $K=2\leftarrow 1$ (1654 cm^{-1}) sub-bands, i.e., around 1638 cm^{-1} , with similar intensity. The 1638 cm^{-1} region was scanned in our previous study and re-scanned with great effort in the current study. No new band was detected in this region. One possible explanation to the mysterious missing of the $K=1\leftarrow 0$ sub-band is that the $K=1$ levels of the upper level is perturbed by a Fermi resonance between the ν_4 mode and the overtone of the degenerate HCCH bending modes which was predicted to be 774 cm^{-1} based on the MP2/aug-cc-pVTZ level of theory. The $K=0$ and $K=2$ levels of the upper state are associated with the E symmetry spin function while

the corresponding $K=1$ levels are associated with the A symmetry spin function. The $K=1$ levels might interact with an A symmetry level of the HCCH bending overtone, causing a significant shift of the $K=1\leftarrow 0$ sub-band. A schematic diagram of the proposed Fermi resonance is shown in Fig. 6.3.

The corresponding a -type prolate top microwave transitions of HCCH-NH₃ had been reported previously, with K up to 1 and J to 2.(75) We extended the measurements with K up to 2 and J up to 3. Since the $K = 0$ and $K = 1$ levels are equally populated because of the spin statistics, the ¹⁴N nuclear quadrupole hyperfine structures of $K = 1 \leftarrow 0$ and $K = 2 \leftarrow 1$ transitions are of similar intensity. The $K = 3 \leftarrow 2$ transitions, which are also associated with the E -symmetry spin function, were observed with much less intensity because of collisional relaxation to the $K = 1$ levels. We also re-measured all previously reported transitions for consistency. The experimental microwave transitions with ¹⁴N nuclear hyperfine splitting are listed in Table 6.2, together with the difference between the observed and calculated frequencies. The ¹⁴N nuclear hyperfine components of the $J, K=3, 1\leftarrow 2, 1$ transition are depicted in Fig. 6.4 (a).

The rotational transitions were fitted with a standard semi-rigid symmetric top Hamiltonian using Pickett's SPFIT program.(202) The resulting spectroscopic constants are listed in Table 6.4. The constants obtained are very close to those reported previously, except that sextic centrifugal distortion constants are needed because $K = 3 \leftarrow 2$ transitions are also included in the fit. The B rotational constant of excited state is essentially the same as that of the ground state while the centrifugal distortion constant D_J increases, indicating the geometry of the complex remains unchanged while the C-H...N hydrogen bond gets weaker upon the ν_4 excitation.

A simulated spectrum is also shown in Fig. 6.1. The much greater intensity observed for the R verse the P branch was reproduced. This intensity pattern results from the Hönl-London factor for vibrational band of a symmetric top rotor at the very low rotational temperature achieved in the jet expansion.

6.3.3 The OCS-NH₃ Complex

No high resolution spectroscopic study of the OCS-NH₃ complex had been reported previously. The C_{3v} symmetric and T-shaped conformers of OCS-NH₃ were predicted to have only a small energy difference, with the C_{3v} symmetric conformer being slightly more stable. It is therefore not known a priori which conformer or both of them will be detected experimentally. Although the whole

available quantum cascade laser frequency region from 1634 cm^{-1} to 1680 cm^{-1} was scanned very carefully for any vibrational band due to OCS-NH₃, only one weak band centered at 1637.6 cm^{-1} was detected. This is depicted in Fig. 6.5. The band shows a perpendicular band pattern with a strong Q -branch band-head. Its intensity is considerably weaker than that of the $K = 2 \leftarrow 1$ subband of HCCH-NH₃ described above. Furthermore, the lines observed show much more severe predissociation broadening than those observed in the HCCH-NH₃ complex.

This band was tentatively assigned to the C_{3v} symmetric conformer based on the predicted the rotational constants and transition dipole moment. The NH₃ ν_4 band of the T-shaped conformer, on the other hand, was predicted to have a much different vibrational spectral pattern. It was further assigned to the $K = 1 \leftarrow 0$ subband because the $P(1)$, $P(2)$, and $R(0)$ transitions were all present in the spectrum. Applying the same spin statistical consideration for OCS-NH₃ as for HCCH-NH₃ discussed above, one would expect to detect the $K = 2 \leftarrow 1$ subband at the higher frequency region. This was, however, not observed in our laser frequency coverage up to 1680 cm^{-1} . It is worthy to point out as discussed in Sec. 2.4.3 the doubly degenerate excited vibrational levels of a perpendicular band of a symmetric top molecule are split by a large first-order Coriolis interaction which shifts the band origin of the $K + 1 \leftarrow K$ subband to:(196)

$$\begin{aligned} \nu = \nu_0 + [A'(1 - 2\zeta) - B'] + 2[A'(1 - \zeta) - B']K \\ + [(A' - B') - (A'' - B'')]K^2 \end{aligned} \quad (6.3.3.1)$$

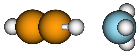


where ν is the subband origin and ζ is the first-order Coriolis coupling constant. Missing of the $K = 2 \leftarrow 1$ sub-band might due to a large $2[A(1 - \zeta) - B]$ spacing between the two sub-bands. Since the intensity of the $K = 1 \leftarrow 0$ subband is very weak, it is very likely that the $K = 2 \leftarrow 1$ subband may simply be too weak to be detected with the sensitivity of the current spectrometer.

In the preliminary spectroscopic analysis, the observed infrared transitions were fitted to a symmetric top rotor Hamiltonian with the rotational constants of the ground and excited vibrational states kept the same. The search for the microwave transitions was guided using the experimental B constant obtained from the preliminary analysis. The a -type pure rotational transitions were identified straightforwardly, with the characteristic ¹⁴N nuclear quadrupole hyperfine structure. The detected rotational transitions with J up to 5 are listed in Table 6.2. The ¹⁴N nuclear hyperfine structure of $J, K = 3, 0 \leftarrow 2, 0$ transition

is shown in Fig. 6.4 (b). Consistent with the infrared study, the intensity of the microwave transitions of OCS-NH₃ is much weaker than that of HCCH-NH₃. The rotational transitions were fitted with a standard semi-rigid symmetric top Hamiltonian, including the ¹⁴N nuclear quadrupole coupling term. The current rotational study therefore confirmed the assignment of the rovibrational transitions proposed above. The observed rovibrational transitions were then fitted with a standard semi-rigid rotor Hamiltonian for a perpendicular band. The spectroscopic constants obtained are listed in Table 6.5. It is noticed that the *B* rotational constant changes mildly, -0.02%, upon ν_4 excitation in OCS-NH₃, compared to 0.005% in HCCH-NH₃.

As mentioned before, the T-shaped conformer was predicted to be less stable than the observed *C*_{3v} symmetric conformer by only 2.2 kJ/mol. In the recorded infrared spectrum (see Fig. 6.5), besides the symmetric top OCS-NH₃ subband, the rest of the peaks are transitions of the NH₃ monomer, except the broad peak at 1637.709 cm⁻¹. We initially speculated that the T-shaped OCS-NH₃ might be the carrier for this unassigned broad peak. However, no corresponding transitions of the T-shaped conformer were found in the microwave spectrum. The failure to detect the T-shaped conformer confirms the *ab initio* prediction that the symmetric top conformer is more stable.

Table 6.1: *Ab initio* equilibrium structures, dissociation energies (ΔE_0), harmonic (v_{har}) and anharmonic (v_{anh}) frequencies of NH_3 ν_4 deformation, and spectroscopic constants for HCCH- NH_3 and the C_{3v} symmetric and T-shaped conformers of OCS- NH_3 .

	HCCH- NH_3	C_{3v} symmetric OCS- NH_3	T-shaped OCS- NH_3	
				
ΔE_0 1 ^a (kJ/mol)	16.5	10.0	8.2	
ΔE_0 2 (kJ/mol)	14.6	8.8	7.0	
ΔE_0 3 (kJ/mol)	9.2	6.4	4.8	
ΔE_0 4 (kJ/mol)	10.2	7.0	4.8	
ΔE_0 5 (kJ/mol)	9.3	n/a	n/a	
v_{har} (cm^{-1})	1669.1	1668.6	1666.6	1669.5 ^c
v_{anh} ^b (cm^{-1})	1627.0	1621.8	1615.9	1627.0
v'_{anh} ^b (cm^{-1})	1627.7	1622.2	n/a	n/a
A_0 (MHz)	195782	200748	7045	
B_0 (MHz)	2728	1494	2914	
C_0 (MHz)	n/a	n/a	2079	
D_J (kHz)	5.12	1.50	18	
D_{JK} (kHz)	509	474	25	
$A_{\nu=1}$ (MHz)	199877	209602	7305	7397
$B_{\nu=1}$ (MHz)	2669	1485	2955	2959
$C_{\nu=1}$ (MHz) ^c	2668	1484	2120	2129

^a 1: MP2/aug-cc-pVTZ(raw);

2:MP2/aug-cc-pVTZ(BSSE);

3:MP2/aug-cc-pVTZ(BSSE+har-ZPE);

4:MP2/aug-cc-pVTZ(BSSE+anh-ZPE);

5:CCSD(T)/6-311+G(3df,2p)(BSSE+scaled-har-ZPE) from Ref . (91).

^b Anharmonicity lifts the degeneracy of the excited NH_3 ν_4 deformation, as pointed out by Oka.(193)

^c The T-shaped conformer is an asymmetric top, thus has non-degenerate NH_3 ν_4 modes and unequal B and C rotational constants.

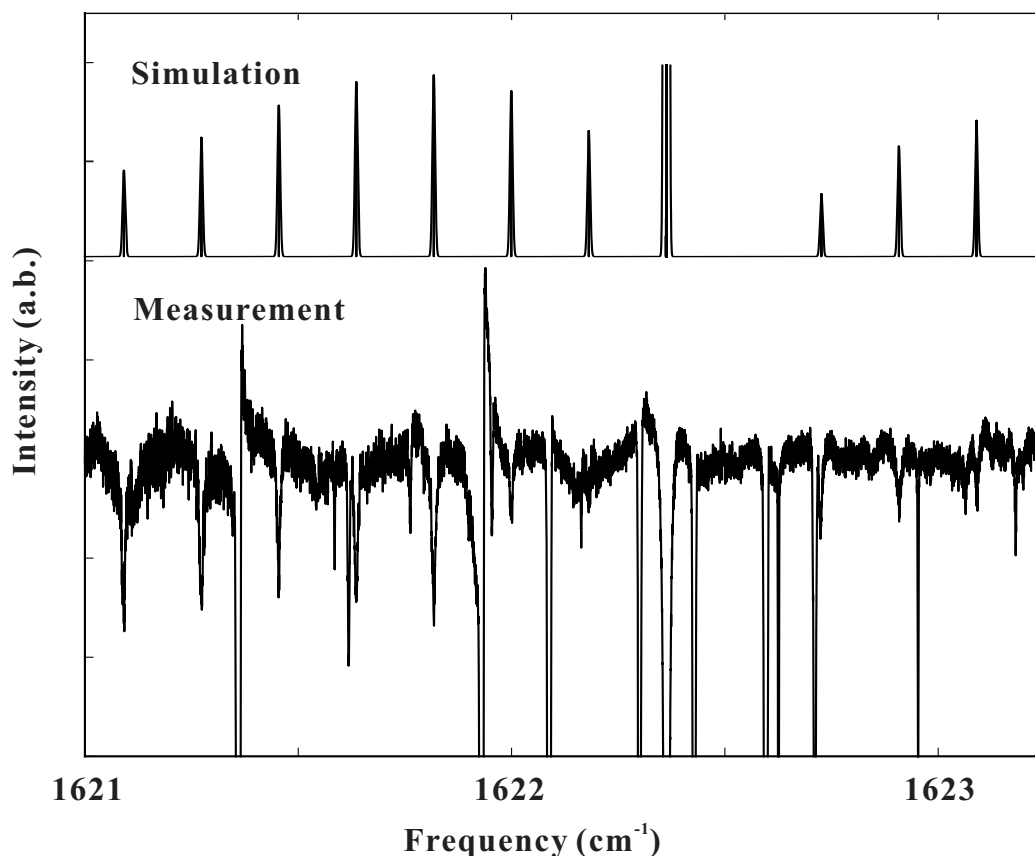


Figure 6.2: Observed infrared spectrum of the $K = 0 \leftarrow 1$ sub-band of HCCH-NH₃ at 1622 cm⁻¹. Several very strong NH₃ monomer transitions are present in the spectrum. Essentially, all unassigned lines are due to the NH₃ monomer. The full width half maximum of the HCCH-NH₃ transitions is ~ 0.005 cm⁻¹, slightly larger than the intrinsic line width of ~ 0.002 cm⁻¹, which is due to vibrational predissociation. Simulation of the spectrum with a rotational temperature of 4 K using the SPCAT program is provided in the upper trace.

Table 6.2: Observed microwave transitions of HCCH-NH₃ and OCS-NH₃ (in MHz).

$J'K'$	F'	$J''K''$	F''	HCCH-NH ₃	Δv^b	OCS-NH ₃	Δv^b
1 0	1	0 0	1			5448.3207	0.6
	2		1			5449.2573	2.0
	0		1			5450.6695	1.4
2 0	2	1 0	2	5996.4415	3.2	10897.1010	0.1
	1		0	5996.5962	2.7	10897.2572	0.3
	2		1	5997.3359	1.2	10898.0414	1.2
	3		2	5997.4092	8.3	10898.1065	0.8
	1		1	5998.8251	0.4		
2 1	2	1 1	1	5994.8918	0.1	10893.6791	0.7
	2		2	5995.3354	2.5		
	1		1	5995.6453	9.6	10894.4634	0.9
	3		2	5995.8145	1.5	10894.6523	0.1
	1		0	5996.7507	0.4	10895.6364	0.1
3 0	3	2 0	3	8994.9376	0.4	16345.6342	1.7
	2		1	8995.7436	0.9	16346.4841	1.9
	3		2	8995.8890	4.3	16346.6342	4.5
	4		3	8995.9320	3.2	16346.6768	0.7
	2		2	8997.2346	2.4	16348.0478	0.2
3 1	3	2 1	3	8992.6776	1.0	16340.5782	2.8
	3		2	8993.1555	0.9	16341.0885	4.4
	4		3	8993.4175	2.8	16341.3620	1.7
	2		2	8994.1584	0.4	16342.1410	0.2
3 2	3	2 2	2			16324.4750	0.4
	2		1			16326.0382	1.7
	4		3			16325.4821	1.3

^a $\mathbf{F} = \mathbf{I}_N + \mathbf{J}$ ^b $\Delta v = v_{\text{experimental}} - v_{\text{calculated}}$ (in kHz)

Table 6.3: Observed infrared transitions of HCCH-NH₃ $K = 2 \leftarrow 1$, $K = 0 \leftarrow 1$ subband and OCS-NH₃ $K = 1 \leftarrow 0$ subband (in cm⁻¹).

$J' \leftarrow J''$	HCCH-NH ₃ $K = 2 \leftarrow 1$	Δv	HCCH-NH ₃ $K = 0 \leftarrow 1$	Δv	OCS-NH ₃ $K = 1 \leftarrow 0$	Δv
<i>P</i> -branch						
11 \leftarrow 12	1652.5440	-0.0001				
10 \leftarrow 11	1652.7250	-0.0003				
9 \leftarrow 10	1652.9082	-0.0001	1620.5467	-0.0013		
8 \leftarrow 9	1653.0911	-0.0002	1620.7278	-0.0004	1636.6666	-0.0004
7 \leftarrow 8			1620.9092	-0.0006	1636.7667	-0.0006
6 \leftarrow 7	1653.4573	0.0005	1621.0911	-0.0003	1636.8650	-0.0024
5 \leftarrow 6	1653.6400	0.0006	1621.2733	0.0003	1636.9670	-0.0008
4 \leftarrow 5	1653.8219	-0.0000	1621.4542	-0.0003	1637.0681	0.0000
3 \leftarrow 4	1654.0038	-0.0004	1621.6359	0.0002	1637.2690	0.0046
2 \leftarrow 3	1654.1857	0.0005	1621.8179	0.0002	1637.1728	0.0002
1 \leftarrow 2			1621.9995	0.0002	1637.3692	0.0006
0 \leftarrow 1			1622.1808	0.0002		
<i>R</i> -branch ^a						
1 \leftarrow 0					1637.6693	0.0007
2 \leftarrow 1	1655.0943	-0.0010	1622.7242	-0.0020	1637.7684	-0.0001
3 \leftarrow 2	1655.2756	-0.0002	1622.9085	0.0006	1637.8685	0.0000
4 \leftarrow 3	1655.4566	-0.0004	1623.0909	0.0012	1637.9674	-0.0008
5 \leftarrow 4	1655.6377	-0.0001	1623.2725	0.0011	1638.0679	-0.0001
6 \leftarrow 5	1655.8187	0.0002			1638.1682	0.0005
7 \leftarrow 6	1655.9995	0.0004			1638.2673	-0.0002
8 \leftarrow 7	1656.1786	-0.0004			1638.3674	0.0003
9 \leftarrow 8	1656.3595	0.0003			1638.4670	0.0003
10 \leftarrow 9	1656.5388	0.0001			1638.5658	-0.0003
11 \leftarrow 10	1656.7183	0.0002			1638.6670	0.0010
12 \leftarrow 11	1656.8969	-0.0004			1638.7647	-0.0003
13 \leftarrow 12	1657.0767	0.0006				
14 \leftarrow 13	1657.2529	-0.0006				

^a The unresolved *Q*-branch transitions are not included in the fit.

6.3 Results

$J'K'$	F'	$J''K''$	F''	HCCH-NH ₃	Δv^b	OCS-NH ₃	Δv^b
4 0	4	3 0	4	11993.3234	1.2		
	3		2	11994.2455	5.6		
	4		3	11994.3152	0.3		
	5		4	11994.3392	1.8		
	3		3	11995.5906	0.6		
4 1	4	3 1	4	11990.0958	2.7		
	4		3	11990.8376	0.7		
	3		2	11990.9114	5.1		
	5		4	11990.9550	0.2		
	3		3	11991.9177	3.0		
5 0	4	4 0	3	14992.5149	6.4		
	5		4	14992.5613	4.6		
	6		5	14992.5749	2.6		
5 1	5	4 1	4	14988.2605	4.4		
	4		3	14988.2971	0.3		
	6		5	14988.3304	0.8		
6 0	5	5 0	4	17990.5478	3.6		
	7		6	17990.5876	2.1		
6 1	6	5 1	5	17985.4453	1.9		
	7		6	17985.4940	6.7		

^a $\mathbf{F} = \mathbf{I}_N + \mathbf{J}$ ^b $\Delta v = v_{\text{experimental}} - v_{\text{calculated}}$ (in kHz)

Table 6.4: Experimental spectroscopic constants of the vibrational ground and the ν_4 excited states of HCCH-NH₃.

	Ground	$\nu_4=1$
ν_0 (cm ⁻¹)	0	1630.4548(2)
A (cm ⁻¹)	8.18301(7) ^a	
B (MHz)	2724.56494(20)	2724.15(16)
D_J (kHz)	6.791(42)	13.64(93)
D_{JK} (kHz)	896.26(15)	538(44)
H_J (Hz)	-5.4(11) ^a	
H_{JK} (Hz)	129(10) ^a	
H_{KJ} (Hz)	745(16) ^a	
eQq_{aa}^N (MHz)	3.1307(4) ^a	

^a Fixed to the same value for both vibrational ground and excited state.

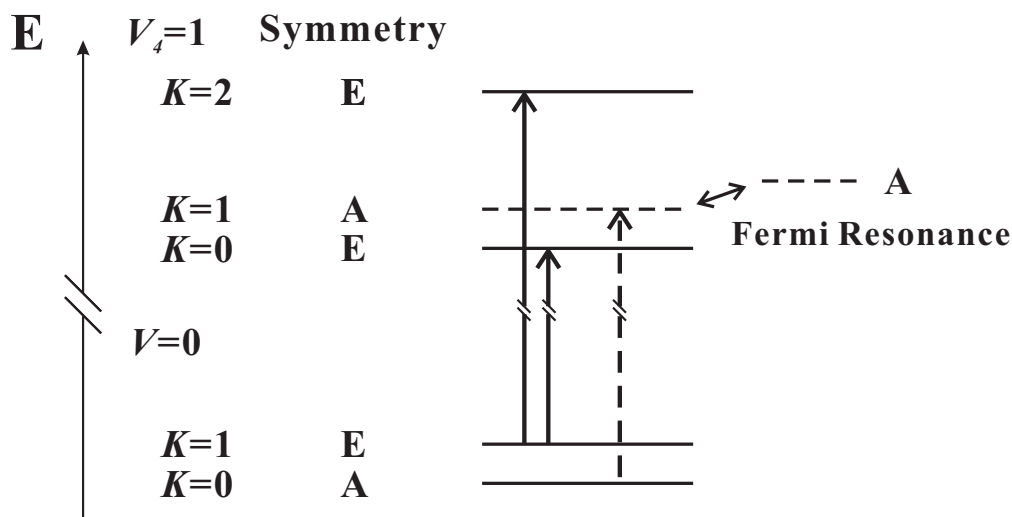


Figure 6.3: Proposed Fermi resonance causing the shift of $K=1$ level of HCCH-NH₃. -

Table 6.5: Experimental spectroscopic constants of the vibrational ground and excited states of OCS-NH₃.

	ν_0	$\nu_4=1$
OCS-NH ₃		$K = 1 \leftarrow 0$
ν (cm ⁻¹)	0	1637.61882(16)
B_0 (MHz)	1499.349248(52) ^a	1499.021(73)
D_J (kHz)	1.87152(101)	1.87152 ^b
D_{JK} (kHz)	425.461(81)	425.461 ^b
eQq_{aa}^N (MHz)	-2.97507(84)	

^a The number in parentheses are standard deviation in units of the last digits (1σ)

^b Fixed at the corresponding vibrational ground state value.

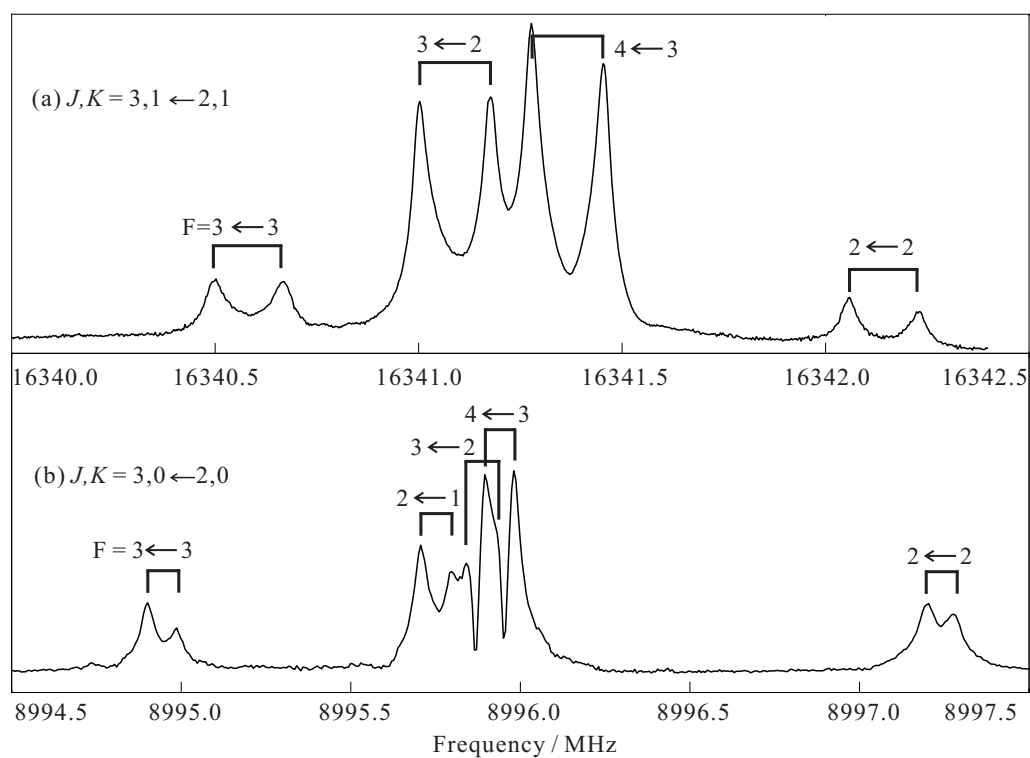


Figure 6.4: Observed composite microwave spectrum of (a) $J, K = 3, 1 \leftarrow 2, 1$ transitions of HCCH-NH₃ and (b) $J, K = 3, 0 \leftarrow 2, 0$ transitions of OCS-NH₃ with the ¹⁴N nuclear quadrupole hyperfine structures. Each line consists of two Doppler components resulting from a molecular expansion parallel to the MW cavity axis. The $F = 2 \leftarrow 1$ component of HCCH- NH₃ is buried under the center profile.

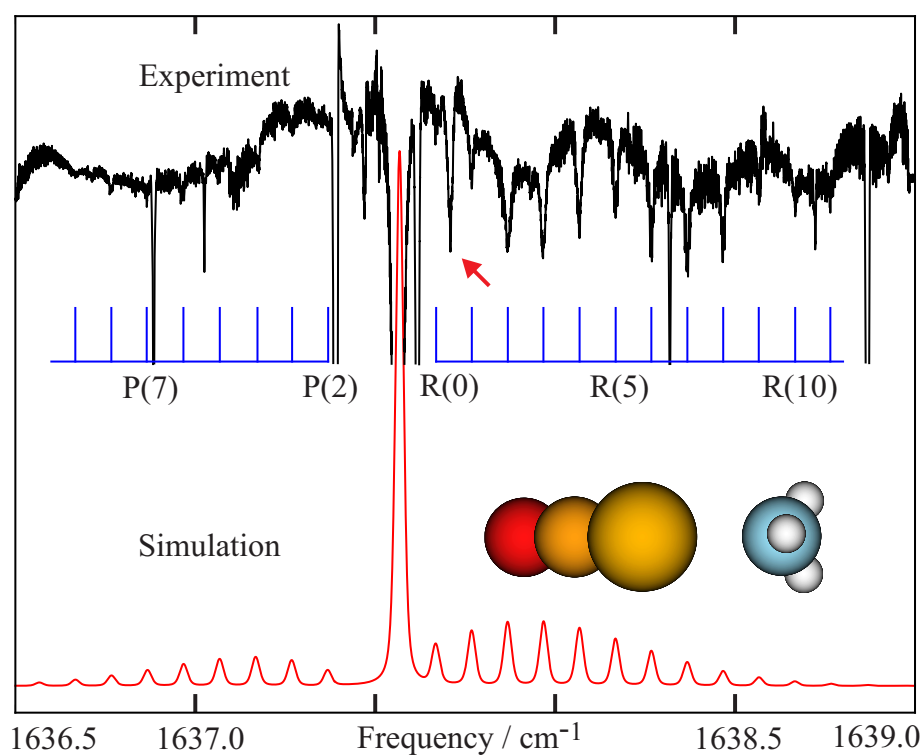


Figure 6.5: Observed infrared spectrum of OCS-NH₃ at 6 μm, together with the corresponding simulated spectrum using the PGOPHER program. The spectrum consists of several scans and each scan is averaged with 50 sweeps. The strong transitions with a line width of $\sim 0.015 \text{ cm}^{-1}$ are due to the NH₃ monomer. The broad peak at 1637.709 cm^{-1} (marked with an arrow) is unassigned. See further discussions in text.

6.4 Discussion

6.4.1 Structure and Dynamics

Both the infrared and microwave spectra measured are consistent with the C_{3v} symmetric structures of the HCCH-NH₃ and OCS-NH₃ complexes. The spectroscopic constants obtained allow us to carry out structural analyses,^(75, 162) assuming there is no distortion of the subunits upon complexation. For the structures of the complexes, five additional degrees of freedom are needed to describe the relative orientation and separation of the two subunits, as illustrated in Fig. 6.6.

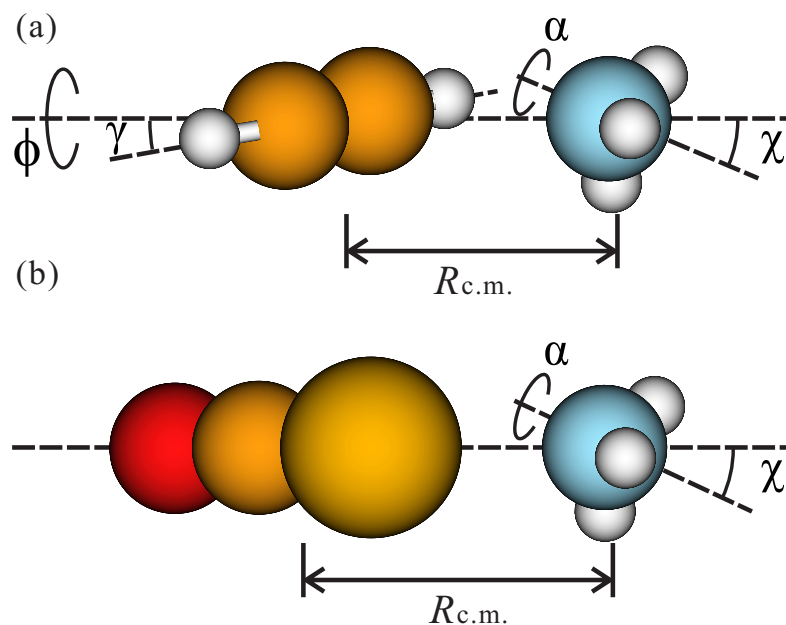


Figure 6.6: Definition of coordinates used to describe the structure of (a) HCCH-NH₃ and (b) OCS-NH₃. The distance between the centers of mass of the two subunits is $R_{c.m.}$. The motions of the NH₃ and HCCH subunits with respect to the *a*-axis of the complex are described by the cones traced out by their highest symmetry axes with an averaged angle of χ and γ , respectively. Their relative orientation is specified by ϕ . For OCS-NH₃ complex ϕ is set to zero. The rotation of NH₃ along its C_3 axis is described by angle α .

The value of χ can be estimated from the measured quadrupole coupling constants eQq_{aa}^N by assuming that the electric field gradient at the nitrogen nucleus

doesn't change upon complexation.

$$eQq_{aa}^N = eQq_{NH_3}^N \langle P_2(\cos \chi) \rangle = eQq_{NH_3}^N \left(\frac{3\langle \cos^2 \chi \rangle - 1}{2} \right) \quad (6.4.1.1)$$

With the value of $eQq_{NH_3}^N = -4.089$ MHz taken from NH_3 monomer,(161) χ is determined to be $23.29(2)^\circ$ and $25.23(2)^\circ$ for $HCCH-NH_3$ and $OCS-NH_3$, respectively. For comparison, χ is 20.4° for the $HCN-NH_3$ complex with a strong hydrogen bond.(76) The magnitude of χ can be correlated to the binding strength of the complex. Stronger binding interactions between ammonia and HCN and between ammonia and HCCH result in smaller χ values, and therefore smaller vibrational amplitudes of NH_3 . The χ values mentioned above are consistent with the binding strength order: $HCN-NH_3 > HCCH-NH_3 > OCS-NH_3$. Similarly, the angle γ specifies the average vibrational amplitude of the HCCH or OCS subunit with respect to the a -axis of the corresponding complex. Since these subunits contain no quadrupolar nucleus, we are not able to apply the same method to obtain the γ value. For the $HCCH-NH_3$ complex, this angle can be assumed to have the same value as in $HCN-NH_3$ complex(76), since these two complexes have similar $C-H \cdots N$ hydrogen bonds and the mass of the HCCH and HCN subunits are essentially the same. For the much heavier OCS subunit in the $OCS-NH_3$ complex, the angle γ can be expected to be much smaller and was fixed to zero in the following structural analyses.(254)

The moments of inertia for the complex consists of the contribution from the end-over-end pseudo-diatomic rotation of the complex and those from the two subunits. For the $HCCH-NH_3$ complex:

$$\begin{aligned} I_b = & \mu_R \langle R_{c.m.}^2 \rangle \\ & + I_b^{NH_3} \left(\frac{1 + \langle \cos^2 \chi \rangle}{2} \right) + I_c^{NH_3} \left(\frac{\langle \sin^2 \chi \rangle}{2} \right) \\ & + I_b^{C_2H_2} \left(\frac{1 + \langle \cos^2 \gamma \rangle}{2} \right) \end{aligned} \quad (6.4.1.2)$$

where μ_R is the reduced mass of the two subunits and $I_b^{NH_3}$, $I_c^{NH_3}$, and $I_b^{C_2H_2}$ are the effective principle moments of inertia of NH_3 and $HCCH$, taken from the free monomer values.(118, 267) The separation of the centers of mass of $HCCH$ and NH_3 ($R_{c.m.}$) was calculated to be $4.05941(79)$ Å. Similarly, $R_{c.m.}$ in $OCS-NH_3$ was calculated to be $4.360748(27)$ Å for the $OCS-NH_3$ complex, with the γ value fixed to zero and the moment of inertia of OCS monomer take from the free monomer value.(258, 182) With the structural parameters of $HCCH$ and OCS fixed at

their respective experimental values of the corresponding monomers,(109, 158) the C-H \cdots N hydrogen bond length and the S \cdots N bond length ($R_{\dots N}$) have been determined to be 2.3981(27) Å and 3.3232(1) Å, respectively. Considering the excited vibrational state, the B rotational constant varies very little upon ν_4 excitation of NH₃ in both complexes, suggesting the bending excitation has minimal influence on the structures of these complexes. Similar phenomenon has also been found in a number of other complexes, for example, the ν_2 bending excitation of water in Ar-H₂O.(277) All of the structural parameters determined from spectroscopic constants are listed in Table 6.6. The errors indicated are purely from the uncertainties of the experimental spectroscopic constants, without taking into account the approximation made.

The rovibrational transitions detected for both HCCH-NH₃ and OCS-NH₃ have notable homogeneous broadening. This is likely due to vibrational predissociation where the excitation of ν_4 vibration of NH₃ is coupled to the excitation of intermolecular stretching mode C-H \cdots N or S \cdots N, which leads to the dissociation of the complex. For a well resolved transition measured with the same laser spectrometer without any lifetime broadening, the typical full width at half maximum (FWHM) fitted with a Gaussian line shape was 0.0015 cm⁻¹. (140) The broadening due to vibrational predissociation has been estimated with a Lorentzian line shape to be 0.005 cm⁻¹ (FWHM) for HCCH-NH₃ and 0.01 cm⁻¹ (FWHM) for OCS-NH₃, respectively. The expression $\tau = 1/(2\pi\Gamma)$ with Γ is the Lorentzian FWHM, leads to a rough estimation of 1 ns and 0.5 ns for the excited states lifetime for HCCH-NH₃ and OCS-NH₃, respectively.

More severe predissociation broadening had been reported for HCCH-NH₃ when the bonded C-H stretching mode was excited.(100) The stronger coupling of the bonded C-H stretch than the NH₃ deformation to the intermolecular H \cdots N stretching mode is reasonable since the transition dipole moment of the former is aligned with that of the stretching mode, whereas that of the latter is perpendicular to it. The stronger coupling of the ν_4 excitation of NH₃ to the S \cdots N stretch in OCS-NH₃ is difficult to rationalize. If such vibrational coupling depends strongly on the electric dipole-dipole interaction, one may propose that the possible cause is the larger dipole moment of OCS (0.7 Debye), as compared to the non-polar HCCH. But previous study(100) of the predissociation lifetime of HCCH-NH₃, HCN-NH₃, and HCCH-H₂O(29) shows that HCCH-NH₃ has a much broader predissociation line width than the other two, even though the dipole moment of ammonia (1.5 Debye) is less than that of water (1.9 Debye),

and HCCH is non-polar. Further studies would be desirable to unravel the exact cause.

6.4.2 Dissociation energies

The van der Waals (vdW) stretching force constant (k_s) of the complex could be estimated using the pseudo-diatomic approximation:(175)

$$k_s = \frac{\hbar^4 \mu_R}{2D_J h} \frac{I_{AB} - I_A - I_B}{I_{AB}^4} \quad (6.4.2.1)$$

where D_J is the centrifugal distortion constant. I_{AB} , I_A , and I_B are the principle b -inertial moment of the AB complex and the A and B monomer, respectively. The experimental effective principle moments of inertia are used for the subunits and the complex. The stretching force constants for HCCH-NH₃ and OCS-NH₃ are calculated to be 7.34(10) and 4.6872(25) N/m respectively, corresponding to the harmonic ($\sqrt{k/\mu}$) vdW vibrational frequencies of 110.0(8) cm⁻¹ and 77.45(2) cm⁻¹, respectively. If a Lennard-Jones type potential was assumed, the dissociation energy (ΔE_0) could be estimated by the following equation:(26)

$$\Delta E_0 = \frac{1}{72} k_s R_{c.m.}^2 \quad (6.4.2.2)$$

The ΔE_0 of 10.1(1) kJ/mol and 7.455(4) kJ/mol are obtained for the HCCH-NH₃ and OCS-NH₃, respectively. The errors indicated are from the uncertainties of the experimental spectroscopic constants.

Table 6.6: Experimental and *ab initio* structural parameters and dissociation energies of HCCH-NH₃ and OCS-NH₃^a.

	HCCH-NH ₃	<i>ab initio</i>	OCS-NH ₃	<i>ab initio</i>
χ	23.29(2) ^o		25.23(2) ^o	
$R_{c.m.}$	4.05941(79) Å		4.360748(27) Å	
$R_{\dots N}$	2.3981(27) Å	2.2852 Å	3.3232(1) Å	3.2263 Å
k_s	7.34(10) N/m		4.6872(25) N/m	
ν_s	110.0(8) cm ⁻¹		77.45(2) cm ⁻¹	
ΔE_0	10.1(1) kJ/mol	10.2 kJ/mol	7.455(4) kJ/mol	7.0 kJ/mol

^a See text and Figure 6.6 for the definition of these parameters.

The noticeable larger dissociation energy of HCCH-NH₃ compared to that of OCS-NH₃ highlights the strength of a C-H \cdots N weak hydrogen bond, even though it is comparatively weaker than the O-H \cdots N or N-H \cdots N bond. It is known that

in these neutral complexes, the electrostatic interactions are often the driving force for the orientation preference exhibited by a particular complex. Assuming simple dipole-quadrupole and quadrupole-quadrupole interactions at the corresponding center-of-mass distances, one can obtain the attractive electrostatic interaction energies of 0.7 and 11.0 kJ/mol for the T-shaped and the C_{3V} symmetric HCCH \cdots NH₃, respectively. Clearly, electrostatic interaction plays an important role in the C_{3V} symmetric preference of HCCH \cdots NH₃. Similarly, the electrostatic interaction energies for the C_{3V} symmetric and T-shaped OCS \cdots NH₃ was calculated to be 1.6 and 0.4 kJ/mol.

6.4.3 Calculations of electrostatic interactions

The much stronger electrostatic interaction in HCCH \cdots NH₃ versus in OCS \cdots NH₃ can also be visualized in terms of the electrostatic potentials mapped on the electron density isosurface obtained from the *ab initio* calculations. As one can see, the attractive field strength experienced by the N atom of ammonia in HCCH \cdots NH₃ is considerably larger than in OCS \cdots NH₃ (see Fig. 6.8). Furthermore, the preference for a C_{3V} symmetric instead of a T-shaped orientation in OCS \cdots NH₃ can also be visualized in the term of the attractive field strength experienced by the N atom of ammonia as shown in Fig. 6.7 and Fig. 6.8, although the preference here is quite subtle.

Potential energies for the various electrostatic interactions in the dipole-dipole interaction of C_{3V} symmetric conformer of the complexes are given by:(123)

$$E_{d-d} = -2 \frac{\mu^A \mu^B}{4\pi\epsilon_0 r^3} \quad (6.4.3.1)$$

where A and B are the two subunits. dipole-quadrupole interaction (C_{3V} symmetric conformation, with the dipole moment pointing to or away from the quadrupole):

$$E_{d-q} = \pm 3 \frac{\mu^A Q_{ZZ}^B}{4\pi\epsilon_0 r^4} \quad (6.4.3.2)$$

dipole-quadrupole interaction (T-shaped conformation, with the dipole moment of NH₃ pointing to HCCH in HCCH-NH₃ or pointing away from OCS in OCS-NH₃):

$$E_{d-q} = \mp 1.5 \frac{\mu^A Q_{ZZ}^B}{4\pi\epsilon_0 r^4} \quad (6.4.3.3)$$

quadrupole-quadrupole interaction (C_{3v} symmetric conformer):

$$E_{q-q} = 6 \frac{Q_{ZZ}^A Q_{ZZ}^B}{4\pi\epsilon_0 r^5} \quad (6.4.3.4)$$

quadrupole-quadrupole interaction (T-shaped conformer):

$$E_{q-q} = -3 \frac{Q_{ZZ}^A Q_{ZZ}^B}{4\pi\epsilon_0 r^5} \quad (6.4.3.5)$$

By taking the experimental values for the dipole moments of ammonia (1.472 Debye)(160) and OCS (0.715 Debye)(251), quadrupole moment of acetylene (6.335 DebyeÅ)(90), ammonia (-2.320 DebyeÅ)(129), and OCS (-0.584 DebyeÅ)(24), and the distance between the subunits determined from this work, the electrostatic interaction energies were estimated and listed in Table 6.7 (negative means attractive).

Table 6.7: Electrostatic interaction energies of HCCH-NH₃ and OCS-NH₃ (in kJ/mol)

	C_{3v} -HCCH-NH ₃	T-shaped HCCH-NH ₃	C_{3v} -OCS-NH ₃	T-shaped OCS-NH ₃
d-d			-1.5	
q-d	-6.2	-3.1	0.4	-0.2
d-q			-0.8	
q-q	-4.8	2.4	0.3	-0.2
sum	-11.0	-0.7	-1.6	-0.4

We would also like to point out that the harmonic frequency calculations reported above predict a red shift of the bonded C-H stretch by 96 cm⁻¹ compared to the calculated monomer value, in reasonable agreement with the experimental value of 75.1042(38) cm⁻¹.(100) A recent report on Cl₃CH⋯NH₃ also showed that the shift in the C-H stretch was well reproduced at the harmonic level.(101) Unfortunately, the limited laser frequency coverage prevents us to obtain the experimental shifts of the ν_4 NH₃ band in the two complexes to make the similar comparisons with the calculations.

It is of interest to compare the most stable structures of the isoelectronic OCS-NH₃, N₂O-NH₃ and CO₂-NH₃ complexes. While OCS-NH₃ is a C_{3v} symmetric top with an S⋯N intermolecular bond, the latter two have T-shaped structure with N of ammonia pointing to the middle atom of the linear molecule. This is because the much larger electric dipole moment of OCS results in strong electric dipole-dipole interaction with NH₃, favoring the symmetric top structure. For

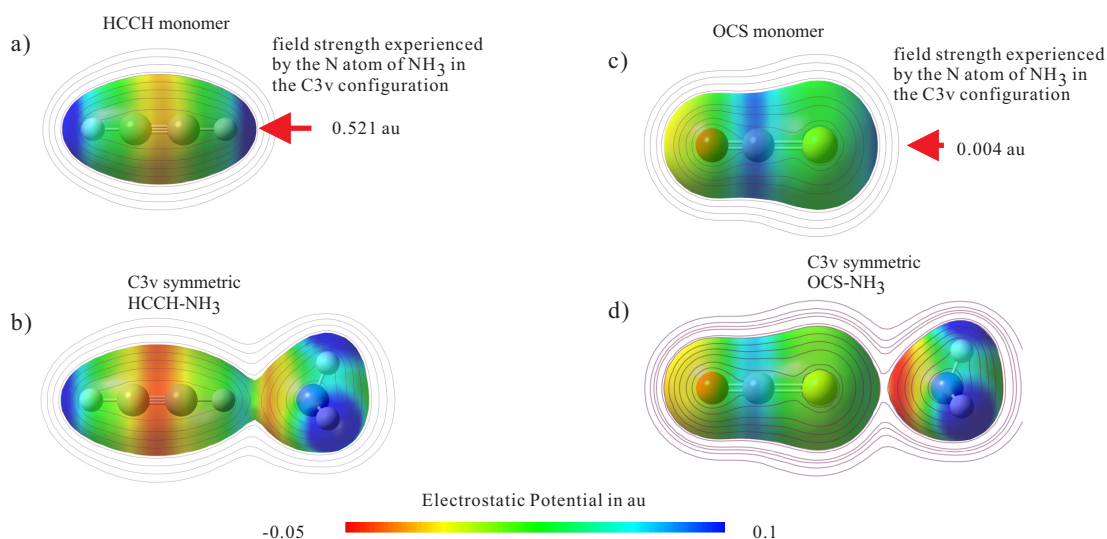


Figure 6.7: Electrostatic potential of HCCH-NH₃ - *Ab initio* electrostatic potential (from -0.05 au to 0.1 au) mapped on the electron density isosurface of 0.01 for a) HCCH, b) HCCH-NH₃, c) OCS, and d) OCS-NH₃. The blue part of the surface shows a positive electrostatic potential and hence attracts the electronegative N atom of ammonia. In a) and c), the arrows indicate the attractive field strength experienced by the N atom of ammonia if an ammonia molecule is placed at the position as in the corresponding complexes observed.

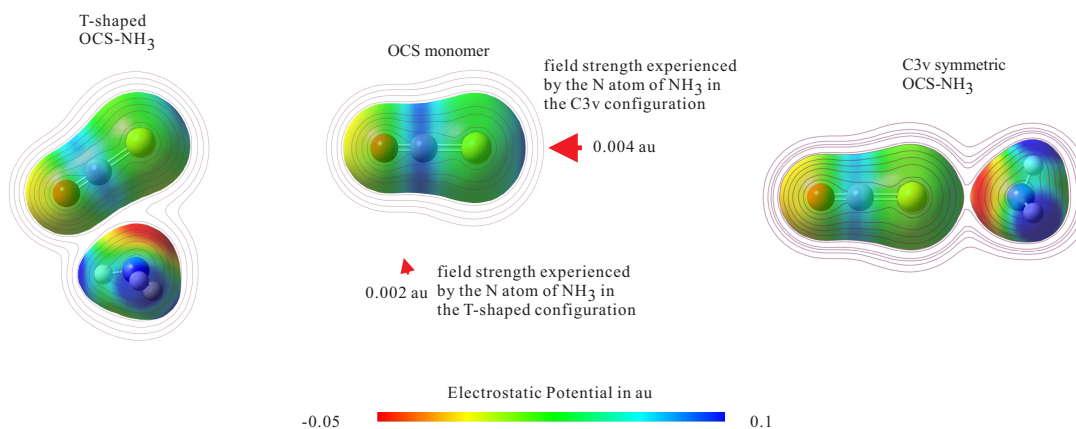


Figure 6.8: Electrostatic potential of HCCH-NH₃ - *Ab initio* electrostatic potential (from -0.05 au to 0.1 au) mapped on the electron density isosurface of 0.01 for OCS, C_{3V} and T-shaped OCS-NH₃. The blue part of the surface shows a positive electrostatic potential and hence attracts the electronegative N atom of ammonia. For the two possible binding sites of ammonia, the attractive field strengths experienced by the N atom of ammonia are different, showing a subtle preference for the linear configuration.

N_2O and CO_2 , which have small or zero electric dipole moments, the interactions with NH_3 are dominated by the induction and isotropic London dispersion forces.(143) Similar structural trend had been reported for the corresponding complexes with water. For example, the $\text{OCS-H}_2\text{O}$ (254) complex displays a similar “linear” conformation with the electropositive sulfur binding to the negative oxygen of water, while $\text{CO}_2\text{-H}_2\text{O}$ (200) and $\text{N}_2\text{O-H}_2\text{O}$ (309) are T-shaped.

6.5 Conclusions

Pure rotational spectra and rovibrational spectra at $6\ \mu\text{m}$ of the HCCH-NH_3 and OCS-NH_3 complexes have been detected and analyzed. The structures of both complexes have been determined to be of C_{3v} symmetry. The non-polar acetylene binds to ammonia through a weak $\text{C-H}\cdots\text{N}$ hydrogen bond and carbonyl sulfide binds to ammonia mainly through permanent electric dipole-dipole interaction. The experimental dissociation energy has been found to be considerably larger for HCCH-NH_3 . The stronger binding energy of HCCH-NH_3 highlights the strength of the comparably weak $\text{C-H}\cdots\text{N}$ hydrogen bond. The comparison between the experimental and calculated dissociation energies indicates the importance of anharmonic contributions to the ZPE corrected dissociation energies.

6.6 Propylene Oxide (PO)-(water) $_N$ complex

The study of the HCCH/OCS-NH_3 complexes described in this chapter shows that the rovibrational energy levels of a hydrogen bonded molecular complex can be adequately analyzed using the semi-rigid rotor model. The spectroscopic constants obtained are closely related to the equilibrium geometry and can provide direct experimental evidence of the structure of the molecular complex.

To extend the investigation to larger hydrogen bonded molecular complexes with a mid-size organic subunit, the high resolution infrared spectra of Propylene Oxide (PO)-water complexes are measured. As introduced in Chapter 1, the PO molecule is a model chiral molecule that can bind to a number of water molecules through different binding sites. Therefore, the $\text{PO-(H}_2\text{O)}_N$ complexes are model systems to study the solvation of chiral molecule in aqueous solution. It has been found that the Vibrational Circular Dichroism (VCD) spectrum of PO in water solution shows an active VCD band at $1650\ \text{cm}^{-1}$, which was attributed to the bending motions of the water subunits that are hydrogen bonded to PO.(144)

6.6 Propylene Oxide (PO)-(water)_N complex

Through hydrogen bonding interactions with the chiral PO molecule, the bending mode of the water molecule becomes VCD active. In other words, chirality of the PO molecule is “transferred” to the surrounding water molecules.

It is therefore desirable to probe the water bending bands of the PO-(water)_N complexes in a supersonic free jet expansion condition in order to obtain detailed and accurate structural and energetic information about such water clusters in the gas phase. Comparisons of such gas phase studies with the solution data will allow one to separate the bulk solvent effects from those water molecules which are explicitly hydrogen bonded to the chiral solute. The infrared gas phase work at the water bending region is particularly valuable since it provides the opportunity for a direct comparison with the solution data recorded in the same region. One can also compare the band origins obtained to the *ab initio* values to access the quality of current theoretical calculations of the vibrational frequencies.

The binary PO-H₂O and ternary PO-(H₂O)₂ complex are expected to be the most abundant complexes in a supersonic free jet expansion under suitable conditions. With the good sensitivity of the IR spectrometer, one expect them to be observed despite their sizes. Water can bind to the two lone electron pairs of the O atom of PO either on the same side as the methyl group of PO (*syn*) or on the opposite side (*anti*). So there are *syn* and *anti* conformers for both of the binary and ternary complexes. of the PO-H₂O and PO-(H₂O)₂ complexes have been detected using a cavity based microwave spectrometer.(244, 245) The spectroscopic constants and the derived binding energies are listed in Table 6.8 and Table 6.9. Geometry optimization and further anharmonic frequency calculation of these conformers are carried out at the MP2/6-311++g(d,p) level of theory for the PO-H₂O and PO-(H₂O)₂ complex as part of the thesis work. The geometries of the most stable conformer of the PO-H₂O and PO-(H₂O)₂ complexes are shown in Fig. 6.9 and Fig. 6.10, respectively. The calculated binding energies and the harmonic and anharmonic vibrational frequencies are listed in Table 6.8 and Table 6.9.

In the experimental measurement, the PO water complexes are generated according to the optimized sample condition reported in previous cavity microwave study.(244, 245) Very dense and complicated spectral features are observed from 1650 cm⁻¹ to 1680 cm⁻¹. The spectra are provided in Fig. 6.11, Fig. 6.12, Fig. 6.13, Fig. 6.14, Fig. 6.15, Fig. 6.16

The observed spectral features are only observed with both water and PO present. They most likely belong to the water bending modes of the *syn* and *anti* PO-H₂O complexes, although the *syn* and *anti* conformers of the PO-(H₂O)

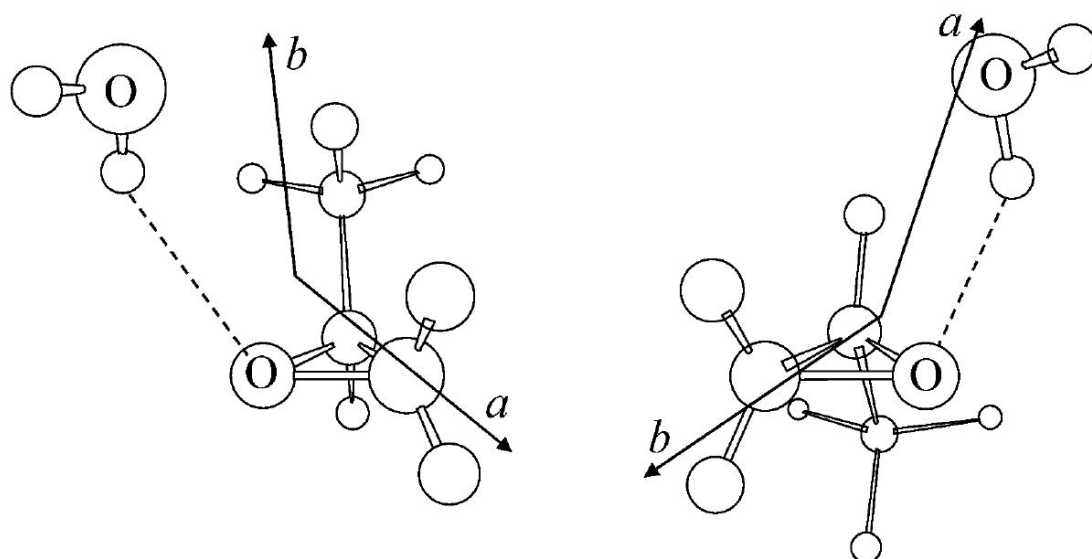


Figure 6.9: Geometry of PO-H₂O - Geometries of the two most stable conformers of PO-H₂O taken from Ref. (244).

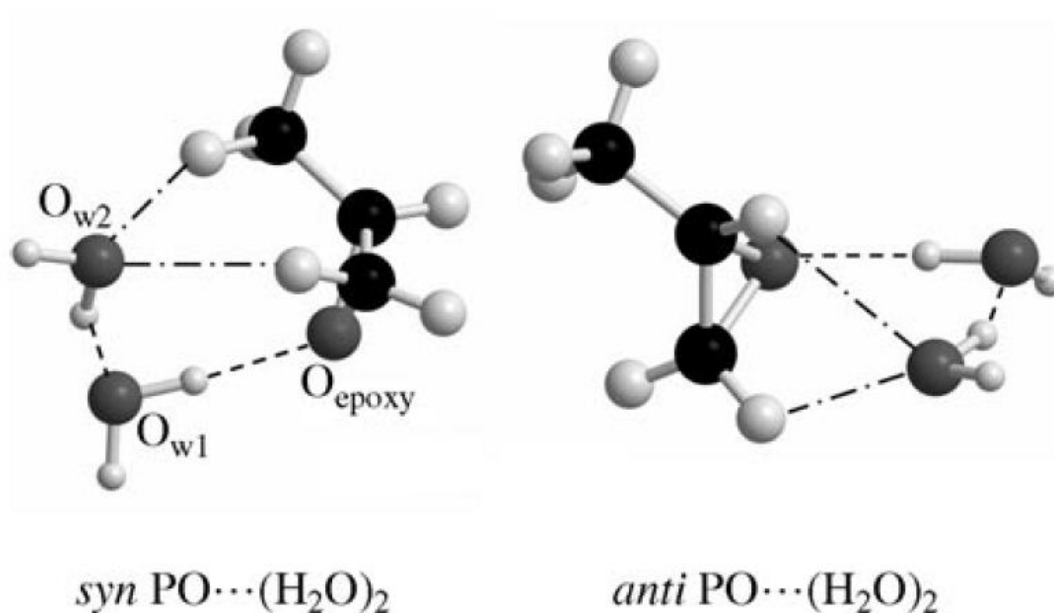


Figure 6.10: Geometry of PO-(H₂O)₂ - Geometries of the two most stable conformers of PO-(H₂O)₂ taken from Ref. (245).

6.6 Propylene Oxide (PO)-(water)_N complex

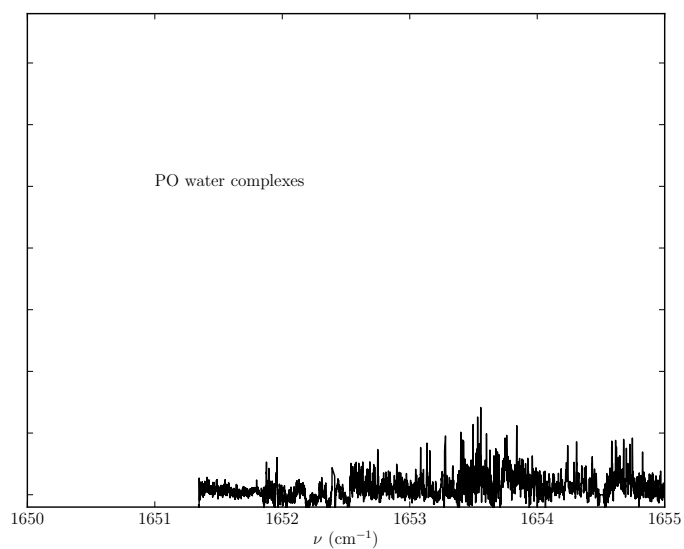


Figure 6.11: Spectrum of PO water complexes from 1650 cm⁻¹ to 1655 cm⁻¹ -

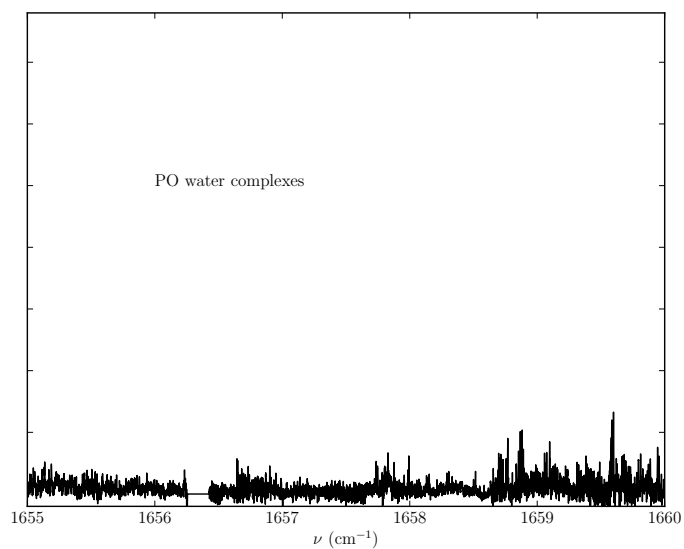


Figure 6.12: Spectrum of PO water complexes from 1655 cm⁻¹ to 1660 cm⁻¹ -

6.6 Propylene Oxide (PO)-(water)_N complex

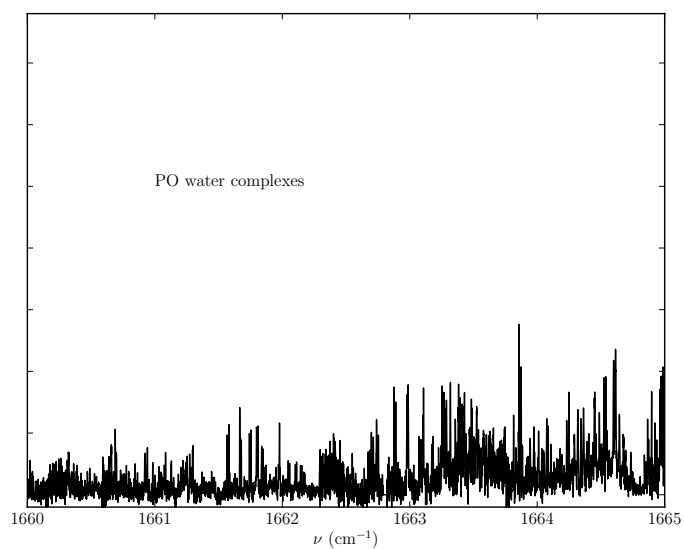


Figure 6.13: Spectrum of PO water complexes from 1660 cm⁻¹ to 1665 cm⁻¹ -

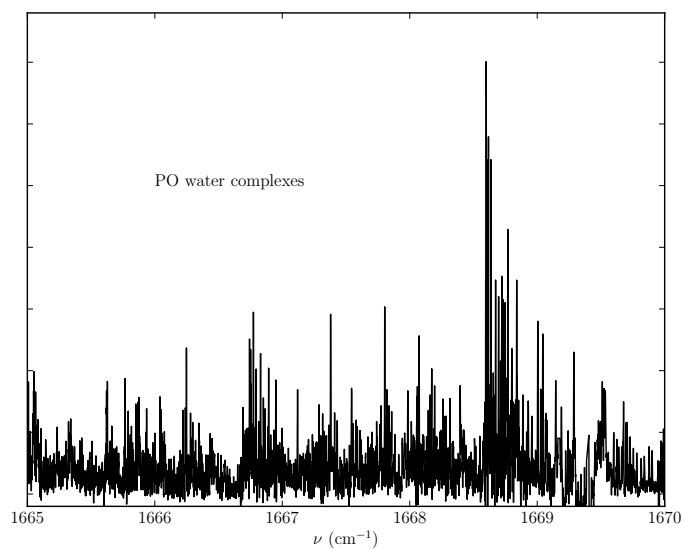


Figure 6.14: Spectrum of PO water complexes from 1665 cm⁻¹ to 1670 cm⁻¹ -

6.6 Propylene Oxide (PO)-(water)_N complex

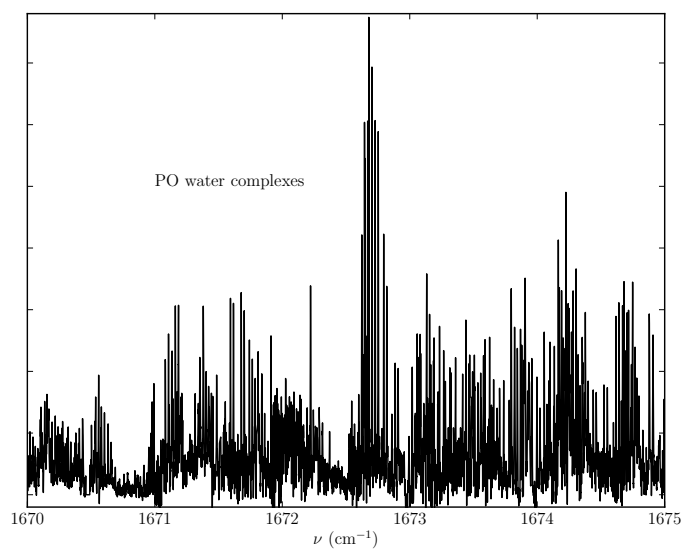


Figure 6.15: Spectrum of PO water complexes from 1670 cm⁻¹ to 1675 cm⁻¹ -

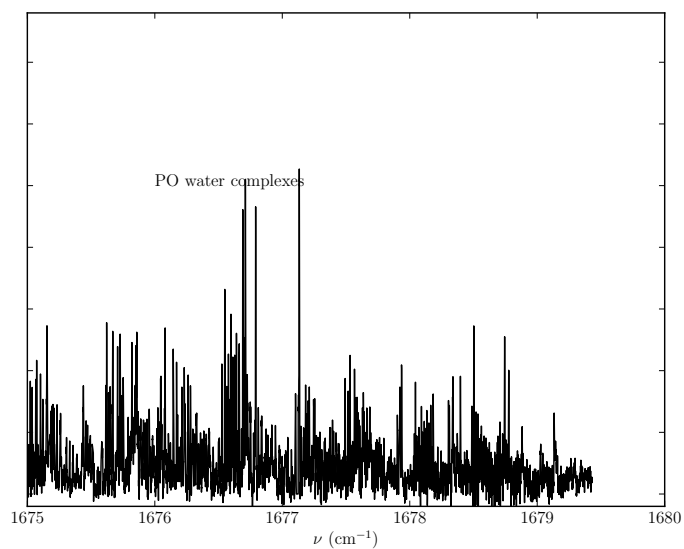


Figure 6.16: Spectrum of PO water complexes from 1675 cm⁻¹ to 1680 cm⁻¹ -

6.6 Propylene Oxide (PO)-(water)_N complex

Table 6.8: Spectroscopic constants of the vibrational ground states from microwave study are fit from Ref. (244). Note that the Standard error (1σ) in parentheses expressed are in units of the last digits. Due to the fact that only 15 and 19 transitions are used to fit 8 or 7 independent parameters, the lack of statistical sufficiency leads to underestimation of the error of fit parameters in the weighted least square fit. So the *correct* error of the spectroscopic parameters are larger than those reported in Ref. (244).

	<i>syn</i> -PO-H ₂ O	<i>anti</i> -PO-H ₂ O
A (MHz)	6063.2695(14)	9478.8578(14)
B (MHz)	3035.74238(83)	2281.5636(11)
C (MHz)	2352.71365(75)	2080.54388(96)
D_J (kHz)	5.994(33)	5.279(45)
D_{JK} (kHz)	41.515(99)	-39.37(12)
D_K (kHz)	-88.60(51)	0
d_1 (kHz)	-1.671(25)	-0.958(35)
d_2 (kHz)	-0.593(15)	-0.272(22)
k_s (N/m)	8.9	5.0
v_s (cm ⁻¹)	105	79
ΔE (kJ/mol)	7.2	5.0
v_{har} (cm ⁻¹)	1661.378	1659.677
v_{anh} (cm ⁻¹)	1604.904	1602.263
ΔE^a raw (kJ/mol)	29.89	29.80
ΔE BSSE (kJ/mol)	22.30	22.37
ΔE BSSE+har-ZPE (kJ/mol)	14.09	14.15
ΔE BSSE+anh-ZPE (kJ/mol)	14.72	14.63

^a All *ab initio* calculation performed at the MP2/6-311++g(d,p) level of theory

complexes are also likely to contribute to the weak lines. The two strong spectral features around 1670 cm⁻¹ indicates that the band origin of these complexes are very likely around this region, which is ~ 70 cm⁻¹ to the blue of the band origin of the gas phase water molecule (Fig. 2.9). However, the anharmonic frequencies from *ab initio* calculations are ~ 70 cm⁻¹ lower than the experimental values. The over estimated harmonic frequencies from the *ab initio* calculation is therefore closer to the estimated experimental band origins, which may subject to anharmonic couplings as discussed in Sec. 2.3.2. Obviously, the ‘‘agreement’’ of the harmonic frequency with the experimental value is a ‘‘right answer for the wrong reasons’’. The over 50 cm⁻¹ error of the infrared frequencies from *ab initio* calculations of such kind is well anticipated as discussed in Sec. 2.2.

The observed solution phase VCD active band around 1650 cm⁻¹ cannot be

6.6 Propylene Oxide (PO)-(water)_N complex

Table 6.9: Spectroscopic constants of the vibrational ground states from microwave study, derived binding strength, and *ab initio* binding energies and harmonic and anharmonic water bending frequencies for PO-(H₂O)₂

	<i>syn</i> -PO-(H ₂ O) ₂	<i>anti</i> -PO-(H ₂ O) ₂
<i>A</i> (MHz)	3200.394	3846.901
<i>B</i> (MHz)	1744.6903	1529.8990
<i>C</i> (MHz)	1556.9635	1311.7199
Δ_J (kHz)	2.067	1.351
Δ_{JK} (kHz)	5.74	8.14
δ_J (kHz)	0.077	0.142
δ_K (kHz)	0.2	-12.6
v_{har} (cm ⁻¹)	1690.641/1663.472	1688.715/1659.126
v_{anh} (cm ⁻¹)	1628.087/1616.570	1627.376/1612.889

directly related to the gas phase measurements. Presence of the chiral molecule in water solution is a “perturbation” to the surrounding water molecules. The observed 1650 cm⁻¹ band from the PO solution is likely mainly originated from the bending of water molecules in the first solvation shell of the PO molecule, which usually contains 4~8 water molecules. The water bending origin is blue shifted to the bulk water value at 1644 cm⁻¹ when perturbed from gas phase value at 1595 cm⁻¹. The blue shift can be interpreted as a deeper normal mode potential of the bulk water compared to the gas phase molecules. It is noticed that observed VCD active band value is between the estimated bending band origins of small size binary and ternary complex around 1670 cm⁻¹ and those of the bulk water value. Based on the experimental observation, the degree of blue shift decrease from the ~ 70 cm⁻¹ for the binary or ternary complexes to ~ 50 cm⁻¹ for the solvation shell of PO molecule. However, as the size increase from binary to ternary complex, the *ab initio* calculation shows that the blue shift is actually increased. More experiments can be done to study the controlled temperature dependency and matrix isolation spectrum of this system to provide more information about the degree of the blue shift of water bending under difference circumstances.

Detailed assignments of the rotational structure of the observed spectrum proved difficult. The spectral analysis is further complicated by the existing of several conformers. So the rovibrational transitions are very dense. One may be able to crack the assignment using MW-IR double resonance experiments. Assuming that the structure of the complex remains essentially the same in the ground and the first excited vibrational state, i.e. their related spec-

6.6 Propylene Oxide (PO)-(water)_N complex

troscopic constants remain the same, we simulate the expected IR spectra of the PO-H₂O and PO-(H₂O)₂ complexes. Simulation is performed using Pickett's CALPGM/SPFIT program(202) and the AABS software package for Assignment and Analysis of Broadband Spectra(124, 3) is used to aid the display and assign the spectrum. The simulated rovibrational transitions of the *syn* and *anti* PO-H₂O complexes are shown in Fig. 6.17.

The spectral analysis is further complicated by the existing of several conformers. So the rovibrational transitions are very dense. The dense spectra presented in the PO water complex vividly demonstrate that as the size of the system getting larger, the rotational energy levels will eventually get so dense that no fine rotational structure can be resolved. (176)

6.6 Propylene Oxide (PO)-(water)_N complex

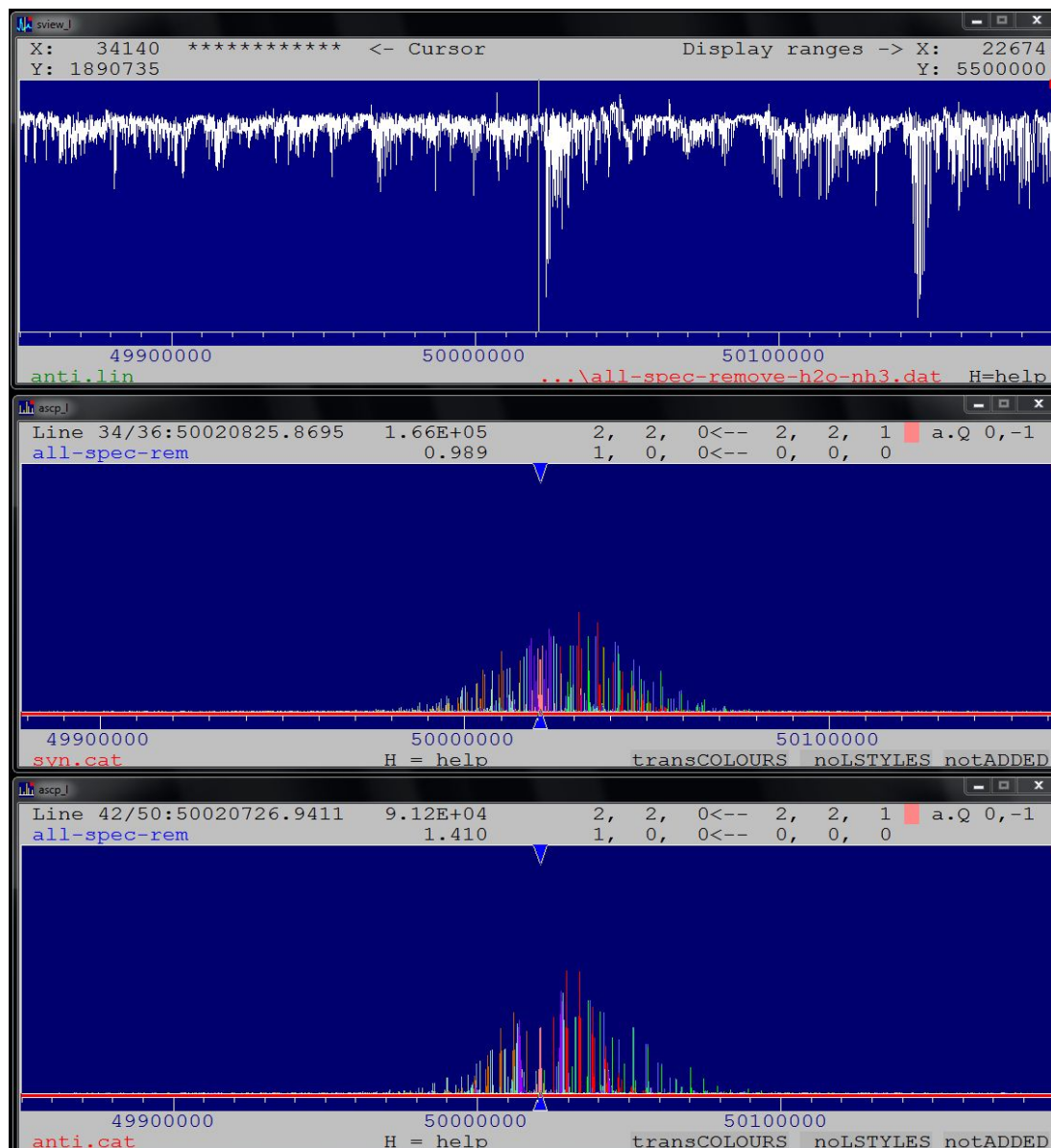


Figure 6.17: Simulation of PO-H₂O spectrum - The rotational constants from ground state are used for both the ground and excitation state. Since the transitions dipole moment of the water bending mode has all *a*, *b*, *c* type components, all three types of rovibrational transitions are simulated. The rotational temperature is set to 1 K. *J* upto 10 rotational levels are simulated. SPCAT and AABS program are used as shown in screen shot.

7

Conclusions

High resolution molecular spectroscopic studies of several prototype molecular complexes and the design, construction and evaluation of the tunable quantum cascade laser (QCL) multipass direct absorption spectrometer are described in this thesis.

The instrumentation development presented in Chapter 4 is one of the main achievements of my thesis work. This is the first high resolution infrared spectrometer which utilizes QCL as the light source to measure high resolution infrared spectrum of molecular complexes in Canada. Both the advantages and limitation of the QCL are explored and several signal enhancement techniques are evaluated. The continuous wave, external cavity QCL is coupled with an astigmatic multipass cell and a cavity enhanced absorption cell to increase the optical absorption path. The rapid scan direct absorption and wave length modulation technique are applied to record spectra of both room temperature gas phase molecules or molecular complexes in supersonic free jet expansions. The combination of the astigmatic multipass cell with the rapid scan scheme is used for high resolution spectroscopic studies of molecular complexes, because such a combination enables one to search for a wide frequency range in a short time and offers excellent sensitivity for the detection of molecular complexes.

As the foundation to understand the complicated high resolution infrared spectra of the chiral molecular complexes, spectra of “small” molecular complexes containing water or ammonia subunit are investigated. In Chapter 5, the high resolution infrared spectra of weakly bounded van der Waals rare gas (Rg)-NH₃/H₂O complexes are measured and analysed. For such complexes, the rotation-vibration separation and the semi-rigid rotor model are not suitable. Instead, pseudo-diatomic Hamiltonian with water internal rotor states that are

mixed with Fermi resonance and Coriolis coupling terms are applied to these weakly bounded systems. For Ar-H₂O complex, high lying (2₁₂) and $n = 1$, (1₁₀) internal rotor states of water subunit are determined, while a number of other internal rotor states that cannot be clearly related to the hindered water internal rotation have also been observed, indicating extra rotation-vibration couplings that need to be re-investigated in the pseudo-diatomic Hamiltonian. These new measurements will aid further theoretical calculation of the rovibrational states for the Ar-H₂O complex.

Similarly, the Ne-H₂O, Ar-NH₃ and Ne-NH₃ complexes are also measured in the 6 μ m region, where the bending motions of the H₂O or NH₃ subunit are probed and modeled by pseudo-diatomic Hamiltonian. It is the first time that these fundamental molecular complexes are studied using high resolution infrared spectroscopy. For such Rg-NH₃/H₂O complexes, the interaction energy, i.e., the depth of the well on PES, increases as the atomic weight and the susceptibility increase, which is experimentally demonstrated by the fewer number of internal rotor states observed and the intensity of the absorption transitions. The reason why there is no infrared spectrum of He-H₂O at 6 μ m has also been discussed and confirmed experimentally.

In comparison, two molecular complexes with relatively stronger intermolecular interactions: HCCH-NH₃ and OCS-NH₃ are studied in Chapter 6. Both the high resolution infrared spectra at 6 μ m and microwave spectra are reported. The $K = 0 \leftarrow 1$ and $K = 2 \leftarrow 1$ sub-bands of the HCCH-NH₃ and $K = 1 \leftarrow 0$ sub-band of OCS-NH₃ are observed. Both complexes are experimentally determined to be C_{3v} symmetric and their spectra can be modeled by the semi-rigid rotor approximation. The weak hydrogen bond interaction in the HCCH-NH₃ complex is stronger than the quadrupole interaction in the OCS-NH₃ complex. Our experimental data shows that the actual order of interaction energy with ammonia is: Ne < Ar << OCS < HCCH. The reason for the increase of the interaction energies for HCCH, which possess a much smaller molecular weight than OCS and Ar, is from the anisotropic distribution of the electric charge in the linear molecules, which allows multipole-multipole interactions in these complexes. The observation of the C_{3v} symmetric instead of the “T-shaped” OCS-NH₃ complex also demonstrates that the multipole-multipole interaction is stronger than the van der Waals interaction. Yet, the interaction in the HCCH-NH₃ complex is even greater than that in the OCS-NH₃ complex due to the unique weak C-H...N hydrogen bond.

The spectroscopic constants obtained from the rovibrational and pure rotational transitions provide direct experimental data to determine the structure of molecular complexes. The chiral recognition effect can be studied by the structure and relative energies of the different conformers of chiral molecule contact pairs. In Chapter 3, the chiral self-recognition effects in the 2-fluoroethanol binary complex is studied using cavity based Fourier transform microwave spectroscopy. The structure and relative stabilities of the 4 conformers of the binary complexes are determined. The delicate balance between the formation of intra- and intermolecular hydrogen bonds, a property that may be crucial for the protein-altering process in a fluoroalcohol/water solution, has been examined. In addition, the effects of fluorine on the stability of the binary 2-fluoroethanol complex have also been discussed.

The high resolution infrared spectra of molecular complex containing a chiral molecule propylene oxide with water molecules is measured at $6\ \mu\text{m}$ in Sec. 6.6 to study the sequential solvation of the chiral molecule in aqueous solution and the “chiral transfer” effects. The complicated rovibrational spectral features from $1650\ \text{cm}^{-1}$ to $1680\ \text{cm}^{-1}$ indicate existence of a number of $\text{PO}-(\text{water})_N$ conformers. It can be deduced that the water bending band origins of the $\text{PO}-(\text{water})_N$ complex are blue shifted by $\sim 70\ \text{cm}^{-1}$ compared to the gas phase water, which is greater than $\sim 50\ \text{cm}^{-1}$ blue shift in the bulk water. Although high resolution infrared spectra of the $\text{PO}-(\text{water})_N$ complexes have been recorded, no definite assignment has been achieved despite several serious attempts. This highlights the challenges one faces dealing with high resolution infrared spectroscopy of larger molecular systems. While rotational spectroscopic studies, such as one presented in Chapter 3, have provided rich information on structures of molecular complexes in the ground vibrational state, the progress in the infrared region has been slow, partly due to the complicated vibrational dynamics. To help with the assignments, one may implement a microwave-infrared double resonance set up. For example, by pumping a known microwave transition, one can monitor the intensity change of the infrared transitions and make the initial infrared assignment. In general, investigations of infrared spectra of chiral molecule-water complexes will allow us to follow the sequential solvation of a chiral molecule in water in the first few crucial steps with clearly determined atom-by-atom resolution and bridge the gas phase measurements to the infrared measurements in solution.

Appendix A

Measurement of Infrared Frequency

A.1 Frequency standard

Accurate measurement of the optical frequency is of fundamental importance for high-resolution spectroscopy. It is important to accurately determine the transition frequencies and energy levels of rovibrational states. It should be noted that in general, frequency measurement is more accurate than wavelength measurement because wavelength depends on the refractive index n , while frequency is independent of it. Diffraction and local inhomogeneities of local refractive index leads to deviation of light wave from the ideal plane wave, which leads to local deviations of the phase front of the light wave.

A frequency standard can be used for frequency calibration or reference. It is a stable and universal oscillator, ranging from the earth's orbital around the sun to tuning forks. As the reciprocal of time, it was initially defined after the international system (SI) unit of *second*, which was $1/86,400$ of a mean solar day. Nowadays, the **primary frequency standard**, as defined by Comité International des Poids et Mesures (CIPM), is the caesium atomic clock at 9.192631770 GHz, which is the two hyperfine levels of the ground state of the caesium 133 atom. The SI unit of second is defined after it as the duration of 9,192,631,770 periods of this transition. For example, the primary time and frequency standard for the United States is National Institute of Standards and Technology (NIST) Boulder laboratories' NIST-F1 atomic clock (114). Another widely used frequency standard is the hydrogen maser at 1.420405752 GHz, which has superior short-term performance.

With fast electronic counters, frequencies up to a few GHz can be measured directly and compared with the primary frequency standard. With nonlinear mixing elements, the overtones of these GHz range frequencies can provide the basis to build up a microwave-optical frequency chain and heterodyne techniques are usually used to get accurate measurement of the optical frequency of infrared and visible lasers. The frequency standard in the optical region is the Iodine-stabilized He-Ne laser, which is a He-Ne laser stabilized by saturated absorption of the 6-3,P(33) transition $^{127}\text{I}_2$ filled in an intracavity cell. Its main gain at the visible region is $473,612,214,712 \pm 5$ kHz. Another frequency standard is the transportable CH_4 -stabilized He-Ne standard at $3.39 \mu\text{m}$ (74), which is based on the $F_2^{(2)}[P(7), \nu_3]$ optical transition in methane.

These He-Ne standard laser frequencies are used to calibrate the Fourier Transform Infrared Spectrometer (FTIR) and tunable infrared spectrometers used to measure rovibrational transitions of room temperature(264) or ultra-cooled(119) small molecule and ions. These infrared frequencies are then fitted with spectroscopic constants to further remove inaccuracies. The accuracy of the measured frequencies, used as the infrared frequency standards, are usually to 0.00001 cm^{-1} .(304)

A.2 HITRAN database

A commonly used infrared frequency database is the PNNL vapor phase infrared spectral library. In our experiments, we use the HITRA-2008 Database (Version 13.0) as our frequency standard.(216) Here is 3 example entries of the database. They are the $1_{10} \leftarrow 1_{01}$ and $2_{12} \leftarrow 1_{01}$ transition of H_2O and the $2_{12} \leftarrow 1_{01}$ transition of H_2^{17}O .

```

11 1616.711490 2.462E-19 1.059E+01.10480.467 23.79440.700.006150
0 1 0          0 0 0 1 1 0          1 0 1
376743303067671736      9.0    9.0

```

```

13 1649.573820 9.884E-23 7.124E+00.10470.453 23.77350.760.004150
0 1 0          0 0 0 2 1 2          1 0 1
355643301884671736     90.0   54.0

```

```

11 1653.267070 2.566E-19 6.928E+00.10470.453 23.79440.760.004150
0 1 0          0 0 0 2 1 2          1 0 1
375643303084671736     15.0    9.0

```

Each entry of the database represents a ro-vibrational transition with the parameters listed in Fig. A.1.

HITRAN Line-by-line Parameters		
Parameter	Field size	Definition
Mol	I2	Molecule number
Iso	I1	Isotopologue no.(1 = most abundant, 2 = second most abundant, ...)
ν_{if}	F12.6	Transition wavenumber in vacuum [cm⁻¹]
S_{if}	E10.3	Intensity [cm⁻¹/(molecule·cm²) @ 296K]
A_{if}	E10.3	Einstein A-coefficient [s⁻¹]
Y_{air}	F5.4	Air-broadened half-width (HWHM) [cm⁻¹/atm @ 296K]
Y_{self}	F5.4	Self-broadened half-width (HWHM) [cm⁻¹/atm @ 296K]
E''	F10.4	Lower-state energy [cm⁻¹]
n_{air}	F4.2	Temperature-dependence coefficient of Y_{air}
δ_{air}	F8.6	Air pressure-induced shift [cm⁻¹/atm @ 296K]
v', v''	2A15	Upper and Lower "global" quanta
q', q''	2A15	Upper and Lower "local" quanta
ierr	6I1	Uncertainty indices for ν_{if}, S_{if}, Y_{air}, Y_{self}, n_{air}, δ_{air}
iref	6I2	Reference pointers for ν_{if}, S_{if}, Y_{air}, Y_{self}, n_{air}, δ_{air}
*	A1	Flag for line-coupling algorithm
g', g''	2F7.1	Upper and Lower statistical weights

160-character total

Figure A.1: HITRAN line-by-line parameters -

To simulate the reference gas spectrum for frequency calibrate, pure Gaussian line shape with calculated Doppler line width is used, as introduced in Sec. A.3. The pressure broadening and pressure shift are ignored. In the HITRAN database, absorption at certain frequency is defined in Eqn. ??:

$$\frac{dI(v)}{I(v)} = -k(v)dl$$

with the unit of k is $\frac{1}{cm}$. The integrated absorption of a transition at ν_0 is:

$$S = \int k(\nu - \nu_0)d(\nu - \nu_0) \quad (\text{A.2.0.1})$$

the unit of S is $\frac{1}{cm} \times cm^{-1}$. Assuming there is a normalized line shape function $g(\nu - \nu_0)$ for this transition,

$$\int g(\nu - \nu_0)d(\nu - \nu_0) = 1 \quad (\text{A.2.0.2})$$

A.3 Spectra line shape

absorption coefficient of the light intensity at certain frequency is then:

$$k(v - v_0) = Sg(v - v_0) \quad (\text{A.2.0.3})$$

the unit of $g(v - v_0)$ is $\frac{1}{\text{cm}^{-1}}$. Absorption at certain frequency is:

$$\frac{I(v, L)}{I_0} = e^{-k(v-v_0)L} \quad (\text{A.2.0.4})$$

$$= e^{-Sg(v-v_0)L} \quad (\text{A.2.0.5})$$

The integrated absorption S can be written as proportional to the number of absorbing molecules per unit volume N :

$$S = S^C \times C \quad (\text{A.2.0.6})$$

$$C = N_L \times P \quad (\text{A.2.0.7})$$

where the unit of S^C is $\frac{1}{\text{cm}} \times \text{cm}^{-1} \times \frac{1}{\#molecule/\text{cm}^3}$, N_L is the Loschmidt number $2.479 \times 10^{19} \frac{\#molecule/\text{cm}^3}{\text{atm}}$. In the HITRAN database, the listed transition intensity is given as S^C . So overall, absorption coefficient at certain frequency of a transition is:

$$k = S^C \times g(v) \times 2.479 \times 10^{19} \times P(\text{atm}) \times L(\text{cm}) \quad (\text{A.2.0.8})$$

A.3 Spectra line shape

In the coherent microwave spectra measured using the cavity-based Fourier Transform Microwave Spectrometer (FTMW), the resolution is several kHz as shown in Chapter 6. With such high resolution, the hyperfine spectral structure introduced in Sec. 2.2.1 can be studied to elucidate the structural information.

The line shape of the mid-infrared rovibrational spectroscopy studied in this thesis have the contribution from the heterogeneous (Doppler) and homogeneous (e.g. predissociation) line widths, and the laser line width. Typical line width of the supersonic free jet expansion sample is 0.001 cm^{-1} and 0.01 cm^{-1} for low pressure room-temperature gas. Such IR line broadening contribution typically obscure such hyperfine structures, and the averaged rovibrational energy structure is studied.

Doppler Broadening Gaussian line shape is the normal distribution line shape to describe homogeneous broadening:

$$f(x) = \frac{1}{\sqrt{2\pi\sigma^2}} e^{-\frac{(x-\mu)^2}{2\sigma^2}} \quad (\text{A.3.0.9})$$

The height of the peak is $1/\sqrt{2\pi}\sigma$ and the full width at half maximum (FWHM) is:

$$e^{-(x-\mu)^2/(2\sigma^2)} = \frac{1}{2} \quad (\text{A.3.0.10})$$

$$x = \mu \pm \sqrt{2 \ln 2} \times \sigma \quad (\text{A.3.0.11})$$

Gaussian line shape is used for **Doppler broadening**. Because of the Doppler effect, the received frequency of the molecule (f_r) is shifted from the source frequency (f_s) by the speed of the molecule (v):

$$f_r = \left(1 \pm \frac{v}{c}\right) f_s \quad (\text{A.3.0.12})$$

So if the resonance frequency of the molecule is $f_r = f_0$, the excitation frequency should be:

$$f_s = \frac{f_0}{1 \pm v/c} \quad (\text{A.3.0.13})$$

So the distribution of the speed of molecules leads to the distribution of the source frequency:

$$P(f)df = P(v_f) \frac{dv}{df} df \quad (\text{A.3.0.14})$$

where

$$v_f = c\left(\frac{f}{f_0} - 1\right) \quad (\text{A.3.0.15})$$

$$\frac{dv}{df} = \frac{c}{f_0} \quad (\text{A.3.0.16})$$

Therefore:

$$P(f)df = P_v\left(c\left(\frac{f}{f_0} - 1\right)\right) \frac{c}{f_0} df \quad (\text{A.3.0.17})$$

$$(\text{A.3.0.18})$$

For room-temperature low pressure gas, **Maxwell-Boltzmann Distribution** can be used to calculate the normalized fraction of particles with the velocity component v to $v + dv$ in single direction and overall speed:

$$P(f)df = \frac{1}{f_0} \sqrt{\frac{mc^2}{2\pi kT}} \exp \left[\frac{-mc^2(f - f_0)^2}{2kT f_0^2} \right] df \quad (\text{A.3.0.19})$$

$$P(v_i) dv_i = \sqrt{\frac{m}{2\pi kT}} \exp \left[\frac{-mv_i^2}{2kT} \right] dv_i \quad (\text{A.3.0.20})$$

$$P(v) dv = \sqrt{\frac{2}{\pi}} \left(\frac{m}{kT} \right)^{3/2} v^2 \exp \left(\frac{-mv^2}{2kT} \right) dv \quad (\text{A.3.0.21})$$

This gives $\sigma^2 = kT f_0^2 / mc^2$. So the Doppler FWHM is:

$$\text{FWHM} = 2\sqrt{2 \ln 2} \sigma \quad (\text{A.3.0.22})$$

$$= \sqrt{8 \ln 2} \sqrt{kT f_0^2 / mc^2} \quad (\text{A.3.0.23})$$

$$= \sqrt{8 \ln 2} \frac{f_0}{c} \sqrt{kT/m} \quad (\text{A.3.0.24})$$

The broadening of the supersonic free jet expansion line shape is also mainly from Doppler Broadening. Although greatly reduced by the homemade slit nozzle (Sec. 4.3), the velocity distribution of the expansion sample along the direction of the laser beam propagation is still large enough to contribute to the line width of the jet sample.

Pressure Broadening Lorentzian line shape is the Cathy distribution to describe line shape which are subject to homogeneous broadening in which all atoms interact in the same way with the frequency range contained in the line shape.

$$f(x) = \frac{1}{\pi} \left[\frac{\gamma}{(x - x_0)^2 + \gamma^2} \right] \quad (\text{A.3.0.25})$$

Height is $\frac{1}{\pi\gamma}$ and the full width at half maximum:

$$\frac{1}{\pi} \left[\frac{\gamma}{(x - x_0)^2 + \gamma^2} \right] = \frac{1}{2\pi\gamma} \quad (\text{A.3.0.26})$$

$$x = x_0 \pm \gamma \quad (\text{A.3.0.27})$$

Since collision between gas phase molecules leads to the limited life-time (T_2) of a particular state of the molecule, Fourier transform and auto-correlation

method can be used to derive the pressure broadening line shape of the spectrum, which is the Lorentzian line shape with FWHM depends on the pressure of the gas sample:

$$\Delta v_{1/2} = \frac{1}{\pi T_2} \quad (\text{A.3.0.28})$$

$$\Delta v_{1/2} = bp \quad (\text{A.3.0.29})$$

where b is the pressure broadening coefficient that mostly measured from experiments. The pressure broadening coefficient is further associated with the partial and total pressure of the sample, for example in HITRAN08 database described in Appendix A.

Predissociation Broadening Similar to pressure broadening, predissociation of the molecular complex from the excited state leads to a limited life time (τ) and hence broadening of the Lorentzian line shape with FWHM (Γ).

$$\tau = \frac{1}{2\pi\Gamma} \quad (\text{A.3.0.30})$$

This relation is used to estimate the lifetime of the excited states of HCCH-NH₃ and OCS-NH₃ complex in Sec. 6.

A.4 Detection Limit

The spectrum measured from the experiments is the absorption of light intensity as a function of light frequency, i.e., $k(\nu)$ as defined in Eqn. A.2.0.1. The detection limit of a certain molecule is based on the integrated absorption of a certain transition, i.e., S as defined in Eqn. A.2.0.1. These two functions are connected by the line shape profile $g(\nu - \nu_0)$.

$$k = S \times g \quad (\text{A.4.0.31})$$

$$S = \frac{\sum k_i g_i}{\sum g_i^2} \quad (\text{A.4.0.32})$$

Thus the standard deviation of the S can be derived from the standard deviation of k , and is depend on the sampling rate of the line shape function g_i .

$$\frac{(S - \bar{S})^2}{n - 1} = \frac{1}{n - 1} \frac{\sum g^2(k_i - S \times g_i)^2}{\sum g_i^4} \quad (\text{A.4.0.33})$$

$$= \frac{\sum (k_i - S \times g_i)^2}{n - 1} \frac{1}{\sum g_i^2} \quad (\text{A.4.0.34})$$

$$\sigma_S^2 = \frac{\sigma_k^2}{\sum g_i^2} \quad (\text{A.4.0.35})$$

with

$$\sum g_i^2 = \frac{\sum g_i^2 \delta v}{\delta v} = \frac{\int g^2(f) dv}{\delta v} \quad (\text{A.4.0.36})$$

$$(\text{A.4.0.37})$$

the standard deviation of the integrated transition absorption σ_S can be calculate from the standard deviation of the absorption spectrum σ_k and the line shape function $g(v)$:

$$\sigma_S = \sigma_k \sqrt{\frac{\delta v}{\int g(v)^2 dv}} \quad (\text{A.4.0.38})$$

For Lorentzian line shape:

$$\int g(v)^2 dv = \frac{1}{2\pi\gamma} \quad (\text{A.4.0.39})$$

$$\sigma_S = \sigma_k \sqrt{2\pi\gamma\delta v} \quad (\text{A.4.0.40})$$

For Gaussian line shape:

$$\int g(v)^2 dv = \frac{1}{2\sigma\sqrt{\pi}} \quad (\text{A.4.0.41})$$

$$\sigma_S = \sigma_k \sqrt{2\sqrt{\pi}\sigma\delta v} \quad (\text{A.4.0.42})$$

With the standard deviation of the integrated absorption peak σ_S and the knowledge of the S^C from the HITRAN database, we can then calculate the detection limit of a particular molecule based on this transition, which is usually presented as 3σ value.

Appendix B

The Classical Treatment of Molecular Vibration and Rotation

The classical view for a molecule is the “ball and spring” model in which the nuclei are represented by particles with certain masses and are connected by weightless springs that represent the binding electrons. Further more, we assume the springs obey Hooke’s law so that the motion is harmonic. Analysis of the dynamics of the vibration and rotation of this model using classical mechanics sets the stage for the quantum mechanical analysis of the rovibrational energy levels in Sections 2.2.1.

We first treat the molecule as a rigid rotor such that the distance between the nuclei do not vary. The motion of a rigid body has been concisely discussed in Landau’s classical Course of Theoretical Physics(132) which we largely follow. Six degrees of freedom are needed to describe the motion of the rigid rotor: XYZ to describe the translation of the rigid rotor in space fixed coordinates and θ, ϕ, χ as the Euler angles to describe the rotation of body fixed frame of the rigid rotor. The next step is to release the constraint of rigid motion, allowing each of the nuclei of the molecule to vibrate with small amplitude around their equilibrium positions. $3N - 6$ internal coordinates are needed to describe a non-linear polyatomic molecule. We introduce the normal coordinates Q using Wilson’s **GF** method.

B.1 Rigid Rotor

B.1.1 Definition of the rigid rotor coordinate

We can define two sets of frames to describe the rigid rotor as shown in Fig B.2:

- fixed system XYZ , so called “space-fixed frame”
- moving system xyz , so called “body-fixed frame” that rotates along the molecule and meets the Eckart conditions (Sec B.2).

The 6 degrees of freedom of a rigid rotor are:

- 3 components of vector R_0 to describe the position of center of mass the rigid rotor
- the 3 independent Euler angles to describe orientation of the body-fixed frame of the rigid rotor in the space-fixed frame, θ, ϕ, χ

Definition of Euler angles is shown in Fig. B.1 following the definition by Wilson(280) and Papoušek and Aliev (195).

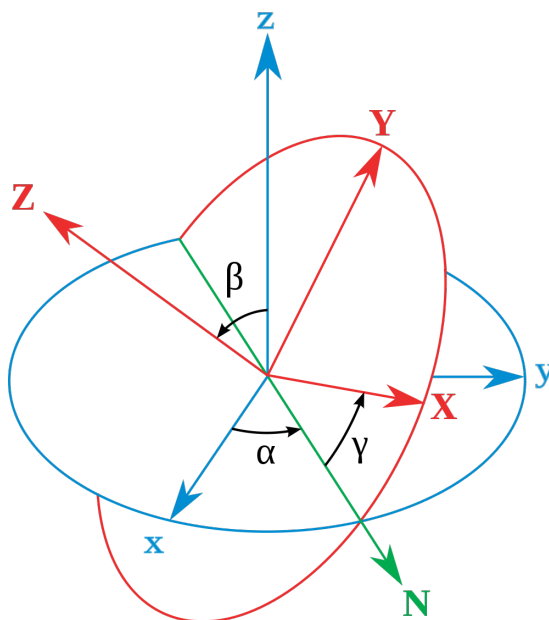


Figure B.1: Euler angles - The XYZ (fixed) system is shown in blue, the xyz (rotated) system is shown in red. The line of nodes, labeled N , is shown in green, taken from Ref. (306).

Following Eqn. B.1.1.1, the Euler angles (θ, ϕ, χ) describes an arbitrary point of the rigid rotor in the space-fixed coordinate $\mathbf{r}(0)$ changes to $\mathbf{r}(\alpha, \beta, \gamma)$ after the three consecutive rotation, where:

$$\mathbf{r}(\alpha, \beta, \gamma) = \mathbf{R}(\alpha, \beta, \gamma)\mathbf{r}(0) \quad (\text{B.1.1.1})$$

$$\mathbf{R}(\alpha, \beta, \gamma) = \begin{pmatrix} \cos \alpha & -\sin \alpha & 0 \\ \sin \alpha & \cos \alpha & 0 \\ 0 & 0 & 1 \end{pmatrix} \begin{pmatrix} \cos \beta & 0 & \sin \beta \\ 0 & 1 & 0 \\ -\sin \beta & 0 & \cos \beta \end{pmatrix} \begin{pmatrix} \cos \gamma & -\sin \gamma & 0 \\ \sin \gamma & \cos \gamma & 0 \\ 0 & 0 & 1 \end{pmatrix} \quad (\text{B.1.1.2})$$

Relation between the dynamics of Eulerian angles (ϕ, ψ, θ) and angular velocity in lab fixed frame (xyz):

$$\omega_x = \dot{\phi} \sin \theta \sin \psi + \dot{\theta} \cos \psi \quad (\text{B.1.1.3})$$

$$\omega_y = \dot{\phi} \sin \theta \cos \psi - \dot{\theta} \sin \psi \quad (\text{B.1.1.4})$$

$$\omega_z = \dot{\phi} \cos \theta + \dot{\psi} \quad (\text{B.1.1.5})$$

Therefore, arbitrary infinitesimal displacement of the rigid rotor can be represented as the sum of two parts:

1. infinitesimal translation of the rotor: $d\mathbf{R}$ with respect to R_0
2. infinitesimal rotation about the center of mass: θ, ϕ, χ

With the coordinate a nucleus in the body-fixed frame to be a_i , the coordinate of the nucleus in the space-fixed frame is:

$$R_i = R_0 + S^{-1}(\theta, \phi, \chi)a_i \quad (\text{B.1.1.6})$$

This is illustrated in Fig B.2.

B.1.2 Moment of inertia

Rotation of a rigid body can be represented by its angular momentum.

$$\mathbf{J} = \mathbf{r} \times \mathbf{p} \quad (\text{B.1.2.1})$$

$$J_x = yp_z - zp_y \quad (\text{B.1.2.2})$$

$$J_y = zp_x - xp_z \quad (\text{B.1.2.3})$$

$$J_z = xp_y - yp_x \quad (\text{B.1.2.4})$$

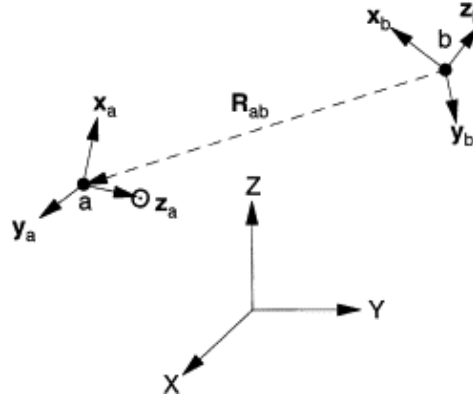


Figure B.2: Space-fixed and body-fixed coordinate -

Due to isotropy of space, the angular momentum is conservative without the application of torque. Torque applied on a certain rotation axis: $\mathbf{M} = \mathbf{r} \times \mathbf{F}$ determines the change of angular momentum:

$$\frac{d\mathbf{J}}{dt} = \mathbf{M} \quad (\text{B.1.2.5})$$

An arbitrary infinitesimal displacement of a rigid body can be decomposed into translation and rotation:

$$\frac{d\mathbf{r}}{dt} = \frac{d\mathbf{R}}{dt} + \frac{d\phi}{dt} \times \mathbf{r} \quad (\text{B.1.2.6})$$

$$\mathbf{v} = \mathbf{V} + \boldsymbol{\Omega} \times \mathbf{r} \quad (\text{B.1.2.7})$$

Thus it is always possible to choose an origin O' so that the motion of the rigid body at the instant considered is a pure *rotation* about an axis through O' , which is called *instantaneous axis of rotation*.

The kinetic energy is:

$$\begin{aligned} T &= \frac{1}{2}mv^2 \\ &= \sum \frac{1}{2}m(\mathbf{V} + \boldsymbol{\Omega} \times \mathbf{r})^2 \\ &= \sum \frac{1}{2}mV^2 + \sum m\mathbf{V} \cdot \boldsymbol{\Omega} \times \mathbf{r} + \sum \frac{1}{2}m(\boldsymbol{\Omega} \times \mathbf{r})^2 \\ &= \frac{1}{2}\mu V^2 + \mathbf{V} \times \boldsymbol{\Omega} \cdot \sum m\mathbf{r} + \frac{1}{2} \sum m[\Omega^2 r^2 - (\boldsymbol{\Omega} \cdot \mathbf{r})^2] \quad (\text{B.1.2.8}) \end{aligned}$$

note that the second term is zero since we choose center of mass as origin. We can rewrite the kinetic energy of rotation in tensor form, i.e. in terms of the components of the vector \mathbf{r} and $\boldsymbol{\Omega}$:

$$\begin{aligned} T_{rot} &= \frac{1}{2} \sum m(\Omega_i^2 x_i^2 - \Omega_i x_i \Omega_k x_k) \\ &= \frac{1}{2} \sum m(\Omega_i \Omega_k \delta_{ik} x_i^2 - \Omega_i \Omega_k x_i x_k) \\ &= \frac{1}{2} \Omega_i \Omega_k \sum m(x_i^2 \delta_{ik} - x_i x_k) \end{aligned} \quad (\text{B.1.2.9})$$

In terms of the moment of inertia tensor $I_{ik} = \sum m(x_i^2 \delta_{ik} - x_i x_k)$, we have:

$$I_{xx} = \sum m(y^2 + z^2) \quad (\text{B.1.2.10})$$

$$I_{yy} = \sum m(z^2 + x^2) \quad (\text{B.1.2.11})$$

$$I_{zz} = \sum m(x^2 + y^2) \quad (\text{B.1.2.12})$$

$$I_{zy} = I_{yz} = \sum m y z \quad (\text{B.1.2.13})$$

$$I_{xz} = I_{zx} = \sum m z x \quad (\text{B.1.2.14})$$

$$I_{xy} = I_{yx} = \sum m y x \quad (\text{B.1.2.15})$$

$$T = \frac{1}{2} \mu V^2 + \frac{1}{2} I_{ik} \Omega_i \Omega_k \quad (\text{B.1.2.16})$$

another way to derive the kinetic energy from angular momentum:

$$\begin{aligned} T &= \frac{1}{2} \sum m \dot{\mathbf{r}}^2 \\ &= \frac{1}{2} \boldsymbol{\omega} \cdot \mathbf{J} \\ &= \frac{1}{2} (I_{xx} \omega_x^2 + I_{yy} \omega_y^2 + I_{zz} \omega_z^2 - 2I_{yz} \omega_y \omega_z - 2I_{zx} \omega_z \omega_x - 2I_{xy} \omega_x \omega_y) \\ &= \frac{1}{2} \begin{pmatrix} \omega_x & \omega_y & \omega_z \end{pmatrix} \begin{pmatrix} I_{xx} & -I_{xy} & -I_{xz} \\ -I_{yx} & I_{yy} & -I_{yz} \\ -I_{zx} & -I_{zy} & I_{zz} \end{pmatrix} \begin{pmatrix} \omega_x \\ \omega_y \\ \omega_z \end{pmatrix} \end{aligned} \quad (\text{B.1.2.17})$$

\underline{I} is the moment of inertia tensor (Eqn. B.1.2.25), using the body-fixed xyz coordinate. In the form of principal momentum of inertia, the kinetic energy transform to:

$$T = \frac{1}{2} \mu V^2 + \frac{1}{2} \underline{I} \boldsymbol{\omega}^2 \quad (\text{B.1.2.18})$$

and the angular momentum of the rigid rotor is:

$$L = \underline{I} \cdot \omega \quad (\text{B.1.2.19})$$

$$\mathbf{J} = \sum \mathbf{r} \times m\mathbf{v} \quad (\text{B.1.2.20})$$

$$= \sum m[\mathbf{r} \times (\omega \times \mathbf{r})] \quad (\text{B.1.2.21})$$

$$= \sum m[\omega r^2 - \mathbf{r}(\omega \cdot \mathbf{r})] \quad (\text{B.1.2.22})$$

$$J_i = I_{ik}\Omega_k \quad (\text{B.1.2.23})$$

We have the component of angular momentum at each axis:

$$\begin{pmatrix} J_x \\ J_y \\ J_z \end{pmatrix} = \begin{pmatrix} I_{xx} & -I_{xy} & -I_{xz} \\ -I_{yx} & I_{yy} & -I_{yz} \\ -I_{zx} & -I_{zy} & I_{zz} \end{pmatrix} \begin{pmatrix} \omega_x \\ \omega_y \\ \omega_z \end{pmatrix} \quad (\text{B.1.2.24})$$

The Hermitian \underline{I} can always be diagonalised with appropriate choice of coordinate.

$$\underline{I} = \begin{bmatrix} m(y^2 + z^2) & 0 & 0 \\ 0 & m(x^2 + z^2) & 0 \\ 0 & 0 & m(x^2 + y^2) \end{bmatrix} \quad (\text{B.1.2.25})$$

Such axes are called principal axes of inertia, and the values of the diagonal components of the tensor are called the principal moments of inertia. Convention is such that we choose $I_a \leq I_b \leq I_c$ (note that $I_a + I_b \geq I_c$) and name the principal axes of inertia as a -, b -, and c -axis. And the rotational kinetic energy can be written as:

$$T = \frac{1}{2} \left[\frac{L_a^2}{I_a} + \frac{L_b^2}{I_b} + \frac{L_c^2}{I_c} \right] \quad (\text{B.1.2.26})$$

Based on the difference of the principal moments of inertia, the rigid rotors can be classified into different categories:

- rotator (with 2 degrees of freedom for rotation): $I_a=0, I_b = I_c$
- spherical top: $I_a = I_b = I_c$
- symmetric top: prolate top: $I_a < I_b = I_c$ oblate top: $I_a = I_b < I_c$
- asymmetric top: $I_a < I_b < I_c$

Notice that these naming reflect the shape of the rigid rotor (note a prolate spheroid requires its principal axes $a = b < c$) rather than the inertia ellipsoid that mentioned below. The shapes of a prolate and an oblate spheroid are illustrated in Fig B.3.

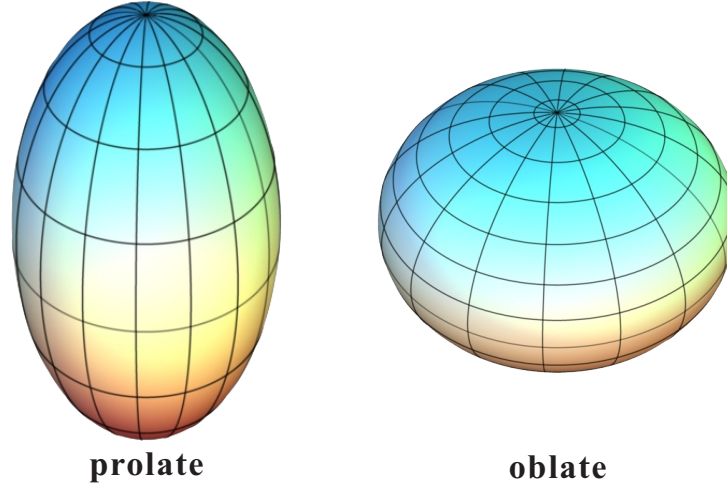


Figure B.3: Plot of a prolate and an oblate spheroid -

B.1.3 Dynamics of rigid rotor

The dynamics of a rigid rotor is determined by Euler's equations.

$$I_1 \dot{\omega}_1 + (I_3 - I_2) \omega_2 \omega_3 = M_1 \quad (\text{B.1.3.1})$$

$$I_2 \dot{\omega}_2 + (I_1 - I_3) \omega_3 \omega_1 = M_2 \quad (\text{B.1.3.2})$$

$$I_3 \dot{\omega}_3 + (I_2 - I_1) \omega_1 \omega_2 = M_3 \quad (\text{B.1.3.3})$$

where M are the applied torques. For example, solution for a symmetric top shows that the angular velocity along the symmetric axis is constant and angular velocities along the other two axes have:

$$\omega_1 = A \cos kt \quad (\text{B.1.3.4})$$

$$\omega_2 = A \sin kt \quad (\text{B.1.3.5})$$

$$(\text{B.1.3.6})$$

This shows that the angular velocity ω rotates uniformly with frequency k about the symmetric axis of the rigid rotor and its projection along the symmetric top is a constant.

Usually, the dynamics of asymmetric top rigid rotor is more complicated but geometrical visualization of the angular velocities can provide us insights into its dynamic. We write the rotational kinetic energy of the rigid rotor as:

$$T = \frac{1}{2} I_a \omega_a^2 + \frac{1}{2} I_b \omega_b^2 + \frac{1}{2} I_c \omega_c^2 \quad (\text{B.1.3.7})$$

B.2 Separation of Rotations and Vibrations

Since the rigid rotor experience torque-free motion in the free space, the conservation of kinetic energy requires $T = 0$, which imposes a constraint on the angular velocity vector ω . In the principal axes frame, ω traces out an ellipsoid, which has axes half of the values of the principal moments of inertia and along the principal axes of inertia. This ellipsoid is called inertia ellipsoid. A second constraint comes from the conservation of angular momentum. Since

$$2T = \omega \cdot \mathbf{L} \quad (\text{B.1.3.8})$$

and T and \mathbf{L} are constants, the dot product of the angular velocity ω with a constant vector \mathbf{L} is a constant. In the lab-fixed coordinate, this means ω must lie on an invariable plane defined by its dot product with the conserved angular momentum vector. Results of the two constraints is the Poinsot's construction, as shown in Fig B.4 In lab-fixed coordinate, the instantaneous angular velocity vector ω traces out the point of intersection between a fixed invariable plane and the kinetic-energy ellipsoid that is tangent to it and rolls around on it without slipping.

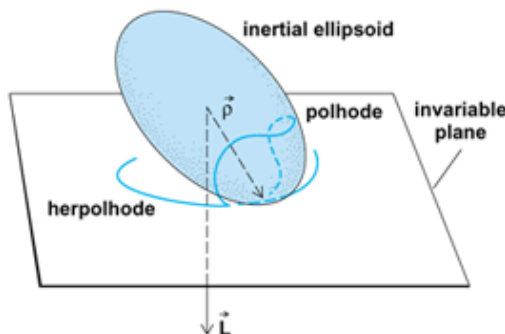


Figure B.4: Poinsot's construction -

B.2 Separation of Rotations and Vibrations

Now we allow each of the nuclei of the molecule to vibrate with small amplitude around their equilibrium positions. So the model is a semi-rigid molecule. Such displacement is represented by d_i in space-fixed space so that the position of the nucleus in the body-fixed space is $r_i = a_i + d_i$. With Eqn B.1.1.6, the coordinates of the nucleus in the space-fixed frame is:

$$R_i = R_0 + S^{-1}(\theta, \phi, \chi)r_i \quad (\text{B.2.0.9})$$

$$R'_i = R'_0 + \omega \times r_i + d' \quad (\text{B.2.0.10})$$

B.2 Separation of Rotations and Vibrations

It is clearly seen in Eqn B.2.0.10 that there are 6 constraints applied to d_i so that on both sides of the equation there are $3N$ degrees of freedom.

Essentially, the linear transformation of the coordinates:

$$\begin{pmatrix} r_1 \\ r_2 \\ \vdots \\ r_{3N-6} \\ T_x \\ T_y \\ T_z \\ R_x \\ R_y \\ R_z \end{pmatrix} = \begin{pmatrix} B_v \\ B_r \end{pmatrix} \begin{pmatrix} d_{1x} \\ d_{1y} \\ d_{1z} \\ \vdots \\ d_{Nz} \end{pmatrix} \quad (\text{B.2.0.11})$$

The transformation B_r transform the space-fixed coordinates to the translation and rotation coordinates $T R$, which are independent of the internal coordinates r from the transformation B_v . By setting $T, R = 0$, we have the Eckart conditions:

$$\sum m_i d_i = 0 \quad (\text{B.2.0.12})$$

$$\sum m_i a_i \times d_i = 0 \quad (\text{B.2.0.13})$$

The physical meaning of the Eckart conditions are:

1. during a molecular vibration the center of mass of the molecule must remain unshifted
2. during a molecular vibration there is no zero-order angular momentum

So that the transformation following the Eckart conditions defines the molecular-fixed axis frame we usually use. It can be shown that the first Eckart conditions eliminate the coupling between the translation and rotation, and translation and vibration. The second Eckart condition can remove the major terms of the rotation-vibration coupling, but cannot completely eliminate the rotation-vibration coupling.

In the space-fixed frame, the rotation-vibration kinetic energy of the rigid body is:

$$2T = \sum m_{xyz} (\omega \times r) \cdot (\omega \times r) + \sum m_i d_i'^2 + 2\omega \cdot \sum m_i d_i \times d_i' \quad (\text{B.2.0.14})$$

The first 2 terms are corresponding to the pure rotational and vibrational energies. The last term is the rotation-vibration coupling term called Coriolis energy. It should be noted that the Coriolis term is small compared to the vibrational term since it depends both on the displacement d_i and angular velocity ω . Therefore, this term is usually combined with the rotational term and treat other two terms separately.

B.3 Normal mode Vibration

The following **GF** method developed by Wilson(283) is efficient method to decouple the classical vibrational motions of the semi-rigid molecule. With the transformation from space-fixed coordinates to internal coordinates:

$$\underline{r}_{3N-6} = (\underline{B}_v)_{(3N-6) \times 3N} \underline{d}_{3N} \quad (\text{B.3.0.15})$$

We can rewrite the kinetic energy of the vibration of the semi-rigid molecule as:

$$\begin{aligned} 2T &= \underline{d}'^T \underline{M} \underline{d}' \\ &= \underline{r}'^T \underline{B}_v^T \underline{M} \underline{B}_v \underline{r}' \end{aligned} \quad (\text{B.3.0.16})$$

By introducing the **G** (Geometry) matrix as $\underline{G} = \underline{B}_v \underline{M}^{-1} \underline{B}_v^T$, the vibrational energy can be written as:

$$2T = \underline{r}'^T \underline{G}^{-1} \underline{r}' \quad (\text{B.3.0.17})$$

Similarly, the expression for the potential energy V can be written in the following form by introducing the **F** (Force) matrix.

$$2V = \underline{r}^T \underline{F} \underline{r} \quad (\text{B.3.0.18})$$

We can then define the normal coordinates \underline{Q} of the semi-rigid molecule from linear combination of an arbitrary set of internal coordinates as:

$$\underline{r} = \underline{L} \underline{Q} \quad (\text{B.3.0.19})$$

$$\begin{aligned} 2T &= \underline{Q}'^T \underline{L}^T \underline{G}^{-1} \underline{L} \underline{Q}' \\ &= \underline{Q}'^T \underline{E} \underline{Q}' \end{aligned} \quad (\text{B.3.0.20})$$

$$\begin{aligned} 2V &= \underline{Q}^T \underline{L}^T \underline{F} \underline{L} \underline{Q} \\ &= \underline{Q}^T \underline{\Lambda} \underline{Q} \end{aligned} \quad (\text{B.3.0.21})$$

B.4 Classical rotation-vibration Hamiltonian

Here we introduced the \mathbf{L} matrix and the diagonal $\mathbf{\Lambda}$ matrix which that satisfying:

$$\mathbf{L}^{-1}\mathbf{GFL} = \mathbf{\Lambda} \quad (\text{B.3.0.22})$$

This means $\mathbf{\Lambda}$ contains the eigenvalues of \mathbf{GF} and \mathbf{L} is its eigenvectors.

With the normal coordinates \underline{Q} the vibration of the semi-rigid molecule is decoupled into $3N - 6$ set of independent vibration equations with the solutions:

$$r_i = L_{ik} \cos(\lambda_k^{1/2}t + \theta) \quad (\text{B.3.0.23})$$

L_{ik} is the amplitude of vibrational coordinates r_i and θ is the phase of the normal vibration which is the same for all coordinates r_i .

Therefore, vibration of the semi-rigid molecule can be represented as $3N - 6$ normal modes that the quadratic terms in the potential function are diagonal.

$$\begin{aligned} V(Q) &= V_e + \frac{1}{2} \sum_k \lambda_k Q_k^2 + \frac{1}{6} \sum_{kst} \Phi_{kst} Q_k Q_s Q_t + \frac{1}{24} \sum_{kstu} \Phi_{kstu} Q_k Q_s Q_t Q_u \quad (\text{B.3.0.24}) \\ &\approx V_e + \frac{1}{2} \sum_k \lambda_k Q_k^2 \quad (\text{B.3.0.25}) \end{aligned}$$

B.4 Classical rotation-vibration Hamiltonian

Similar to the transformation from the Cartesian displacement d to the internal coordinates r , B.3.0.15 we have the transformation from the normal coordinates Q to the Cartesian displacement d .

$$\underline{\sqrt{m}d}_{3N} = (\underline{l})_{3N \times (3N-6)} \underline{Q}_{3N-6} \quad (\text{B.4.0.26})$$

We can now re-write the rotation-vibration kinetic energy of the rigid-body B.2.0.14 as:

$$\begin{aligned} T &= \frac{1}{2} I_{\alpha\beta} \omega_\alpha \omega_\beta \\ &\quad + \sum_r \sum_s \omega_\alpha \zeta_{rs}^{(\alpha)} Q_r Q'_s \\ &\quad + \frac{1}{2} \sum_r Q_r'^2 \quad (\text{B.4.0.27}) \end{aligned}$$

where α, β, γ are cyclic permutations of x, y, z , and the Coriolis coupling constant between two normal modes Q_r and Q_s is:

$$\zeta_{rs}^{(\alpha)} = \sum_n e_{\alpha,\beta,\gamma} l_{nr}^{(\beta)} l_{ns}^{(\gamma)} j \quad (\text{B.4.0.28})$$

B.4 Classical rotation-vibration Hamiltonian

with $e_{\alpha,\beta,\gamma}$ is the permutation symbol. The physical significance of the Coriolis coupling constants is the scale the amount of angular momentum about the α -axis generated by the two normal vibrations.

We can define the linear vibrational momentum:

$$\begin{aligned} J_\alpha &= \frac{\partial T}{\partial \omega_\alpha} \\ &= I_{\alpha,\beta} \omega_\beta + \sum_r \sum_s \zeta_{rs}^{(\alpha)} Q_r Q'_s \end{aligned} \quad (\text{B.4.0.29})$$

$$\begin{aligned} P_r &= \frac{\partial T}{\partial Q'_r} \\ &= \sum_s \omega_\alpha \zeta_{rs}^{(\alpha)} Q_s + Q'_r \end{aligned} \quad (\text{B.4.0.30})$$

So the energy is :

$$\begin{aligned} T &= \frac{1}{2} J_\alpha \omega_\alpha + \frac{1}{2} \sum_r P_r Q'_r \\ &= \frac{1}{2} J_\alpha \omega_\alpha + \frac{1}{2} \sum_r P_r^2 - \frac{1}{2} \sum_r P_r \sum_s \omega_\alpha \zeta_{rs}^{(\alpha)} Q_s \\ &= \frac{1}{2} (J_\alpha - \Pi_\alpha) \omega_\alpha + \frac{1}{2} \sum_r P_r^2 \end{aligned} \quad (\text{B.4.0.31})$$

Here we introduce the arbitrarily defined internal momentum Π arise from vibration:

$$\Pi_\alpha = \sum_r \sum_s \zeta_{rs}^{(\alpha)} Q_r P_s \quad (\text{B.4.0.32})$$

With the effective moment of inertia defined as:

$$\underline{J - \Pi} = \underline{I' \omega \omega} = \underline{\mu (J - \Pi)} \quad (\text{B.4.0.33})$$

The classical Hamiltonian of the rotation-vibration semi-rigid body can be written in the normal modes as:

$$\begin{aligned} H &= \frac{1}{2} (J_\alpha - \Pi_\alpha) \mu_{\alpha\beta} (J_\beta - \Pi_\beta) \\ &\quad + \frac{1}{2} \sum_r P_r^2 \\ &\quad + V \end{aligned} \quad (\text{B.4.0.34})$$

Appendix C

Angular momentum

C.1 Operators

The angular momentum along each space fixed axis is:

$$L_x = yp_z - zp_y = -iy\hbar\partial/\partial z + iz\hbar\partial/\partial y \quad (\text{C.1.0.1})$$

$$L_y = zp_x - xp_z = -iz\hbar\partial/\partial x + ix\hbar\partial/\partial z \quad (\text{C.1.0.2})$$

$$L_z = xp_y - yp_x = -ix\hbar\partial/\partial y + iy\hbar\partial/\partial x \quad (\text{C.1.0.3})$$

The square of the total angular momentum:

$$L^2 = L_x^2 + L_y^2 + L_z^2 \quad (\text{C.1.0.4})$$

raising and lowering operator for L_z^2 :

$$L_{\pm} = L_x \pm iL_y \quad (\text{C.1.0.5})$$

For every pair of observables whose operators do not commute, i.e., *incompatible observables*, we have the “Generalized Uncertainty Principle”:

$$\delta_A^2 \delta_B^2 \geq \left(\frac{1}{2i} \langle [\hat{A}, \hat{B}] \rangle\right)^2 \quad (\text{C.1.0.6})$$

As an example the canonical of the position ($\hat{A} = x$) and momentum ($\hat{B} = (\hbar/i)d/dt$) operator:

$$[\hat{x}, \hat{p}] = i\hbar \quad (\text{C.1.0.7})$$

$$\delta_x^2 \delta_p^2 \geq \left(\frac{1}{2i} i\hbar\right)^2 \quad (\text{C.1.0.8})$$

$$\delta_x \delta_p \geq \frac{\hbar}{2} \quad (\text{C.1.0.9})$$

C.1.1 compatible operators

have the same set of eigenfunctions and can be observed simultaneously. An example of compatible operators is the angular momentum at one axis (e.g. L_z) and square of the total angular momentum (L^2):

$$([L^2, L_x] = 0) \tag{C.1.1.1}$$

$$([L^2, L_y] = 0) \tag{C.1.1.2}$$

$$([L^2, L_z] = 0) \tag{C.1.1.3}$$

or more compactly,

$$[L^2, \mathbf{L}] = 0 \tag{C.1.1.4}$$

The angular momentum at one axis and the position or momentum are compatible operators:

$$[L_z, z] = 0; [L_z, p_z] = 0 \tag{C.1.1.5}$$

C.1.2 Incompatible operators

Incompatible operators do not have the same set of eigenfunctions and cannot be observed simultaneously. Angular momentum at different axes are incompatible operators:

$$([L_x, L_y] = i\hbar L_z) \tag{C.1.2.1}$$

$$([L_y, L_z] = i\hbar L_x) \tag{C.1.2.2}$$

$$([L_z, L_x] = i\hbar L_y) \tag{C.1.2.3}$$

Also angular momentum and position or momentum at different axes are incompatible operators:

$$([L_z, x] = i\hbar y); ([L_z, p_x] = i\hbar p_y) \tag{C.1.2.4}$$

$$([L_z, y] = -i\hbar x); ([L_z, p_y] = -i\hbar p_x) \tag{C.1.2.5}$$

The commutator of ladder operator L_{\pm} with L_z is:

$$([L_z, L_{\pm}]) = \pm\hbar L_{\pm} \tag{C.1.2.6}$$

$$([L_+, L_-]) = 2\hbar L_z \tag{C.1.2.7}$$

$$([L^2, L_{\pm}]) = 0 \tag{C.1.2.8}$$

C.2 Eigenstates

The square of the total angular momentum $\hat{\mathbf{J}}^2$, the projection of total angular momentum on the body-fixed axis \hat{J}_z , and the projection of total angular momentum on the space-fixed \hat{J}_Z have common eigenfunctions $|Jkm\rangle$. Note that there are 3 degree of freedom for the rotational Hamiltonian, but \hat{J}_z and \hat{J}_Z do not commute.

$$|Jkm\rangle = \psi_{Jkm}(\theta, \phi, \chi) = e^{ik\chi} e^{im\phi} \Theta(\theta) \quad (\text{C.2.0.9})$$

Θ is an associated Legendre polynomial, and

$$k, m = -J, -J + 1, \dots, J - 1, J \quad (\text{C.2.0.10})$$

The **eigenvalues** of the operators are:

$$\hat{\mathbf{J}}^2|Jkm\rangle = \hbar^2 J(J + 1)|Jkm\rangle \quad (\text{C.2.0.11})$$

$$\hat{J}_z|Jk\rangle = \hbar k|Jk\rangle \quad (\text{C.2.0.12})$$

$$\hat{J}_Z|Jm\rangle = \hbar m|Jm\rangle \quad (\text{C.2.0.13})$$

J can take integer or a half-integer value: 0, 1/2, 1, 3/2, ... Note that rotation of a rigid body (extrinsic angular momentum) can only take integer value. Spin (\mathbf{S}), which is intrinsic angular momentum allows both integer and half-integer values.

The diagonal eigenvalue of the square of total angular momentum $\hat{\mathbf{J}}^2$ is fixed $J(J + 1)$. The eigenvalue of angular momentum on a certain axis varies from $-J$ to J in N integer steps.

The off-diagonal matrix elements are:

$$\langle Jm|J_{\pm}|J'm'\rangle = \hbar[J(J + 1) - m'(m' \pm 1)]^{\frac{1}{2}} \delta_{JJ'} \delta_{m, m' \pm 1} \quad (\text{C.2.0.14})$$

$$\langle Jm|J_x|J'm'\rangle = \frac{\hbar}{2}[J(J + 1) - m'(m' \pm 1)]^{\frac{1}{2}} \delta_{JJ'} \delta_{m, m' \pm 1} \quad (\text{C.2.0.15})$$

$$\langle Jm|J_y|J'm'\rangle = \mp \frac{\hbar}{2} i [J(J + 1) - m'(m' \pm 1)]^{\frac{1}{2}} \delta_{JJ'} \delta_{m, m' \pm 1} \quad (\text{C.2.0.16})$$

Note that the *standard phase convention* are the matrix elements of J_x are real while those of J_y are purely imaginary.

Squared operators have following matrix elements:

$$\hat{\mathbf{J}}^4 |Jkm\rangle = \hbar^4 J^2 (J+1)^2 |Jkm\rangle \quad (\text{C.2.0.17})$$

$$\hat{J}_Z^2 |Jm\rangle = \hbar^2 m^2 |Jm\rangle \quad (\text{C.2.0.18})$$

$$\langle l, m | L_x^2 | l, m \rangle = \frac{\hbar^2}{2} [l(l+1) - m^2] \quad (\text{C.2.0.19})$$

$$\langle l, m | L_x^2 | l, m \pm 2 \rangle = \frac{\hbar^2}{4} \sqrt{[l(l+1) - m(m \pm 1)][l(l+1) - (m \pm 1)(m \pm 2)]} \quad (\text{C.2.0.20})$$

C.3 Eigenfunctions

The angular momentum operators are rewrite in spherical coordinates:

$$\mathbf{L} = \frac{\hbar}{i} \left(\hat{\phi} \frac{\partial}{\partial \theta} - \hat{\theta} \frac{1}{\sin \theta} \frac{\partial}{\partial \phi} \right) \quad (\text{C.3.0.21})$$

$$L_z = \frac{\hbar}{i} \frac{\partial}{\partial \phi} \quad (\text{C.3.0.22})$$

$$L_x = \frac{\hbar}{i} \left(-\sin \phi \frac{\partial}{\partial \theta} - \cos \phi \cot \theta \frac{\partial}{\partial \phi} \right) \quad (\text{C.3.0.23})$$

$$L_y = \frac{\hbar}{i} \left(+\cos \phi \frac{\partial}{\partial \theta} - \sin \phi \cot \theta \frac{\partial}{\partial \phi} \right) \quad (\text{C.3.0.24})$$

$$L^2 = -\hbar^2 \left[\frac{1}{\sin \theta} \frac{\partial}{\partial \theta} \left(\sin \theta \frac{\partial}{\partial \theta} \right) + \frac{1}{\sin^2 \theta} \frac{\partial^2}{\partial \phi^2} \right] \quad (\text{C.3.0.25})$$

Solution of Eqn. C.3.0.25 in the $|Jm\rangle$ representation are the spherical harmonics functions:

$$|Jm\rangle = Y_{Jm}(\theta, \phi) \quad (\text{C.3.0.26})$$

By separation of variables, the spherical harmonics functions contain two parts: the azimuthal angle function and the polar angle function. For angular momentum in azimuthal axis:

$$L_z |Jm\rangle = \hbar m |Jm\rangle \quad (\text{C.3.0.27})$$

$$\frac{\hbar}{i} \frac{\partial}{\partial \phi} |Jm\rangle = \hbar m |Jm\rangle \quad (\text{C.3.0.28})$$

which is azimuthal equation with normalized exponential solution $|Jm\rangle = (2\pi)^{\frac{1}{2}} e^{im\phi}$.

C.3 Eigenfunctions

For polar angle differential equation, the wave function $\Theta_{Jm}(\theta)$ has analytical form and is related to the associated Legendre functions:

$$P_J^m(\cos \theta) = \sin^m \theta \left[\frac{d}{d(\cos \theta)} \right]^m P_J(\cos \theta) \quad (\text{C.3.0.29})$$

$$P_J(\cos \theta) = \frac{1}{2^J J!} \left[\frac{d}{d(\cos \theta)} \right]^J (\cos^2 \theta - 1)^J \quad (\text{C.3.0.30})$$

P_J are the ordinary Legendre polynomials.

For $m \geq 0$,

$$\Theta_{Jm}(\theta) = (-1)^m \sqrt{\frac{2J+1}{2} \frac{(J-m)!}{(J+m)!}} P_J^m(\cos(\theta)) \quad (\text{C.3.0.31})$$

For $m < 0$, $|m|$ should replace m and $(-1)^m$ is omitted, following the phase choice in Eqn. C.2.0.16

For reference purpose, the first few spherical harmonics (Eqn. C.3.0.26) are listed:

$$Y_{00} = \frac{1}{\sqrt{4\pi}} \quad (\text{C.3.0.32})$$

$$Y_{10} = \sqrt{\frac{3}{4\pi}} \cos \theta \quad (\text{C.3.0.33})$$

$$Y_{1,\pm 1} = \mp \sqrt{\frac{3}{8\pi}} e^{\pm i\phi} \sin \theta \quad (\text{C.3.0.34})$$

Note that the spherical harmonics are an orthonormal set over the unit sphere.

Appendix D

Order of Magnitude

In the above sections, we have hieratic separation of the total Hamiltonian of a molecule to the rotation, vibration, electric, and electron spin and hyperfine parts. This section is largely based on the insightful monograph by Takeshi Oka(192).

The electron spin-spin and spin-orbital interaction W_{es} is $\sim 10\text{ cm}^{-1}$, The nuclear spin-electron spin and nuclear spin- electron orbital interaction W_{hfs} is $\sim 30\text{ MHz}$.

For a molecular system, the angular momentum of electron and nuclei are both quantized to the order of \hbar .

$$rmv \sim RMV_r \sim \hbar \quad (\text{D.0.0.1})$$

Since the electronic orbital radius r and internuclear distance R are comparable, we have $mv \sim MV_r$. That is the nuclear velocity of rotation V_r and electron velocity are on the order of

$$V_r \sim \kappa^4 v \sim 300\text{ms}^{-1} \quad (\text{D.0.0.2})$$

The electronic dissociation energy is on the order of

$$W_e \sim \frac{1}{2}mv^2 \sim 100\text{nm} \quad (\text{D.0.0.3})$$

The rotation energy is on the order of

$$W_{rot} \sim \frac{1}{2}MV_r^2 \sim \kappa^4 Ry \sim 10\text{cm}^{-1} \quad (\text{D.0.0.4})$$

where Ry is the Rydberg constant.

Similarly for vibrational velocity:

$$V_v \sim 3000ms^{-1} \quad (\text{D.0.0.5})$$

and for vibrational energy:

$$W_{vib} \sim \kappa^2 \sim 1000\text{cm}^{-1} \quad (\text{D.0.0.6})$$

The fact that vibrational displacement ΔR is on the order of κR of nuclear distance R allows us to analyse operator O of any physical quantity that is vibrational and rotational dependent using time-independent perturbation method.

$$\begin{aligned} \hat{O} = & O_e + \sum_k O_k q_k + \frac{1}{2} \sum_{kl} O_{kl} q_k q_l + \frac{1}{3!} \sum_{klm} O_{klm} q_k q_l q_m + \dots \\ & + \sum_{\alpha\beta} O_{\alpha\beta} J_\alpha J_\beta + \dots \end{aligned} \quad (\text{D.0.0.7})$$

Expansion coefficients of the operator in the vibrational coordinates are in the order of O , κO , $\kappa^2 O$, respectively. The rotational operator J^2 carries the magnitude κ^4 . For example, the first order rotational correction is on the order of $\kappa W_{rot} \sim \kappa^5 Ry$. The vibrational separation is $\sim \kappa^2 Ry$, so that the second-order perturbation gives the quartic centrifugal distortion constant on the order of $\kappa^8 Ry \sim 30\text{MHz}$ and the third order perturbation gives the sextic centrifugal distortion constant on the order of $\kappa^{12} Ry \sim 30\text{kHz}$. The Coriolis interaction is on the order of rotational energy $\kappa^4 Ry$. The other vibration-rotation coupling constants are on the order of $\kappa^6 Ry$.

The interaction between the molecular rotation magnetic moment with the nuclear spin is extremely small $\sim 3\text{kHz}$. So the separation of nuclear spin and molecular rovibronic Hamiltonian is efficient that we have nuclear spin modifications such as ortho-, para- H_2O . See section 2.5.3.2 A summary of the orders of magnitude of atomic and molecular interactions are provided by Oka and reproduced in Fig. 2.1.

Appendix E

Supersonic Free Jet Expansion

The supersonic free jet expansion technique is used to produce cold and collision-less gas phase pioneered by Smalley, Wharton, and Levy.⁽²³⁴⁾ The theory and application of the technique can be found in the literatures.^(30, 233, 136, 137, 135, 179, 150, 149, 134, 260, 131) A supersonic molecular beam consists of a high pressure gas reservoir, a nozzle orifice with dimension much smaller than the mean free path λ_0 of the gas at the reservoir pressure P_0 , and pumping capacity to maintain the low downstream pressure. Collision of the gas molecules at the nozzle orifice narrows down the velocity distribution of the sample and an low translational temperature bath is achieved. For example, with 100 atm gas expansion, bath temperature as low as 0.03 K can be achieved and a pure Ar jet can be cooled to 2 K. Figure. E.1 shows the velocity distribution of a room-temperature ammonia sample, the supersonic free jet expansion of the ammonia sample and its velocity distribution when seeded in Xenon carrier gas.

When a poly-atomic molecule is seeded in the supersonic free jet expansion, the internal energy of the seeded molecule is transferred to the cold temperature bath of the beam during the collision process exiting the nozzle. The density of the jet rapidly reduce along the downstream path and the jet cooling effect is terminated once the jet enters a collision-less stage. Since the molecules are under cold and collision-less condition, the supersonic free jet expansion technique greatly increase the population on the ground rovibrational levels and decreased the spectral line width of the spectrum. In Fig. E.2, the spectra of NO_2 under conventional room-temperature, pure NO_2 supersonic beam and seeded in Ar beam is shown to demonstrate the cooling effect of the technique.

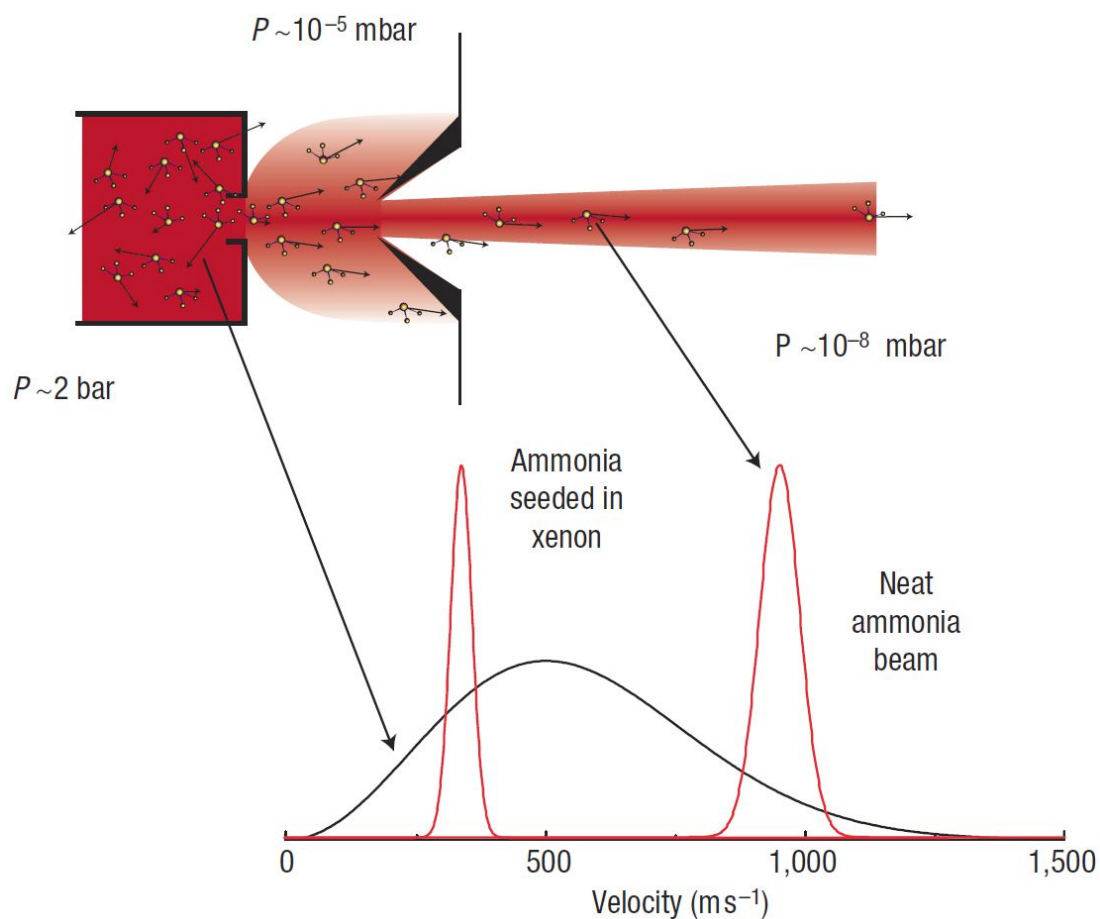


Figure E.1: Velocity distribution in a Supersonic free jet expansion - Schematic drawing of the adiabatic gas expansion of high-pressure ammonia gas expanded through a small hole into vacuum. The velocity distribution of room-temperature ammonia molecules in the container is broad. In the supersonic expansion of the ammonia gas, the distribution is narrowed and around 1000 m/s. The velocity distribution is narrowed by using Xenon carrier gas. The terminal velocity of the seed gas will then be the same as that of the carrier gas. Since Xenon is heavier than ammonia, the velocity distribution is centered around 400 m/s. Figure adapted from Ref. (260).

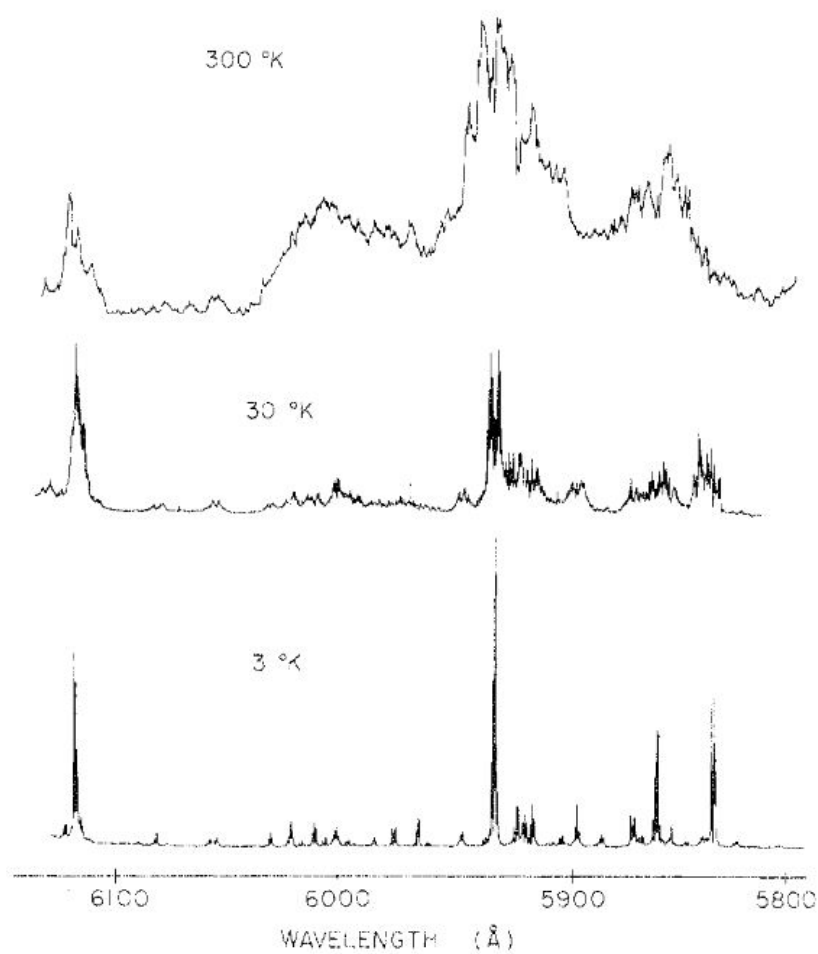


Figure E.2: Spectra of NO₂ in supersonic beam - Fluorescence excitation spectrum of NO₂. Top: conventional room-temperature sample of pure NO₂O at 0.04 Torr. Middle: a supersonic beam of pure NO₂. Bottom: a supersonic beam beam of 5% NO₂ in Ar. Figure adapted from Ref. (234).

With the speed of sound at

$$a = \sqrt{\frac{\gamma k T}{m}} \quad (\text{E.0.0.1})$$

where γ is the heat capacity ratio C_p/C_v and is 5/3 for a mono-atomic gas such as He, Ne, and Ar Noble gas, Mach number is defined as the ratio of the speed of the jet vs. the speed of sound in such medium and has been shown as:

$$M = \frac{u}{a} = A \left(\frac{L}{D}\right)^{\gamma-1} \quad (\text{E.0.0.2})$$

where L is the downstream distance, D is the nozzle diameter, and A is a constant that depends on γ and is 3.26 for a monatomic gas. The name of the supersonic free jet expansion comes from the fact that the Mach number is greater than 1 under such experimental conditions. The schematic drawing of the supersonic free jet expansion is shown in Fig. E.3.

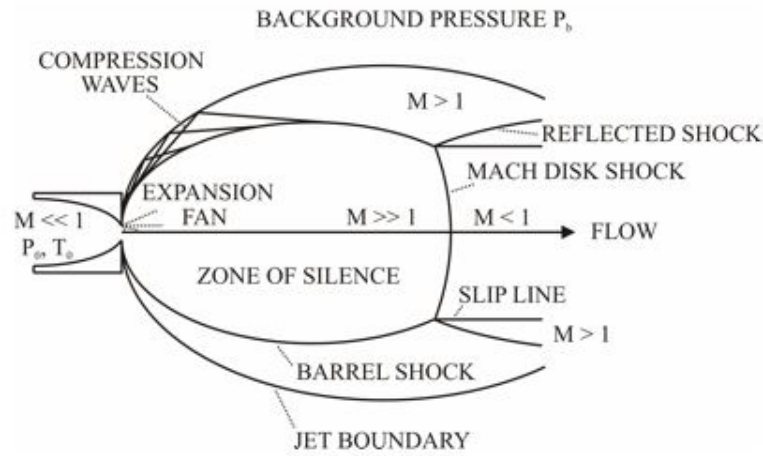


Figure E.3: Supersonic free jet expansion - Schematic drawing of the adiabatic gas expansion from a supersonic free jet. Figure adapted from Lawrence Berkeley National Lab MISTERS Webpage.

The relation of the temperature, pressure and density of the reservoir and in the expansion is:

$$\frac{T}{T_0} = \left(\frac{P}{P_0}\right)^{\frac{\gamma-1}{\gamma}} = \left(\frac{\rho}{\rho_0}\right)^{\gamma-1} = \frac{1}{1 + \frac{\gamma-1}{2M^2}} \quad (\text{E.0.0.3})$$

A simulation of a supersonic free jet expansion of 300 K 10 atm mono-atomic gas from a 1 mm diameter nozzle, is shown in Fig. E.4. As shown in the plot, within

several cm apart from the nozzle, the temperature of the jet flow drastically decreased to several Kelvin.

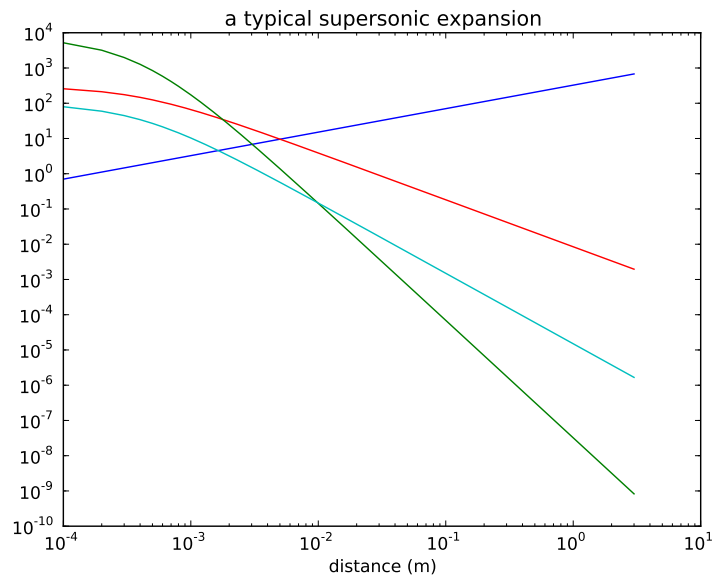


Figure E.4: Simulation of temperature, pressure and density in supersonic free jet expansion - Blue: Mach Number; Green: Pressure (Pa); Red: temperature (K). The simulation is for isotropic region of the jet, follows Eqn. E.0.0.3.

Appendix F

Confocal Off-axis cell

As shown in Fig. F.1, the position of the spots $[x_n \ y_n]$ after the incident beam that defined by its position on the entrance mirror $x_0 \ y_0$ and its slope $x'_0 \ y'_0$, can be calculated in the following Pierce(204),

$$x_n = x_0 \cos n\theta + \sqrt{\frac{d}{4f-d}}(x_0 + 2fx'_0) \sin n\theta \quad (\text{F.0.0.1})$$

$$y_n = y_0 \cos n\theta + \sqrt{\frac{d}{4f-d}}(y_0 + 2fy'_0) \sin n\theta \quad (\text{F.0.0.2})$$

where $\cos \theta = 1 - \frac{d}{2f}$

Following Herriott *et al.*(94), the expressions of x_n and y_n can also be rearranged to

$$x_n = A \sin (n\theta + \alpha) \quad (\text{F.0.0.3})$$

$$y_n = B \sin (n\theta + \beta) \quad (\text{F.0.0.4})$$

with

$$\tan \alpha = \frac{\sqrt{\frac{4f}{d} - 1}}{1 + 2f \frac{x'_0}{x_0}} \quad (\text{F.0.0.5})$$

$$\tan \beta = \frac{\sqrt{\frac{4f}{d} - 1}}{1 + 2f \frac{y'_0}{y_0}} \quad (\text{F.0.0.6})$$

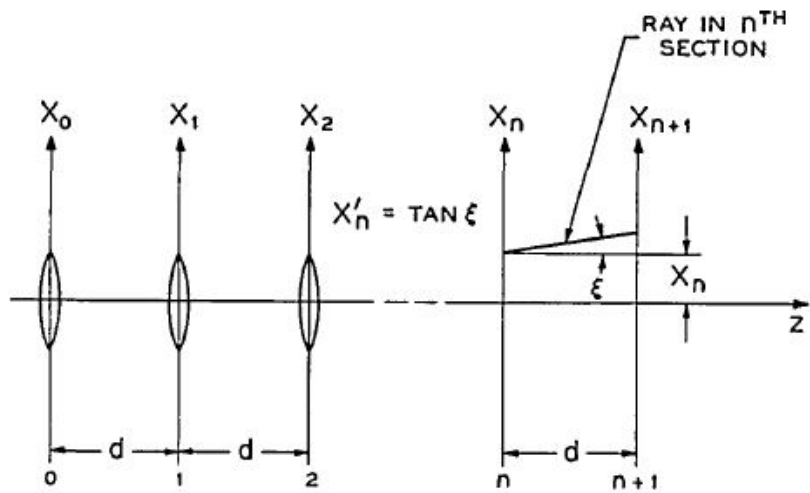


Fig. 1. Series of equally spaced thin lenses.

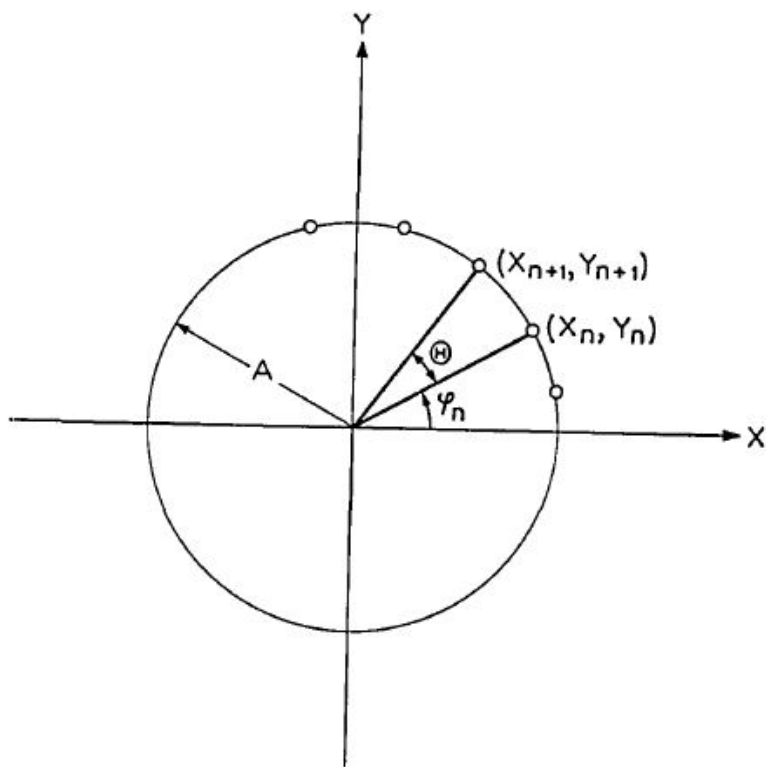


Fig. 2. Projections of intersection points (x_n, y_n) lying on circle.

Figure F.1: Beam geometry in a Herriott cell - adapted from Ref. (94).

and

$$A^2 = \frac{4f}{4f-d}(x_0^2 + dx_0x'_0 + dfx_0'^2) \quad (\text{F.0.0.7})$$

$$B^2 = \frac{4f}{4f-d}(y_0^2 + dy_0y'_0 + dfy_0'^2) \quad (\text{F.0.0.8})$$

Here we can see, the beam pattern is an eclipse. If we impose the requirement that the spots are on a circle, which means:

$$\begin{aligned} A &= B \\ \alpha &= \beta \pm \frac{\pi}{2} \\ \tan \alpha \tan \beta &= -1 \end{aligned} \quad (\text{F.0.0.9})$$

this leads to

$$x_0^2 + dx_0x'_0 + dfx_0'^2 = y_0^2 + dy_0y'_0 + dfy_0'^2 \quad (\text{F.0.0.10})$$

$$1 + 2f\left(\frac{x'_0}{x_0} + \frac{y'_0}{y_0}\right) + 4f^2\frac{x'_0y'_0}{x_0y_0} = 1 - \frac{4f}{d} \quad (\text{F.0.0.11})$$

from these 2 equations, we can determine x'_0 y_0 from x_0 y'_0 [for simplicity set to 0] or vice versa.

$$x'_0 = -\frac{2x_0}{d} \quad (\text{F.0.0.12})$$

$$y_0^2 = x_0^2\left(\frac{4f}{d} - 1\right) \quad (\text{F.0.0.13})$$

with

$$A^2 = x_0^2 + y_0^2 = \frac{4f}{d}x_0^2 \quad (\text{F.0.0.14})$$

The slope x'_0 can also be expressed as

$$x'_0 = \frac{A}{\sqrt{fd}} \quad (\text{F.0.0.15})$$

if we set x'_0 to 0 and prescribe y_0

$$y'_0 = -\frac{2y_0}{d} \quad (\text{F.0.0.16})$$

$$x_0^2 = y_0^2\left(\frac{4f}{d} - 1\right) \quad (\text{F.0.0.17})$$

with

$$A^2 = x_0^2 + y_0^2 = \frac{4f}{d}y_0^2 \quad (\text{F.0.0.18})$$

the slope y'_0 can also be expressed as

$$y'_0 = \frac{A}{\sqrt{fd}} \quad (\text{F.0.0.19})$$

The relative angle between $x_0 y_0$ and $x_1 y_1$ is θ . the slope is determined by the maximum radius. So once A is determined, we can calculate the slope and then the offset, which combined with the radius tells the relative position of $x_0 y_0$ and $x_1 y_1$.

number of passes Reentrant condition of the Herriott cell is:

$$\theta \times 2N = 360 \times M \quad (\text{F.0.0.20})$$

with θ is the rotation angle of the spots on each reflection in degree:

$$\cos \theta = 1 - \frac{d}{2f} \quad (\text{F.0.0.21})$$

$2N$ is the number of passes, N is the number of spots per mirror; M is the number of circles these spots made.

In the ring-down cell arrangement, $\theta \sim 63$ degree [d=55 cm, f=50 cm], in this case the 'reasonable' reentrant condition we have is

$$63 \times 2 \times 20 = 360 \times 7 \quad (\text{F.0.0.22})$$

so this is $N = 20$, $M=7$.

McManus(170) suggested $N = 2M \pm 2$ for narrow fringe, under the $d \sim 2f$ condition. Numerical relation of N and M are classified into several families. For example $N = 20$, $M = 7$ is the $N = 2M \pm 6$ family.

Altmann(6) considered increasing mirror distance from f in the $f < d < 2f$ range, in which the only family appeared is the $N = 2M + 1$ family. In this family, the max number of passes/minimum free spectrum range is obtained when $d > 2f$; $\theta > 90$ degree.

Appendix G

Interference fringes

Interference fringes appear as light go through two parallel reflecting surface, or the so called Fabry-Pérot interferometer or etalon. The transmission spectrum shows repeated constructive peaks on certain wavelength due to resonance of certain wavelength between the two surfaces. The free spectral range, which is the spacing between two successive transmitted peaks is:

$$\Delta\lambda = \frac{\lambda_0^2}{2nl \cos \theta + \lambda_0} \approx \frac{\lambda_0^2}{2nl \cos \theta} \quad (\text{G.0.0.1})$$

with λ_0 is the central wavelength and n is the index of refraction of the cavity medium, θ is the incident angle, and l is the thickness of the cavity. Usually n is taken as 1 and θ taken as 0.

The thickness of the cavity can be estimated from the measured spectrum by

$$l \approx \frac{\lambda_0^2}{2n\Delta\lambda} \quad (\text{G.0.0.2})$$

$$l(\text{mm}) \approx \frac{\lambda_0^2(\mu\text{m})}{2000\Delta\lambda(\mu(m))} \quad (\text{G.0.0.3})$$

This is the cell calibration function is FTIR measurement. Another approximated form is

$$l(\text{mm}) \approx \frac{n\lambda_1\lambda_2(\mu\text{m})}{2000(\lambda_1 - \lambda_2)(\mu(m))} \quad (\text{G.0.0.4})$$

Appendix H

Nuclear Quadrupole Interaction

The interaction from the nuclear spin angular momentum with the spin angular momentum from the nuclei and electrons includes nuclear spin-spin and nuclear spin-orbit interactions. Also a nucleus with the nuclear spin quantum number I has multipole moments up to 2^{2I} -pole, with an integer I leads to electric and half integer I leads to magnetic. For example, an integer I has electric monopole (charge), quadrupole (2^2), hexadecapole (2^4), etc., while half integer I has magnetic dipole (2^1), octopole (2^3), etc. The magnetic spin-rotation coupling is due to the interaction of the nuclear magnetic dipole moment with the magnetic field produced by the rotating charge cloud of the molecule. A much larger interaction is for nucleus with an electric quadrupole moment (non-spherical charge distribution of the nucleus), its interaction with the non-spherical electric field distribution leads to the nuclear quadrupole coupling.

The quadrupole interaction energy of the nucleus with the non-spherical electric field is usually written as eQV_{ZZ} :

$$E = \frac{1}{2} \left(\sum_n q_n Z_n^2 \right) \left(\frac{\partial^2 V}{\partial Z^2} \right) \quad (\text{H.0.0.1})$$

$$= eQV_{ZZ} \quad (\text{H.0.0.2})$$

Q is usually given in units of mb (1b = 1barn = 10^{-28}m^2)

Coupled representation of angular momenta give rise to:

$$F = J + I, J + I - 1, \dots, |J - I| \quad (\text{H.0.0.3})$$

Quantum mechanical treatment leads to the effective Hamiltonian H_Q which

account for quadrupole coupling to first order:

$$\hat{H}_Q = eQq_J \frac{3(\vec{I} \cdot \vec{J})^2 + \frac{3}{2}(\vec{I} \cdot \vec{J}) - \vec{I}^2 \vec{J}^2}{2J(2J-1)I(2I-1)} \quad (\text{H.0.0.4})$$

$$q_J = \left\langle \frac{\partial^2 V}{\partial Z^2} \right\rangle_{J, M_J=J} \quad (\text{H.0.0.5})$$

The diagonal matrix elements is straightforward:

$$E_Q = eQq_J \frac{2J+3}{J} Y(J, I, F) \quad (\text{H.0.0.6})$$

$$Y(J, I, F) = \frac{\frac{3}{4}C(C+1) - I(I+1)J(J+1)}{2(2J+3)(2J-1)I(2I-1)} \quad (\text{H.0.0.7})$$

$$C = F(F+1) - J(J+1) - I(I+1) \quad (\text{H.0.0.8})$$

Where $Y(J, I, F)$ is the ‘‘Casimir function’’.

For symmetric top molecule or molecular complex, such as the HCCH-NH₃ and OCS-NH₃ complex studied in Chapter 6,

$$E_Q = eQq \left[\frac{3K^2}{J(J+1)} - 1 \right] Y(J, I, F) \quad (\text{H.0.0.9})$$

where $\chi = \chi_{aa} = -2\chi_{bb/cc}$

Appendix I

Supplementary Materials for Chapter 3

Figure S2. Side views of the optimized geometries of the six dimeric FE conformers at the MP2/6-311++G(d,p) level of theory.

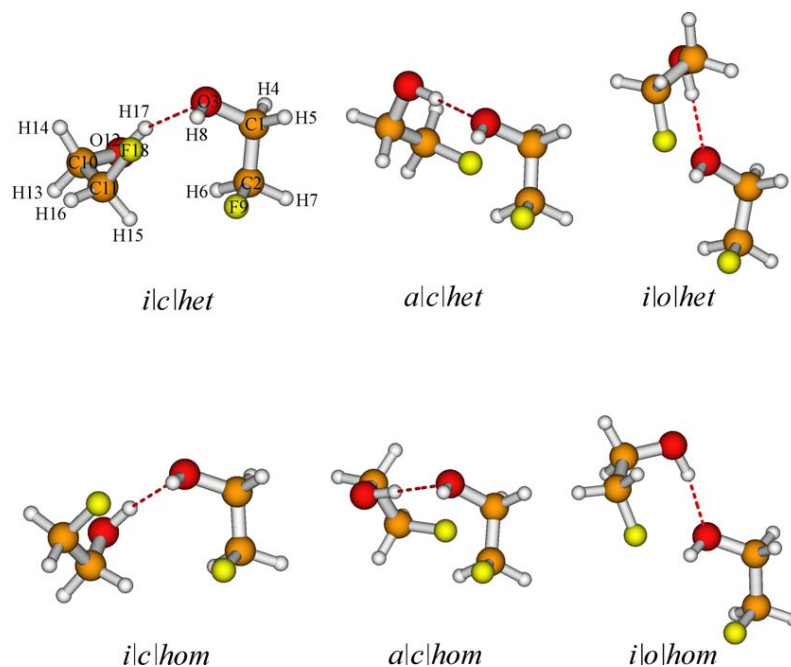


Table S1. Raw and ZPE-corrected relative dissociation energies of the nine conformations of the FE monomer. Also listed are values for the two important dihedral angles.

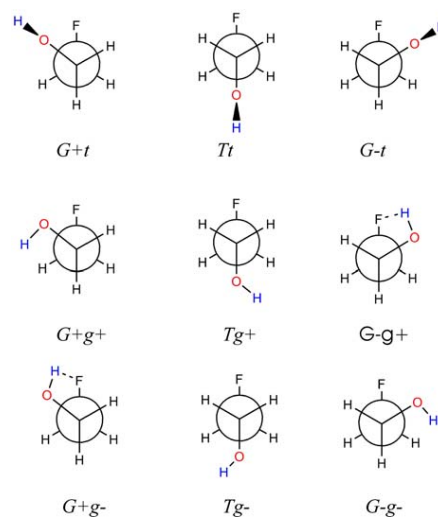
Conformer	$\Delta D_c^{[a]}$ /kJmol ⁻¹	$\Delta D_0^{[b]}$ /kJmol ⁻¹	$\tau(\text{FCOO})^\circ$	$\tau(\text{CCOH})^\circ$
<i>G+g-</i>	0.0	0.0	63.6	-57.1
<i>G-g+</i>	0.0	0.0	-63.6	57.1
<i>G+tt</i>	8.9	7.2	72.1	-157.9
<i>G-t</i>	8.9	7.2	-72.1	157.9
<i>Tt</i>	9.4	7.6	177.9	171.3
<i>Tg-</i>	10.5	9.9	-178.9	-68.4
<i>Tg+</i>	10.5	9.9	178.9	68.4
<i>G-g-</i>	11.0	10.1	-64.0	-57.5
<i>G+g+</i>	11.0	10.1	64.0	57.5

[a] Relative raw dissociation energy. [b] Relative ZPE corrected dissociation energy.

Table S2 Cartesian coordinates of the *G+g-* FE conformer

<i>G+g-</i>	x / Å	y / Å	z / Å
C1	0.677461	0.575838	0.287070
C2	-0.714168	0.558105	-0.284496
O3	1.456834	-0.508789	-0.189454
H4	0.622037	0.573314	1.379229
H5	1.182635	1.487598	-0.029914
H6	-0.690481	0.521816	-1.372393
H7	-1.295251	1.415008	0.055823
H8	0.991646	-1.318011	0.051341
F9	-1.360558	-0.601452	0.157345

Figure S1. Newman projections of the 9 FE monomer conformations. The capital letters are for $\tau(\text{FCOO})$ and the lower case for $\tau(\text{CCOH})$.



Atom numbering for Table S2.

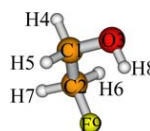


Table S3. Cartesian coordinates (in Å) of the six most stable dimeric FE conformers. The atom numbering is shown in Figure S2.

	<i>i/c/het</i>			<i>a/c/het</i>			<i>j/o/het</i>		
	<i>x</i> / Å	<i>y</i> / Å	<i>z</i> / Å	<i>x</i> / Å	<i>y</i> / Å	<i>z</i> / Å	<i>x</i> / Å	<i>y</i> / Å	<i>z</i> / Å
C1	-2.183156	-0.575471	0.497245	1.584670	.214976	-.942253	-0.969383	1.846014	0.330172
C2	-1.997513	0.067254	-0.858019	2.104944	-.775772	.068493	-0.193612	3.053019	-0.137641
O3	-0.944725	-0.768584	1.169145	.882027	1.280796	-.307051	-0.586538	0.677751	-0.380028
H4	-2.627414	-1.565579	0.364881	.870787	-.280678	-1.601393	-0.824591	1.714997	1.409702
H5	-2.861867	0.033906	1.105440	2.414850	.610682	-1.538878	-2.033338	2.001192	0.133894
H6	-1.293086	-0.499738	-1.469429	2.630426	-1.601001	-.418822	-0.524107	3.959003	0.377842
H7	-2.956335	0.179126	-1.372236	1.297732	-1.150879	.698189	-0.276002	3.174240	-1.219900
H8	-0.568598	0.102250	1.348126	1.480680	1.673039	.337417	0.359338	0.538830	-0.246111
F9	-1.455065	1.346144	-0.674701	3.019484	-.112641	.901239	1.157955	2.853961	0.161530
C10	2.253632	-0.615887	-0.406015	-2.357093	.335590	.708675	-0.460722	-2.594290	0.511369
C11	1.955565	0.843418	-0.147664	-2.368231	-.970616	-.051395	0.932347	-2.600168	-0.076277
O12	1.103370	-1.374741	-0.721290	-1.932440	1.422472	-.081903	-1.423354	-2.019951	-0.343933
H13	0.500558	-1.332652	0.037913	-3.383642	.545544	1.027960	-0.755773	-3.636155	0.674240
H14	2.918611	-0.675407	-1.273323	-1.739119	.219872	1.609895	-0.431609	-2.094513	1.489964
H15	2.786226	-1.028200	0.461630	-2.811202	-1.773694	.545108	1.617805	-3.187579	0.541063
H16	1.296634	1.255768	-0.914187	-2.896196	-.860096	-1.000977	0.918714	-2.973858	-1.102019
H17	2.878075	1.425588	-0.074536	-.970673	1.353952	-.182577	-1.239136	-1.068760	-0.386997
F18	1.286938	0.980040	1.084656	-1.050160	-1.352688	-.352951	1.443830	-1.289209	-0.122165
	<i>i/c/hom</i>			<i>a/c/hom</i>			<i>j/o/hom</i>		
	<i>x</i> / Å	<i>y</i> / Å	<i>z</i> / Å	<i>x</i> / Å	<i>y</i> / Å	<i>z</i> / Å	<i>x</i> / Å	<i>y</i> / Å	<i>z</i> / Å
C1	-2.173404	0.614194	0.549154	-1.575641	-0.036188	0.991883	-0.965103	-1.884380	-0.342840
C2	-2.165855	-0.733668	-0.133226	-2.004436	-0.778826	-0.248903	-0.185536	-3.049039	0.216931
O3	-0.857780	1.096065	0.787296	-0.962673	1.211202	0.666497	-0.616233	-0.668686	0.304297
H4	-2.653917	0.515559	1.526217	-0.826788	-0.623332	1.524213	-2.031532	-2.043744	-0.163967
H5	-2.746595	1.329397	-0.051814	-2.440268	0.126057	1.645701	-0.794760	-1.814951	-1.424109
H6	-1.563025	-1.451706	0.427989	-2.447285	-1.745996	0.002920	-0.489347	-3.988929	-0.252199
H7	-3.183209	-1.111941	-0.267997	-1.167603	-0.906245	-0.936728	-0.296514	-3.107598	1.301891
H8	-0.459431	1.332191	-0.059124	-1.615756	1.724048	0.177468	0.328623	-0.521428	0.169713
F9	-1.585198	-0.594131	-1.398861	-2.980518	-0.013624	-0.903410	1.170881	-2.847903	-0.056633
C10	1.669495	-1.018444	0.103253	2.507079	0.581003	0.046184	-0.440330	2.693256	0.413276
C11	2.430414	0.155133	-0.469179	2.386049	-0.900171	-0.228293	0.933584	2.580691	-0.207591
O12	1.184416	-0.782459	1.409303	1.547113	1.337679	-0.657067	-1.424990	1.970862	-0.293358
H13	2.359789	-1.865715	0.166922	3.496351	0.906009	-0.293737	-0.730011	3.749068	0.386496
H14	0.861858	-1.287614	-0.590792	2.446565	0.753597	1.129297	-0.384723	2.382806	1.465549
H15	3.169098	0.527579	0.243361	3.193434	-1.462419	0.249998	0.891327	2.776861	-1.280867
H16	2.904903	-0.109286	-1.418151	2.367260	-1.092435	-1.303280	1.644173	3.253251	0.280986
H17	0.506665	-0.091734	1.341065	0.702585	1.245704	-0.189183	-1.268989	1.030795	-0.112347
F18	1.543740	1.216480	-0.733415	1.173594	-1.376481	0.298151	1.429768	1.272713	-0.047513

Table S4. Observed rotational transition frequencies of *i/c/het* conformer.

# of line	J' Ka' Kc'	J Ka Kc	Freq. _{exp} /MHz	RSD ^{tbl} /MHz					
1	1 1 1	0 0 0	3509.0035	0.0004	25	2 1 1	1 0 1	5756.0182	-0.0006
2	5 2 4	5 1 4	3795.4418	0.0018	26	3 1 3	2 1 2	6253.1625	0.0004
3	4 2 3	4 1 3	3952.3259	-0.0001	27	3 0 3	2 0 2	6342.9820	0.0001
4	4 2 2	4 1 3	3985.3633	-0.0065	28	3 2 2	2 2 1	6351.8146	0.0068
5	3 2 2	3 1 2	4079.2014	0.0033	29	3 2 1	2 2 0	6360.6598	-0.0014
6	2 1 2	1 1 1	4169.7177	0.0008	30	3 1 2	2 1 1	6447.7139	-0.0004
7	2 2 1	2 1 1	4175.0955	0.0014	31	8 3 6	8 2 6	6806.5952	0.0019
8	2 2 0	2 1 1	4177.3028	0.0077	32	4 0 4	3 1 2	6818.6237	0.0018
9	2 0 2	1 0 1	4232.3699	0.0009	33	6 3 4	6 2 4	7009.5662	-0.0012
10	2 1 1	1 1 0	4299.4535	-0.0025	34	6 3 3	6 2 4	7013.5165	-0.0047
11	2 2 1	2 1 2	4369.7012	-0.0054	35	5 3 3	5 2 3	7063.4925	-0.0017
12	2 2 0	2 1 2	4371.9060	0.0033	36	5 3 2	5 2 3	7064.8055	0.0038
13	3 2 2	3 1 3	4468.3554	-0.0011	37	4 3 2	4 2 2	7094.9705	-0.0001
14	3 2 1	3 1 3	4479.4084	-0.0035	38	4 3 1	4 2 2	7095.3008	-0.0003
15	4 1 3	3 2 1	4503.8822	0.0163	39	3 3 1	3 2 1	7110.9403	0.0138
16	4 1 3	3 2 2	4514.9620	-0.0129	40	3 3 0	3 2 1	7111.0160	-0.0147
17	4 2 3	4 1 4	4600.6536	0.0010	41	3 3 1	3 2 2	7121.9815	0.0232
18	4 2 2	4 1 4	4633.6784	0.0072	42	3 3 0	3 2 2	7122.0453	0.0066
19	5 2 4	5 1 5	4767.1115	-0.0023	43	4 3 2	4 2 3	7128.0006	0.0008
20	3 0 3	2 1 1	4819.3352	0.0001	44	4 3 1	4 2 3	7128.3306	0.0009
21	5 2 3	5 1 5	4843.6447	-0.0020	45	5 3 3	5 2 4	7140.0368	-0.0125
22	3 0 3	2 1 2	5013.9306	0.0036	46	5 3 2	5 2 4	7141.3440	-0.0012
23	6 2 4	6 1 6	5119.4713	0.0013	47	6 3 4	6 2 5	7160.8400	-0.0003
24	2 1 2	1 0 1	5561.4196	-0.0009	48	6 3 3	6 2 5	7164.7879	-0.0014
					49	7 3 5	7 2 6	7193.5230	0.0022
					50	4 0 4	3 1 3	7207.7733	0.0017

51	3 1 3	2 0 2	7582.2103	0.0005	12	2 2 1	2 1 1	4457.2063	0.0050
52	3 1 2	2 0 2	7971.3607	-0.0004	13	2 2 0	2 1 2	4460.3162	0.0016
53	4 1 4	3 1 3	8334.9754	-0.0009	14	3 2 1	3 1 3	4461.8601	-0.0019
54	4 0 4	3 0 3	8447.0060	-0.0023	15	4 2 2	4 1 4	4463.9212	-0.0034
55	2 2 1	1 1 0	8474.5482	-0.0003	16	5 2 3	5 1 5	4466.5018	-0.0003
56	2 2 0	1 1 0	8476.7607	0.0008	17	6 2 4	6 1 6	4469.6125	0.0030
57	2 2 1	1 1 1	8539.4164	-0.0021	18	3 0 3	2 1 1	4548.4316	0.0000
58	2 2 0	1 1 1	8541.6278	0.0001	19	3 0 3	2 1 2	4551.5343	0.0022
59	4 1 3	3 1 2	8594.1541	-0.0003	20	2 1 2	1 0 1	5508.8974	-0.0012
60	4 1 4	3 0 3	9574.2040	-0.0008	21	2 1 1	1 0 1	5512.0012	-0.0002
61	4 1 3	3 0 3	10222.5325	-0.0004	22	5 1 4	4 2 2	5609.1229	0.0058
62	3 2 2	2 1 1	10526.9154	0.0029	23	3 1 3	2 1 2	6034.6807	0.0005
63	3 2 1	2 1 1	10537.9706	-0.0017	24	3 0 3	2 0 2	6036.2367	0.0011
					25	3 1 2	2 1 1	6037.7889	-0.0022
					26	4 0 4	3 1 2	6558.8595	0.0010
					27	4 0 4	3 1 3	6565.0731	-0.0023
					28	3 1 3	2 0 2	7519.3806	0.0020
					29	3 1 2	2 0 2	7525.5943	-0.0014
					30	4 1 4	3 1 3	8046.1409	0.0006
					31	4 0 4	3 0 3	8048.2179	-0.0023
					32	4 1 3	3 1 2	8050.2830	0.0001
					33	2 2 1	1 1 0	8482.4321	0.0058
					34	5 0 5	4 1 3	8568.6847	-0.0010
					35	5 0 5	4 1 4	8579.0394	-0.0038
					36	4 1 4	3 0 3	9529.2842	0.0021
					37	4 1 3	3 0 3	9539.6382	0.0000
					38	5 1 5	4 1 4	10057.5166	-0.0005

Table S5. Observed rotational transition frequencies of *i/c/hom* conformer.

# of line	J' Ka' Kc'	J Ka Kc	Freq. _{exp} /MHz	RSD ^{rel} /MHz
1	1 1 1	0 0 0	3497.8514	-0.0035
2	1 1 0	0 0 0	3498.8809	0.0019
3	2 1 2	1 1 1	4023.1586	-0.0020
4	2 0 2	1 0 1	4024.1954	-0.0006
5	2 1 1	1 1 0	4025.2338	-0.0073
6	8 2 7	8 1 7	4439.8249	-0.0001
7	7 2 6	7 1 6	4444.0594	0.0002
8	6 2 5	6 1 5	4447.7534	0.0013
9	5 2 4	5 1 4	4450.9134	0.0007
10	4 2 3	4 1 3	4453.5475	-0.0061
11	3 2 2	3 1 2	4455.6403	-0.0006

39	5 2 4	4 2 3	10060.0708	-0.0036	14	3 2 1	3 1 2	5900.0929	-0.0011
40	5 0 5	4 0 4	10060.1076	-0.0013	15	2 2 0	2 1 1	6049.2303	0.0064
41	5 1 4	4 1 3	10062.6944	0.0001	16	2 2 1	2 1 2	6386.3938	0.0004
42	3 2 2	2 1 2	10496.5248	0.0065	17	5 0 5	4 1 4	6449.9032	-0.0011
43	6 0 6	5 1 4	10577.8779	-0.0005	18	3 2 2	3 1 3	6560.2434	-0.0007
44	5 1 5	4 0 4	11538.5845	0.0023	19	3 1 3	2 0 2	6593.0114	-0.0016
45	5 1 4	4 0 4	11554.1187	-0.0015	20	7 1 6	6 2 5	6611.5930	0.0167
46	6 1 6	5 1 5	12068.7834	-0.0001	21	4 2 3	4 1 4	6793.5960	-0.0081
47	6 0 6	5 0 5	12071.8898	-0.0016	22	5 2 4	5 1 5	7087.4184	-0.0062
48	6 1 5	5 1 4	12075.0021	-0.0024	23	4 1 4	3 0 3	7995.1403	0.0006
49	7 0 7	6 1 5	12586.4161	0.0012	24	5 1 5	4 0 4	9357.7370	0.0006

Table S6. Observed rotational transition frequencies of *a/c/het* conformer.

# of line	J' Ka' Kc'	J Ka Kc	Freq. _{exp} /MHz	RSD ^[a] /MHz
1	6 1 5	6 0 6	3510.5666	0.0002
2	1 1 1	0 0 0	3635.2991	0.0000
3	7 1 6	7 0 7	4080.3147	-0.0292
4	6 1 5	5 2 4	4641.1437	0.0001
5	4 0 4	3 1 3	4684.3499	0.0012
6	8 1 7	8 0 8	4767.1070	0.8863
7	2 1 2	1 0 1	5141.7436	0.0000
8	8 2 6	8 1 7	5189.0037	-0.0004
9	9 2 7	9 1 8	5209.4625	0.0090
10	6 2 4	6 1 5	5377.4228	0.0023
11	5 2 3	5 1 4	5543.0817	0.0017
12	9 1 8	9 0 9	5571.5834	0.4502
13	4 2 2	4 1 3	5724.8641	-0.0011

Table S7. Observed rotational transition frequencies of *a/c/hom* conformer.

# of line	J' Ka' Kc'	J Ka Kc	Freq. _{exp} /MHz	RSD ^[a] /MHz
1	1 1 1	0 0 0	3.5962444	.0000055
2	4 0 4	3 1 2	4.3851722	.0000001
3	4 0 4	3 1 3	4.9558205	.0000025
4	3 0 3	2 0 2	5.0043808	-.0000033
5	5 2 4	5 1 4	5.2145132	-.0000023
6	5 2 3	5 1 4	5.3332927	-.0000022
7	4 4 1	5 3 2	5.4139526	-.0000036
8	4 4 1	5 3 3	5.4161260	-.0000066
9	4 2 3	4 1 3	5.4441077	-.0000016
10	2 1 1	1 0 1	5.4591927	-.0000036
11	4 2 2	4 1 3	5.4954131	-.0000023
12	3 2 2	3 1 2	5.6299354	-.0000082
13	2 2 1	2 1 1	5.7704489	.0000056
14	2 2 0	2 1 1	5.7738892	.0000016
15	2 2 0	2 1 2	6.0592514	.0000004

S7

16	3 2 2	3 1 3	6.2005836	.0000010
17	3 2 1	3 1 3	6.2177553	-.0000037
18	5 2 4	5 1 5	6.6391671	-.0000091
19	4 0 4	3 0 3	6.6565785	-.0000003
20	4 2 3	3 2 2	6.6880076	.0000002
21	4 3 2	3 3 1	6.6972802	.0000127
22	4 3 1	3 3 0	6.6977465	-.0000249
23	3 1 3	2 0 2	6.7051388	-.0000011
24	4 2 2	3 2 1	6.7221413	-.0000001
25	5 0 5	4 1 4	6.7577483	.0000025
26	5 2 3	5 1 5	6.7579466	.0000118
27	7 1 6	6 2 4	6.8128428	-.0000001
28	4 1 3	3 1 2	6.8738352	-.0000008
29	6 2 5	6 1 6	6.9344591	.0000006
30	6 0 6	5 1 4	7.1418207	-.0000084
31	3 1 2	2 0 2	7.2757871	.0000034
32	5 1 5	4 1 4	8.1111665	-.0000007
33	4 1 4	3 0 3	8.1945719	-.0000035
34	5 0 5	4 0 4	8.2957417	-.0000011
35	2 2 1	1 1 1	9.3061305	.0000099
36	2 2 0	1 1 1	9.3095708	.0000030
37	5 1 5	4 0 4	9.6491600	-.0000026
38	6 3 4	6 2 4	9.6826545	-.0000001
39	6 3 3	6 2 4	9.6891587	.0000031
40	6 1 6	5 1 5	9.7248544	-.0000009
41	5 3 3	5 2 3	9.7661521	.0000026
42	5 3 2	5 2 3	9.7683255	.0000026
43	4 3 2	4 2 2	9.8150258	-.0000007
44	4 3 1	4 2 2	9.8155699	.0000002
45	3 3 1	3 2 2	9.8570585	.0000013
46	3 3 0	3 2 2	9.8571363	-.0000308
47	4 3 2	4 2 3	9.8663312	.0000020
48	4 3 1	4 2 3	9.8668753	.0000028
49	5 3 3	5 2 4	9.8849316	.0000033
50	5 3 2	5 2 4	9.8871050	.0000008
51	6 3 4	6 2 5	9.9171201	-.0000017
52	6 0 6	5 0 5	9.9198929	-.0000010
53	6 3 3	6 2 5	9.9236243	-.0000041
54	7 3 5	7 2 6	9.9676124	.0000183
55	7 3 4	7 2 6	9.9838091	.0000007

56	6 2 5	5 2 4	10.0201464	.0000006
57	8 3 6	8 2 7	10.0413882	.0000008
58	6 3 4	5 3 3	10.0523349	-.0000004
59	6 2 4	5 2 3	10.1358325	.0000016

[a] Root-mean square deviation of the fit.

References

- [1] <http://www.gaussian.com/g.whitepap/vib.htm>. 13
- [2] <http://www.gaussian.com/g.whitepap/thermo.htm>. 13
- [3] Z. Kisiel, PROSPE-Programs for Rotational Spectroscopy, available at <http://info.ifpan.edu.pl/Bkisiel/prospe.htm>. 54, 153, 228
- [4] M.S. ALBERT AND D. BALAMORE. *Nuclear Instruments and Methods in Physics Research Section A: Accelerators, Spectrometers, Detectors and Associated Equipment*, **402**:441–453, January 1998. 135
- [5] SIEGHARD ALBERT, KAREN KEPPLER ALBERT, HANS HOLLENSTEIN, CARINE MANCA TANNER, AND MARTIN QUACK. John Wiley & Sons, Ltd, 2011. 24, 28
- [6] J. ALTMANN, R. BAUMGART, AND C. WEITKAMP. *Appl. Opt.*, **20**(6):995–999, 1981. 95, 268
- [7] G. AMAT, H.H. NIELSEN, AND G. TARRAGO. Dekker, 1971. 11, 19, 20, 36
- [8] U. ANDRESEN, H. DREIZLER, J.U. GRABOW, AND W. STAHL. *Review of scientific instruments*, **61**(12):3694–3699, 1990. 58
- [9] VINCENZO AQUILANTI, ELENA CORNICCHI, MARC MOIX TEIXIDOR, NADJA SAENDIG, FERNANDO PIRANI, AND DAVID CAPPELLETTI. *Angewandte Chemie International Edition*, **44**(16):2356–2360, 2005. 135, 172
- [10] E. ARUNAN, G. R. DESIRAJU, R. A. KLEIN, J. SADLEJ, S. SCHEINER, I. ALKORTA, D. C. CLARY, R. H. CRABTREE, J. J. DANNENBERG, P. HOBZA, H. G. KJAERGAARD, A. C. LEGON, B. MENNUCCI, AND D. J. NESBITT. *Pure. Appl. Chem.* (submitted). 194
- [11] E. ARUNAN, SAGARIKA DEV, AND PANKAJ K. MANDAL. *Applied Spectroscopy Reviews*, **39**(2):131–181, 2004. 1
- [12] JOHN B. ASBURY, TOBIAS STEINEL, C. STROMBERG, K. J. GAFFNEY, I. R. PILETIC, ALEXI GOUN, AND M. D. FAYER. *Phys. Rev. Lett.*, **91**(23):237402, December 2003. 194
- [13] JAMES D. AYERS, RANDY L. APODACA, WILLIAM R. SIMPSON, AND DOUGLAS S. BAER. *Appl. Opt.*, **44**(33):7239–7242, 2005. 94
- [14] Z BACIC AND J C LIGHT. *Annual Review of Physical Chemistry*, **40**(1):469–498, 1989. 40, 138
- [15] K.L. BAK, J. GAUSS, T. HELGAKER, P. JØRGENSEN, AND J. OLSEN. *Chemical Physics Letters*, **319**(5):563–568, 2000. 71
- [16] Y. A. BAKHIRKIN, A. A. KOSTEREV, R. F. CURL, F. K. TITTEL, D. A. YAREKHA, L. HVOZDARA, M. GIOVANNINI, AND J. FAIST. *Applied Physics B: Lasers and Optics*, **82**(1):149–154, 2006. 78, 101, 126
- [17] YURY A. BAKHIRKIN, ANATOLIY A. KOSTEREV, CHAD ROLLER, ROBERT F. CURL, AND FRANK K. TITTEL. *Appl. Opt.*, **43**(11):2257–2266, 2004. 78, 93, 101, 123
- [18] I. BAKO, T. RADNAI, AND M.C.B. FUNEL. *The Journal of chemical physics*, **121**:12472, 2004. 57
- [19] TJ BALLE AND WH FLYGARE. *Review of Scientific Instruments*, **52**(1):33–45, 1981. 58
- [20] MOTOHIRO BANNO, KAORU OHTA, SAYURI YAMAGUCHI, SATORU HIRAI, AND KEISUKE TOMINAGA. *Acc. Chem. Res.*, **42**(9):1259–1269, 2009. 194
- [21] A. J. BARNES. *J. Mol. Struct.*, **704**(1-3):3–9, October 2004. 194
- [22] ZLATKO BAČIĆ AND ROGER E. MILLER. *J. Phys. Chem.*, **100**(31):12945–12959, January 1996. 194
- [23] MATTIAS BECK, DANIEL HOFSTETTER, THIERRY AELLEN, JEROME FAIST, URSULA OESTERLE, MARC ILEGEMS, EMILIO GINI, AND HANS MELCHIOR. *Science*, **295**(5553):301–305, 2002. 77
- [24] ZUZANA BENKOVA AND ANDRZEJ J. SADLEJ. *Molecular Physics*, **102**(7):687–699, 2004. 218
- [25] A. BERKESSEL, J.A. ADRIO, D. HÜTTENHAIN, AND J.M. NEUDÖRFL. *Journal of the American Chemical Society*, **128**(26):8421–8426, 2006. 57
- [26] R. P. A. BETTENS, R. M. SPYCHER, AND A. BAUDER. *Mol. Phys.*, **86**(3):487, 1995. 35, 216

REFERENCES

- [27] JS BINKLEY AND JA POPLÉ. *International Journal of Quantum Chemistry*, **9**(2):229–236, 1975. 59, 68
- [28] P. BIRZA, T. MOTYLEWSKI, D. KHOROSHEV, A. CHIROKOLAVA, H. LINNARTZ, AND J. P. MAIER. *Chemical Physics*, **283**(1-2):119–124, October 2002. 88
- [29] P. A. BLOCK, MARK D. MARSHALL, L. G. PEDERSEN, AND R. E. MILLER. *J. Chem. Phys.*, **96**(10):7321, 1992. 215
- [30] A. A. BOCHKAREV, P. A. RAPAPORT, AND N. I. TIMOSHENKO. *Journal of Applied Mechanics and Technical Physics*, **14**(1):24–27, January 1973. 260
- [31] K.A. BOLIN, M. PITKEATHLY, A. MIRANKER, L.J. SMITH, AND C.M. DOBSON. *Journal of molecular biology*, **261**(3):443–453, 1996. 57
- [32] N. BORHO AND Y. XU. *Angewandte Chemie International Edition*, **46**(13):2276–2279, 2007. 3, 58, 71
- [33] N. BORHO AND Y. XU. *Phys. Chem. Chem. Phys.*, **9**(32):4514–4520, 2007. 66
- [34] N. BORHO AND Y. XU. *Journal of the American Chemical Society*, **130**(18):5916–5921, 2008. 3, 58, 71, 72
- [35] NICOLE BORHO AND MARTIN A. SUHM. *Physical Chemistry Chemical Physics*, **4**(12):2721–2732, 2002. 128
- [36] NICOLE BORHO AND YUNJIE XU. *Physical Chemistry Chemical Physics*, **9**(32):4514, 2007. 3
- [37] NICOLE BORHO AND YUNJIE XU. *Physical Chemistry Chemical Physics*, **9**(11):1324–1328, 2007. 128
- [38] S. F. BOYS AND F. BERNARDI. *Mol. Phys.*, **19**(4):553, 1970. 197
- [39] SF BOYS AND F. BERNARDI. *Molecular Physics*, **19**(4):553–566, 1970. 59
- [40] MATTHEW D. BROOKES, CHANGHONG XIA, JIAN TANG, JAMES A. ANSTEY, BRYAN G. FULSOM, KE-XIAN AU YONG, JENNA M. KING, AND A. R. W. MCKELLAR. *Spectrochimica Acta Part A: Molecular and Biomolecular Spectroscopy*, **60**(14):3235–3242, 2004. 75, 98
- [41] C.L. BRUMMEL, S.W. MORK, AND L.A. PHILIPS. Technical report, DTIC Document, 1991. 61
- [42] M. BUCK. *Quarterly reviews of biophysics*, **31**(03):297–355, 1998. 57
- [43] K.S. BUCKTON AND R.G. AZRAK. *The Journal of Chemical Physics*, **52**:5652, 1970. 59, 61
- [44] M. BULSKI, P. E. S. WORMER, AND A. VAN DER AVOIRD. *The Journal of Chemical Physics*, **94**(12):8096, 1991. 136, 138
- [45] P.R. BUNKER AND P. JENSEN. 11, 26, 38, 45
- [46] P.R. BUNKER AND P. JENSEN. Series in Chemical Physics. Taylor & Francis, 2004. 11
- [47] S. CALIFANO. Wiley, 1976. 11
- [48] FEDERICO CAPASSO. *Optical Engineering*, **49**(11):111102–111102–9, November 2010. 76
- [49] G. CHALASIŃSKI, M. M. SZCZEŚNIAK, AND S. SCHEINER. *The Journal of Chemical Physics*, **94**(4):2807, 1991. 136, 138
- [50] DAVID CHANDLER. *Nature*, **437**(7059):640–647, September 2005. 134
- [51] A. S. C. CHEUNG, TONGMEI MA, AND HONGBING CHEN. *Chemical Physics Letters*, **353**(3-4):275–280, 2002. 123
- [52] KT CHUNG AND P.M. PARKER. *The Journal of Chemical Physics*, **43**:3865, 1965. 36
- [53] R. C. COHEN, KERRY L. BUSAROW, K. B. LAUGHLIN, GEOFFREY A. BLAKE, M. HAVENITH, Y. T. LEE, AND R. J. SAYKALLY. *The Journal of Chemical Physics*, **89**(8):4494–4504, October 1988. 135, 142, 153
- [54] R. C. COHEN, KERRY L. BUSAROW, Y. T. LEE, AND R. J. SAYKALLY. *The Journal of Chemical Physics*, **92**(1):169–177, 1990. 42, 135, 140, 142, 153
- [55] R. C. COHEN AND R. J. SAYKALLY. *The Journal of Physical Chemistry*, **94**(20):7991–8000, October 1990. 135
- [56] R. C. COHEN AND R. J. SAYKALLY. *The Journal of Chemical Physics*, **95**(11):7891–7906, December 1991. 43, 135, 136, 139, 141, 142, 145, 150, 153
- [57] R. C. COHEN AND R. J. SAYKALLY. *The Journal of Physical Chemistry*, **96**(3):1024–1040, February 1992. 88, 181
- [58] R. C. COHEN AND R. J. SAYKALLY. *The Journal of Chemical Physics*, **98**(8):6007–6030, April 1993. 135

REFERENCES

- [59] DAVID E. COOPER AND T. F. GALLAGHER. *Appl. Opt.*, **24**(9):1327–1334, 1985. 101
- [60] C. COTTAZ, I. KLEINER, G. TARRAGO, L.R. BROWN, J.S. MARGOLIS, R.L. POYNTER, H.M. PICKETT, T. FOUCHET, P. DROSSART, AND E. LELLOUCH. *J. Mol. Spec.*, **203**(2):285–309, October 2000. 198, 201
- [61] J.D. CRUZAN, M.R. VIANT, M.G. BROWN, D.D. LUCAS, K. LIU, AND R.J. SAYKALLY. *Chemical physics letters*, **292**(4):667–676, 1998. 48
- [62] B.T. DARLING AND D.M. DENNISON. *Physical Review*, **57**(2):128, 1940. 15
- [63] SCOTT DAVIS, MICHAEL FRNK, DAIRENE UY, AND DAVID J. NESBITT. *Chemical Physics Letters*, **344**(1-2):23–30, 2001. 102
- [64] A. DEPIANTE, E. J. CAMPBELL, AND S. J. BUELOW. *Review of Scientific Instruments*, **60**(5):858–862, 1989. 75, 98, 101
- [65] T.H. DUNNING JR. *The Journal of Chemical Physics*, **90**:1007, 1989. 59, 68
- [66] GEOFFREY DUXBURY, NIGEL LANGFORD, MICHAEL T. MCCULLOCH, AND STEPHEN WRIGHT. *Chemical Society Reviews*, **34**(11):921–934, 2005. 113
- [67] A. EARNSHAW AND NORMAN GREENWOOD. Butterworth-Heinemann, 2 edition, December 1997. 135
- [68] C. EMMELUTH, V. DYCZMONS, T. KINZEL, P. BOTSCHWINA, M.A. SUHM, AND M. YÁÑEZ. *Phys. Chem. Chem. Phys.*, **7**(5):991–997, 2005. 57, 66
- [69] GREGORY S. ENGEL, WALTER S. DRISDELL, FRANK N. KEUTSCH, ELISABETH J. MOYER, AND JAMES G. ANDERSON. *Appl. Opt.*, **45**(36):9221–9229, 2006. 123
- [70] M.B. ENGHOFF, P. VON HESSBERG, C.J. NIELSEN, AND M.S. JOHNSON. *The Journal of Physical Chemistry A*, **107**(39):7667–7670, 2003. 57
- [71] JEROME FAIST, FEDERICO CAPASSO, DEBORAH L. SIVCO, CARLO SIRTORI, ALBERT L. HUTCHINSON, AND ALFRED Y. CHO. *Science*, **264**(5158):553–556, 1994. 76
- [72] L.B. FAVERO, B.M. GIULIANO, S. MELANDRI, A. MARIS, AND W. CAMINATI. *Chemistry-A European Journal*, **13**(20):5833–5837, 2007. 59, 71
- [73] W.H. FLYGARE. Prentice-Hall, 1978. 9
- [74] SETH M. FOREMAN, ADELA MARIAN, JUN YE, EVGENY A. PETRUKHIN, MIKHAIL A. GUBIN, OLIVER D. MÜCKE, FRANCO N. C. WONG, ERICH P. IPPEN, AND FRANZ X. KÄRTNER. *Opt. Lett.*, **30**(5):570–572, Mar 2005. 234
- [75] G. T. FRASER, K. R. LEOPOLD, AND W. KLEMPERER. *J. Chem. Phys.*, **80**(4):1423, 1984. 193, 195, 202, 213
- [76] G. T. FRASER, K. R. LEOPOLD, D. D. NELSON, A. TUNG, AND W. KLEMPERER. *J. Chem. Phys.*, **80**(7):3073, 1984. 214
- [77] G. T. FRASER, F. J. LOVAS, R. D. SUENRAM, AND K. MATSUMURA. *Journal of Molecular Spectroscopy*, **144**(1):97–112, November 1990. 135, 142, 153
- [78] G. T. FRASER, D. D. NELSON, A. CHARO, AND W. KLEMPERER. *J. Chem. Phys.*, **82**(6):2535, 1985. 181, 195
- [79] G. T. FRASER, A. S. PINE, AND W. A. KREINER. *The Journal of Chemical Physics*, **94**(11):7061, 1991. 181
- [80] A. FRIED, B. HENRY, B. WERT, S. SEWELL, AND J.R. DRUMMOND. *Applied Physics B: Lasers and Optics*, **67**(3):317–330, 1998. 95
- [81] M. J. FRISCH, G. W. TRUCKS, H. B. SCHLEGEL, G. E. SCUSERIA, M. A. ROBB, J. R. CHEESEMAN, J. A. MONTGOMERY, JR., T. VREVEN, K. N. KUDIN, J. C. BURANT, J. M. MILLAM, S. S. IYENGAR, J. TOMASI, V. BARONE, B. MENNUCCI, M. COSSI, G. SCALMANI, N. REGA, G. A. PETERSSON, H. NAKATSUJI, M. HADA, M. EHARA, K. TOYOTA, R. FUKUDA, J. HASEGAWA, M. ISHIDA, T. NAKAJIMA, Y. HONDA, O. KITAO, H. NAKAI, M. KLENE, X. LI, J. E. KNOX, H. P. HRATCHIAN, J. B. CROSS, V. BAKKEN, C. ADAMO, J. JARAMILLO, R. GOMPERTS, R. E. STRATMANN, O. YAZYEV, A. J. AUSTIN, R. CAMMI, C. POMELLI, J. W. OCHTERSKI, P. Y. AYALA, K. MOROKUMA, G. A. VOTH, P. SALVADOR, J. J. DANNENBERG, V. G. ZAKRZEWSKI, S. DAPPRICH, A. D. DANIELS, M. C. STRAIN, O. FARKAS, D. K. MALICK, A. D. RABUCK, K. RAGHAVACHARI, J. B. FORESMAN, J. V. ORTIZ, Q. CUI, A. G. BABOUL, S. CLIFFORD, J. CIOSLOWSKI, B. B. STEFANOV, G. LIU, A. LIASHENKO, P. PISKORZ, I. KOMAROMI, R. L. MARTIN, D. J. FOX, T. KEITH, M. A. AL-LAHAM, C. Y. PENG, A. NANAYAKKARA, M. CHALLACOMBE, P. M. W. GILL, B. JOHNSON, W. CHEN, M. W. WONG, C. GONZALEZ, AND J. A. POPL. Gaussian, Inc., Wallingford, CT, 2004. 59, 71, 196

REFERENCES

- [82] W. GANS AND JAN C. A. BOEYENS. Springer, 1998. 194
- [83] SHEKHAR GARDE, GERHARD HUMMER, AND MICHAEL E. PAULAITIS. *Faraday Discussions*, **103**:125, 1996. 134
- [84] K. GAST, A. SIEMER, D. ZIRWER, AND G. DAMASCHUN. *European Biophysics Journal*, **30**(4):273–283, 2001. 57
- [85] MANFRED GEHRTZ, GARY C. BJORKLUND, AND EDWARD A. WHITTAKER. *J. Opt. Soc. Am. B*, **2**(9):1510–1526, 1985. 101
- [86] T. C. GERMANN AND H. S. GUTOWSKY. *The Journal of Chemical Physics*, **98**(7):5235, 1993. 135, 142, 153
- [87] WALTER GORDY AND ROBERT LEE COOK. John Wiley & Sons Inc, 2nd edition, October 1970. 31, 32
- [88] DZ-HUNG GWO, M. HAVENITH, K.L. BUSAROW, R.C. COHEN, C.A. SCHMUTTENMAER, AND R.J. SAYKALLY. *Molecular Physics*, **71**:453–460, October 1990. 181
- [89] GREGORY E. HALL AND SIMON W. NORTH. *Annual Review of Physical Chemistry*, **51**(1):243–274, 2000. 101
- [90] H. HAMANO. *The Journal of Chemical Physics*, **34**(5):1678, 1961. 218
- [91] MICHAEL HARTMANN AND LEO RADOM. *J. Phys. Chem. A*, **104**(5):968–973, February 2000. 197, 199, 205
- [92] M. HAVENITH, G. HILPERT, M. PETRI, AND W. URBAN. *Molecular Physics: An International Journal at the Interface Between Chemistry and Physics*, **81**(4):1003, 1994. 102
- [93] J.P.I. HEARN, R.V. COBLEY, AND B.J. HOWARD. *The Journal of chemical physics*, **123**:134324, 2005. 58, 72
- [94] D. HERRIOTT, H. KOGELNIK, AND R. KOMPFFNER. *Appl. Opt.*, **3**(4):523–526, 1964. 93, 95, 265, 266
- [95] DONALD R. HERRIOTT AND HARRY J. SCHULTE. *Appl. Opt.*, **4**(8):883–889, 1965. 95
- [96] G. HERZBERG. *Reviews of Modern Physics*, **14**(2-3):219, April 1942. 39
- [97] G. HERZBERG. *Molecular Spectra and Molecular Structure: Infrared and Raman Spectra of Polyatomic Molecules*. R.E. Krieger Pub. Co., 1991. 9
- [98] G. HERZBERG AND K.P. HUBER. *Molecular Spectra and Molecular Structure*. Van Nostrand Reinhold, 1950. 9
- [99] G. HERZBERG AND K.P. HUBER. Number v. 4 in *Molecular Spectra and Molecular Structure*. Van Nostrand, 1979. 9
- [100] G. HILPERT, G. T. FRASER, AND A. S. PINE. *J. Chem. Phys.*, **105**(15):6183, 1996. 193, 195, 199, 215, 218
- [101] M. HIPPLER, S. HESSE, AND M.A. SUHM. *Phys. Chem. Chem. Phys.*, **12**(41):13555–13565, 2010. 218
- [102] PAVEL HOBZA AND ZDENEK HAVLAS. *Chem. Rev.*, **100**(11):4253–4264, November 2000. 195
- [103] PAVEL HOBZA, VLADIMÍR SPIRKO, ZDENEK HAVLAS, KONSTANTIN BUCHHOLD, BERND REIMANN, HANS-DIETER BARTH, AND BERNHARD BRUTSCHY. *Chem. Phys. Lett.*, **299**(2):180–186, January 1999. 194
- [104] MATTHEW P. HODGES, RICHARD J. WHEATLEY, AND ALLAN H. HARVEY. *The Journal of Chemical Physics*, **117**(15):7169, 2002. 136, 138
- [105] D. HOFSTETTER, J. FAIST, IRINA T. SOROKINA, AND KONSTANTIN L. VODOPYANOV. pages 61–98. Springer-Verlag, Berlin & Heidelberg, 2003. 76
- [106] D.P. HONG, M. HOSHINO, R. KUBOI, AND Y. GOTO. *Journal of the American Chemical Society*, **121**(37):8427–8433, 1999. 57
- [107] J.T. HOUGEN. NBS monograph. U.S. Government Printing Office, 1970. 18
- [108] T. A. HU, E. L. CHAPPELL, AND S. W. SHARPE. *The Journal of Chemical Physics*, **98**(8):6162–6169, 1993. 98, 101
- [109] T. R. HUET, M. HERMAN, AND J. W. C. JOHNS. *J. Chem. Phys.*, **94**(5):3407, 1991. 215
- [110] J M HUTSON. *Annual Review of Physical Chemistry*, **41**(1):123–154, 1990. 40, 139
- [111] JEREMY M. HUTSON. *The Journal of Chemical Physics*, **92**(1):157–168, 1990. 41, 135, 140
- [112] SHEEBA JEM IRUDAYAM AND RICHARD H HENCHMAN. *Journal of physics. Condensed matter: an Institute of Physics journal*, **22**(28):284108, July 2010. PMID: 21399280. 135
- [113] A. JASANOFF AND A.R. FERSHT. *Biochemistry*, **33**(8):2129–2135, 1994. 57

REFERENCES

- [114] SR JEFFERTS, TP HEAVNER, TE PARKER, AND JH SHIRLEY. **6673**:667309-1, 2007. 233
- [115] P. JENSEN AND P.R. BUNKER. Wiley, 2000. 11
- [116] BOGUMIL JEZIORSKI, ROBERT MOSZYNSKI, AND KRZYSZTOF SZALEWICZ. *Chem. Rev.*, **94**(7):1887-1930, November 1994. 194
- [117] WOLFGANG JGER AND YUNJIE XU. John Wiley & Sons, Ltd, 2011. 1, 2
- [118] Y. KABBADJ, M. HERMAN, G. DI LONARDO, L. FUSINA, AND J. W. C. JOHNS. *J. Mol. Spec.*, **150**(2):535-565, December 1991. 214
- [119] MASATOSHI KAJITA. *Phys. Rev. A*, **74**:035403, Sep 2006. 234
- [120] V. L. KASYUTICH, C. E. CANOSA-MAS, C. PFRANG, S. VAUGHAN, AND R. P. WAYNE. *Applied Physics B: Lasers and Optics*, **75**(6):755-761, 2002. 94
- [121] V. L. KASYUTICH, P. A. MARTIN, AND R. J. HOLDSWORTH. *Applied Physics B: Lasers and Optics*, **85**(2):413-420, 2006. 94
- [122] DEVINDER KAUR, A. M. DE SOUZA, J. WANNA, SAMEER A. HAMMAD, LOUIS MERCORELLI, AND DAVID S. PERRY. *Appl. Opt.*, **29**(1):119-124, 1990. 95
- [123] S. KIELICH. **1**, pages 192-387. Royal Society of Chemistry, Cambridge, 1972. 217
- [124] ZBIGNIEW KISIEL, LECH PSZCZOLKOWSKI, IVAN R. MEDVEDEV, MANFRED WINNEWISSER, FRANK C. DE LUCIA, AND ERIC HERBST. *Journal of Molecular Spectroscopy*, **233**(2):231-243, October 2005. 54, 153, 228
- [125] DANIEL KIVELSON AND E. BRIGHT WILSON. *The Journal of Chemical Physics*, **20**(10):1575-1579, October 1952. 36
- [126] A. KOSTEREV, G. WYSOCKI, Y. BAKHIRKIN, S. SO, R. LEWICKI, M. FRASER, F. TITTEL, AND R.F. CURL. *Applied Physics B: Lasers and Optics*, **90**(2):165-176, February 2008. 78
- [127] ANATOLIY A. KOSTEREV, ALEXANDER L. MALINOVSKY, FRANK K. TITTEL, CLAIRE GMACHL, FEDERICO CAPASSO, DEBORAH L. SIVCO, JAMES N. BAILLARGEON, ALBERT L. HUTCHINSON, AND ALFRED Y. CHO. *Appl. Opt.*, **40**(30):5522-5529, 2001. 78
- [128] R. KRISHNAN, JS BINKLEY, R. SEEGER, AND J.A. POPLER. *The Journal of Chemical Physics*, **72**:650, 1980. 59
- [129] S. G. KUKOLICH. *Chemical Physics Letters*, **5**(7):401-404, May 1970. 218
- [130] SUSUMU KUMA, MIKHAIL N. SLIPCHENKO, TAKAMASA MOMOSE, AND ANDREY F. VILESOV. *The Journal of Physical Chemistry A*, **114**(34):9022-9027, 2010. 135, 142
- [131] N. KURZ, M. R. DIETRICH, GANG SHU, T. NOEL, AND B. B. BLINOV. *Physical Review A*, **82**(3):030501, 2010. 260
- [132] L.D. LANDAU AND E.M. LIFSHITZ. Course of theoretical physics. Butterworth-Heinemann, 1976. 26, 241
- [133] ROBERT LASCOLA AND DAVID J. NESBITT. *The Journal of Chemical Physics*, **95**(11):7917-7932, December 1991. 38, 43, 135, 140, 142, 153
- [134] SANG KUK LEE. *Chemical Physics Letters*, **358**(1-2):110-114, May 2002. 260
- [135] A C LEGON. *Annual Review of Physical Chemistry*, **34**(1):275-300, October 1983. 260
- [136] D H LEVY. *Annual Review of Physical Chemistry*, **31**(1):197-225, October 1980. 260
- [137] DONALD H. LEVY. *Science*, **214**(4518):263 - 269, October 1981. 260
- [138] SONG LI, RUI ZHENG, YU ZHU, AND CHUANXI DUAN. *The Journal of Chemical Physics*, **135**(13):134304-134304-7, October 2011. 171
- [139] SONG LI, RUI ZHENG, YU ZHU, AND CHUANXI DUAN. *Journal of Molecular Spectroscopy*, **272**(1):27-31, February 2012. 143, 166
- [140] X. LIU, Y. XU, Z. SU, W. S. TAM, AND I. LEONOV. *Applied Physics B*, **102**(3):629-639, July 2010. 132, 215
- [141] XUNCHEN LIU, NICOLE BORHO, AND YUNJIE XU. *Chemistry - A European Journal*, **15**(1):270-277, 2009. 3
- [142] YAQIAN LIU, MARTIN A. SUHM, AND PETER BOTSCHWINA. *Phys. Chem. Chem. Phys.*, **6**(19):4642, 2004. 195
- [143] F. LONDON. *Z. Physik.*, **63**:245, 1930. 220
- [144] MARTIN LOSADA, PHUONG NGUYEN, AND YUNJIE XU. *The Journal of Physical Chemistry A*, **112**(25):5621-5627, June 2008. 220
- [145] MARTIN LOSADA, HA TRAN, AND YUNJIE XU. *The Journal of Chemical Physics*, **128**(1):014508-014508-11, January 2008. 3

REFERENCES

- [146] MARTIN LOSADA AND YUNJIE XU. *Physical Chemistry Chemical Physics*, **9**(24):3127, 2007. 3
- [147] J.D. LOUCK. *Journal of Molecular Spectroscopy*, **61**(1):107–137, 1976. 15
- [148] J.D. LOUCK AND H.W. GALBRAITH. *Reviews of Modern Physics*, **48**(1):69, 1976. 15
- [149] CHRISTOPHER M. LOVEJOY AND DAVID J. NESBITT. *Review of Scientific Instruments*, **58**(5):807–811, May 1987. 98, 101, 260
- [150] CHRISTOPHER M. LOVEJOY, MICHAEL D. SCHUDER, AND DAVID J. NESBITT. *The Journal of Chemical Physics*, **86**(10):5337, 1987. 260
- [151] MICHAEL M. T. LOY. *Physical Review Letters*, **32**(15):814, April 1974. Copyright (C) 2009 The American Physical Society; Please report any problems to prola@aps.org. 113
- [152] Q. Y. LU, Y. BAI, N. BANDYOPADHYAY, S. SLIVKEN, AND M. RAZEGHI. *Applied Physics Letters*, **97**(23):231119–231119–3, December 2010. 77
- [153] KA LUM, DAVID CHANDLER, AND JOHN D. WEEKS. *J. Phys. Chem. B*, **103**(22):4570–4577, 1999. 134
- [154] ARKADIY LYAKH, RICHARD MAULINI, ALEXEI G. TSEKOUN, ROWEL GO, AND C. KUMAR N. PATEL. *Proceedings of SPIE*, **7953**(1):79531L–79531L–10, February 2011. 77
- [155] PASQUALE MADDALONI, GIANLUCA GAGLIARDI, PIETRO MALARA, AND PAOLO DE NATALE. *J. Opt. Soc. Am. B*, **23**(9):1938–1945, 2006. 94
- [156] AHMED MAHJOUN, AMRITA CHAKRABORTY, VALERIA LEPERE, KATIA LE BARBU-DEBUS, NIKHIL GUCHHAIT, AND ANNE ZEHNACKER. *Phys. Chem. Chem. Phys.*, **11**(25):5160, 2009. 194
- [157] JAN MAKAREWICZ. *The Journal of Chemical Physics*, **129**(18):184310, 2008. 41, 135, 136, 137, 138, 171
- [158] ARTHUR G. MAKI AND DONALD R. JOHNSON. *J. Mol. Spec.*, **47**(2):226–233, August 1973. 215
- [159] P. MALARA, P. MADDALONI, G. GAGLIARDI, AND P. DE NATALE. *Opt. Express*, **14**(3):1304–1313, 2006. 94
- [160] MARK D. MARSHALL, KAMIL CAN IZGI, AND J. S. MUENTER. *The Journal of Chemical Physics*, **107**(4):1037, 1997. 218
- [161] MARK D. MARSHALL AND J. S. MUENTER. *J. Mol. Spec.*, **85**(2):322–326, February 1981. 214
- [162] K. MATSUMURA, F. J. LOVAS, AND R. D. SUENRAM. *J. Mol. Spec.*, **144**(1):123–138, November 1990. 213
- [163] M. T. MCCULLOCH, G. DUXBURY, AND N. LANGFORD. *Molecular Physics: An International Journal at the Interface Between Chemistry and Physics*, **104**(16):2767 – 2779, June 2009. 114
- [164] M. R. MCCURDY, Y. A. BAKHIRKIN, AND F. K. TITTEL. *Applied Physics B: Lasers and Optics*, **85**(2):445–452, 2006. 78
- [165] MATTHEW R. MCCURDY, YURY BAKHIRKIN, GERARD WYSOCKI, AND FRANK K. TITTEL. *Journal of Biomedical Optics*, **12**(3):034034, 2007. 78
- [166] A. R. W. MCKELLAR, YUNJIE XU, AND WOLFGANG JAEGER. *The Journal of Physical Chemistry A*, **111**(31):7329–7337, August 2007. 2
- [167] J. B. MCMANUS, P. L. KEBABIAN, AND M. S. ZAHNISER. *Appl. Opt.*, **34**(18):3336–3348, 1995. 95, 96
- [168] J. B. MCMANUS, D. D. NELSON, J. H. SHORTER, R. JIMENEZ, S. HERNDON, S. SALESKA, AND M. ZAHNISER. *Journal of Modern Optics*, **52**(16):2309 – 2321, May 2009. 95
- [169] J. BARRY MCMANUS. *Appl. Opt.*, **46**(4):472–482, 2007. 95
- [170] J. BARRY MCMANUS AND PAUL L. KEBABIAN. *Appl. Opt.*, **29**(7):898–900, 1990. 95, 268
- [171] J. BARRY MCMANUS, MARK S. ZAHNISER, DAVID D. NELSON, LEAH R. WILLIAMS, AND CHARLES E. KOLB. *Spectrochimica Acta Part A: Molecular and Biomolecular Spectroscopy*, **58**(11):2465–2479, 2002. 95
- [172] D.A. MCWHORTER, E. HUDSPETH, AND B.H. PATE. *The Journal of chemical physics*, **110**:2000, 1999. 59, 61
- [173] DMITRY G. MELNIK, SANDHYA GOPALAKRISHNAN, TERRY A. MILLER, FRANK C. DE LUCIA, AND SERGEY BELOV. *The Journal of Chemical Physics*, **114**(14):6100, 2001. 181
- [174] L. MENZEL, A. A. KOSTEREV, R. F. CURL, F. K. TITTEL, C. GMACHL, F. CAPASSO, D. L. SIVCO, J. N. BAILLARGEON, A. L. HUTCHINSON, A. Y. CHO, AND W. URBAN. *Applied Physics B: Lasers and Optics*, **72**(7):859–863, 2001. 78, 131

REFERENCES

- [175] D.J. MILLEN. *Can. J. Chem.*, **63**:1477, 1985. 35, 216
- [176] R. E. MILLER. *The Journal of Physical Chemistry*, **90**(15):3301–3313, July 1986. 228
- [177] R. E. MILLER. *Science*, **240**(4851):447–453, April 1988. 40, 139, 194
- [178] ROGER E. MILLER. *Accounts of Chemical Research*, **23**(1):10–16, January 1990. 40, 139, 194
- [179] TERRY A. MILLER. *Science*, **223**(4636):545 – 553, February 1984. 260
- [180] I. M. MILLS. *Pure and Applied Chemistry*, **11**(3-4):325–344, 1965. 37
- [181] A. S. N. MURTHY AND C. N. R. RAO. *Appl. Spectrosc. Rev.*, **2**(1):69, 1968. 194
- [182] M. MÜRTZ, P. PALM, W. URBAN, AND A.G. MAKI. *J. Mol. Spec.*, **204**(2):281–285, December 2000. 214
- [183] D. D. NELSON, G. T. FRASER, K. I. PETERSON, K. ZHAO, W. KLEMPERER, F. J. LOVAS, AND R. D. SUENRAM. *The Journal of Chemical Physics*, **85**(10):5512, 1986. 181, 184
- [184] D. D. NELSON, J. H. SHORTER, J. B. MC-MANUS, AND M. S. ZAHNISER. *Applied Physics B: Lasers and Optics*, **75**(2):343–350, 2002. 95, 114
- [185] D J NESBITT. *Annual Review of Physical Chemistry*, **45**(1):367–399, 1994. 40, 139, 194
- [186] DAVID J. NESBITT. *Chemical Reviews*, **88**(6):843–870, 1988. 40, 139, 194
- [187] DAVID J. NESBITT AND ROBERT LASCOLA. *The Journal of Chemical Physics*, **97**(11):8096, 1992. 135, 142, 153
- [188] DAVID J. NESBITT AND RON NAAMAN. *The Journal of Chemical Physics*, **91**(7):3801, 1989. 40, 139
- [189] DAVID J. NESBITT AND MARTIN A. SUHM. *Physical Chemistry Chemical Physics*, **12**(29):8151, 2010. 40
- [190] HARALD H. NIELSEN. *Physical Review*, **77**(1):130, January 1950. 39
- [191] J. NOROOZ OLIAEE, M. DEGHANY, A. R. W. MCKELLAR, AND N. MOAZZEN-AHMADI. *The Journal of Chemical Physics*, **135**(4):044315–044315–11, July 2011. 2
- [192] T. OKA. *Handbook of High-resolution Spectroscopy*, 2011. 10, 18, 258
- [193] TAKESHI OKA. *J. Chem. Phys.*, **47**(12):5410, 1967. 205
- [194] I. PAK, M. HEPP, D. A. ROTH, AND G. WIN-NEWISSER. *Review of Scientific Instruments*, **68**(4):1668–1674, 1997. 102
- [195] D. PAPOUŠEK AND M.R. ALIEV. Number v. 17 in *Studies in physical and theoretical chemistry*. Elsevier Scientific Pub. Co., 1982. 11, 17, 242
- [196] DUŠAN PAPOUŠEK AND MAMED RAGIMOVICH ALIEV. Elsevier, 1982. 203
- [197] JESSICA A. PARR, GUOSHENG LI, IGOR FEDOROV, ANTHONY J. MCCAFFERY, AND HANNA REISLER. *J. Phys. Chem. A*, **111**(31):7589–7598, 2007. 195
- [198] JOSHUA B. PAUL, LARRY LAPSON, AND JAMES G. ANDERSON. *Appl. Opt.*, **40**(27):4904–4910, 2001. 94
- [199] JOSHUA B. PAUL, JAMES J. SCHERER, ANTHONY O’KEEFE, LARRY LAPSON, JANELLE R. ANDERSON, CLAIRE F. GMACHL, FEDERICO CAPASSO, ALFRED Y. CHO, D. CHRISTESEN STEVEN, AND J. SEDLACEK ARTHUR. **4577**, pages 1–11. SPIE, 2002. 94
- [200] K. I. PETERSON AND W. KLEMPERER. *J. Chem. Phys.*, **80**(6):2439, 1984. 220
- [201] HERBERT M. PICKETT. *The Journal of Chemical Physics*, **56**(4):1715, 1972. 40
- [202] HERBERT M. PICKETT. *J. Mol. Spec.*, **148**(2):371–377, August 1991. 54, 153, 201, 202, 228
- [203] H.M. PICKETT, J.C. PEARSON, AND C.E. MILLER. *Journal of Molecular Spectroscopy*, **233**(2):174–179, October 2005. 54
- [204] JOHN ROBINSON PIERCE. Van Nostrand, 1954. 265
- [205] DF PLUSQUELLIC. *Optical Technology Division Software Web Site, NIST*. 65
- [206] DF PLUSQUELLIC, RD SUENRAM, B. MATE, JO JENSEN, AND AC SAMUELS. *The Journal of Chemical Physics*, **115**:3057, 2001. 65
- [207] MARTIN QUACK AND MERKT, editors. 11
- [208] K.N. RAO AND C.W. MATHEWS. *Molecular Spectroscopy: Modern Research*. Academic Press, 1985. 19, 20, 36

REFERENCES

- [209] P. L. RASTON, W. JAEGER, H. LI, R. J. LE ROY, AND P.-N. ROY. *Physical Review Letters*, **108**(25):253402, June 2012. 2
- [210] P. L. RASTON, Y. XU, W. JAEGER, A. V. POTAPOV, L. A. SURIN, B. S. DUMESH, AND S. SCHLEMMER. *Physical Chemistry Chemical Physics*, **12**(29):8260, 2010. 2
- [211] H. REIERSEN AND A.R. REES. *Protein Engineering*, **13**(11):739–743, 2000. 57
- [212] BERND REIMANN, KONSTANTIN BUCHHOLD, SASCHA VAUPEL, BERNHARD BRUTSCHY, ZDENĚK HAVLAS, VLADIMÍR ŠPIRKO, AND PAVEL HOBZA. *J. Phys. Chem. A*, **105**(23):5560–5566, June 2001. 194
- [213] M. REZAEI, K. H. MICHAELIAN, A. R. W. MCKELLAR, AND N. MOAZZEN-AHMADI. *Physical Chemistry Chemical Physics*, **14**(23):8415, 2012. 2
- [214] MOJTABA REZAEI, N. MOAZZEN-AHMADI, A.R.W. MCKELLAR, BERTA FERNNDEZ, AND DAVID FARRELLY. *Molecular Physics*, **0**(0):1–8, January. 2
- [215] D. ROCCATANO, G. COLOMBO, M. FIORONI, AND A.E. MARK. *Proceedings of the National Academy of Sciences*, **99**(19):12179, 2002. 57
- [216] L.S. ROTHMAN, I.E. GORDON, A. BARBE, D.CHRIS BENNER, P.F. BERNATH, M. BIRK, V. BOUDON, L.R. BROWN, A. CAMPARGUE, J.-P. CHAMPION, K. CHANCE, L.H. COUDERT, V. DANA, V.M. DEVI, S. FALLY, J.-M. FLAUD, R.R. GAMACHE, A. GOLDMAN, D. JACQUEMART, I. KLEINER, N. LACOME, W.J. LAFERTY, J.-Y. MANDIN, S.T. MASSIE, S.N. MIKHAILENKO, C.E. MILLER, N. MOAZZEN-AHMADI, O.V. NAUMENKO, A.V. NIKITIN, J. ORPHAL, V.I. PEREVALOV, A. PERRIN, A. PREDOI-CROSS, C.P. RINSLAND, M. ROTGER, M. SIMECKOV, M.A.H. SMITH, K. SUNG, S.A. TASHKUN, J. TENNYSON, R.A. TOTH, A.C. VANDAELE, AND J. VANDER AUWERA. *Journal of Quantitative Spectroscopy and Radiative Transfer*, **110**(9-10):533–572, June. 33, 52, 87, 104, 112, 113, 139, 234
- [217] M.E. SANZ, V. CORTIJO, W. CAMINATI, J.C. LÓPEZ, AND J.L. ALONSO. *Chemistry-A European Journal*, **12**(9):2564–2570, 2006. 58
- [218] RICHARD J. SAYKALLY. *Acc. Chem. Res.*, **22**(9):295–300, 1989. 194
- [219] L. F. SCATENA, M. G. BROWN, AND G. L. RICHMOND. *Science*, **292**(5518):908–912, May 2001. 134
- [220] T. SCHARGE, C. CÉZARD, P. ZIELKE, A. SCHÜTZ, C. EMMELUTH, AND M.A. SUHM. *Phys. Chem. Chem. Phys.*, **9**(32):4472–4490, 2007. 57
- [221] T. SCHARGE, C. EMMELUTH, T. HÄBER, AND M.A. SUHM. *Journal of molecular structure*, **786**(2):86–95, 2006. 57, 59, 60, 61, 71, 72
- [222] T. SCHARGE, T. HÄBER, AND M.A. SUHM. *Phys. Chem. Chem. Phys.*, **8**(40):4664–4667, 2006. 57
- [223] C. A. SCHMUTTENMAER, R. C. COHEN, J. G. LOESER, AND R. J. SAYKALLY. *The Journal of Chemical Physics*, **95**(1):9, 1991. 181
- [224] C. A. SCHMUTTENMAER, R. C. COHEN, AND R. J. SAYKALLY. *The Journal of Chemical Physics*, **101**:146, 1994. 181, 182, 183
- [225] C. A. SCHMUTTENMAER, J. G. LOESER, AND R. J. SAYKALLY. *The Journal of Chemical Physics*, **101**(1):139, 1994. 181
- [226] N. SCHÖNBRUNNER, J. WEY, J. ENGELS, H. GEORG, AND T. KIEFHABER. *Journal of molecular biology*, **260**(3):432–445, 1996. 57
- [227] MICHAEL D. SCHUDER, JR. DAVID D. NELSON, AND DAVID J. NESBITT. *The Journal of Chemical Physics*, **94**(9):5796–5811, 1991. 98, 101
- [228] N. SEURRE, K. LE BARBU-DEBUS, F. LAHMANI, A. ZEHACKER, N. BORHO, AND M. A. SUHM. *Physical Chemistry Chemical Physics*, **8**(8):1007–1016, 2006. 128
- [229] KAMBIZ SHAHNAZI. *Applied Optics*, **37**(12):2502–2504, April 1998. 101
- [230] S. W. SHARPE, Y. P. ZENG, C. WITTIG, AND R. A. BEAUDET. *The Journal of Chemical Physics*, **92**(2):943–958, 1990. 98, 101
- [231] R L SHOEMAKER. *Annual Review of Physical Chemistry*, **30**(1):239–270, 1979. 113
- [232] JOEL A. SILVER. *Applied Optics*, **31**(6):707–717, February 1992. 101
- [233] R. E. SMALLEY. *The Journal of Chemical Physics*, **61**(10):4363, 1974. 260
- [234] RICHARD E. SMALLEY, LENNARD WHARTON, AND DONALD H. LEVY. *Accounts of Chemical Research*, **10**(4):139–145, April 1977. 260, 262
- [235] G. SPRINGHOLZ, T. SCHWARZL, W. HEISS, AND ANTHONY KRIER. pages 265–301. Springer-Verlag, London, 2006. 75

REFERENCES

- [236] THOMAS STEINER AND GAUTAM R. DESIRAJU. *J. Chem. Soc. Chem. Commun.*, **1998**(8):891–892, 1998. 194
- [237] J.I. STEINFELD. *Dover books on chemistry*. Dover Publications, 2005. 11
- [238] J.T. STEWART, B.E. BRUMFIELD, AND B.J. MCCALL. **TA03**, 2011. 143, 156
- [239] J.T. STEWART, B. M. GIBSON, AND B.J. MCCALL. **WF03**, 2012. 143, 156
- [240] ANTHONY J. STONE. Clarendon Press, 1997. 194
- [241] H L STRAUSS. *Annual Review of Physical Chemistry*, **34**(1):301–328, October 1983. 40
- [242] Z. SU, N. BORHO, AND Y. XU. *Journal of the American Chemical Society*, **128**(51):17126–17131, 2006. 3, 66
- [243] ZHENG SU, WAI SHUN TAM, AND YUNJIE XU. *The Journal of Chemical Physics*, **124**(2):024311, 2006. 75, 89, 96, 98, 100
- [244] ZHENG SU, QING WEN, AND YUNJIE XU. *Journal of the American Chemical Society*, **128**(20):6755–6760, May 2006. 3, 59, 71, 221, 222, 226
- [245] ZHENG SU AND YUNJIE XU. *Angewandte Chemie International Edition*, **46**(32):6163–6166, August 2007. 3, 221, 222
- [246] JAMES M. SUPPLEE, EDWARD A. WHITTAKER, AND WILFRIED LENTH. *Appl. Opt.*, **33**(27):6294–6302, 1994. 101
- [247] L. A. SURIN, A. V. POTAPOV, B. S. DUMESH, S. SCHLEMMER, Y. XU, P. L. RASTON, AND W. JAEGER. *Physical Review Letters*, **101**(23):233401, December 2008. 2
- [248] SAKAE SUZUKI, R. E. BUMGARNER, PAUL A. STOCKMAN, PETER G. GREEN, AND GEOFFREY A. BLAKE. *The Journal of Chemical Physics*, **94**(1):824, 1991. 135, 142
- [249] CRAIG A TAATJES AND JOHN F HERSHBERGER. *Annual Review of Physical Chemistry*, **52**(1):41–70, 2001. 101
- [250] WAI SHUN TAM, IGOR LEONOV, AND YUNJIE XU. *Review of Scientific Instruments*, **77**(6):063117, 2006. 75, 83, 93, 123, 129
- [251] KEIICHI TANAKA, TAKEHIKO TANAKA, AND ISAO SUZUKI. *The Journal of Chemical Physics*, **82**(7):2835, 1985. 218
- [252] JIAN TANG, YUNJIE XU, A. R. W. MCKELLAR, AND WOLFGANG JAEGER. *Science*, **297**(5589):2030–2033, September 2002. 2
- [253] FU-MING TAO AND WILLIAM KLEMPERER. *The Journal of Chemical Physics*, **101**(2):1129, 1994. 136, 138
- [254] YOSHIO TATAMITANI AND TERUHIKO OGATA. *J. Chem. Phys.*, **121**(20):9885, 2004. 214, 220
- [255] JAVIX THOMAS, FUMIE X. SUNAHORI, NICOLE BORHO, AND YUNJIE XU. *Chemistry: A European Journal*, **17**(16):4582–4587, 2011. 3
- [256] F. K. TITTEL, G. WYSOCKI, A. KOSTEREV, AND Y. BAKHIRKIN. pages 467–493. 2008. 78
- [257] ROBER TOTH. 113
- [258] S. TRANCHART, I. HADJ BACHIR, T.R. HUET, A. OLAFSSON, J.-L. DESTOMBES, S. NAÏM, AND A. FAYT. *J. Mol. Spec.*, **196**(2):265–273, August 1999. 214
- [259] . URBAN, V. PIRKO, D. PAPOUSEK, J. KAUPPINEN, S.P. BELOV, L.I. GERSHTEIN, AND A.F. KRUPNOV. *Journal of Molecular Spectroscopy*, **88**(2):274–292, August 1981. 201
- [260] SEBASTIAAN Y. T. VAN DE MEERAKKER, HENDRICK L. BETHLEM, AND GERARD MEIJER. *Nat Phys*, **4**(8):595–602, 2008. 260, 261
- [261] BENJAMIN J. VAN DER VEKEN, WOUTER A. HERREBOUT, ROMAN SZOSTAK, DIMITRIJ N. SHCHEPKIN, ZDENEK HAVLAS, AND PAVEL HOBZA. *J. Am. Chem. Soc.*, **123**(49):12290–12293, December 2001. 194
- [262] JENNIFER VAN WIJNGAARDEN AND WOLFGANG JÄGER. *Molecular Physics*, **98**(19):1575–1588, 2000. 135
- [263] JENNIFER VAN WIJNGAARDEN AND WOLFGANG JÄGER. *The Journal of Chemical Physics*, **114**(9):3968, 2001. 181
- [264] T.D. VARBERG AND K.M. EVENSON. *Instrumentation and Measurement, IEEE Transactions on*, **42**(2):412–414, 1993. 234
- [265] R. VASUDEV. *Applied Physics B: Lasers and Optics*, **87**(1):163–167, 2007. 123, 125
- [266] D. VERDES AND H. LINNARTZ. *Chemical Physics Letters*, **355**(5-6):538–542, April 2002. 135, 145
- [267] Š. URBAN, ROMOLA D’CUNHA, K NARAHARI RAO, AND D PAPOUŠEK. *Can. J. Phys.*, **62**(12):1775–1791, 1984. 214

REFERENCES

- [268] ZHONGCHENG WANG, MICHAEL ELIADES, KEITH CARRON, AND JOHN W. BEVAN. *Review of Scientific Instruments*, **62**(1):21–26, 1991. 102
- [269] JAMES K. G. WATSON. *The Journal of Chemical Physics*, **45**(4):1360–1361, August 1966. 36
- [270] JAMES K. G. WATSON. *The Journal of Chemical Physics*, **46**(5):1935–1949, March 1967. 36
- [271] JAMES K. G. WATSON. *Molecular Physics: An International Journal at the Interface Between Chemistry and Physics*, **15**(5):479, 1968. 15
- [272] JAMES K. G. WATSON. *The Journal of Chemical Physics*, **48**(1):181–185, January 1968. 36
- [273] JAMES K. G. WATSON. *The Journal of Chemical Physics*, **48**(10):4517–4524, May 1968. 36
- [274] JAMES K.G. WATSON. *Canadian Journal of Physics*, **79**(2):521, February 2001. 39
- [275] J.K.G. WATSON. *Molecular Physics*, **15**(5):479–490, 1968. 15
- [276] J.K.G. WATSON. *Vibrational spectra and structure*, **6**:1–89, 1977. 36, 64
- [277] MILES J. WEIDA AND DAVID J. NESBITT. *The Journal of Chemical Physics*, **106**(8):3078, 1997. 110, 117, 135, 141, 142, 143, 145, 146, 153, 165, 166, 167, 215
- [278] QING WEN AND WOLFGANG JÄGER. *J. Phys. Chem. A*, **110**(24):7560–7567, 2006. 135
- [279] E. BRIGHT WILSON. *International Journal of Quantum Chemistry*, **16**(S13):5–14, June 2009. 20
- [280] E.B. WILSON, J.C. DECIUS, AND P.C. CROSS. *Dover Books on Chemistry Series*. Dover Publications, 1955. 11, 13, 242
- [281] E.B. WILSON JR. *The Journal of Chemical Physics*, **4**:313, 1936. 15
- [282] E.B. WILSON JR. *The Journal of Chemical Physics*, **5**:617, 1937. 15
- [283] E.B. WILSON JR. *The Journal of Chemical Physics*, **7**:1047, 1939. 15, 250
- [284] E.B. WILSON JR AND JB HOWARD. *The Journal of Chemical Physics*, **4**:260, 1936. 15
- [285] G. WYSOCKI, R. F. CURL, F. K. TITTEL, R. MAULINI, J. M. BULLIARD, AND J. FAIST. *Applied Physics B: Lasers and Optics*, **81**(6):769–777, 2005. 78
- [286] G. WYSOCKI, R. LEWICKI, R.F. CURL, F.K. TITTEL, L. DIEHL, F. CAPASSO, M. TROCCOLI, G. HOFLEER, D. BOUR, S. CORZINE, R. MAULINI, M. GIOVANNINI, AND J. FAIST. *Applied Physics B: Lasers and Optics*, **92**(3):305–311, 2008. 78
- [287] S.S. XANTHEAS. *The Journal of chemical physics*, **104**:8821, 1996. 59, 69
- [288] WANG XIAO-GANG AND CARRINGTON JR TUCKER. Edmonton, 2010. 177
- [289] YUNJIE XU. *Molecular Physics: An International Journal at the Interface Between Chemistry and Physics*, **87**(5):1071–1082, 1996. 102
- [290] YUNJIE XU. *Molecular Physics: An International Journal at the Interface Between Chemistry and Physics*, **88**(3):859 – 874, June 1996. 102
- [291] YUNJIE XU, NICHOLAS BLINOV, WOLFGANG JAEGER, AND PIERRE-NICHOLAS ROY. *The Journal of Chemical Physics*, **124**(8):081101–081101–4, February 2006. 2
- [292] YUNJIE XU AND WOLFGANG JAEGER. *The Journal of Chemical Physics*, **119**(11):5457–5466, September 2003. 2
- [293] YUNJIE XU, WOLFGANG JAEGER, JIAN TANG, AND A. R. W. MCKELLAR. *Physical Review Letters*, **91**(16):163401, October 2003. 2
- [294] YUNJIE XU AND WOLFGANG JÄGER. *J. Chem. Phys.*, **106**(19):7968, 1997. 58, 193, 196
- [295] YUNJIE XU AND WOLFGANG JGER. John Wiley & Sons, Ltd, 2011. 1
- [296] YUNJIE XU, XUNCHEN LIU, ZHENG SU, RAVIRAJ M. KULKARNI, WAI SHUN TAM, CHEOLHWA KANG, IGOR LEONOV, LISA D’AGOSTINO, MANIJEH RAZEGHI, RENGARAJAN SUDHARSANAN, AND GAIL J. BROWN. **7222**, pages 722208–11, San Jose, CA, USA, 2009. SPIE. 132
- [297] YUNJIE XU AND A. R. W. MCKELLAR. *The Journal of Chemical Physics*, **104**(7):2488–2496, February 1996. 102
- [298] YUNJIE XU, JENNIFER VAN WIJNGAARDEN, AND WOLFGANG JAEGER. *International Reviews in Physical Chemistry*, **24**(2):301–338, 2005. 1
- [299] GUOCHUN YANG AND YUNJIE XU. *The Journal of Chemical Physics*, **130**(16):164506–164506–9, April 2009. 3

REFERENCES

- [300] GUOCHUN YANG AND YUNJIE XU. **298** of *Topics in Current Chemistry*, pages 189–236. Springer Berlin / Heidelberg, 2011. 3
- [301] JUN YE AND JOHN L. HALL. *Physical Review A*, **61**(6):061802, 2000. 101
- [302] JUN YE, LONG-SHENG MA, AND JOHN L. HALL. *Opt. Lett.*, **21**(13):1000–1002, 1996.
- [303] JUN YE, LONG-SHENG MA, AND JOHN L. HALL. *J. Opt. Soc. Am. B*, **15**(1):6–15, 1998. 101
- [304] L. YU-YAN, L. HONG-PING, G. YUAN-QING, L. JIE-LI, L. XIAO-YONG, H. GUANG-MING, L. FENG-YAN, AND L. JIN-RUI. *Chinese Physics*, **9**:184, 2000. 234
- [305] LU YUAN HAO, SHI QIANG, GUO RONG WU, LI QI, DANG FENG, QING SHI ZHU, AND ZHANG HONG. *Review of Scientific Instruments*, **73**(5):2079–2085, 2002. 95
- [306] R.N. ZARE. George Fisher Baker non-resident lectureship in chemistry at Cornell University. Wiley, 1988. 11, 242
- [307] A. ZEHACKER AND M.A. SUHM. *Angewandte Chemie International Edition*, **47**(37):6970–6992, 2008. 72
- [308] JUNRONG ZHENG, KYUNGWON KWAK, AND M. D. FAYER. *Acc. Chem. Res.*, **40**(1):75–83, January 2007. 194
- [309] D. ZOLANDZ, D. YARON, K. I. PETERSON, AND W. KLEMPERER. *J. Chem. Phys.*, **97**(5):2861, 1992. 220
- [310] E. ZWART AND W. LEO MEERTS. *Chemical Physics*, **151**(3):407–418, April 1991. 135, 142, 181
- [311] A. ZYBIN, Y. A. KURITSYN, V. R. MIRONENKO, AND K. NIEMAX. *Applied Physics B: Lasers and Optics*, **78**(1):103–109, 2004. 101